

IMPROVEMENT OF POWER CONVERSION  
EFFICIENCY OF SILICON SOLAR CELL COATED WITH  
METALLIC-POLYMER NANOCOMPOSITES

TAY BING YUAN

MASTER OF SCIENCE

FACULTY OF SCIENCE  
UNIVERSITI TUNKU ABDUL RAHMAN

MAY 2022

**IMPROVEMENT OF POWER CONVERSION EFFICIENCY OF  
SILICON SOLAR CELL COATED WITH METALLIC-POLYMER  
NANOCOMPOSITES**

**BY**

**TAY BING YUAN**

A dissertation submitted to the Department of Chemical Science,  
Faculty of Science,  
Universiti Tunku Abdul Rahman,  
in partial fulfillment of the requirements for the degree of  
Master of Science  
May 2022

## **ABSTRACT**

### **IMPROVEMENT OF POWER CONVERSION EFFICIENCY OF SILICON SOLAR CELL COATED WITH METALLIC-POLYMER NANOCOMPOSITES**

**TAY BING YUAN**

Silicon solar cell is an excellent candidate for the mass implementation of the photovoltaic device to harness solar energy. However, they are usually protected with a piece of silicon glass panel on their surface, which results in a reduction in light transmission. In addition, the high refractive index of silicon causes surface light reflection. Therefore, an efficient light harvesting scheme must be implemented to suppress the optical losses. In this study, a novel approach by depositing an anti-reflective coating on the glass surface of solar modules was demonstrated. The poly(methyl methacrylate-*co*-acrylic acid-*co*-trimethoxyvinylsilane), P(MMA-*co*-AA-*co*-TMVS) nanospheres with an average particle size of 97 nm were prepared through an emulsion polymerization process. Coating a functional array of polyacrylic nanospheres with 7 wt% of TMVS via the immersion self-assembly coating method resulted in the highest relative power conversion efficiency (PCE) enhancement of about 42%. Such an anti-reflective array of polyacrylic nanospheres was able to endure prolonged natural weathering exposure and remained reasonably high in relative PCE enhancement of 11.9-14.0% up to 130 days of outdoor exposure. The relative PCE improvement of solar modules was elevated

significantly to 73.2% by depositing an array of P(MMA-*co*-AA-*co*-TMVS) nanospheres containing 7 wt% of TMVS and 12.5 ppm of silver nanoparticles (AgNPs) with 10-30 nm in size. The encapsulated AgNPs were synthesized through a chemical reduction process with dodecylamine (S value of 2.78) as the capping agent at 0 °C. By introducing an additional protective layer of silane coating with hydrophobic nature, the solar modules overlaid with an array of polyacrylate nanocomposites were shielded from degradation and became more resistant to natural weathering processes. After 188 days of outdoor exposure, the highest relative PCE enhancement of 24.0% was retained for the pre-coated solar modules treated with 1.0 v/v% of nonafluorohexyltrimethoxysilane compared to the initial relative PCE enhancement of 68.1% before outdoor exposure.

## **ACKNOWLEDGEMENT**

This research is not individual achievement instead is the result of help and support from many people all this while. I would like to express my sincere gratitude and appreciation to my supervisors Assistant Professor Dr Chee Swee Yong and Assistant Professor Dr Mohammad Aminuzzaman as well as my external co-supervisor Associate Professor Dr Lee Chee Leong for their encouraging, immense knowledge and motivation. Their invaluable advice and guidance assisted me a lot in completing the research, which I greatly valued.

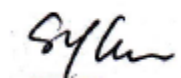
Other than that, I would like to thank my university, Universiti Tunku Abdul Rahman (UTAR), for the good environment and facilities as well as the research funding (UTARRF Grant No. IPSR/RMC/UTARRF/2014-C1/L03) to complete this project. I would also like to address my appreciation to all the laboratory officers in UTAR for the thought-provoking discussion and assistance provided throughout the project. Moreover, I am grateful to Mr Mohd Norizam Md Daud from Universiti Kebangsaan Malaysia (UKM) for the instrumentation support in the Advanced Silicon Solar Cells Laboratory.

I am thankful to my seniors for providing support, encouragement, useful feedback and insightful comments on my work. They are willing to help when the need arises. Last but not least, an honourable mention goes to my family and friends for their unconditional support, both financially and emotionally throughout my master's degree.

## APPROVAL SHEET

This dissertation/ entitled “**IMPROVEMENT OF POWER CONVERSION EFFICIENCY OF SILICON SOLAR CELL COATED WITH METALLIC-POLYMER NANOCOMPOSITES**” was prepared by TAY BING YUAN and submitted as partial fulfilment of the requirements for the degree of Master of Science at Universiti Tunku Abdul Rahman.

Approved by:



---

(Asst. Prof. Dr CHEE SWEE YONG)

Date: 2/5/2022

Assistant Professor/Supervisor

Department of Chemical Science

Faculty of Science

Universiti Tunku Abdul Rahman

---

(Asst. Prof. Dr MOHAMMOD AMINUZZAMAN) Date:

Assistant Professor/Co-supervisor

Department of Chemical Science

Faculty of Science

Universiti Tunku Abdul Rahman

**FACULTY OF SCIENCE**  
**UNIVERSITI TUNKU ABDUL RAHMAN**

Date: 2 May 2022

**SUBMISSION OF DISSERTATION**

It is hereby certified that **Tay Bing Yuan** (ID No: **19ADM06941**) has completed this dissertation entitled “IMPROVEMENT OF POWER CONVERSION EFFICIENCY OF SILICON SOLAR CELL COATED WITH METALLIC-POLYMER NANOCOMPOSITES” under the supervision of Dr Chee Swee Yong (Supervisor) from the Department of Chemical Science, Faculty of Science, and Dr Mohammod Aminuzzaman (Co-Supervisor) from the Department of Chemical Science, Faculty of Science.

I understand that University will upload softcopy of dissertation in pdf format into UTAR Institutional Repository, which may be made accessible to UTAR community and public.

Yours truly,

A handwritten signature in black ink, appearing to read 'Tay Bing Yuan', is written over a horizontal line.

(Tay Bing Yuan)

## DECLARATION

I hereby declare that the thesis/dissertation is based on my original work except for quotations and citations which have been duly acknowledged. I also declare that it has not been previously or concurrently submitted for any other degree at UTAR or other institutions.



(TAY BING YUAN)

Date 2 May 2022



## TABLE OF CONTENTS

	Page
<b>ABSTRACT</b>	ii
<b>ACKNOWLEDGEMENTS</b>	iv
<b>APPROVAL SHEET</b>	v
<b>SUBMISSION SHEET</b>	vi
<b>DECLARATION</b>	vii
<b>LIST OF TABLES</b>	xiv
<b>LIST OF FIGURES</b>	xviii
<b>LIST OF ABBREVIATIONS</b>	xxvi

## CHAPTERS

<b>1.0</b>	<b>INTRODUCTION</b>	<b>1</b>
1.1	Nanostructures	1
1.2	Metallic nanoparticles	2
	1.2.1 Synthesis of metallic nanoparticles	3
	1.2.2 Plasmonic effect of metallic nanoparticles	5
1.3	Polymeric nanoparticles	8
	1.3.1 Polymer	8
	1.3.2 Emulsion polymerization	10
1.4	Metallic-nanoencapsulated functional polymer	12
1.5	Light scattering effect of spherical nanoparticles	13
1.6	Silane coupling agent	15
	1.6.1 Dipodal silane coupling agent	17
	1.6.2 Non-functional silane coupling agent	19
1.7	Chemical bath deposition – self-assembly coating method	20
1.8	Solar cell	22
	1.8.1 Type of Si solar cell	24
	1.8.2 Electrical characteristics of solar cell	26
1.9	Problem statement	27
1.10	Objectives	32

<b>2.0</b>	<b>LITERATURE REVIEW</b>	<b>33</b>
2.1	Fabrication of silver nanoparticles	33
2.2	Factors affecting the formation of silver nanoparticles	36
2.2.1	Effect of initial concentration of metal precursor	36
2.2.2	Effect of concentration of reducing agent	38
2.2.3	Effect of concentration of capping agent	39
2.2.4	Effect of reaction temperature	41
2.3	Synthesis of polyacrylates nanoparticles	42
2.4	Preparation of metallic-polymer nanocomposites	44
2.5	Silane coupling agent	46
2.5.1	Silane coupling agent in the polymeric matrix	50
2.5.2	Dipodal silane	51
2.5.3	Non-functional silane for superhydrophobicity	54
2.5.4	Factor affecting the adhesion durability of silane coating	58
2.6	Improvement of power conversion efficiency of solar cells	60
2.6.1	Incorporation of metallic nanoparticles	61
2.6.2	Factors affecting the light trapping efficiency of solar attributed by metallic nanoparticles	65
2.6.3	Anti-reflective coating of polyacrylate matrix	69
2.6.4	Factors affecting the light trapping efficiency of solar attributed by anti-reflective coatings	72
<b>3.0</b>	<b>METHODOLOGY</b>	<b>74</b>
3.1	Chemicals	74
3.2	Instrumentation	77
3.3	Experimental procedures	77
3.3.1	Synthesis of AgNPs via chemical reduction method	78
3.3.2	Encapsulation of AgNPs into polymeric nanospheres via emulsion polymerization	79
3.3.2.1	Synthesis of polymeric nanospheres via emulsion polymerization	79

3.3.2.2	Preparation of metallic-polymer nanocomposite	81
3.3.3	Deposition of nanostructures on glass substrates	81
3.3.4	Chemically surface modification of precoated glass substrates	82
3.4	Characterization	83
3.4.1	Ultraviolet-visible spectroscopy	84
3.4.2	Field emission scanning electron microscopy	84
3.4.3	Energy dispersive X-ray spectroscopy	85
3.4.4	Fourier transform infrared spectroscopy	85
3.4.5	X-ray diffractometry	86
3.4.6	Total solids content	86
3.4.7	Particle size analysis	87
3.4.8	Atomic force microscopy	87
3.4.9	Thermogravimetric analysis	88
3.4.10	Differential scanning calorimetry	88
3.4.11	Transmission electron microscopy	89
3.4.12	Contact angle analysis	89
3.4.13	Water droplet analysis	89
3.5	Peeling test	90
3.6	Weathering resistance test	90
3.7	Electrical measurement of solar modules	91
<b>4.0</b>	<b>FABRICATION AND CHARACTERIZATION OF SILVER NANOPARTICLES</b>	<b>92</b>
4.1	Synthesis of silver nanoparticles via the chemical reduction method	92
4.1.1	Effect of reducing agent on the physical properties of AgNPs	92
4.1.2	Effect of capping agent and reaction temperature on the physical properties of AgNPs	94
4.1.3	Localized surface plasmon resonance effect of fabricated AgNPs	102

4.1.4	Crystallinity of AgNPs	107
4.1.5	Elemental composition of AgNPs functionalized by a capping agent	109
4.1.6	Functional groups of DDA-capped AgNPs	110
4.1.7	Optical properties of AgNPs	114
4.1.8	Percentage yield of AgNPs	116
<b>5.0</b>	<b>SYNTHESIS AND CHARACTERIZATION OF P(MMA-<i>CO-AA-CO-TMVS</i>) NANOSPHERES</b>	<b>117</b>
5.1	Synthesis of P(MMA- <i>co-AA-co-TMVS</i> ) nanospheres	117
5.1.1	Total solids content and percentage of monomer conversion of P(MMA- <i>co-AA-co-TMVS</i> ) copolymer emulsion	119
5.1.2	Structural properties of P(MMA- <i>co-AA-co-TMVS</i> )	120
5.1.3	Optical properties of P(MMA- <i>co-AA-co-TMVS</i> )	124
5.1.4	Elemental composition of P(MMA- <i>co-AA-co-TMVS</i> )	126
5.1.5	Functional groups of P(MMA- <i>co-AA-co-TMVS</i> )	128
5.1.6	Crystallinity of P(MMA- <i>co-AA-co-TMVS</i> )	136
5.1.7	Thermal stability of P(MMA- <i>co-AA-co-TMVS</i> )	138
5.2	Effect of coating method and amount of TMVS incorporated on the deposition of P(MMA- <i>co-AA-co-TMVS</i> ) nanospheres on a glass substrate	147
5.2.1	Surface morphological characteristics of deposited P(MMA- <i>co-AA-co-TMVS</i> ) nanoarray	148
5.2.2	Electrical measurement of solar modules	151
5.3	Effect of amount of TMVS on the surface wettability of P(MMA- <i>co-AA-co-TMVS</i> ) nanoarray	156
5.4	Effect of curing temperature on the adhesion durability of P(MMA- <i>co-AA-co-TMVS</i> ) nanospheres	158
5.5	Effect of natural weathering exposure on the adhesion strength of P(MMA- <i>co-AA-co-TMVS</i> ) nanospheres	162
5.5.1	Surface morphological characteristics of deposited P(MMA- <i>co-AA-co-TMVS</i> ) nanoarray	162

5.5.2	Electrical measurement of solar modules	167
<b>6.0</b>	<b>FABRICATION AND CHARACTERIZATION OF METALLIC-POLYMER NANOCOMPOSITES</b>	<b>175</b>
6.1	Encapsulation of AgNPs into P(MMA- <i>co</i> -AA- <i>co</i> -TMVS) nanospheres via emulsion polymerization	175
6.1.1	Topological characteristics of metallic-polymer nanocomposites	175
6.1.2	Crystallinity of metallic-polymer nanocomposites	178
6.1.3	Thermal stability of metallic-polymer nanocomposites	180
6.2	Effect of concentration and particle size of AgNPs entrapped into P(MMA- <i>co</i> -AA- <i>co</i> -TMVS) nanospheres on the light harvesting efficiency of nanocomposites	182
6.2.1	Electrical measurement of solar modules	182
6.2.2	Optical transmission of the polyacrylic coating	190
<b>7.0</b>	<b>GENERATION OF HYDROPHOBIC SURFACE USING A MIXTURE OF A DIPODAL AND FLUOROALKYL SILANES</b>	<b>192</b>
7.1	Elevation of adhesion strength of ARC system utilizing a dipodal silane	192
7.1.1	Effect of concentration of BTO silane	194
7.1.1.1	Surface morphological characteristics of the BTO silane coating	195
7.1.1.2	Optical transmission of the BTO silane coating	197
7.1.1.3	Surface wettability of the BTO silane coating	200
7.1.1.4	Electrical measurement of solar modules	203
7.1.1.5	Adhesive durability of the BTO silane coating	207
7.2	Generation of a highly hydrophobic surface via surface modification using a mixture of dipodal and fluoroalkyl silanes	210

7.2.1	Effect of concentration of fluoroalkyl silane	212
7.2.1.1	Optical transmission of the silane mixture coating	213
7.2.1.2	Surface wettability of the silane mixture coating	215
7.2.1.3	Electrical measurement of solar modules	219
7.3	Effect of natural weathering exposure on the adhesive durability of the coating system	221
7.3.1	Surface morphological characteristics of the polymeric array with a silane coating	222
7.3.2	Surface wettability of the polymeric array with a silane coating	226
7.3.3	Electrical measurement of solar modules	231
<b>8.0</b>	<b>CONCLUSIONS AND FUTURE PERSPECTIVE</b>	<b>237</b>
8.1	Conclusion	237
8.1.1	Fabrication and characterization of silver nanoparticles	237
8.1.2	Synthesis and characterization of P(MMA- <i>co</i> -AA- <i>co</i> -TMVS) nanospheres	238
8.1.3	Fabrication and characterization of functional P(MMA- <i>co</i> -AA- <i>co</i> -TMVS) nanospheres encapsulated with silver nanoparticles	239
8.1.4	Generation of a hydrophobic surface using a silane mixture of a dipodal and a fluoroalkyl silanes	240
8.2	Recommendations and future perspective	241
	<b>REFERENCES</b>	<b>243</b>
	<b>APPENDICES</b>	<b>262</b>
	<b>LIST OF PUBLICATIONS</b>	<b>269</b>

## LIST OF TABLES

Table	Page
1.1 The molecular formula and structure of MMA and AA	9
2.1 Commercially available coupling agent (Kalita and Netravali, 2015)	48
3.1 Chemical reagents used for the synthesis of AgNPs	75
3.2 Chemical reagents used for the synthesis of polymeric nanospheres	75
3.3 Chemical reagents used for chemically surface modification	76
3.4 Chemical reagents used for the cleaning of Si substrates	76
3.5 List of instruments	77
3.6 The S value corresponds to the amount of DDT and DDA added	79
3.7 Ingredients for emulsion polymerization	80
4.1 The particle size range of fabricated AgNPs corresponding to the S value and type of capping agent	95
4.2 The particle size of AgNPs obtained by using different concentrations of DDA at the reaction temperature of 0 °C and 25 °C	99
4.3 The particle size, absorbance, wavelengths with the respective calculated $E_{bg}$ of the AgNPs corresponding to the S value of DDA	104
4.4 FTIR spectrum data of DDA and DDA-functionalized AgNPs	113
5.1 The total solids content and the percentage of monomer conversion of P(MMA-co-AA) emulsion incorporated with different wt% TMVS	120
5.2 The mean particle size and particle size distribution of the polyacrylate nanostructures corresponding to the wt% of TMVS incorporated	122

5.3	The absorbance and wavelength of the absorption peak corresponding to the amount of TMVS incorporated into the polymeric matrix	125
5.4	Data extracted from FTIR of AA, MMA, TMVS, P(MMA- <i>co</i> -AA) and P(MMA- <i>co</i> -AA- <i>co</i> -TMVS)	132
5.5	The amorphous content and degree of crystallinity correlated with the P(MMA- <i>co</i> -AA) nanospheres with the incorporation of various wt% of TMVS	138
5.6	$T_d$ and percentage of residue at 550 °C of P(MMA- <i>co</i> -AA- <i>co</i> -TMVS) with different wt% of TMVS	141
5.7	$T_g$ of P(MMA- <i>co</i> -AA- <i>co</i> -TMVS) variants	146
5.8	Photovoltaic parameters of the uncoated and coated solar modules, with the latter being deposited with P(MMA- <i>co</i> -AA- <i>co</i> -TMVS) nanospheres containing various wt% of TMVS using (a) the immersion and (b) the dip coating methods	152
5.9	The average WCA of a water droplet formed on the surface of the modified glass substrate, corresponding to the amount of TMVS incorporated into the P(MMA- <i>co</i> -AA- <i>co</i> -TMVS) nanostructures	157
5.10	The output power of solar modules with and without a coating of P(MMA- <i>co</i> -AA- <i>co</i> -TMVS) nanospheres containing 7 wt% of TMVS, corresponding to the curing temperature and the peeling cycle	159
5.11	Average output power of uncoated and coated solar modules, with the latter deposited with P(MMA- <i>co</i> -AA- <i>co</i> -TMVS) nanospheres containing various wt% of TMVS via (a) the immersion and (b) the dip coating techniques as a function of the duration of natural weathering exposure	169



6.1	Photovoltaic parameters of the uncoated and coated solar modules, with the latter being coated with P(MMA- <i>co</i> -AA- <i>co</i> -TMVS) nanospheres encapsulated with (a) AgNPs (3-7 nm) and (b) AgNPs (10-30 nm) corresponding to AgNP concentration	184
6.2	Photovoltaic parameters of the uncoated and coated solar modules, with the latter being deposited with P(MMA- <i>co</i> -AA- <i>co</i> -TMVS) nanospheres containing different wt% of TMVS and encapsulated with 12.5 ppm of AgNPs with the particle size range of 10-30 nm	189
6.3	UV-Vis transmittance of the uncoated and coated glass substrates, with the latter being coated with P(MMA- <i>co</i> -AA- <i>co</i> -TMVS) nanospheres with 7 wt% of TMVS, and with the polyacrylic nanospheres encapsulated with 12.5 ppm of 10-30 nm AgNPs and 25.0 ppm of 3-7 nm AgNPs respectively	190
7.1	Light transmittance of glass substrates pre-coated with metallic-polymer nanocomposites and further chemically modified with various concentrations of the BTO silane	199
7.2	Photovoltaic parameters of both the untreated and treated solar modules, with the latter pre-coated with metallic-polymer nanocomposites and subsequently chemically surface modified with various concentrations of BTO silane	205
7.3	Output power measurement of both the uncoated and coated solar modules, with the latter pre-coated with metallic-polymer nanocomposites and further chemically surface modified with various concentrations of BTO silane as a function of the coating conditions	207
7.4	Light transmittance of glass substrates which had been pre-coated with metallic-polymer nanocomposites and followed by further surface modification with a mixture of 1.0 v/v% of BTO with various concentrations of FAS	214

7.5	Photovoltaic parameters of both the untreated and treated solar modules, with the latter pre-coated with metallic-polymer nanocomposites and subsequently chemically modified with a silane mixture of BTO and FAS, as a function of the concentration of FAS	220
7.6	The average WCA of glass substrates pre-coated with metallic-polymer nanocomposites and further chemically surface-modified with various silanes coatings before and after 188 days of natural weathering exposure	227
7.7	Photovoltaic parameters of both the untreated and treated solar modules, with the latter pre-coated with metallic-polymer nanocomposites and further chemically surface modified with various silane coatings, before and after 188 days of natural weathering exposure	231
7.8	The shunt resistance and series resistance of solar modules pre-coated with metallic-polymer nanocomposites and further chemically surface modified with various silanes coatings before and after 188 days of natural weathering exposure	234

## LIST OF FIGURES

Figure		Page
1.1	Schematic representation of LSPR effect (Willets and Duyne, 2007)	6
1.2	A schematic diagram illustrates surface plasmon polariton (Willets and Duyne, 2007)	7
1.3	Schematic representations of the type of metallic-encapsulated polymer nanocomposites (from left to right): single-core capsule, dispersed core in a polymer gel, multi-layer capsule, dual-core capsule and single-core-multi-shell capsule (Sarabia and MasPOCH, 2015)	12
1.4	Schematic diagram of Rayleigh and Mie scatterings (Lin, et al., 2014)	14
1.5	The overall bonding process of silanation (Krayden, 2009)	17
1.6	The structural formula of TMVS	17
1.7	General molecular structure of a dipodal silane	18
1.8	Schematic representation of the CBD technique	21
1.9	Schematic representation of a Si solar cell (RGS, 2015)	23
1.10	Different types of Si solar cells (Bagher, et al., 2015)	26
2.1	UV-Vis absorption spectrum of the AgNPs synthesized with different concentrations of AgNO <sub>3</sub> (Song, et al., 2008)	37
2.2	UV-Vis absorption spectrum of the AgNPs synthesized with different concentrations of NaBH <sub>4</sub> (Song, et al., 2008)	39
2.3	UV-Vis absorption peak of AgNPs synthesized with different concentrations of SDS (Song, et al., 2008)	40
2.4	An example of acrylate coupling reaction (Barry, 2018)	50
2.5	Hydrolytic stability of dipodal silanes (blue) compared to monopodal silanes (black) (Arkles, et al., 2014)	53
2.6	Cassie state of a superhydrophobic surface (Barry, 2018)	55

2.7	Structure designs of plasmonic-enhanced solar cells: (a) incorporation of metallic nanostructures on the surface of the active layer; (b) integration of metallic nanoparticles in the photoactive layer; (c) fabrication of metallic nanocolloids at the interface between the active layer and the metal contact (Chou and Chen, 2014)	62
3.1	Schematic diagram of the experimental setup for solar cell output power measurement	91
4.1	Schematic diagrams representing (a) absorption of $\text{BH}_4^-$ ion layer to the surface of AgNPs and (b) electrostatic repulsion between nanoparticles (Singh, et al., 2018)	93
4.2	FESEM images of AgNPs which were synthesized in an ice bath (0 °C) with different S value of DDT: (a) 2.78, (b) 5.56, (c) 11.1 and (d) 16.7 with a magnification of $\times 130000$ , $\times 65000$ , $\times 15000$ and $\times 10000$ respectively	95
4.3	FESEM images of AgNPs which were synthesized in an ice bath (0 °C) with different S value of DDA: (a) 2.78, (b) 16.7, (c) 22.2 and (d) 27.8 with a magnification of $\times 80000$	96
4.4	A schematic diagram of steric stabilization of AgNPs by capping agent molecules	98
4.5	FESEM images of AgNPs which were synthesized at room temperature (25 °C) with two S values of DDA: (a) 2.78 and (b) 16.7, with a magnification of $\times 20000$	99
4.6	Representation of the La Mer's mechanism of the nucleation and growth process of particles	100
4.7	Number of the resonance absorption peak of silver nanoparticles with different shapes and structures (Petryayeva and Krull, 2011)	103
4.8	UV-Vis spectra of AgNPs which were synthesized in an ice bath with different S values of DDA: (a) 2.78, (b) 16.7, (c) 27.8; and (d) overlay spectrum	106
4.9	XRD pattern of the AgNPs functionalized by DDA	108

4.10	EDX spectra of AgNPs stabilized with (a) DDT and (b) DDA, and the respective chemical structure of the capping agents	110
4.11	FTIR spectra of (a) DDA and (b) DDA-functionalized AgNPs	111
4.12	The solutions of DDA-capped AgNPs which were fabricated with DDA with the S value of (a) 2.78, (b) 16.7 and (c) 27.8 at 0 °C; while (d) was fabricated with DDA with the S value of 16.7 at 25 °C	115
5.1	The chemical structure of P(MMA- <i>co</i> -AA- <i>co</i> -TMVS) (Lee, et al., 2021)	118
5.2	The average particle size of P(MMA- <i>co</i> -AA- <i>co</i> -TMVS) nanostructures as a function of the amount of TMVS incorporated	121
5.3	Particle size distribution of P(MMA- <i>co</i> -AA- <i>co</i> -TMVS) nanostructures with the incorporation of (a) 0 wt%, (b) 5 wt%, (c) 7 wt% and (d) 9 wt% of TMVS	122
5.4	FESEM images of the P(MMA- <i>co</i> -AA) polymeric nanospheres incorporated with (a) 0 wt % (b) 5 wt % (c) 7 wt % and (d) 9 wt % of TMVS, with a magnification of ×40000	124
5.5	Overlaid UV-Vis spectra of P(MMA- <i>co</i> -AA) nanospheres incorporated with different amounts of TMVS	126
5.6	EDX spectra and the respective chemical structure of (a) P(MMA- <i>co</i> -AA) and (b) P(MMA- <i>co</i> -AA- <i>co</i> -TMVS)	127
5.7	FTIR spectra of (a) AA, (b) MMA, (c) P(MMA- <i>co</i> -AA) (d) FTIR spectrum of TMVS (e) FTIR spectrum of P(MMA- <i>co</i> -AA- <i>co</i> -TMVS) with 7 wt% of TMVS	129 130 131
5.8	XRD pattern of P(MMA- <i>co</i> -AA) polymer nanospheres	137
5.9	(a) TGA thermogram of P(MMA- <i>co</i> -AA) (b) TGA thermogram of P(MMA- <i>co</i> -AA- <i>co</i> -TMVS) with 7 wt% of TMVS (Lee, et al., 2021)	139 140

5.10	(a) DSC thermogram of P(MMA- <i>co</i> -AA) nanospheres	144
	(b) DSC thermogram of P(MMA- <i>co</i> -AA- <i>co</i> -TMVS) with 7 wt% of TMVS	145
5.11	AFM images of P(MMA- <i>co</i> -AA- <i>co</i> -TMVS) nanostructures deposited on a glass surface via the immersion and dip coating methods corresponding to the amount of TMVS in the copolymers	150
5.12	Relative enhancement in PCE of solar module coated with P(MMA- <i>co</i> -AA- <i>co</i> -TMVS) nanospheres containing various wt% of TMVS via the immersion and the dip coating techniques	151
5.13	The images of $\alpha$ -Si solar modules coated with P(MMA- <i>co</i> -AA- <i>co</i> -TMVS) nanospheres that were deposited via (left) the immersion technique, and (right) the dip coating technique	156
5.14	The image of a water droplet formed on the surface of a glass substrate which was captured by the contact angle analyzer fitted in the Laplace-Young model	156
5.15	Relative PCE enhancement of solar modules deposited with P(MMA- <i>co</i> -AA- <i>co</i> -TMVS) nanospheres with 7 wt% of TMVS, which were subjected to three cycles of peeling process correlating to different curing temperatures	159
5.16	(a) AFM images of the nanoarray of P(MMA- <i>co</i> -AA- <i>co</i> -TMVS) nanospheres containing various wt% of TMVS, which was deposited on a glass substrate via the immersion and the dip coating methods after 34 days of natural weathering exposure	164
	(b) AFM images of the nanoarray of P(MMA- <i>co</i> -AA- <i>co</i> -TMVS) nanospheres containing various wt% of TMVS, which was deposited on a glass substrate via the immersion and the dip coating methods after 130 days of natural weathering exposure	165

5.17	(a) Average relative enhancement in PCE of $\alpha$ -Si solar modules coated with P(MMA- <i>co</i> -AA- <i>co</i> -TMVS) nanospheres with different wt% of TMVS through the immersion coating methods as a function of the duration of outdoor natural weathering exposure	170
	(b) Average relative enhancement in PCE of $\alpha$ -Si solar modules coated with P(MMA- <i>co</i> -AA- <i>co</i> -TMVS) nanospheres with different wt% of TMVS through the dip coating methods as a function of the duration of outdoor natural weathering exposure	171
5.18	Schematic diagram of coupling of P(MMA- <i>co</i> -AA- <i>co</i> -TMVS) on the glass surface of solar modules via formation of siloxane linkages	172
6.1	Schematic representation of a polymeric nanosphere shell encapsulated with AgNP cores	176
6.2	TEM image of metallic-polymer nanocomposites	177
6.3	XRD pattern of metallic-polymer nanocomposites with 7 wt% of TMVS	179
6.4	TGA thermogram of metallic-polymer nanocomposite with 7 wt% of TMVS	181
6.5	Relative PCE enhancement of solar modules coated with metallic-polymer nanocomposites containing different sizes of AgNPs, as a function of the concentration of AgNPs	183
6.6	<i>J-V</i> curves of solar modules with and without a coating of P(MMA- <i>co</i> -AA- <i>co</i> -TMVS) nanospheres with 7 wt% of TMVS, and with the polyacrylic nanospheres encapsulated with 12.5 ppm of AgNPs (10-30 nm) and 25.0 ppm of AgNPs (3-7 nm)	185
6.7	Relative PCE enhancement of solar modules deposited with P(MMA- <i>co</i> -AA- <i>co</i> -TMVS) nanospheres encapsulated with 12.5 ppm of AgNPs with the particle size range of 10-30 nm by varying the wt% of TMVS in the copolymer	188

6.8	UV-Vis spectra of glass substrates with and without a coating of P(MMA- <i>co</i> -AA- <i>co</i> -TMVS) nanospheres with 7 wt% of TMVS, and with the polyacrylic nanospheres encapsulated with 12.5 ppm of AgNPs (10-30 nm) and 25.0 ppm of AgNPs (3-7 nm) respectively	191
7.1	The chemical structure of 1,8-bis(triethoxysilyl)octane dipodal silane	193
7.2	FESEM images of glass substrates pre-coated with metallic-polymer nanocomposites and further chemically surface modified with various concentration of BTO silane: (a) 0.1 v/v%, (b) 1.0 v/v%, (c) 3.0 v/v% and (d) 5.0 v/v%, with a magnification of $\times 40000$ , $\times 30000$ , $\times 10000$ and $\times 4000$ respectively	196
7.3	Schematic representation of a BTO silane crosslinked network	197
7.4	UV-Vis spectra of glass substrates pre-coated with metallic-polymer nanocomposites and further chemically modified with various concentrations of the BTO silane	198
7.5	The image of a water droplet formed on the surface of a treated glass substrate which was captured by the contact angle analyzer fitted in the Laplace-Young model (Lee, et al., 2021)	201
7.6	The images of a water droplet formed on the surface of a glass substrate pre-coated with metallic-polymer nanocomposites and subsequently modified with various concentrations of BTO	202
7.7	Relative PCE enhancement of solar modules pre-coated with metallic-polymer nanocomposites followed by surface modified with various concentrations of BTO silane	204
7.8	Schematic diagram of light trapping of an $\alpha$ -Si solar module pre-coated with metallic-polymer nanocomposites and further chemically surface modified using different concentrations of BTO silane	206



7.9	Relative enhancement in PCE of solar modules pre-coated with metallic-polymer nanocomposite and further chemically surface modified with various concentrations of dipodal silane corresponding to the coating conditions	208
7.10	The chemical structure of nonafluorohexyltrimethoxysilane	211
7.11	UV-Vis spectra of glass substrates which had been pre-coated with metallic-polymer nanocomposites and followed by further surface modification with a mixture of 1.0 v/v% of BTO with various concentrations of FAS	213
7.12	Schematic representation of a silane mixture of BTO and FAS crosslinked network	215
7.13	The images of a water droplet formed on the surface of a glass substrate which has been pre-coated with metallic-polymer nanocomposites and further chemically surface-modified with either a pristine FAS or a mixture of BTO and FAS, corresponding to the concentration of FAS	217
7.14	Relative enhancement in PCE of solar modules which had been pre-coated with metallic-polymer nanocomposites and subsequently chemically modified with a silane mixture of BTO and FAS corresponding to the concentration of FAS	219
7.15	AFM images of the glass substrates pre-coated with metallic-polymer nanocomposites and subsequently chemically modified with various silane coatings, as a function of the duration of natural weathering exposure	224
7.16	The images of a water droplet formed on the glass substrates which had been pre-coated with metallic-polymer nanocomposites and subsequently chemically modified with various silane coatings, as a function of the duration of natural weathering exposure	228

7.17	Relative PCE enhancement of solar modules pre-coated with metallic-polymer nanocomposites and further chemically surface modified with various silanes coatings before and after 188 days of natural weathering exposure, compared to the uncoated solar module	233
------	---	-----

## LIST OF ABBREVIATIONS

AA	Acrylic acid
$\alpha$ -Si	Amorphous silicon
ARC	Anti-reflective coating
AFM	Atomic force microscopy
$E_{bg}$	Bandgap energy
BTO	1,8-Bis(triethoxysilyl)octane
CBD	Chemical bath deposition
$T_d$	Degradation temperature
DSC	Differential scanning calorimetry
DDT	1-Dodecanethiol
DDA	Dodecylamine
EDX	Energy dispersive X-ray
FESEM	Field emission scanning electron microscopy
FF	Fill factor
FAS	Fluoroalkyl silane
FTIR	Fourier transform infrared
$T_g$	Glass transition temperature
LSPR	Localized surface plasmon resonance
MMA	Methyl methacrylate
$V_{oc}$	Open circuit voltage
PSA	Particle size analysis
P(MMA- <i>co</i> -AA)	Poly(methyl methacrylate- <i>co</i> -acrylic acid)
KPS	Potassium persulphate
PCE	Power conversion efficiency
$J_{sc}$	Short circuit current density
SCA	Silane coupling agent
Si	Silicon
AgNP	Silver nanoparticle
AgNO <sub>3</sub>	Silver nitrate
NaBH <sub>4</sub>	Sodium borohydride
SDS	Sodium dodecyl sulfate

TGA	Thermogravimetric analysis
TEM	Transmission electron microscopy
TMVS	Trimethoxyvinylsilane
UV-Vis	Ultraviolet-visible
WCA	Water contact angle
XRD	X-ray diffractometry

## **CHAPTER 1**

### **INTRODUCTION**

#### **1.1 Nanostructures**

Nanostructures are solid materials that either have an internal nanoscale structure or an external nanoscale dimension with the size range of 1 to 100 nm that are composed of unbounded, agglomerated and aggregated particles (Nasrollahzadeh, et al., 2019). Bulk substances with large particle sizes possess constant physical properties disregarding their size. However, the physicochemical properties of the materials below a critical size (at nanoscale) are dependent upon their particle size and the details of the matters (Mavani and Shah, 2013). The properties of nanostructures will alter significantly when the particle size of materials approaches the nanoscale which is smaller than the phase-coherent length or free path scattering length for electrons, with the increase in the total surface area (Ramrakhiani, 2012).

There are three factors that drive to the existence of distinctive and special features of nanostructures, which are large total surface area, quantum size effect and lattice contraction. The intrinsic properties of nanostructures include geometrical structure, ionization potential, electromagnetic, mechanical strength, and optical feature (Ramrakhiani, 2012). Owing to the unique characteristics of nanostructures which differ from bulk substances, nanostructure materials have attracted vast attention from researchers and are widely applied in various fields, such as optical devices, industrial catalysts,

cancer therapy, drug delivery, UV blocking textile, water disinfection, interactive food, electronic packaging and photovoltaic devices (Zaman, et al., 2014).

## **1.2 Metallic nanoparticles**

Metallic nanoparticles had received much attention from researchers owing to their promising plasmon excitation and electro-optical properties, namely localized surface plasmon resonance (LSPR) effect with its extraordinary size-dependent properties. LSPR frequency is highly dependent on the size, shape and dielectric nature of the nanoparticle interface with the surrounding environment (Khan, et al., 2019). Besides that, metallic nanoparticles also exhibit unique and significant features, namely large surface energy, photostability, photoluminescence, ease of functionalization and quantum confinement, which have resulted in their exploitation in several applications in different fields (Swami, et al., 2004).

Noble metallic nanoparticles, which include copper, silver and gold, have received much more attention compared to other metallic nanoparticles due to their optical property of broad absorption in the visible range of the electromagnetic solar spectrum (Tay, et al., 2020). They exhibit an extraordinary performance in absorbing and scattering light radiation. Noble metallic nanoparticles have been well studied with the presence of a capping agent, such as alkanethiol, polymer, and ligands, to serve as a protective group. Among the noble metallic nanoparticles, silver and gold are better studied

compared to copper due to their outstanding chemical stability. Silver and gold are less susceptible to oxidation reaction and thus resulted in less formation of the oxide layer. The only matter which can be tuned to diverse wavelengths in the visible electromagnetic radiation is silver nanoparticles (AgNPs). Owing to the highest efficiency of plasmon excitation exhibited, AgNPs are becoming significantly important materials in many technologies (Mavani and Shah, 2013).

### **1.2.1 Synthesis of metallic nanoparticles**

Fabrication and construction of metallic nanoparticles with different structural properties are dependent on their applications since the novel physical and chemical properties of nanomaterials highly depend on their size and shape (Mody, et al., 2010). Two general techniques to prepare metallic nanoparticles are top-down approach (microfabrication process) and bottom-up approach (self-assembly process) (Patra and Baek, 2014).

A capping agent which is also known as a stabilizer, is used as the protecting group to prevent and restrict the particles from aggregation, agglomeration and over-growth during the wet-chemical synthesis process. The formation of the bulk particle is thermodynamically favoured in the absence of repulsive force due to the large surface energy of nanoparticles that causes the coalescing and coagulation between particles (Harish, et al., 2018). Beyond that, capping agent is a prerequisite in stabilizing the metallic nanoparticles by interfacing, confining, limiting and controlling their structural and physiochemical

properties through manipulation of selective stabilizer adsorption. The reaction kinetics is regulated via the creation of a surfactant layer during the colloid growth process. Without a capping agent, the formation of metal oxide as a continuous phase is favoured instead of discrete nanoparticles (Phan and Nguyen, 2017). A capping agent is functioning through several mechanisms which include van der Waals forces, stabilization of steric, electrostatic, depletion and hydration forces (Ajitha, et al., 2016).

Being a type of stabilizers, capping agents are mostly amphiphilic molecules that consist of a polar head (hydrophilic) and a non-polar hydrocarbon tail (hydrophobic). The functionality of the stabilizer depends upon both the hydrophilic head and the hydrophobic tail. The hydrophilic head coordinates with the center metal atom of nanoparticles while the hydrophobic tail will interact with the surrounding medium. The polar head consists of donor atoms with functional groups, while the donor atoms carry unpaired electrons which can form coordinate bonds to the unsaturated surface of metal atoms through dynamic adsorption and desorption (Gulati, et al., 2018). Other than that, the capping agent is also crucial in determining the stability, reactivity, dispersibility, solubility and solvent interaction of the synthesized nanoparticles (Suriati, et al., 2014). Hence, an appropriate capping agent should be adopted. Moreover, some of the stabilizers are capable to play the additional role of a reducing agent to reduce the metal salt during a nano-fabrication process (Ajitha, et al., 2016).

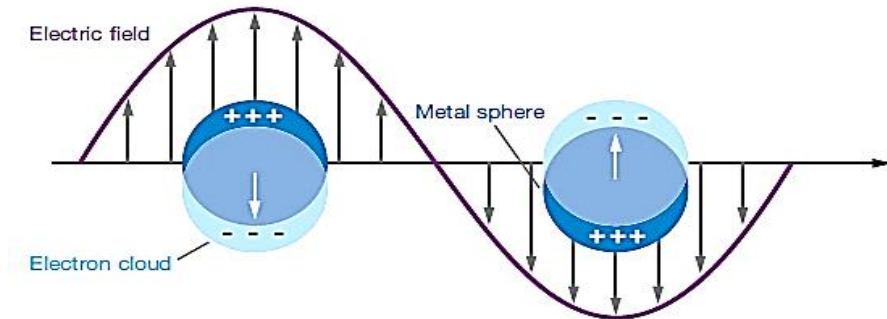


### **1.2.2 Plasmonic effect of metallic nanoparticles**

Surface plasmon effect was discovered by a scientist named Michael Faraday in 1857 during his research on the optical property of colloidal metallic nanoparticles. Surface plasmon is a phenomenon of the irradiation of metallic nanoparticles via electromagnetic radiation and results in the coherent oscillation of free electrons at the surface of metal ions and electromagnetic fields (Haugan, 2011). In other words, the interaction between incident light and a substance is mediated by surface electromagnetic excitations at the interface of dielectric metal. Consequently, the electromagnetic field in the immediate vicinity of the interface is magnificently improved (Maradudin, 2014). There are two well-known surface plasmons observed in the excited metallic nanoparticles surface, which are localized surface plasmon and surface plasmon polaritons.

Localized surface plasmon resonance (LSPR) is a collective charge density oscillation confined locally by metallic nanoparticles. It is an optical phenomenon that happens when the light wave trapped inside the conductive nanoparticles is smaller than the light wavelength, however, the natural frequency of incident light matches the conduction electron's oscillation frequency (Chou and Chen, 2014). The particular interaction results in coherent localized plasmon oscillations with a resonant frequency, as shown in Figure 1.1. The oscillation wavelength, intensity and resonant frequency have a strong correlation with the separation distance between particles, particle size, shape,

density of electrons, dielectric constant of surrounding and electronic structure of particles (Pettryayeva and Krull, 2011).

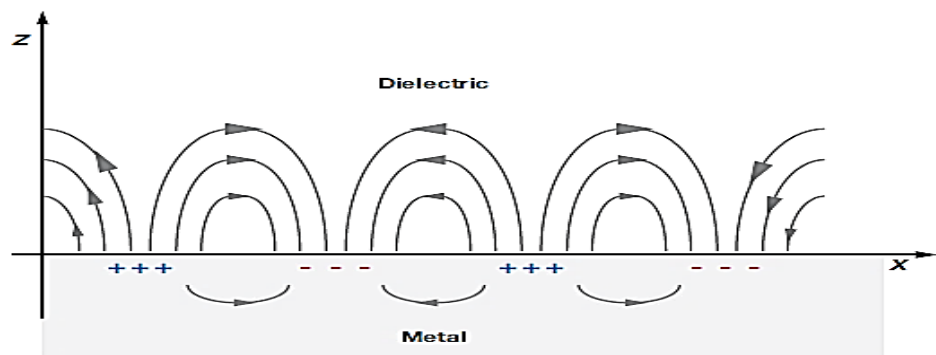


**Figure 1.1:** Schematic representation of LSPR effect (Willems and Duyne, 2007)

When the metal nanoparticles are excited by electromagnetic radiation at a certain frequency, an electromagnetic field is created. The free electrons are dislocated relative to fixed positive lattice ion due to the propagation of an electromagnetic wave, an attraction force resulting from Coulomb attraction between electrons and nuclei. Consequently, the free electrons (electron cloud) are oscillating coherently corresponding to the conduction band of the metal (Kelly, et al., 2002). The charge is separated and a dipole oscillation with the parallel direction axis to the electric field of light occurs due to the electron's oscillation behaviour on the surface of the particles. This causes incident light to scatter at a certain wavelength, which is known as the metal nanoparticles' dipole plasmonic resonance wavelength. The maximum amplitude at a specific oscillation frequency facilitates the LSPR effect (Elnoby, et al., 2018). As a result, improving the localized field as well as absorbing and scattering more light radiation. The process is known as LSPR because the excited plasmon is localized and cannot be propagated inside the nanoparticle (Chou and Chen, 2014). The noble metallic nanoparticles exhibit stronger LSPR than other

metallic nanoparticles. Most noble metallic nanoparticles have a resonance wavelength that falls within visible and infrared spectra (Barman, et al., 2018).

The second type of excited plasmon is known as surface plasmon polariton or propagating plasmon. This phenomenon occurs with the association of coherent oscillations of electromagnetic waves and the propagation of plasmon in x- and y-directions along with the planar interface between metal and dielectric layer with an amplitude that decays exponentially with distancing into each medium from the interface, as illustrated in Figure 1.2 (Willets and Duyne, 2007). The electromagnetic field of a surface plasmon polariton is confined at the metal surface, where the electric field is improved vertically to the surface (Chou and Chen, 2014) When the incident light is irradiated on the surface of metallic nanoparticles, surface plasmon polariton is excited with a symmetric propagation and causes the bending of light travelling along with the metal-dielectric interface or moving in a lateral direction inside the interface, which may then be absorbed by the photoactive dielectric material (Haugan, 2011).



**Figure 1.2:** A schematic diagram illustrates surface plasmon polariton (Willets and Duyne, 2007)

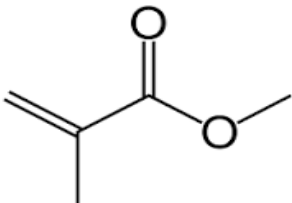
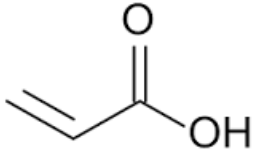
### **1.3 Polymeric nanoparticles**

Polymeric nanoparticles are colloidal materials that are made up of multiple repeating subunits, namely monomers through a polymerization process (Lu, et al., 2011). The use of polymeric nanoparticles is attributed to their numerous advantages, such as simplicity of manufacture and mold into various forms, easy to be modified by adding additives, cost effective processing, good corrosion and chemical resistance, intrinsic low electrical and thermal conductivity, good strength with lightweight, and mechanical flexibility (Hussain and Mishra, 2018). The polymeric nanoparticles have been found with various applications in our daily life since they are readily functionalized. Several polymerization techniques have been developed and are adopted in the synthesis of polymeric nanoparticles, which comprise emulsion polymerization, coacervation and *in situ* polymerization (Alkan, et al., 2014).

#### **1.3.1 Polymer**

A monomer is a basic unit that serves as the building block for a polymer, whereas monomers are bonded and joined together by a covalent bond to form a repeating linked chain and large molecule network (Yamak, 2013). In this study, poly(methyl methacrylate-*co*-acrylic acid) copolymer has been prepared by employing two different monomers, namely methyl methacrylate (MMA) and acrylic acid (AA), via an emulsion polymerization process. Table 1.1 shows the molecular formula and structure of both MMA and AA monomers.

**Table 1.1: The molecular formula and structure of MMA and AA**

Monomer	Formula	Structure
Methyl methacrylate	$\text{CH}_2=\text{C}(\text{CH}_3)\text{COOCH}_3$	
Acrylic Acid	$\text{CH}_2=\text{CHCOOH}$	

MMA is an unsaturated ester with a methyl group ( $-\text{CH}_3$ ) attaches to the carbon atom of the vinyl group ( $\text{CH}_2=\text{CH}-$ ). PMMA and its derivative copolymers are most commonly reported as polyacrylate, which has high demand in various design material development for both interior and exterior applications owing to its supreme photo behavior under UV exposure (Shanti, et al., 2017).

PMMA is a polymer with the properties of high clarity and transparency of ultraviolet radiation and visible light. Besides that, PMMA possesses prominent weather-resistance and lightweight features that resulted in its exploitation in the manufacturing of illuminated light displays, LED light guide panels and lens caps to maximize the light emitting and energy saving of the devices produced (ICIS, 2009). In addition, PMMA copolymer is utilized as an anti-reflective coating (ARC) on the surface of a photovoltaic device in order to maximize light transmission by minimizing the reflection of light (Lee, et al. 2021).

AA is an unsaturated carboxylic acid with a vinyl group connected to the carbonyl (C=O) carbon. AA monomers have a lot of applications in different fields, such as ingredients for making water-absorbent polymers, in addition to the manufacturing of acrylic esters which have been applied in surface and adhesive coatings (Landi, et al., 2005). Furthermore, the wetting behaviour and the stability of polymer dispersions can be improved by copolymerizing the AA monomer into the PMMA polymer chain (Lee, et al., 2021).

Copolymer consists of two or more different type of monomers that incorporate together into a single polymer chain to form a polymer molecular through copolymerization (Scott and Penlidis, 2017). The desirable excellent physical and chemical characteristics of the copolymer are allowed to be integrated by differing the monomers units.

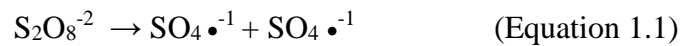
### **1.3.2 Emulsion polymerization**

Emulsion polymerization is a radical addition polymerization reaction that proceeds in a heterogeneous system by associating with the emulsification of hydrophobic building blocks using an oil-in-water emulsifier, where the hydrophobic monomers are dispersed in water as the continuous phase. In general, a typical emulsion polymerization involves monomers with a vinyl group (El-hoshoudy, 2018). The emulsion polymerization is initiated by a free radical initiator which is either water-soluble or oil-soluble. In order to disperse the hydrophobic monomers in an aqueous medium, the emulsifier or surfactant is prominent in the emulsion system. When the concentration of the emulsifier

exceeds the critical micelle concentration (CMC), micelles are formed. The emulsifier can be a protective colloid, an ionic or a non-ionic surfactant. Eventually, a milky latex is obtained where the colloidal polymer particles are dispersed in an aqueous solution.

An emulsion polymerization process consists of three major steps, including the initiation of the monomer radical to start the reaction, followed by the propagation process where more monomers are added to the monomer radical to form a polymer chain. Finally, the growing of a polymer chain is terminated when it reacts with another radical in the system (Yamak, 2013).

Free radical propagation begins with the entering of a water-soluble initiator into a micelle. In this work, potassium persulfate is employed as a thermal initiator. The generation of free radicals by persulfate is shown in Equation 1.1.



Emulsion polymerization is an important technique that has found enormous applications in various fields due to its distinctive advantages, such as simplicity and cost effectiveness which facilitate mass production, yielding polymers with high molecular weight. The polymerization process is comparatively rapid, with controllable temperature and viscosity, which uses water as the solvent to facilitate agitation. Thus, it provides an inherently safe and environmentally friendly process (Chern, 2008).

## 1.4 Metallic-nanoencapsulated functional polymer

Nanoencapsulation is defined as entrapping of particles (core) in a capsule (shell or matrix) at the nanoscale with a variety of shapes, depending on the preparation route and materials. Nano-entrapment technique can be categorized into two main classes: a core surrounded by a shell of the matrix material, and a core embedded inside a shell of matrix material (Sarabia and Maspoch, 2015). Beyond that, two main approaches are established to fabricate metallic-polymer functional nanocomposites, i.e. via direct preparation from a performed polymer and via a polymerization process (Kong, 2016).



**Figure 1.3:** Schematic representations of the type of metallic-encapsulated polymer nanocomposites (from left to right): single-core capsule, dispersed core in a polymer gel, multi-layer capsule, dual-core capsule and single-core-multi-shell capsule (Sarabia and Maspoch, 2015)

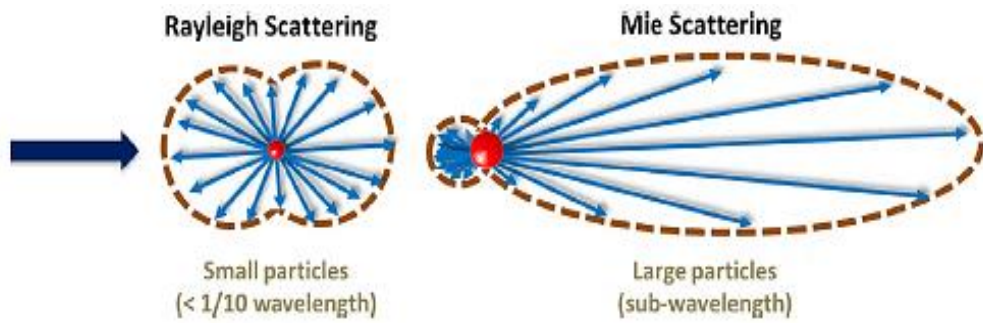
Metallic-nanoencapsulated functional polymer is a nanostructure in which metallic nanoparticles with smaller size are embedded inside a bigger size polymeric nanoparticle. This type of nanostructure combines the advantages and intrinsic properties of both metallic and polymeric nanoparticles, comprising both the optical and electrical characteristics contributed by metallic nanostructures and the dielectric, flexibility, processability and anti-reflective features attributed by polymeric nanostructures. Moreover, the



unique functionalities of both nanostructures are further enhanced to elevate their performance in minimizing the light reflection and maximizing the light scattering and light harvesting mechanisms. In addition, the nanoencapsulation technique has also significantly improved the stability of the embedded metallic nanostructures by preventing the nanoparticles from agglomeration, coagulation and aggregation. Thus, maintaining their particle size as well as their remarkable and extraordinary properties (Kong, 2016).

### **1.5 Light scattering effect of spherical nanoparticles**

Light scattering is an optical phenomenon that emerges upon the propagation and transmission of light radiation through an object. When light strikes on an object, the radiation can either scatter in the forward direction, leading to absorption and refraction, or scatter in the backward direction, resulting in reflection. If a substance possesses a dimension with the same order as the wavelength of light radiation, the photon will be scattered omnidirectionally. The substance that causes light scattering is referred to as a scattering center or scatterer. There are two theories that describe and explain the light scattering of a spherical scatterer (i.e. droplets and particles), namely Rayleigh and Mie scattering theories. The scattering theories are categorized by comparing the particle size of the scatterer and the wavelength of incident light (Zhang, et al., 2012). The size of spherical particles affects the incident light propagation dramatically in terms of the scattering modes (Lin, et al., 2014). Rayleigh and Mie scatterings are illustrated in Figure 1.4.



**Figure 1.4:** Schematic diagram of Rayleigh and Mie scatterings (Lin, et al., 2014)

Rayleigh scattering is predominant when the diameter of a dielectric spherical particle is much smaller than the wavelength of the light radiation, approximately less than one-tenth of the wavelength. In Rayleigh scattering, the light radiation is scattered omnidirectionally with the same magnitude in the intensity of both forward and reverse scattering (Lin, et al., 2014). Rayleigh scattering is well explained by the blue sky, where the air molecules like nitrogen and oxygen are well within the criteria of Rayleigh scattering theory, thus the blue light of the sun with a shorter wavelength is scattered more efficiently than the longer red light (Zhang, et al., 2012). On the other hand, Mie scattering theory is applicable to the particles with the size that are comparable with the wavelength of the incident light. For Mie scattering, the intensity of the forward scattering is higher in magnitude than the reverse scattering (Lin, et al., 2014). The natural phenomena of the appearance of a white glare around the sun and white clouds in the sky are owing to the dominant Mie scattering of large atmospheric particulates which is not strongly wavelength dependent.

## **1.6 Silane coupling agent**

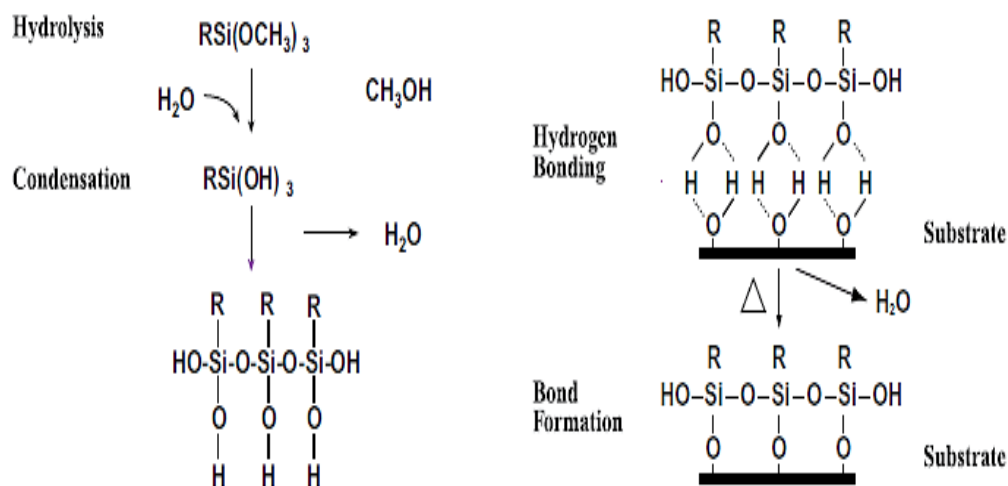
Silane coupling agent (SCA) is a bi-functional chemical compound with a general structure of four substituents attached to single silicon (Si) atom, which may have more than one diverse reactive functional group in the molecular structure (Pape, 2011). In general, the SCAs used for surface modification are categorized into two classes, functional and non-functional silanes. Functional silane is employed for biomolecule immobilization, polymer compounds and adhesive technologies; while non-functional silane is applied to modify the surface energy and wettability of a substance without imparting chemical reactivity to the substrate (Arkles, et al., 2014).

SCA serves as an adhesion promoter which is capable of forming a strong chemical bond (coupling) between two dissimilar materials (Barry, 2018). In other words, it acts as the interphase region and plays the role of bonding and bridging agent to enhance the adhesion strength of two dissimilar materials. As a matter of fact, organic and inorganic substances are very different in their physical and chemical characteristics, such as chemical reactivity, coefficient of thermal expansion, compatibility and surface properties. Hence, a strong adhesive bond between these two dissimilar substances is rather difficult to form. Therefore, organofunctional silanes are widely applied to improve the physical properties of the composite materials and effectively adhere the organic matters to the substrates with different polarities by forming a substantial cohesive bond structure (Sterman and Marsden, 1966).

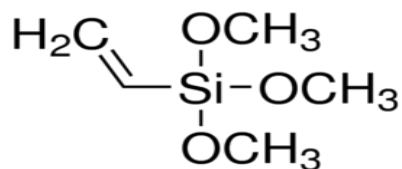
When inorganic substrates are reinforced with organic substances, the interphase region between these two matters is involved in a complex interaction of both chemical and physical factors, which comprise retention of product features, adhesion, dielectric, coefficient of expansion, and mechanical strength (Krayden, 2009). By applying an SCA, coupling bonds are formed at the interphase region which is able to impart resistance to and withstand the environmental and destructive forces like moisture and heat that may enervate the adhesive and bond strengths (Pape, 2011).

Silanation reaction is a process where the silane crosslink is formed through a hydrolyzation mechanism which involves two steps, i.e., hydrolysis and condensation. The hydrolyzable groups present in the organosilane compound like alkoxy silane groups (R-O-Si) are hydrolyzed to form silanol groups (Si-OH) by reacting with water. The silanol groups on adjacent silane are then condensed with a surface hydroxyl group (-OH) on the inorganic substrates to form the chemically stable covalent bonds, namely siloxane bonds (Si-O-Si) with the elimination of water molecules (Liu, et al., 2001). The rate-determining step for the reaction to occur is affected by the physical absorption of the alkoxy group onto the hydroxyl group of silica on a glass substrate and the reachability of the hydroxyl group. The overall silanation process is illustrated in Figure 1.5. In this study, an SCA, namely trimethoxyvinylsilane (TMVS) was employed as the adhesion promoter to enhance the bond durability and adhesion strength between the polymer matrix and the glass surface of photovoltaic cells. This was done by incorporating it into the copolymer nanospheres through the emulsion polymerization process. Figure

1.6 shows the structural formula of TMVS. In addition to that, SCAs can be used to enhance the adhesion of nanostructures on the glass surface of a photovoltaic cell as they are excellent adhesion promoters for glass substrates (Barry, 2018).



**Figure 1.5:** The overall bonding process of silanation (Krayden, 2009)

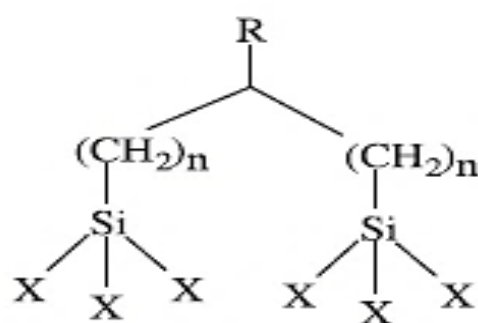


**Figure 1.6:** The structural formula of TMVS

### 1.6.1 Dipodal silane coupling agent

Dipodal functional silane is a bis-organosilane compound similar to common SCA in terms of molecular structure but with the difference of possessing two organosilane moieties in the molecule which are capable to form six covalent bonds to couple with the surface of a substrate. Contrary to mono-functional trialkoxysilane (with the ability to form three covalent bonds), dipodal silane

has higher efficiency to form oxane bonds on a less reactive surface due to the distinctive advantage of offering extra points for surface attachment. The integrity of coated films, composites in the aqueous environment and adhesive primers is dramatically improved via enhanced wettability and crosslink density at interphase. Figure 1.7 shows the general molecular structure of a dipodal silane.



**Figure 1.7:** General molecular structure of a dipodal silane

Dipodal silanes display superior protection to resist deterioration by the intrusion of water between an organic compound and an inorganic substrate. This is because the dipodal material is associated to extend out from the surface and thus provides superior resistance to hydrolysis (Singh, et al., 2014). Based on the equilibrium constant of dissociation of siloxane to silanol, dipodal silanes are excellent adhesion promoters with up to 10000 times higher in hydrolytic stability compared to conventional silanes. Therefore, the mechanical strength and bonding durability of the composite systems are significantly improved with prolonged product shelf life (Kaynak, et al., 2017).

### 1.6.2 Non-functional silane coupling agent

Non-functional SCAs are applied to modify the surface energy and wettability of a substrate under standard conditions without imparting any chemical reactivity. More particularly, they are able to alter the interaction between water and the boundary layer of the substrate's surface with a high degree of control, thus accomplishing different degrees of hydrophilicity and hydrophobicity (Barry, 2018).

A hydrophobic surface is generated and attributed by organosilanes with non-polar organic substituents, such as aliphatic and fluorinated hydrocarbons, in order to induce a more hydrophobic entity to shield the polar surface from interaction with water. Alkylsilane molecules with a longer carbon chain will provide a higher degree of hydrophobicity through the stabilization of a high-density monolayer by  $\pi-\pi$  interactions between adjacent chains (Bulliard, et al., 2010). The hydrophobic effect of the non-polar substitution has a strong correlation to the free energy transfer of hydrocarbon molecules from the aqueous phase to the hydrocarbon phase.

Fluoroalkylsilane (FAS) is a well-known non-functional organosilane with low-surface energy whereby a hydrophobic fluoro group is present at the tail-end of the molecule. The FAS can self-assemble into a thin monolayer film on the surface of a substrate with its molecular axis perpendicular to the surface. The FAS layer is applied to reduce the surface energy of a substrate and consequently, render a superhydrophobic surface (Liu, et al., 2015). A

superhydrophobic surface is a superior anti-wetting state of surface that accomplishes with a water contact angle (WCA) of more than  $150^{\circ}$  and leads to the beading of water into spherical droplets with roll-off angles of less than  $10^{\circ}$ . Thus, it results in the decrement of the water contact area and induces a reduction of adhesion. A superhydrophobic surface can be mimicked by either generating a rough surface on a hydrophobic substance or chemically modifying a rough surface via hydrophobic coating (Vidal, et al., 2019).

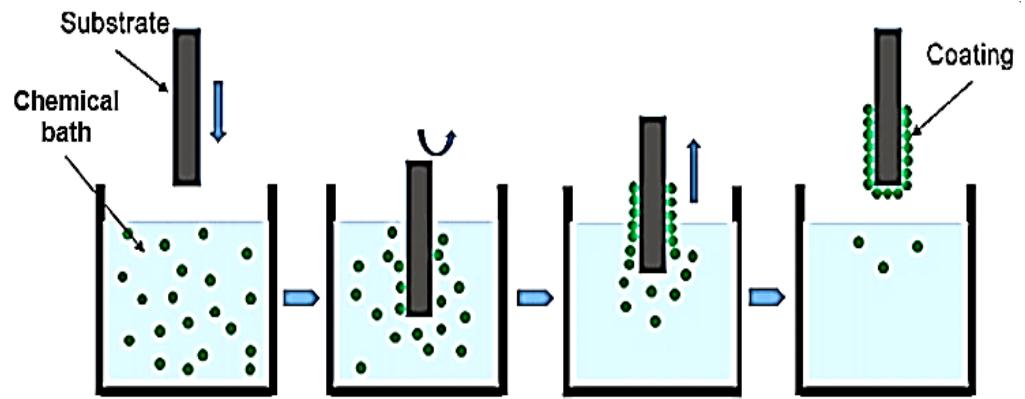
Besides its hydrophobic organic substituent, the capability of a non-polar organosilane to generate a hydrophobic surface is also affected by factors such as the extent of surface coverage and surface distribution of silane compounds, as well as the residual of unreacted groups from both the surface and the silane material (Barry, 2018). In order to form a hydrophobic film with supreme quality, the hydrogen atoms present in the polar hydroxyl groups (water-absorbing sites) on the substrate surface should be mitigated through the silanation process by employing an SCA.

### **1.7 Chemical bath deposition – self-assembly coating method**

Chemical bath deposition (CBD) method is a way to coat a thin layer of particle film by dipping or immersing and withdrawing the substrate into and out from the reservoir solution with precision control, as illustrated in Figure 1.8 (Guire, et al., 2013). Technically, CBD is performed based on the principle of a directed self-assembly coating mechanism, that is driven by various forces, including inertia force, surface tension, gravitational force and viscous drag



(Sahoo, et al., 2018). As a matter of fact, CBD enables the formation of a monolayer film with homogeneous coverage that is highly ordered and densely packed at the Van der Waals radii. The structure and thickness of the coated film can be controlled through manipulation of the kinetic of solids formation, comprising of the functionality of the substrate surface, the number of dipping cycle, temperature (usually below 100 °C), pH value, solution composition, the concentration of precursor solution, withdraw speed and immersion time (Guire, et al., 2013).



**Figure 1.8:** Schematic representation of the CBD technique

A variety of techniques have been proposed to deposit a thin film for solar energy-related applications. Among the developed approaches, the CBD technique which is a cost-effective, simple process with low energy consumption, is conceptually suited for generating a large area of a uniform thin film with extraordinary quality on semiconductors (Nair, et al., 1997). After deposition, the colloidal nanostructures are immobilized to the substrate surface by either covalent or non-covalent interactions with linkers in order to form a durable bond between the nanostructures and the substrate surface. The linkers that are utilized for non-covalent self-assembly include organic

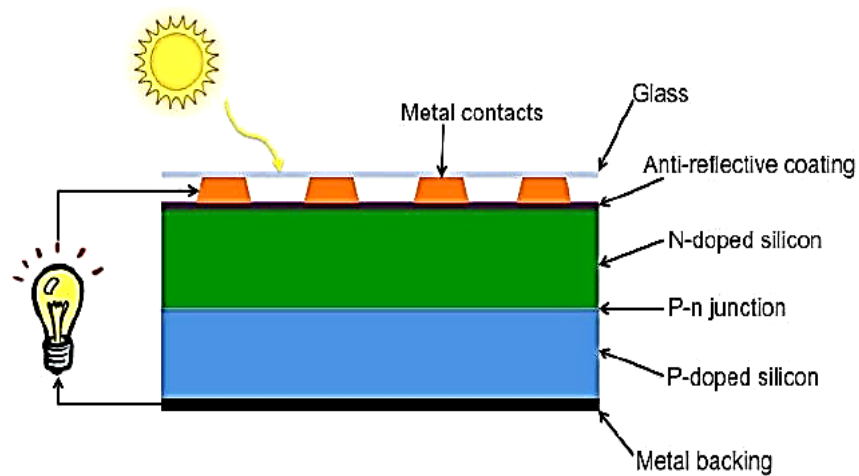
polymers and proteins; while for covalent self-assembly, dithiols and organosilanes are used (Rehacek and Hotovy, 2017).

Self-assembly refers to the spontaneous construction process of particles or discrete components into a complex but stable structure form through bouncing around in the solution with minimum energy. During the self-assembly process, the building blocks will organize into an ordered structure, either through direct specific interactions like inter-particle forces or indirectly via an external field or by utilizing a template (Grzelczak, et al., 2010). The particles in self-assembled structures will arrange themselves in appropriate locations according to their structural or chemical properties and subsequently bond to the surface of the substrate. The colloidal directed self-assembly coating method is crucial in photovoltaic, electro and optical nanotechnologies as it is a simple and cost-effective approach to fabricate anti-reflective coatings with an exact monolayer of film thickness (Askar, et al., 2013).

## **1.8 Solar cell**

Solar cell is a photovoltaic electrical device which is made of semiconductor materials with electrodes contacting both sides of the device. Photovoltaic cell captures the solar energy from sunlight and non-solar energy like photons from incandescent bulbs, and then converts them into electricity by means of the photovoltaic effect (Asim, et al., 2018). Silicon (Si) is the most common semiconductor material to produce solar cells. Si has the advantages of being environmentally friendly and available in sufficiently large quantities as it is

the second most abundant element found on earth's crust. Si is a semiconductor material with a bandgap energy of 1.12 eV which corresponds to the wavelength within infrared radiation. Thus, it is well suited for photovoltaic applications. In fact, Si solar cell is the most efficient photovoltaic device in terms of single-cell (Ranabhat, et al., 2016). Figure 1.9 shows the schematic representation of a Si solar cell.



**Figure 1.9:** Schematic representation of a Si solar cell (RGS, 2015)

In general, the working principle of the photovoltaic cell relies on three basic attributes: the photogeneration of charge carriers (electron-hole pairs) by absorbing the light radiation, the separation of charge carriers at the p-n junction to conductive contact, and the separate extraction of charge carriers to an external circuit (Bagher, et al., 2015). During the illumination and absorption of sunlight by the solar cell in the form of photons, holes and free electrons are generated at the p-junction and the n-junction, respectively. The current is transmitted to operate electrical devices when the DC electrical devices are connected to the p-n junctions of photovoltaic cells.

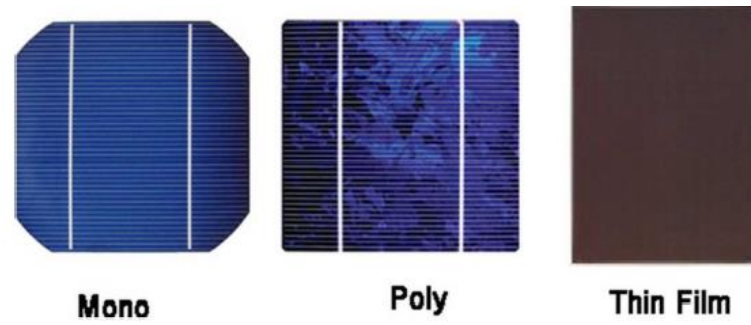
### **1.8.1 Type of Si solar cell**

Three major types of Si solar cells are available in the photovoltaic market. They are divided into groups based on the semiconductor materials used and the manufacturing process involved, namely crystalline, amorphous and hybrid Si photovoltaic cells. In general, a solar cell is named after the semiconductor material utilized for manufacturing (Bagher, et al., 2015).

Crystalline Si is known as an indirect gap semiconductor, whereby both the photons and phonons (vibration of the atomic lattice) are required to excite the electrons from the valence band to the conduction band. The absorption coefficient of an indirect gap semiconductor is comparatively lower than a direct semiconductor due to the engagement of photons and phonons simultaneously. Therefore, the Si layers are thicker (with a minimum thickness of 100  $\mu\text{m}$ ) in order to absorb the light radiation with a longer wavelength in the solar spectrum (Vozel and Arcon, 2011). Crystalline Si solar cells are further categorized into two different groups according to the type of crystalline Si used: monocrystalline and polycrystalline Si (Ranabhat, et al., 2016). Monocrystalline solar cells are built up of single-crystal Si in which the entire crystal lattice is continuous and free of grain boundaries that are fabricated through the Czochralski process. On the other hand, the polycrystalline solar cell is manufactured using metallurgical grade Si through chemical purification of the Siemens process. Both of the crystalline Si solar cells have high power conversion efficiency (PCE) within the range of 10-12%. However, monocrystalline Si solar cells exhibit a higher PCE than

polycrystalline Si solar cells (Simya, et al., 2018). Therefore, monocrystalline Si solar cell occupies about 30% of the photovoltaic market.

Amorphous silicon ( $\alpha$ -Si) solar cell is also known as thin-film Si solar cell, which is manufactured from a thin layer of non-crystalline Si (about 1  $\mu\text{m}$ ) that can perform efficiently in absorbing the light energy at high temperatures. However, twice of the rooftop space is required for an  $\alpha$ -Si solar cell in order to attain a similar output power as a crystalline Si solar cell (Simya, et al., 2018). The only structural difference between amorphous and crystalline Si solar cells is that the former has a single layer sequence of p-i-n junction, which has a region of intrinsic semiconductor between the n-doped and the p-doped layers. The triple layers system of  $\alpha$ -Si solar cell is purposely designed and optimized for maximizing the light radiation absorption from the full solar spectrum. The main advantage of the thin-film solar cell is its cost-effective manufacturing process because lesser semiconductor materials are required. Nonetheless, the  $\alpha$ -Si solar cell has low power conversion efficiency (PCE), only about 6%, and it suffers significant degradation in conversion performance due to the Staebler-Wronski Effect (Bagher, et al., 2015). Thin-film Si solar cell is commonly adopted in applications such as pocket calculators, remote facilities and buildings. Figure 1.10 depicts the three types of Si solar cells mentioned above: Monocrystalline, polycrystalline and thin-film Si solar cells.



**Figure 1.10:** Different types of Si solar cells (Bagher, et al., 2015)

Last but not least, a hybrid Si solar cell is a combination of two types of Si solar cells, by enclosing monocrystalline silicon with thin layers of amorphous silicon. It is very sensitive toward indirect light and lower light levels. Among the three types of solar cells, hybrid Si solar cells demonstrate the best performance in PCE at around 17% (Leonics, 2017).

### 1.8.2 Electrical characteristics of solar cell

A solar simulator is used to characterize the electrical performance of a photovoltaic device. The solar simulator is normally equipped with an arc lamp for illuminating the spectrum of the sun at AM 1.5. The common electrical characteristics are short circuit current density ( $J_{sc}$ ), open circuit voltage ( $V_{oc}$ ), fill factor (FF) and power conversion efficiency (PCE). An internal sweep circuit in the solar simulator system enables the current and voltage measurements that ultimately yield the current density-voltage ( $J$ - $V$ ) curve (Solanki, 2015).

Short circuit current density (unit: mA cm<sup>-2</sup>) is the maximum current per area produced by a photovoltaic device when its terminals are connected in series with the ammeter. Whereas, open circuit voltage (unit: V) is the maximum voltage generated by a photovoltaic cell when its terminals are connected in parallel with the voltmeter (Solanki, 2015; Goh, 2019). Besides, the fill factor is the maximum output power of a photovoltaic cell as a fraction of the ideal output power. It corresponds to the resistive losses in the photovoltaic device. On the other hand, the PCE of a photovoltaic device is defined as the ratio of maximum output power generated to the incident power of solar radiation. It could be calculated based on the electrical characteristics attained from the electrical measurement of the solar cell using a solar simulator as expressed in the equation below:

$$\text{PCE} = J_{sc} \times V_{oc} \times \text{FF} \quad (\text{Equation 1.2})$$

## 1.9 Problem statement

In Malaysia, fossil fuel has the most contribution to electricity supply as it is a prominent source for the generation of electric current. Electric energy is produced primarily through the burning of limited fossil fuels such as fuel oil, coal and natural gas in power plants which has brought large negative impacts and consequences to the surrounding environment. For instance, greenhouse gases are released and cause the depletion of the ozone layer and climate change. Meanwhile, fossil fuel reserves are depleting rapidly due to the increment in the demand for electric energy because of the development of the

economy, and over dependency on fossil fuels as they are non-renewable energy resources (Samsudina, et al, 2016). Therefore, solar energy has attracted widespread attention and has emerged as one of the promising alternative resources to replace fossil fuels and tackle the global energy crisis because of its unique features such as clean, vital renewable and sustainable. With the invention of light harvesting devices, solar energy can be captured and converted into electric energy. As a matter of fact, the amount of solar radiation that is irradiated on the earth over a three days period is equivalent to all fossil energy sources stored on the earth (Bagher, et al., 2015).

Converting solar energy into electric current by a solar cell is considered as a green technique because the photovoltaic system operates using a non-polluting and inexhaustible energy resource without the emission of greenhouse gases (Simya, et al., 2018). Nowadays, > 70% of solar panels that are available in the solar power market are manufactured using Si as the main raw semiconductor material due to its abundance on the earth, non-hazardous, environmental friendly, non-toxicity and well-established processing techniques (Lin, et al., 2014). Nonetheless, the PCE of commercially available Si solar cells is always comparatively lower than the theoretical efficiency reported by laboratories. This is due to the high refractive index of Si ( $n = 3.8$ ) that results in the reflection of incident light at almost 40% (Fang, et al., 2013). Furthermore, the photovoltaic industry has now moved to a new trend of mass-producing thin-film Si solar cells in order to reduce the processing cost. Nevertheless, this will suppress the absorption of photons into the photoactive site of the thin-film solar cell. In addition, solar cells are usually protected with



a piece of Si glass panel on their surface, which leads to a further reduction in light transmission. Therefore, less light radiation is harvested by such solar cells, which has resulted in less generation of free carriers and thus reduces the PCE of the solar modules (Jeng, et al., 2013).

In order to reduce the optical losses, chemical modification of the glass surface of photovoltaic devices becomes significantly important. Several light trapping mechanisms have been established for elevating the light trapping efficiency of Si solar cells via the generation of a surface texture. For instance, via deposition of polymer anti-reflective coating (ARC) and incorporation of nanostructures onto the Si substrate or into the photoactive region of a solar cell. Among the nanostructures studied, metallic nanoparticles have shown a remarkable improvement in the light harvesting efficiency of several types of photovoltaic devices (Chou and Chen, 2014). However, these approaches have their limitations which include limited operating wavelength range, narrow angle of incident radiation, poor adhesion strength and expensive manufacturing process (Solanki, 2015).

To overcome the drawbacks of the light harvesting mechanisms, noble metallic nanoparticles were encapsulated inside polymeric nanospheres in this study because of their capability in scattering the incoming light radiation by means of plasmonic effect, giving rise to the increase in the path length of incident light (Lin, et al., 2014; Goh, 2019). In addition, an adhesion promoter (SCA) was applied in order to enhance the adhesion strength between the nanostructures and the surface of solar cell by forming durable covalent bonds.

Besides that, the surface coverage of the deposited nanostructures was maximized, and a homogeneous and uniform particles distribution of coating was developed. Furthermore, a protective hydrophobic film was coated on the ARC using a mixture of organosilanes in order to prolong the lifetime of the coating and increase the adhesive durability upon natural weathering exposure. A cost-effective coating process has been designed, developed and evaluated in the research work.

In this work, we demonstrate a novel technique of depositing the nanostructures array, including metallic nanoparticles, polymeric nanospheres and metallic-nanoencapsulated functional polymer nanospheres, on the glass surface of an  $\alpha$ -Si solar module, which serves as light trapping and anti-reflective layers to enhance its light trapping efficiency (Lee, et al. 2021). Silver nanoparticles (AgNPs) will be fabricated through a chemical reduction method using silver nitrate as a metal precursor and sodium borohydride as a reducing agent. A suitable capping agent was used to ensure the yielding of excellent quality particles at the nanoscale. On the other hand, poly(methyl methacrylate-*co*-acrylic acid) [P(MMA-*co*-AA)] nanospheres were synthesized via a simple and cost-effective process, namely emulsion polymerization, with the incorporation of TMVS as the SCA. In this study, sodium dodecyl sulfate and potassium persulphate were used as a surfactant and thermal initiator respectively. Subsequently, AgNPs with different concentration were embedded inside polymeric nanospheres during the polymerization process. The nanostructures obtained were then deposited on the glass surface of  $\alpha$ -Si solar cells via a self-assembly coating method, namely CBD, with different

curing temperature. Two different approaches of CBDs were attempted, i.e., immersion and dip coating methods. Subsequently, mixtures of functional and non-functional organosilanes with different ratios were utilized to chemically modify the coating of the nanostructure array on the glass surface of an  $\alpha$ -Si solar module. This is to create a hydrophobic film to protect the nanostructure array. Lastly, the light trapping efficiency of treated solar cells was determined using a solar simulator.

## 1.10 Objectives

The aim of this project is to investigate the improvement of PCE of  $\alpha$ -Si solar module coated with metallic-polymer nanocomposites. To achieve the main research goal, the objectives of this study are including:

1. To synthesize and to encapsulate AgNPs into P(MMA-*co*-AA-*co*-TMVS) nanospheres.
2. To characterize the fabricated nanostructures using UV-Vis spectroscopy, AFM, FESEM, TEM, EDX, FTIR, XRD, PSA, TGA and DSC.
3. To study the coating parameters and coating methods by depositing polyacrylic nanostructures on the glass substrates.
4. To create a protective film with hydrophobic characteristics on the nanoarray of metallic-polymer nanocomposites which has been coated on the surface of a glass surface, by using a mixture of organosilanes.
5. To investigate the effect of the polyacrylic nanoarray and silane coatings on the PCE of solar cells.

## **CHAPTER 2**

### **LITERATURE REVIEW**

#### **2.1 Fabrication of silver nanoparticles**

A variety of synthesis methods have been developed and designed to produce AgNPs. Of that, the reported approaches are mainly categorized into three classes, namely chemical, physical and biological routes (Alaqad and Saleh, 2016). In general, the chemical route is used to prepare pure and well-defined metallic nanoparticles from chemical reactants with colloidal dispersion in organic solvent through a chemical reaction. On the other hand, the physical approach refers to the synthesis that enables mass production of metallic nanoparticles powder with narrow size distribution in a single step using costly instruments through mechanical energy. Last but not least, the biological synthetic process is performed with the utilization of natural reducing and capping agents such as plants extract, polysaccharides and biological microorganisms to obtain AgNPs (Natsuki and Hashimoto, 2015).

The chemical route is further subdivided into a few techniques including the chemical reduction method, polyol method and radiolytic process. Among the proposed approaches, the chemical reduction method has been vastly adopted to obtain AgNPs, due to advantages such as simple process, mild reaction condition, employment of inexpensive instrument, high yield, low preparation cost, yield of high purity nanoparticles without aggregation and controllable

particle size and shape by varying reaction parameters (Song, et al., 2008). A chemical reduction is a bottom-up approach whereby the metal ions in solvent are reduced in optimized conditions and resulted in the formation of small metallic clusters (El-Nour, et al., 2010). Four main components were employed in a chemical reduction process, which comprise metal precursor, reducing agent, stabilizer and solvent. The formation of AgNPs from colloidal solution through the reduction of silver metal salt involves two stages, nucleation and subsequently nuclei growth. Natsuki and Hashimoto (2015) revealed that the structural and geometrical features of AgNPs were strongly correlated with the synthetic stages.

The chemical reduction technique that is adopted in the fabrication of AgNPs uses a reducing agent such as sodium borohydride ( $\text{NaBH}_4$ ), ascorbic acid, sodium citrate, polyethylene glycol, Tollens reagent and formaldehyde. The reducing agent plays an important role in reducing the silver ions,  $\text{Ag}^+$  from silver metal salt into silver particles,  $\text{Ag}^0$  in aqueous solutions. Subsequently, the silver colloids agglomerate into oligomeric aggregates and thus AgNPs are formed. Meanwhile, a protective agent is significant to prevent the nanoparticles from coagulation through the interaction with the colloid's surface (El-Nour, et al., 2010). Different types of capping agents can be applied during the synthesis process. For instance, dodecanethiol (DDT), dodecylamine (DDA), polyvinyl alcohol, polyvinylpyrrolidone (PVP) and sodium dodecyl sulfate (SDS) have been used for this purpose.

According to Mavani and Shah (2013), spherical shaped AgNPs with 20 nm in diameter were synthesized through the reduction of silver nitrate ( $\text{AgNO}_3$ ) by  $\text{NaBH}_4$  with the presence of PVP as a capping agent. Nevertheless, AgNPs with a particle size of 4 nm were synthesized by utilizing the same starting reactants but with a different capping agent, DDT (Farrell, et al., 2013). In another reported journal article, SDS was used as the protective agent to stabilize the particle growth which had successfully fabricated AgNPs with the size range of 30-40 nm through the reduction process (Song, et al., 2008). In addition, some of the chemical reagents can perform as both reducing agent and capping agent simultaneously. For example, polyoxometalate was utilized to reduce silver metal salt while at the same time stabilizing the silver colloidal particles. Consequently, AgNPs with spherical shape and a particle size of 15.3 nm were formed (Troupis, et al., 2002).

Other than the spherical shape, cubic shaped AgNPs could also be fabricated through the reduction of  $\text{AgNO}_3$  using  $\text{NaBH}_4$  as a reducing agent and PVP as a capping agent at specific reaction conditions (Natsuki and Hashimoto, 2015). Moreover, a surfactant named acetyltrimethylammonium bromide was used as a capping agent during the reduction of  $\text{AgNO}_3$  by  $\text{NaBH}_4$  or ascorbic acid to synthesize AgNPs with nanorod shape (Guzel and Erdal, 2018). Sun et al. (2002) studied the synthesis of silver nanowires through the reduction of  $\text{AgNO}_3$  in the presence of PVP as a stabilizer. They found that silver nanowires with diameter ranged 30-40 nm could be produced by varying the reaction parameters, including seeding conditions, reaction temperature and concentration of PVP.

## **2.2 Factors affecting the formation of silver nanoparticles**

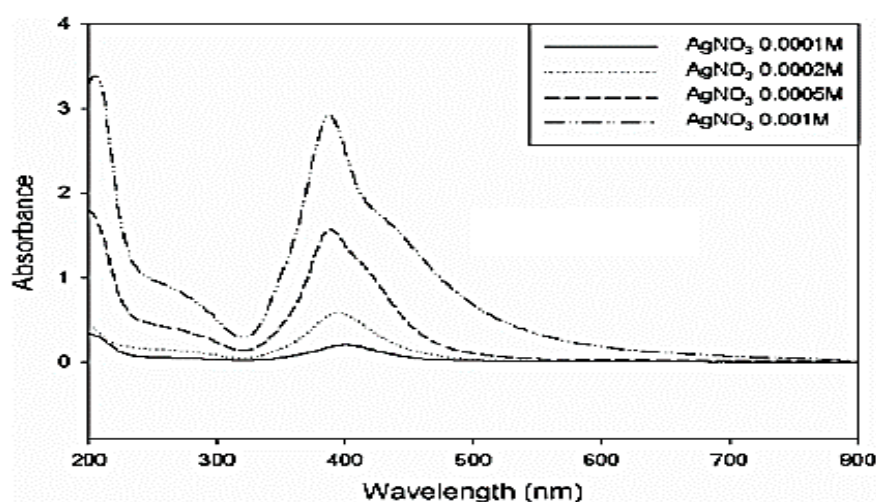
AgNPs with different physical and structural properties, including particle size distribution, crystallinity, particle shape and chemical compositions are fabricated by manipulating the growth of metallic colloidal particles. In order to obtain monodispersed AgNPs with narrow size distribution, all nuclei are required to form simultaneously at the initial nucleation stage in order to have a similar size for subsequent growth. The two particular stages involved in the formation of metallic nanoparticles during a chemical reduction process can be controlled by adjusting the synthetic parameters, including the concentration of metal precursor, reducing agent and capping agent as well as the reaction temperature. Therefore, AgNPs with the desired physical characteristics can be produced (Natsuki and Hashimoto, 2015). According to El-Nour and his team (2009), a small change in reaction parameters might lead to a dramatic alteration in the stability, physical and structural features of the nanoparticles synthesized.

### **2.2.1 Effect of initial concentration of metal precursor**

The concentration of silver metal precursor will manipulate the initial nucleation, nuclei growth, and subsequently the formation of AgNPs. During the chemical reduction of silver metal salt, the silver ions,  $\text{Ag}^+$  from the metal precursor would be reduced by a reducing agent to form silver colloids,  $\text{Ag}^0$  (Song, et al., 2008). According to Anigol et al (2017), the particle size of the synthesized AgNPs decreased with increasing silver ion intensity. Increment in



the absorbance and shifting of a plasmon resonance peak in the UV-Vis spectrum which manifests the LSPR was distinguishable with a change in AgNPs size. The narrowed plasmon peak indicates that the AgNPs were well dispersed in the solvent with the increase of the concentration of silver metal salt, as shown in Figure 2.1. Meanwhile, the concentration of metal salt solution might optically affect the colour of the fabricated AgNPs (Song, et al., 2008). The maximum plasmon peak intensity increased with the concentration of silver metal precursor, meanwhile, the solution turned from yellow colour to brown colour due to the formation of a higher concentration of AgNPs. Besides that, the addition sequence of reagents during the chemical reduction process is crucial for the fabrication of AgNPs. The metal precursor solution should be added dropwise and mixed homogeneously with reducing agent and capping agent solutions in order to obtain AgNPs with high stability. However, a reverse addition sequence of starting materials would result in an immediate precipitation of bulk particles.



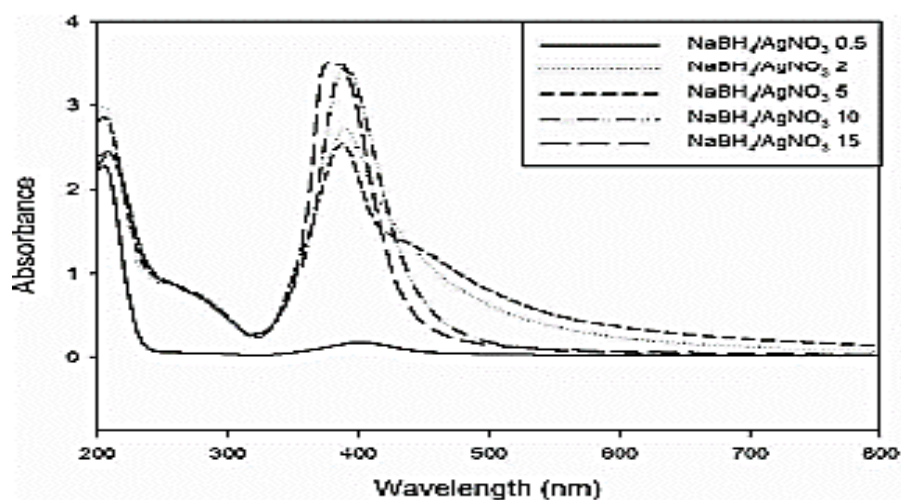
**Figure 2.1:** UV-Vis absorption spectrum of the AgNPs synthesized with different concentrations of AgNO<sub>3</sub> (Song, et al., 2008)

### 2.2.2 Effect of concentration of reducing agent

The concentration of the reducing agent is another parameter that plays an important role in controlling the physical and structural properties of AgNPs during a chemical reduction synthetic process. This particular factor was investigated by varying the molar ratio of the reducing agent to silver metal precursor while the other fabrication parameters remained constant. According to El-Nour et al. (2019), previous studies had proved that the utilization of a strong reducing agent like borohydride favoured the formation of monodispersed nanoparticles with smaller size distribution. The generation of larger colloidal was rather difficult to control. On the other hand, a weak reducing agent like citrate would slow down the rate of reduction and thus result in the broadening of particle size distribution.

Based on the research done by Song, et al. (2008), the percentage yield of AgNPs increased with the increase of the concentration of a reducing agent. The chemical reduction process was more complete as more  $\text{Ag}^+$  was reduced by the reductant to form AgNPs. The information on degree dispersion and size distribution of AgNPs could be obtained via UV-Vis spectroscopy. According to the results reported, AgNPs would agglomerate when only a small amount of reducing agent was added, which was owing to the decrease of electron density on the surface of particles. For example, a low concentration of  $\text{NaBH}_4$  which served as the reducing agent might produce boron hydroxide via hydrolysis of sodium hydroxide and attached to the nanoparticle surface. On the contrary, a reductant with higher concentration resulted in AgNPs with

smaller particle size and better degree of dispersion, which UV-Vis spectrum showed a plasmon absorption peak of higher intensity and narrower width, as illustrated in Figure 2.2. Besides that, the absorption of boron hydroxide was prohibited by a thick  $\text{BH}_4^-$  layer on the surface of nanoparticles. Nonetheless, Solomon et al. (2007) reported that an adequate concentration of reducing agent should be adopted while an excess amount might increase the overall ionic strength and hence, colloidal particles agglomerate and form in a larger size.

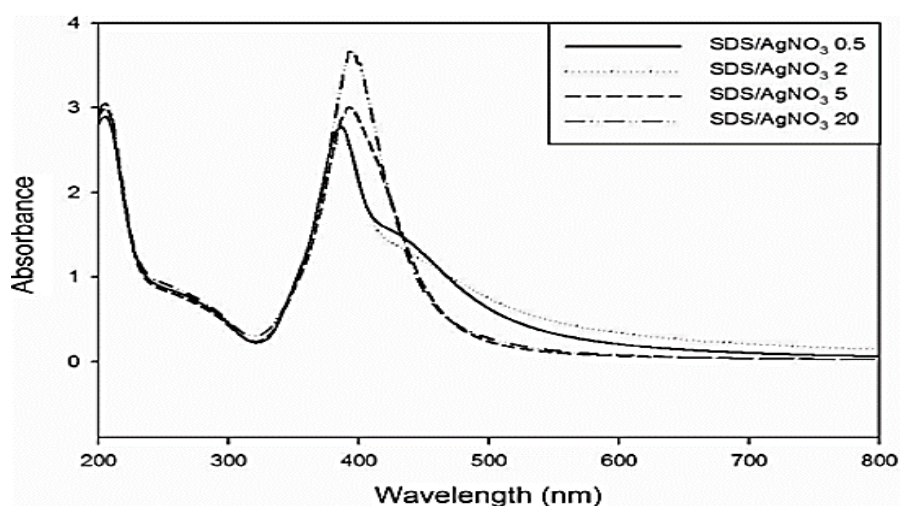


**Figure 2.2:** UV-Vis absorption spectrum of the AgNPs synthesized with different concentrations of  $\text{NaBH}_4$  (Song, et al., 2008).

### 2.2.3 Effect of concentration of capping agent

The capping agent or stabilizer functions as a protective group to prevent the nanoparticles from aggregation and agglomeration by controlling the growth of nuclei through either steric or electrostatic stabilizations. The concentration of the capping agent affects the physical and structural features of metallic nanoparticles dramatically. A small amount of capping agent used might lead

to aggregation and result in the formation of larger AgNPs due to the incomplete covering of colloidal particles by the stabilizer (Natsuki and Hashimoto, 2015). On the other hand, the nanoparticles with smaller particle size and a remarkable degree of dispersion could be fabricated using a higher concentration of stabilizer, which had been manifested by the narrow width and high intensity of plasmon absorption peak as shown in the UV-Vis spectra in Figure 2.3 (Song, et al., 2008). According to Farrell (2013) and Natsuki et al. (2013), the weight ratio of the capping agent (i.e. DDT and PVP) should be optimized during the synthesis of AgNPs via chemical reduction of  $\text{AgNO}_3$  by  $\text{NaBH}_4$  to ensure complete attachment of the stabilizer molecules to the surface of nanoparticles. The adsorbed stabilizer layer keeps the silver colloids apart and prevents them from aggregation. However, an excess amount of stabilizer did not increase the charges or provide a better surface coverage of the silver particles. Instead of further reducing the particle size, bigger size colloidal particles were formed.



**Figure 2.3:** UV-Vis absorption peak of AgNPs synthesized with different concentrations of SDS (Song, et al., 2008)

#### **2.2.4 Effect of reaction temperature**

Temperature is one of the essential factors in the synthesis of AgNPs because it controls the kinetic reaction of the reduction process. The higher the reaction temperature, the higher the rate of reduction. Natsuki and Hashimoto (2015) performed a chemical reduction process at 50 °C to fabricate AgNPs from AgNO<sub>3</sub> by using NaBH<sub>4</sub> as the reducing agent and PVP as the capping agent. The colourless reaction mixture was instantly turned into brown and subsequently black colour. The optical and topology results obtained showed that the rate of reaction increased significantly at higher temperature and resulted in the formation of particles with larger size and irregular shape which were appeared to be linked to each other. In addition, Jiang, et al. (2010) also supported and proved the hypothesis that particle size increased with temperature. The size of triangular-shaped AgNPs was increased from 90 nm to 180 nm when the reaction temperature was increased from 17 °C to 32 °C. A similar trend was also observed for spherical nanoparticles, as the size of the AgNPs grew from 25 nm to 48 nm. At high temperature, the particles gain more energy and move faster. Thus, more effective collisions occur between the colloidal particles and the nucleation and subsequent growth processes are accelerated. As a result, the AgNPs synthesized grow larger in size.

### **2.3 Synthesis of polyacrylates nanoparticles**

The derivative copolymers of MMA are commonly described as polyacrylates which can be synthesized through a copolymerization process. In homogeneous copolymerization, the copolymer product is soluble in a continuous phase. On the other hand, heterogeneous or dispersed-phase copolymerization describes a polymerization system in which at least one of the components is insoluble in the reaction medium. Such system was further developed into a few approaches, namely emulsion, suspension, precipitation and dispersion copolymerization, which provide better temperature and viscosity manipulation. The selection of the copolymerization techniques depends on viscosity considerations and process restrictions (Scott and Penlidis, 2017).

According to Scott and Penlidis (2017), the emulsion polymerization technique is notoriously susceptible to changes in the reaction solution, specifically reaction temperature and pressure, solution pH, ionic strength and type of solvent used. The polymeric nanostructures with a particle size range of 20 nm to 1  $\mu\text{m}$  can be prepared through an emulsion polymerization process (Caruso, 2004). The size distribution of the spherical polymer particles can be altered and adjusted via seeded nucleation and the growth of colloidal seeds in the beginning stage of the polymerization process. The utilization of seed particles enables manipulation of the characteristics of polymeric dispersions by varying both the number and size of seed particles and the amount of comonomers added. Semi-batch or feed processes offer the benefits of preparing polymer dispersions with controllable particles morphology, size distribution, and polymer composition. The characteristics of polyacrylate particles synthesized

through emulsion polymerization depend on the polymerization recipe which includes comonomers ratio, type and concentration of emulsifier.

In emulsion polymerization, surfactant played an important role in the nucleation of polymer colloidal particles, the emulsification of monomer droplets and the stabilization of latex particles (Tang, et al., 2003). Ming and his teammates (1998) synthesized PMMA nanoparticles with a diameter range between 33-46 nm using dodecyltrimethylammonium bromide as the emulsifier and potassium persulfate (KPS) as the initiator through the emulsion polymerization approach. The polymerization system was carried out at 60 °C with magnetic stirring. Besides that, they had also synthesized PMMA nanoparticles via modified microemulsion polymerization by mixing a small portion of monomer, surfactant (sodium dodecyl sulfate, SDS) and initiator in the reactor at the initial stage with a stirring speed of 600 rpm. Subsequently, the remaining ingredients were added dropwise. The addition of monomer in several portions could reduce the polymer particle size. Based on their research, PMMA with particle size greater than 13 nm was produced using a monomer to emulsifier ratio of 10:1 or higher.

Lee et al. (2017) also revealed that the copolymers particle size decreases with increasing concentration of surfactant. In their work, P(MMA-co-AA) nanospheres were fabricated through emulsion polymerization with 95 wt% of MMA and 5 wt% of AA, using SDS as the emulsifier and KPS as the initiator. The semi-batch process was performed at 75 °C with a stirring speed of 600 rpm. The diameter of the polymeric nanospheres was decreased from 156 to 97

nm with an increasing concentration of surfactant from  $0.53\text{--}2.10 \times 10^{-5}$  mol  $\text{cm}^{-3}$ . A sufficient amount of emulsifier enables the generation of particle precursor with homogeneous surface coverage on newly formed colloidal particles (He, et al., 2003). Nonetheless, the concentration of the emulsifier would only induce a small effect on particle size when it is beyond a certain amount. Besides that, the comonomer ratio would also affect the emulsion system and the structural properties of the copolymeric particles. The particle size of a spherical shaped P(MMA-*co*-AA)/n-eicosane was increased from 11.73 to 22.53  $\mu\text{m}$  by increasing the ratio of AA to MMA from 1:100 to 1:10 (Alkan, et al., 2014). Smaller polymeric particles were obtained when the ratio of water to monomer was relatively high due to lesser collision frequency between particles.

#### **2.4 Preparation of metallic-polymer nanocomposites**

Metallic-encapsulated functional polymer nanocomposites have attracted much attention and were vastly exploited in different applications owing to their distinctive and unique characteristics, including effective life cycle costs, unrivalled performance, design flexibility and enhanced features compared to constituent fragments (Awad, et al., 2019). Nanoencapsulation technique is categorized into two major classes, a core that is (a) surrounded by a polymer matrix shell and (b) embedded within a polymeric continuous network. Metallic nanoparticles are most commonly entrapped in functional polymeric nanostructures via heterogeneous emulsion polymerization. The advantages of such system include high purity and uniformity of nanocapsules, dispersible,



small particle size with narrow distribution, readily scalable and accentuated chemical homogeneity (Sarabia and MasPOCH, 2015). On the other hand, the approach of producing metallic-polymer nanocomposites directly from the preformed polymer is dependent on the specific interactions between the metallic colloids and the polymer materials. For instance, hydrophobic, electrostatic and secondary molecular interactions or self-assembly mechanisms that drive to envelop nanostructures onto a certain seed particle (Kong, 2016). According to Asapu, et al. (2016), the polymeric matrix was an effective barrier and prominent protective shell for stabilizing and preventing the metallic cores from aggregation and oxidation during the polymerization process without compromising the plasmonic features. The plasmonic near field improvement effect of encapsulated nanostructures was retained and preserved under high ionic strength and extreme oxidizing conditions. In addition, it was found that a slight alteration in the thickness of the polymeric capsules would significantly revise the plasmonic properties of the embedded metallic particles.

Scarabelli and his teammates (2019) had encapsulated noble metallic nanoparticles (gold and silver with a particle size of  $19 \pm 2$  nm and  $42 \pm 9$  nm, respectively) in di-block copolymers via seeded emulsion polymerization. Both of the noble metallic nanostructures remained unchanged after 24 h of immersion in a 10% aqua regia solution. In addition, AgNPs synthesized via green synthesis with an average diameter of 83 nm were successfully implanted into PMMA by adding the dispersed nanoparticles into the polymer solution which was dissolved in DMF (Awad, et al., 2019). The encapsulated

polymer nanocomposites displayed enhanced optical properties and thermal stabilities. It was found that the characteristics of the core-shell composites were dependent on the type of nanostructures incorporated, and their geometrical properties, concentration and interaction with the polymer material. In this case, PMMA contributed a two-fold benefit, namely accessibility of carboxylate functional group for chemical bonding with metal colloids and high solubility in polar aprotic solvents for the reduction of the silver metal precursor. In addition, various concentrations of commercially available silver and gold nanoparticles, with the size range of 3-7 nm, have been successfully encapsulated inside polyacrylate copolymer nanospheres which had an average particle size of 100 nm (Lee, et al., 2017; 2018). The noble metallic nanostructures were mixed with the comonomers before the initiation of polymerization. The metallic-encapsulated polymer nanospheres obtained were used to elevate the light harvesting efficiency of photovoltaic cells.

## **2.5 Silane coupling agent**

A coupling technique is used to enhance adhesion strength and bond durability with promising resistance toward ageing, environmental and weathering effects. For instance, SCA is used to improve the adhesion of polymeric material on an inorganic substrate to withstand deterioration due to the attack of water on the Si element (Ooij, et al., 2005). SCA can be handled easily when all the conditions are controlled properly. It is responsible for dominant chemical modification of the interface of a composite system by forming durable covalent bonds. Besides, the formation of interpenetrating polymer networks at

the interface region further reinforces the mechanical strength and chemical coupling between dissimilar materials. According to Pape and Plueddemann (1991), SCA can be applied in two ways: (i) to be assembled on an inorganic substrate by dissolving it in an organic solvent or water; and (ii) to be incorporated into a polymer via a polymerization process.

The effectiveness of a coupling agent system can be examined through the measurement of the flexural strength of composites and also the adhesion durability of coatings on a substrate surface. The results obtained showed that SCA does increase the flexural strength of composites to give better retention force during thermal ageing; while coatings with SCA possessed stronger interfacial bonding associated with remarkable resistance toward moisture degradation. Throughout the years of research on the adhesion between polymer and Si substrate, various types of coupling agents with different functional groups have been developed for a variety of applications (Kalita and Netravali, 2015). An effective SCA with an appropriate organofunctional group should be selected for its compatibility and matching of reactivity with the polymer for certain implementations, as shown in Table 2.1.

According to Barry (2018), the reactivity of SCAs with hydroxylated surfaces increases in the series:  $\text{Si-OCH}_2\text{CH}_3 < \text{Si-OCH}_3 < \text{Si-O}_2\text{CCH}_3 < \text{Si-NH-Si} < \text{Si-Cl} < \text{Si-NR}_2$ . As a matter of fact, the concentration of hydroxyl groups on the surface also affects the deposition of silane materials on inorganic substrates significantly (Kaynak, et al., 2017). An investigation of relevant bond energy revealed that the coupling reaction under aprotic and dry

conditions is driven by the generation of the Si-O-surface bond. The reactivity of silane materials toward a substrate surface is also affected by certain secondary factors, such as volatility of byproducts, steric strain attributed by bulky group on Si atom, the capability of the byproducts in catalyzing further reactions and the formation of hydrogen bonds with hydroxyls on the surface.

**Table 2.1:** Commercially available coupling agent (Kalita and Netravali, 2015)

Functional group	Chemical formula	Applicable polymers
Vinyl	$\text{CH}_2=\text{CHSi}(\text{OC}_2\text{H}_5)_3$	Unsaturated polymer
Chloropropyl	$\text{Cl}(\text{CH}_2)_3\text{Si}(\text{OCH}_3)_3$	Epoxy, epoxide
Epoxy	$(\text{C}_3\text{H}_5\text{O})\text{O}(\text{CH}_2)\text{Si}(\text{OCH}_3)_3$	Elastomers, epoxy
Methacryl	$(\text{C}_3\text{H}_5)\text{COO}(\text{CH}_2)_3\text{Si}(\text{OCH}_3)_3$	Unsaturated polymer
Amine	$\text{H}_2\text{N}(\text{CH}_2)_3\text{Si}(\text{OC}_2\text{H}_5)_3$	Phenolic, nylon
Phenyl	$\text{C}_6\text{H}_5\text{Si}(\text{OCH}_3)_3$	Polystyrene
Mercapto	$\text{HS}(\text{CH}_2)_3\text{Si}(\text{OCH}_3)_2$	Almost all resin
Phosphate	$\text{C}_6\text{H}_{10}\text{O}_8\text{Ti}_2\text{H}_4\text{N}$	Polyolefin, polyester

According to Pape and Plueddemann (1991), aliphatic organofunctional silanes are the most suitable coupling agents applied for resins of epoxy, glass-reinforced polyester and phenolic polymer due to the heat stability feature of the aliphatic organic group. The result obtained elucidated that aliphatic silane materials including methyl-, vinyl-, phenyl- and chloropropyl-silanes provide superior adhesion bonds between polyurethane and glass substrate compared to amino silanes. On the other hand, SCA with alkoxy hydrolysable groups are the most widely utilized for surface modification because the alkoxysilanes can

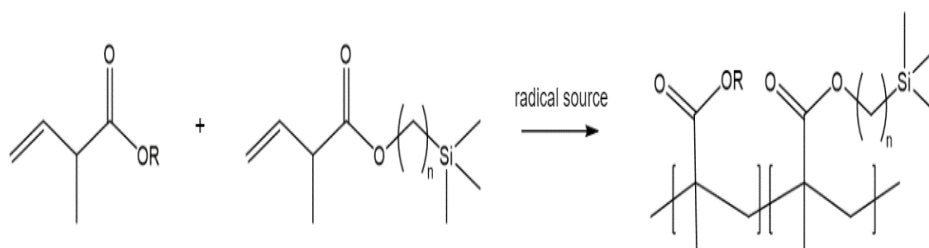
be handled easily and the alcohol byproducts are volatile, safe, low in toxicity and environmentally friendly (Barry, 2018). Methoxy silane is more reactive than ethoxy silane as it is able to undergo coupling with a substrate surface under aprotic and dry conditions. Nonetheless, a suitable catalyst is essential for the less reactive ethoxy silanes when they are applied as coupling agents.

Most of the developed surface treatments using organofunctional silanes as coupling agents are conducted in the presence of water (hydroxyl groups) as part of the reaction medium, either by direct addition or by atmospheric adsorption of moisture or water on the substrate. Various types of commercially available organofunctional silanes have been modified and evaluated by Pape and Plueddemann (1991) for the enhancement of bonding and coupling in the interphase region. These approaches apply modifiers to increase the hydrophobic feature, thermal stability, ionomer bond formation, as well as crosslinking of siloxane structure, and thus reduce the shear degradation of SCA. SCAs can form a self-assembled monolayer on a substrate surface through solution or vapour phase deposition techniques (Lee, et al., 2021). A self-assembled monolayer is defined as a single molecule thick array of matter that is formed on the surface in an ordered manner as a result of physical forces and chemical bonding (Barry, 2018). Nonetheless, the silane film thickness exhibits a linear correlation with the concentration of a silane solution. Ooij, et al. (2005) had found that a multilayer silane film would be formed when a higher concentration of SCA was used. According to the results obtained, the silane film thickness increased from 50 to 250 nm when the concentration of the silane mixture was increased from 2% to 5% by weight.

However, a higher concentration of silane reduces the maximum silanol formation due to the increase in self-condensation reactions. In general, an SCA with a 10% concentration gave the optimal reaction conditions for an outstanding performance, which can significantly improve the bond durability and adhesion strength between two dissimilar materials.

### 2.5.1 Silane coupling agent in the polymeric matrix

The coupling mechanism between organofunctional silane and the organic polymer is complex. The formation of a covalent bond is attributed by either the reaction with the finished polymer or copolymerization with the monomers (Barry, 2018). The bonding of thermoplastic resin is attained via both ways as aforementioned, but principally the former. With thermoplastic polymers, only the siloxane array will crosslink. According to Barry (2018), unsaturated polyester, polyacrylates and polymethacrylates could be modified through copolymerization with SCA that possesses unsaturated organic substitution which facilitates a free-radical polymerization process. Figure 2.4 illustrates an example of acrylate coupling reaction. The reaction takes place at the unsaturated carbon double bond in the presence of an initiator to produce free radical molecules and thus the copolymerization process proceeds.



**Figure 2.4:** An example of acrylate coupling reaction (Barry, 2018)

Vinyl silanes are commonly utilized along with a peroxide thermal initiator to construct the covalent bonds with polymeric matrixes. Lee, et al (2021) had successfully incorporated a vinyl silane, namely TMVS into a polyacrylate copolymer via an emulsion polymerization process. The SCA was mixed with the comonomers before the initiation of copolymerization. It was found that the polyacrylate nanospheres with 7 and 9 wt% of TMVS were able to tolerate five cycles of peeling using a pressure-sensitive adhesive tape, while the polymer was deposited on the surface of a glass substrate. However, the polyacrylate nanospheres without or with less amount of SCA had been removed easily.

On the other hand, the influence of SCA on the properties of vinyl ester mortar composites was investigated by Chmielewska et al. (2006). With the addition of 1 wt% of vinyl- and acryl silanes, the compressive and flexural strengths of the resin were increased by about 15% and 10%, respectively. Kaynak and co-workers (2013) had also proven that the SCA used was able to improve the interface and adhesion strength between incompatible materials with polymer matrix. The results obtained revealed an increase in tensile strength and elastic modulus value, with a slight decrease in the toughness of the sample produced.

### **2.5.2 Dipodal silane**

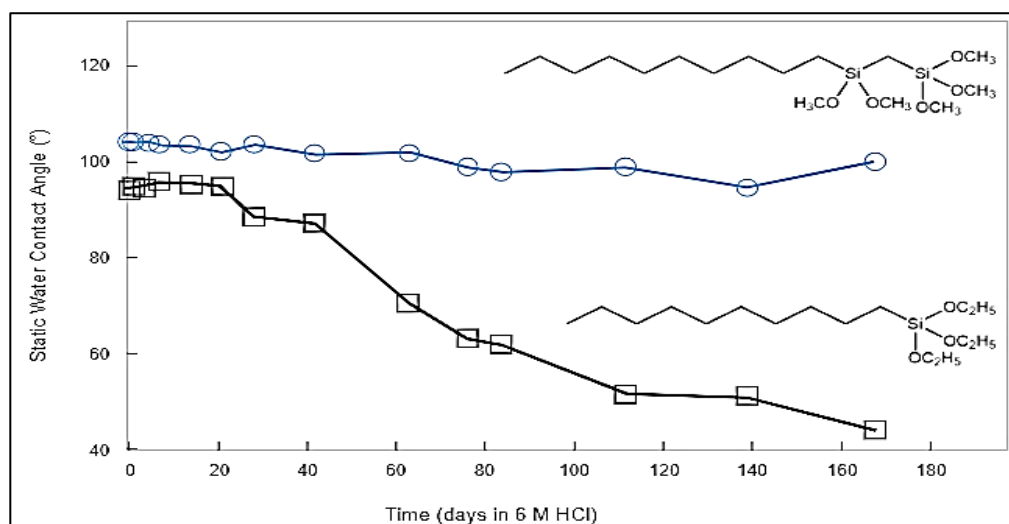
Barry (2018) revealed that the main issue faced by conventional silanes is the occurrence of gelation or phase separation during the formation of siloxanes from silanols through self-condensation. In order to overcome this drawback, around 10 to 40% of dipodal silanes are frequently utilized in conjunction with

conventional SCA to provide outstanding durability and appropriate functionality for certain applications. In this case, the hydrolytic stability, shelf life, substrate bonding as well as mechanical and adhesive strengths of the composite system were significantly improved. The adaptation of dipodal silanes has dramatically impacted surface treatment by displaying superior protection on a metal surface via an aqueous immersion deposition. According to Kaynak, et al. (2017), dipodal silanes exhibit remarkable hydrolytic and thermal stability (above 400 °C) compared to monopodal silanes. Organosilica product of dipodal silanes demonstrated greater water contact angle even after the coated substrate was immersed in a hydrochloric acid solution of 6 M for almost six months, as shown in Figure 2.5 (Arkles, et al., 2014).

In addition, dipodal silanes that are used as additive possess the potential to eliminate the defect of adhesive bonds during the lifetime requirements of various devices. This is established by assembling a promising hydrophobic polysiloxane layer on the surface of a substrate during condensation, thus increasing the crosslink density at the interphase region and preventing the hydrolysis of bis-silanes (Ooij, et al., 2005). On the other hand, a few factors should be taken into consideration during the selection of dipodal silanes, which include the type of substrate, the reaction condition, various silane combinations and primer applications. The silanes mixture is beneficial in improving chemical resistance, coating performance, wet adhesion and corrosion protection. Barry (2018) applied a dipodal silane of bis(triethoxysilyl)ethane in conjunction with a conventional coupling agent at ratios that ranged from 1:5 to 1:10. The silanes mixture was processed



similarly as the traditional silane materials and then deposited on the surface of a substrate. The results showed that the durability of the coatings was elevated with the incorporation of a bis-silane as compared to just using the traditional SCA alone.



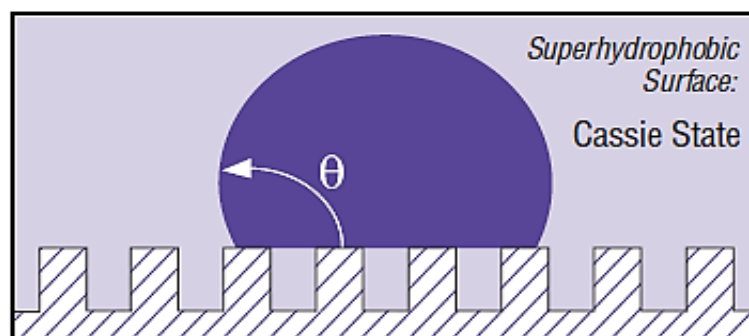
**Figure 2.5:** Hydrolytic stability of dipodal silanes (blue) compared to monopodal silanes (black) (Arkles, et al., 2014)

Most of the dipodal silanes are water insoluble which has restricted their immediate industrial use with water stabilizing functional groups like amine group (Ooij, et al., 2005). In general, a 5% by volume of dipodal silane is normally prepared in a mixture of solvents, e.g., ethanol and water with a ratio of 9:1. The solvent composition will affect the reaction yields by controlling the hydrolysis and self-condensation process of silanes (Paquet, et al., 2012). Particularly, the relative ratio of the solvents exhibits a direct effect on the reactivity of the system and the relative abundance of different species. The relative solvent ratio of water should be lower than the number of hydrolysable groups, with a maximum of 20% w/w. The organic medium of ethanol is

utilized to enhance the miscibility between SCA and water. Meanwhile, the pH of the solvent should be adjusted to 4-5 using acetic acid because an acidic condition is favourable in accelerating the hydrolysis reaction as well as manipulating the condensation reaction to prevent the occurrence of precipitation and avoid the formation of the larger structure, thus maintaining a small molecular size. The protective effect of acidic pH is to stabilize the hydrolyzed silanes against condensation as well as the formation of silanol-bearing derivatives.

### **2.5.3 Non-functional silane for superhydrophobicity**

According to Barry (2018), non-functional hydrophobic silanes are usually used to fabricate a superhydrophobic layer on the surface of a substrate. Specifically, a superhydrophobic surface is a binary structured surface with a WCA of at least  $150^\circ$  and a sliding angle of less than  $10^\circ$ . It could be produced via two approaches, namely chemically modification of rough surface using low-surface-free-energy matters, and fabrication of rough structure on intrinsically hydrophobic substrates. The techniques development of superhydrophobic surfaces and the theory of surface wetting are guided and explained by two well defined theoretical concepts, Cassie-Baxter and Wenzel models (Jin, et al., 2014). The common examples of superhydrophobicity are associated with the asperity surfaces at the sub-micron scale and the measurements of contact angle are the composites of solid surface roughness and air, which are denoted as Cassie state and illustrated in Figure 2.6 (Barry, 2018).



**Figure 2.6:** Cassie state of a superhydrophobic surface (Barry, 2018)

A superhydrophobic layer exhibits a unique characteristic of self-cleaning property which is attributed by the water-repelling feature of non-polar silanes. Owing to the rough surface with high surface tension and low surface energy, the water droplet on the superhydrophobic surface tosses up in the air with the adoption of a perfectly spherical shape to reach a minimum contact area, and subsequently quickly rolls off the surface. The round-shaped water droplets abundantly collect the dust particles on the rough structured superhydrophobic surface and then flow off together to clean the surface hence the self-cleaning purpose is achieved (Liu, et al., 2015). Based on the Cassie-Baxter and Wenzel theories, the hydrophobicity of a surface increases with the increase of surface roughness and the thickness of the coated silane film (Chen, et al., 2012). The film stability could be dramatically enhanced by elevating the hydrophobicity.

According to Saengkaew, et al. (2018), an impressive superhydrophobic surface with excellent self-cleaning characteristics and optically transparent could be produced by functionalizing and depositing the fluoroalkyl silane (FAS), specifically 1H,1H,2H,2H-perfluorodecyl trimethoxysilane and trimethoxy (3,3,3-trifluoropropyl) silane, onto a substrate. Natural rubber encapsulated with silica modified with FAS and TMVS has yielded a

superhydrophobic surface with a WCA of  $180^\circ$ , whereby the water droplets encountered on the surface appeared in a perfect spherical shape. Indeed, FAS was a low surface energy material due to the presence of a hydrophobic functional group of fluoroalkyl at the tail-end of the molecule. Owing to the large electronegativity difference between fluorine and carbon, fluoroalkyl chains offered extraordinary features, which include low friction behaviour and liquid adhesion as well as high thermal stability (Kaynak, et al., 2017).

Saleema, et al. (2011) also proved that the superhydrophobic surface with high WCA could be produced by increasing the etching time and the concentration of FAS. The surface WCA of aluminium alloy substrate coated with FAS had increased from  $146^\circ$  to  $161^\circ$  when the etching time was prolonged from 5 to 15 minutes. Meanwhile, the surface roughness also increased gradually. However, with a further increase in the etching duration, the WCA decreased in spite of high surface roughness, which might be due to the loss of fluoroalkyl fragments. On the other hand, the WCA of a substrate increased from  $60^\circ$  to  $166^\circ$  when the molar ratio of FAS was increased from 0.1 to 0.4. This is attributed to the outward orientation of the low-surface-energy fluoroalkyl functional group from the surface.

A multifunctional transparent superhydrophobic coating has contributed to the imperative advancement in surface wetting with mandatory functionalities of anti-reflection and self-cleaning features. Such advancement has greatly extended the application of the superhydrophobic coating in photovoltaic devices. It renders high water resistance and retains the glass surface

cleanliness of solar cells. The formulation of superhydrophobic solar cells coating utilizing commercially available cost-effective materials has reduced labour costs, offered environmental benefits and extended the durability of materials (Chungsiriporn, et al., 2020). A transparent and superhydrophobic surface of the glass substrate with a WCA of  $169^\circ$  was successfully fabricated by Liu and his teammates (2015) using a fluoroalkyl silane through a sol-gel process. It was found that the degree of superhydrophobicity and WCA gradually increased with the deposition time. By increasing the deposition time, the silane layer thickness and surface roughness had elevated dramatically. In addition, the effectiveness of the self-cleaning property of the chemically modified surface of the glass substrate was proven. The spherical water droplets had efficiently collected the dust particles accumulated on the coating surface and subsequently rolled off from the surface with a sliding angle of less than  $5^\circ$ . Nonetheless, the superhydrophobic coating manifested poor mechanical stability and durability as it can be easily scratched by a pencil (9B grade).

Chen et al. (2012) incorporated silica particles onto a glass surface and subsequent chemically functionalized the surface with a FAS via chemical vapour deposition. The FAS has imparted an outstanding superhydrophobic property to the surface with  $152^\circ$  of WCA and  $8^\circ$  of sliding angle. It was found that the degree of WCA increased with the increasing number of layers of the fluorinated silica nanoparticles that were coated on the surface until a critical layer number was reached. This is because a thicker layer exhibits higher surface roughness. In general, the dimension of surface roughness should be

maintained under 400 nm in order to maximize optical transparency while upholding effective superhydrophobicity (Cho, et al., 2017). Therefore, hydrophobic nature has to be compromised for optical transmission in order to avoid the decline of solar cell performance.

#### **2.5.4 Factor affecting the adhesion durability of silane coating**

The curing process is widely adopted in many industries for the purpose to convert a viscous liquid into a strong rigid amorphous material by means of crosslinking. The curing process generally results in higher elasticity, tensile strength, resistance toward high-temperature exposure and peel off properties. In silane coupling reaction, the heat curing technique is the most commonly performed on the silanated glass to maximize the interfacial bond strength and inhibit the occurrence of reversible reaction of covalent bonds between SCA and the substrate surface. In general, the surface of a substrate treated with an SCA is cured either by heating it at 120 °C for 30-90 minutes or by evacuating it for a duration of 2-6 hours to completely remove the water molecules (Barry, 2018). In such cases, the covalent bonds will form, break and reform to mitigate the internal stress. This has ensured the positional displacement of interface components. Ooij and his research team studied the curing temperature and curing duration of a silane layer in the temperature range of 0-250 °C for 0-180 minutes. The curing temperature of 100 °C with a curing duration of 20-30 minutes was the optimum parameter found. The curing of the silane layer had resulted in the reduction of film thickness and the formation of a denser film.

Numerous reports have proven that the coupling interaction between the surface of an inorganic substrate and SCA could be catalyzed through acid treatment or heating. The cross-linking reaction of siloxane film is accelerated by increasing the curing temperature and time. As reported by Monticelli et al. (2006), the efficiency of the silane coupling mechanism were improved after a hot air-drying process. By air-drying a sample at 38 °C, a dramatic increase in adhesion bond strength was observed with a micro tensile bond strength of 11.6 MPa as compared to the sample that was air-dried at 21 °C. Two phases were formed after the silanation reaction: an outermost physisorbed layer with lesser siloxane bonds and a hydrolytic stable chemisorbed layer on the substrate surface. Introducing heat to the composite system increases the rate of condensation and forms a tightly packed configuration of the coupler molecules on the surface. High curing temperature promotes complete solvent evaporation and facilitates the elimination of the detrimental loosely bound physisorbed silane layer. The presence of a small amount of solvent might be advantageous in promoting silane wetting, however, incomplete removal of solvent might compromise coupling and affect bond strength. Compared to dual-component systems, pre-activated SCA exhibits a higher rate of hydrolysis which results in a complete coupling reaction.

The condensation of silanols to form siloxane bonds is a reversible reaction in the presence of water and is significantly affected by the curing temperature. The condensation reaction is promoted at a high curing temperature. Therefore, a high curing temperature increases the crosslinking density of the silane film and forms a tighter siloxane network. This has offered a high interface fracture

energy and resistance toward water attack. The results obtained by Pavlovic and Kramer (2011) elucidated that the percentage of swelling with water decreased with increasing curing temperature. After a certain curing temperature (100 °C) was reached, the percentage of swelling remained unchanged at a low value. The high crosslink density of the siloxane network had resulted in low hydrophilicity.

## **2.6 Improvement of power conversion efficiency of solar cells**

Throughout the years, several challenges and issues have been encountered in the manufacturing of photovoltaic devices which include the processing cost and light trapping efficiency (Tay, 2019). Thin-film solar cells are a good replacement for the reduction of production cost; however, it has lower PCE which might be due to the unevenly-distributed crystalline structure of silicon. Amorphous silicon solar cell has the lowest efficiency of about 12%, follows by polycrystalline silicon solar cell which has an efficiency of around 17%, while monocrystalline silicon solar cell shows the greatest PCE of 25-30%. The absence and presence of grain boundaries in crystalline silicon solar cells affect the flow of excited electrons significantly; the former does not have any barriers to obstruct the movement of free electrons while the latter inhibits the continuous flow of electrons. Therefore, the efficiency of the amorphous silicon solar cell drops dramatically to about 10-15%. Recently, there have been a lot of research studies being carried out to improve the light harvesting and power conversion efficiencies of solar cells. One of the approaches is by capturing more light radiation into the active region of solar cells through the incorporation of metallic and polymeric nanostructures.



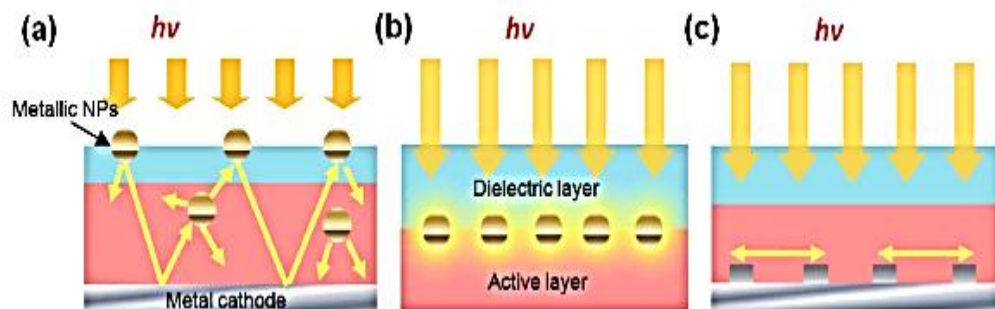
### **2.6.1 Incorporation of metallic nanoparticles**

Metallic nanostructures have shown remarkable light trapping performance in various types of solar cells. The ability of nanostructures, with numerous particle shapes and periodic, to enhance the absorption characteristics of solar cells has been successfully demonstrated. According to Pal, et al. (2019), noble metallic nanoparticles (i.e. copper, silver and gold) have gained widespread attention contrasted to other types of metallic nanostructures. Among them, AgNPs exhibit the highest efficiency of plasmon excitation (Tay, et al., 2020). Owing to the LSPR and scattering effects of AgNPs, the efficiencies in light harvesting and power conversion of solar cells could be enhanced via the incorporation of AgNPs (Petryayeva and Krull, 2011). Moreover, the plasmonic wavelength of AgNPs is near to the bandgap of Si which might also further improve the light trapping mechanisms of photovoltaic devices.

As shown in Figure 2.7, three structure designs of solar cells have been developed and implemented using metallic nanoparticles to improve the performance of photovoltaic devices (Chou and Chen, 2014).

The first approach involves the coating of metallic nanoparticles on the semiconductor surface, which is more suitable for improving the light harvesting efficiency of thin-film crystalline silicon solar cells. Jeng et al. (2015) reported that gold and silver nanostructures were deposited on the surface of both multi-crystalline Si and copper-gallium-diselenide to examine the elevation of light trapping efficiency of photovoltaic cells. The gold and

silver nanoparticles with the concentration of 1% and 5% by volume coated onto the surface of multi-crystalline Si solar cells had improved their PCE by 5.6% and 4.8%, respectively. Besides that, the PCE of copper-galium-diselenide photovoltaic cells was enhanced at 1.2% and 1.4% by depositing gold and silver nanocolloids with a similar concentration of 1% and 5% on the photovoltaic cell surface. The photocurrent of solar cells declined with a further increase in the concentration of the metallic nanoparticles. The results of optical analysis elucidated that the transmittance of gold was greater than silver nanostructures. Reducing the concentration of metallic nanoparticles resulted in an increase in the background transmittance and broadening of the resonance wavelength. This was caused by the weakening of the shadowing effect and the plasmonic resonance. Meanwhile, the broadening of the resonance curve was also a result of non-uniform particle size and the uneven distribution of nanoparticles. Owing to the benefit of light-harvesting over a wider range of wavelengths, the broadening effect was favourable in enhancing the PCE of solar cells.



**Figure 2.7:** Structure designs of plasmonic-enhanced solar cells: (a) incorporation of metallic nanostructures on the surface of the active layer; (b) integration of metallic nanoparticles in the photoactive layer; (c) fabrication of metallic nanocolloids at the interface between the active layer and the metal contact (Chou and Chen, 2014)

In another research study, AgNPs with particle sizes corresponding to 12 nm and 16 nm mass thickness were coated on the surface of thin-film silicon photovoltaic cells through the thermal evaporation technique (Pillai, et al., 2007). These resulted in 33% and 16% of enhancement in the total photocurrent of the photovoltaic devices, respectively. In addition, an overall enhancement in photocurrent over the range of wavelengths between visible and near-infrared in the electromagnetic spectrum was observed with a 7- and 16-fold elevation for wafer-based thin-film photovoltaic cells and thin-silicon-on-insulator, respectively. The surface plasmon effects of AgNPs are excited by incident light and subsequently, the light radiation is coupled into the silicon. A large fraction of the light is trapped inside, either being absorbed into the active layer or coupled out by another nanostructure. On the other hand, the compact layers of AgNPs were deposited on a Si photovoltaic cell surface by employing electron beam evaporation and followed by thermal annealing (Temple, et al., 2009). The PCE of photovoltaic cells was enhanced from 8.51% to 9.06% by introducing AgNPs with different particle diameters ranging from 25 to 95 nm.

Instead of depositing the metallic nanostructures alone on the surface of solar cells, the nanostructures can also be incorporated into an organic matrix and then coated on the surface of silicon solar cells (Tay, et al., 2020). Lee and co-workers (2017; 2018; 2021) demonstrated the incorporation of noble metallic nanoparticles, specifically silver and gold with particle size ranges of 3-7 nm into P(MMA-co-AA) nanospheres with 101 nm in size via an emulsion polymerization process. The copolymer with  $2.5 \times 10^{-3}$  wt% of AgNPs was

coated as a functional monolayer on the  $\alpha$ -Si photovoltaic cell surface via a self-assembly coating technique, using a dip coater. In contrast with the reference photovoltaic cell with a PCE of 2.00%, the performance of the surface-modified photovoltaic device was enhanced to a maximum light conversion efficiency of 5.57% with a relative improvement of 179%. On the other hand, the solar module deposited with polyacrylate embedded with  $3.75 \times 10^{-3}$  wt% of gold nanoparticles had successfully enhanced the PCE to 5.32%, with a relative improvement of 166%. Both the results showed a similar trend that the performance of solar cells was improved by increasing the concentration of the entrapped metallic nanoparticles. However, the light harvesting efficiency diminished when the amount of the encapsulated nanostructures exceeded a certain concentration. Nonetheless, there were still significant enhancements in the PCE compared to the uncoated solar cells.

For the second approach, it involved the incorporation of metallic nanostructures into the absorbing layer to enhance the light trapping mechanism of both dye-sensitized and organic solar cells (Jeng, et al. 2015). Zarick and his teammates (2016) showed an enhancement in light harvesting efficiency of dye-sensitized solar cells by incorporating silica-coated gold-encapsulated silver nanostructures in the active region. A prominent elevation was observed by entrapping hybrid bimetallic nanostructures with a concentration of 0.44 wt% into the dye-sensitized solar cells structure. The relative PCE enhancement of 26% was achieved as the PCE of the photovoltaic device increased from 5.97% to 7.51%.

In the third design of plasmonic photovoltaic devices as depicted in Figure 2.7(c), periodic metallic nanoparticles are introduced to the interface between the active layer and the metal contact. Ferry, et al. (2010) demonstrated a notable light harvesting method comprising a two-dimensional periodic of AgNPs on 160 nm thick hydrogenated amorphous silicon solar cells. A maximum PCE of 6.6% with a relatively short circuit current increment of 46% was achieved by patterning the solar module with AgNPs of 250 nm in size and a plasmonic scatter pitch of 500 nm. Besides that, AgNPs with different particle sizes were assembled as a back reflector layer at the interface region between the absorbing layer and the metal contacts using a self-assembly coating method, specifically vacuum sputtering followed by heat annealing (Zi, et al. 2016). The PCE of a photovoltaic device with AgNPs of 320 nm in size was increased from 5.89% to 7.13% with a relative efficiency improvement of 21.05%.

### **2.6.2 Factors affecting the light trapping efficiency of solar cells attributed by metallic nanoparticles**

Due to the plasmon enhancement and scattering mechanisms of metallic nanostructures, the reflectance of solar cells could be reduced and the light harvesting mechanism could be implemented by incorporating periodic nanoparticles on the surface of solar cells. The physical properties of the metallic nanostructures, such as particle size, shape, particle density and surface coverage will significantly influence their optical properties which include LSPR characteristics and backscattering effects.

According to Jeng, et al. (2015), the particle size of metallic nanostructures should be properly selected so that the incident light could be concentrated and scattered into the active layer of solar cells. This is because the light in semiconductors preferentially couples into the layers with a high electric constant, and thus improves the absorption efficiency. Metallic nanostructures with larger particle size exhibit a stronger scattering effect. However, they may cause greater metal absorption loss too. Based on the results obtained by Pillai, et al. (2007), larger nanoparticles tend to reduce the absorption at shorter wavelengths while increase it at longer wavelengths. On the other hand, smaller metallic nanostructures possess lesser scattering cross-section and lower radiative efficiency, thus leading to a blue-shift effect in the absorption peak. As reported by Mizuno, et al. (2012), the relatively larger nanoparticles (>150 nm) displayed an effective light scattering and their scattering cross-section could be 10 times larger than the geometrical areas.

Dai et al. (2012) reported that AgNPs with various diameters of 68 nm and 85 nm were deposited on the Si substrate surface using the sputter-anneal technique. The results obtained revealed that AgNPs have exciting wavelengths of 380 nm and 420 nm respectively. When the size of nanoparticles increases, there will be a red-shift of the wavelength of the nanostructures which is attributed by a larger relaxation time of electrons. The photovoltaic device reflectance for AgNPs with a bigger size is much lower than the smaller one owing to the higher-order modes of the larger nanoparticles which scatter more light into the photoactive layer of photovoltaic devices. However, if the colloidal size of AgNPs becomes too large, the light harvesting efficiency will

decrease due to the reduction in the scattering cross-section of nanoparticles (Tay, et al., 2020). Zi and his teammates (2016) found that the average reflectance at the wavelengths of 600-900 nm improved from 54.4% to 79.8% when the particle size of AgNPs increased from 110 nm to 680 nm. In terms of PCE, it had been enhanced from 6.35 to 7.13% when the particle size of AgNPs incorporated in the solar cells was increased from 110 nm to 320 nm. Further increase of the size to 680 nm had deteriorated the efficiency to 6.56%. Nevertheless, it still exhibited higher efficiency than the specular control cell. Therefore, metallic nanoparticles with an optimum diameter should be introduced due to the trade-off between obtaining higher-order modes, scattering cross-section and high radiative efficiency (Temple, et al., 2009).

The particle shape is another significant factor that will affect the surface reflectance and light trapping efficiency of solar cells. According to Pillai et al. (2007), the particle shape of nanostructures would not magnificently influence the resonance position, but significantly affect the scattering intensity. Particle flattening and shaping had resulted in the red-shift effect and broadening of the plasmon resonance. The red-shift effect became larger with more flattening of the nanostructures but was smaller for spherical nanoparticles. Temple and his co-workers (2009) also found that the fraction of light scattered into the active layer is highly dependent on the three-dimensional shape of the nanostructures. The results portrayed that the spherical and hemispherical nanoparticles with 100 nm had scattered 65% and 90% of incident light into the substrate, respectively. Besides that, Dai et al. (2012) revealed that AgNPs with irregular shapes have a higher reflectance effect. Nonetheless, the reflectance effect

reduces at a certain wavelength. In short, AgNPs with a uniform and regular spherical shape perform better than those with irregular shapes in terms of light harvesting efficiency.

Last but not least, the surface reflectance and light harvesting mechanisms of solar cells are strongly dependent on the particle density and the surface coverage of coated nanoparticles. In the study of Dai et al. (2012), surface reflectance decreases with increasing particle density and surface coverage of AgNPs. When the surface distribution of AgNPs on the solar cells decreases, the phenomenon of quadrupolar mode resonance of AgNPs happens. This phenomenon was observed only when the surface of silicon was not completely covered by the scattering cross-section of metallic nanoparticles. The scattering cross-section of AgNPs corresponds to the incident light frequency. When there is low particles density, the incident light frequency is further apart from the quadrupolar mode resonance position, and thus the surface reflectance increases. Nonetheless, there is some exception. Based on the study of Temple et al. (2009), less surface distribution gave rise to the higher efficiency improvement of solar cells. When the surface coverage of AgNPs coated on the surface of solar cells reduced from 42% to 31%, the PCE was increased from 7.10% to 9.06% due to the scattering mechanisms of metallic nanoparticles.



### **2.6.3 Anti-reflective coating of polyacrylate matrix**

Owing to its extraordinary performance in enhancing light transmittance and reducing light reflection at interfaces, anti-reflective coating (ARC) as an optical coating has been extensively applied on the surface of optoelectronic and photovoltaic devices (Askar, et al., 2013). A fraction of light is reflected while the rest of it is transmitted when light propagates from one medium to another. Reflection is an optical phenomenon that occurs when the light radiation travels through two media with different refractive indices, resulting in an alteration in the wave-front direction. The degree of light reflection is proportional to the deviation value of the refractive indices. Due to the high refractive index of silicon element, a large fraction of light is reflected by it and thus has dramatically impacted the PCE of silicon photovoltaic devices. Hence, ARC is adopted to address the mismatch of refractive indices at the silicon/air interface and to maximize the absorption of light radiation into the active layer of solar cells (Tay, et al., 2020). The materials with refractive indices that are close to the refractive index of air should be ideal for ARC. However, there are drawbacks of this approach, which include poor adhesion strength, the limited working range of wavelength and the angle of incident light.

According to Gan et al. (2016), polymers with relatively high refractive indices are excellent candidates for ARCs. For instance, PMMA and polystyrene with the refractive indices of 1.5 and 1.6 have high transparency in the visible region in the electromagnetic spectrum. By optimizing the composition and morphology, a lightweight ARC of polymeric matrix exhibits a substantial

material for the light management of photovoltaic devices. As reported by Bacal et al. (2020), a layer of PMMA ARC was incorporated onto the photo-absorber layer of perovskite solar cells to enhance its light harvesting efficiency. A dilute solution of PMMA in chlorobenzene was spin coated as a nanoarray with a thickness of 85 nm on the active layer of solar cells. The coating had relatively improved the short circuit current and PCE by 21.5% and 31%, which achieved an average of 16.21 mA/cm<sup>2</sup> and 3.07%, respectively. It was found that the PMMA layer performed well as an ARC, by which the surface reflectance was decreased from 21.5% to 12.5% over the visible light region. A relative reduction of 42% in reflection was yielded. Meanwhile, the absorption spectrum obtained depicted that the relative photo-absorption of the solar cell coated with the PMMA anti-reflective layer was enhanced by about 11.5%, due to the magnificent changes in the optical features of the sample.

As reported by Lee et al. (2017), P(MMA-*co*-AA) nanospheres with different particle diameters were fabricated via emulsion polymerization by varying the concentration of the surfactant. The copolymer nanostructures with a diameter of 101 nm, which were coated on the glass surface of  $\alpha$ -Si photovoltaic cells, had generated the highest PCE. The light conversion efficiency of the solar cells was improved from 2.0% to 3.14% with a relative enhancement of 57%. The improvement is contributed by a monolayer of densely packed P(MMA-*co*-AA) nanoarray which serves as an effective intermediate layer with a graded refractive index between air and silicon. In addition, silver and gold nanoparticles were encapsulated in the copolymer nanospheres. The PCE of the photovoltaic devices was further improved to 5.57% and 5.32%, respectively.

In another study, the PCE was prominently boosted from 4.9% to 7.5% for a graphene silicon solar cell coated with PMMA film (Jiao, et al., 2016). In this case, the PMMA layer with a thickness range of 60-80 nm corresponded well with the wavelengths of visible light and displayed an accentuate anti-reflective property. However, this technique gave a coating with low stability. The efficiency of the modified solar cells suffered a 10% of degradation ratio after four months.

According to Chen and Sun (2010), a surface-relief grating with a sub-wavelength structure, where the dimension of particles is smaller than the wavelengths of the incident light, exhibited remarkable anti-reflective properties. It was found that the deposition of PMMA thin film as ARC onto the substrate surface of Si solar cells had improved the short circuit current by 23% as compared to the uncoated solar cells. At the same time, the PCE of the solar cells was enhanced from 10.4% to 13.5% with a relative improvement of 30%. On the other hand, Chen et al. (2011) demonstrated the application of ARC of PMMA film on the surface of crystalline Si photovoltaic cell by employing a combination of colloidal lithography, cast moulding and reversal nanoimprint lithography. The ARC of PMMA nanoarray with biomimetic structure had successfully reduced the average reflectance of solar modules from 13.2% to 7.8%; while the light conversion efficiency was increased from 12.85% to 14.2% with a relative improvement of 10.5%.

#### **2.6.4 Factors affecting the light trapping efficiency of solar cells attributed by anti-reflective coatings**

The efficiency of ARC strongly depends on the particle size and film thickness. According to Gan et al. (2016), the short circuit current density and the PCE of photovoltaic devices can be dramatically improved by engineering the film thickness of polymeric ARC to raise light absorption in the spectral range of interest. In this study, the PMMA-coated graphene layer with different polymeric film thickness was spin-coated on the Schottky junction photovoltaic devices as an anti-reflective transparent electrode. In general, thinner PMMA films implied a better anti-reflection effect as they had resulted in higher improvement in the light harvesting efficiency of the solar cells tested in the visible and near-IR region. The PCE of the solar cells deposited with a PMMA ARC (108 nm in thickness) was enhanced from 3.12% to 6.55%, with a relative improvement of 110%. Besides the consideration of the optical properties, PMMA film should be coated at a certain thickness in order to mechanically protect the absorbing layer.

Askar et al. (2013) reported that the efficiency of a traditional quarter wavelength ARC exhibited a linear function to the film thickness and the refractive index of the materials. The fraction of optical reflection from the surface could be tuned by manipulating both of these parameters. To efficiently suppress light reflection, the refractive index of the materials should be similar to the geometric mean of the refractive indices of the two media at the interface. The refractive index of the coatings could be altered by the number of deposited layers. It was found that the coating's thickness should be a quarter

of the wavelength of light radiation. A coating with a thickness of a quarter-wavelength introduced a destructive interference effect that eliminates the light reflection at the interface between the ARC and the substrate. Numerous techniques were implemented to fabricate an ARC with the thickness of a quarter-wavelength. In addition, extensive experiments and theoretical simulations depicted the fact that the minimization of light reflection is strongly correlated to the particle size of anti-reflective materials. As reported by Askar et al. (2012), the silica spheres with a particle size of 110 nm exhibited a much lower reflectance with a higher transmittance (>98%) than the one with 210 nm in size and also the flat control sample, for a broad range of visible wavelengths. Therefore, 110 nm silica coating induced better performance in suppression of light reflection.

## CHAPTER 3

### METHODOLOGY

#### 3.1 Chemicals

In this project, the silver nanoparticles (AgNPs) were synthesized through the chemical reduction method. The chemical reduction method was carried out by using a reducing agent to reduce a silver metal salt in the presence of a suitable capping agent or stabilizer in order to control the particle size by slowing down the nucleation process and limiting the growth of metallic particles (Nersisyan et al., 2003; Tay, 2019). On the other hand, the poly(methyl methacrylate-*co*-acrylic acid-*co*-trimethoxyvinylsilane), P(MMA-*co*-AA-*co*-TMVS) nanospheres were synthesized via emulsion polymerization. Emulsion polymerization is a technique based on the oil-in-water emulsion principle where the monomers act as the discontinuous phase while water acts as the continuous phase with some surfactant stabilizing the emulsion solution (El-hoshoudy, 2018). The synthesized metallic nanoparticles and polymeric nanospheres were characterized and the surface morphology of nanostructures was accessed. Subsequently, both synthesized and commercialized AgNPs were encapsulated inside the polymeric nanospheres and coated on the glass surface of a solar cell through the self-assembly coating method, with the application of a coupling agent. Finally, the precoated glass surface of solar cells was further chemically modified using a mixture of dipodal and fluoroalkyl silanes. This was to fabricate a protective film with superhydrophobic nature on the array of polymeric nanospheres for self-

cleaning purposes. The chemical reagents utilized for the fabrication of AgNPs and polymeric nanospheres are tabulated in Tables 3.1 and 3.2, respectively. Table 3.3 shows the chemical reagents employed for the surface modification of precoated solar cells. Table 3.4 shows the chemical reagents used for the cleaning of silicon (Si) substrates.

**Table 3.1: Chemical reagents used for the synthesis of AgNPs**

<b>Chemical</b>	<b>Function</b>	<b>Manufacturer</b>	<b>Purity / Grade</b>
Commercialized AgNP*	Metallic nanoparticles precursor	Sigma-Aldrich	-
1-Dodecanethiol	Capping agent	Sigma-Aldrich	98%
Dodecylamine	Capping agent	Chem Sola	98%
Ethanol	Organic solvent	Chem Sola	AR grade
Silver nitrate	Metal precursor	System <sup>®</sup>	-
Sodium borohydride	Reducing agent	Alfa Aesar	99%
Toluene	Organic solvent	Chem Sola	AR grade

\* Commercialized AgNPs are stabilized by 1-dodecanethiol with particle size ranges between 3-7 nm

**Table 3.2: Chemical reagents used for the synthesis of polyacrylate**

<b>Chemical</b>	<b>Function</b>	<b>Manufacturer</b>	<b>Purity / Grade</b>
Acrylic acid	Monomer	Merck	99%
Methyl methacrylate	Monomer	Merck	99%
Potassium persulfate	Thermal initiator	R&M Chemicals	99%
Sodium dodecyl sulfate	Emulsifier	System <sup>®</sup>	99%
Trimethoxyvinylsilane*	Additives	Aldrich	98%

\* Trimethoxyvinylsilane is a coupling agent which serves as an adhesion promoter

**Table 3.3: Chemical reagents used for chemically surface modification**

<b>Chemical</b>	<b>Function</b>	<b>Manufacturer</b>	<b>Purity / Grade</b>
1,8-Bis(triethoxysilyl)octane	Surface modifier	Gelest	97%
Nonafluorohexyltrimethoxysilane	Surface modifier	Gelest	97%
Ethanol	Organic solvent	Chem Sola	AR grade

**Table 3.4: Chemical reagents used for the cleaning of Si substrates**

<b>Chemical</b>	<b>Function</b>	<b>Manufacturer</b>	<b>Purity / Grade</b>
Ammonia solution	Reducing agent	R&M Chemicals	30%
Hydrogen peroxide	Oxidizing agent	R&M Chemicals	30%



### 3.2 Instrumentation

The instruments utilized in this project are listed in Table 3.5.

**Table 3.5: List of instruments**

<b>Instrument</b>	<b>Brand, Model</b>
Atomic force microscope	Park Systems, XE-70
Contact angle analyzer	Lauda Scientific, LSA1000
Dip coater	Tefini, DP1000C
Differential scanning calorimeter	Mettler Toledo, DSC823 <sup>e</sup>
Energy dispersive X-ray spectrometer	Bruker, XFlash <sup>®</sup> 6-T   60
Field emission scanning electron microscope	JEOL, JSM-6701F
Fourier transform infrared spectrometer	Perkin Elmer, Spectrum RX1
Laser diffraction particle size analyzer	Malvern, Mastersizer 2000
Programmable direct circuit electronic load LIV tester	Array, 3721A 400W
Thermogravimetric analyzer	Mettler Toledo, TGA/SDTA851 <sup>e</sup>
Transmission electron microscope	Hitachi, HT-7700
Ultraviolet-visible spectrophotometer	Shimadzu, UV-1700
X-ray diffractometer	Shimadzu, XRD-6000

### 3.3 Experimental procedures

In order to study the enhancement of the light harvesting efficiency of amorphous silicon ( $\alpha$ -Si) photovoltaic cells by depositing polymeric nanostructures incorporated with AgNPs on the glass surface of a solar cell, the methodology of this project was performed in five major parts, they are (1) synthesis of AgNPs through chemical reduction method, (2) encapsulation of

AgNPs into polyacrylic nanospheres via emulsion polymerization, (3) coating of the nanostructures on the glass surface of an  $\alpha$ -Si solar cell, (4) surface modification of precoated glass surface using a mixture of dipodal and fluoroalkyl silanes, and (5) testing on the light trapping efficiency of solar cell.

### 3.3.1 Synthesis of AgNPs via chemical reduction method

Chemical reduction method was performed to produce AgNPs. The chemicals required for this process are shown in Table 3.1. The stock solutions, 0.02 M of silver nitrate ( $\text{AgNO}_3$ ) and 0.36 M of sodium borohydride ( $\text{NaBH}_4$ ) were prepared by dissolving the chemicals separately in 50 mL of ethanol with sonication. First of all, 9 mL of  $\text{NaBH}_4$  solution was added to different beakers. The capping agent was then added to each of the beakers having  $\text{NaBH}_4$  solution in it, at the  $\frac{[\text{Capping agent}]}{[\text{AgNO}_3]}$  molar ratios, denoted as S, varied from 1.37 to 27.8, as shown in Table 3.6. The solutions were mixed well using a magnetic stirrer. Subsequently, 9 mL of  $\text{AgNO}_3$  solution was added dropwise into each of the beakers. The mixtures were stirred for one hour to complete the reaction. In order to recover the AgNPs, the solutions were centrifuged at 7800 rpm for 10 minutes. The supernatant was discarded and replaced with fresh ethanol. This step was repeated three times in order to remove the impurities and unreacted starting materials. Then, 15 mL of dispersing solvent was added to the AgNPs obtained and the suspensions were sonicated in order to re-disperse the nanoparticles. Finally, the solution was transferred into a sample vial. The procedure for the synthesis of AgNPs was carried out either at room temperature or in an ice bath. In this study, 1-dodecanethiol (DDT) or

dodecylamine (DDA) was used as the capping agent to control the particle size of nanoparticles and prevent the particles from aggregation and agglomeration.

**Table 3.6: The S value corresponds to the amount of DDT and DDA added**

<b>S value</b>	1.37	2.78	5.56	11.1	16.7	22.2	27.8
<b>Mole of AgNO<sub>3</sub></b> ( $\times 10^{-4}$ mol)	1.80	1.80	1.80	1.80	1.80	1.80	1.80
<b>Mole of DDT</b> ( $\times 10^{-3}$ mol)	-	0.50	1.00	2.00	3.00	-	-
<b>Mole of DDA</b> ( $\times 10^{-3}$ mol)	0.25	-	-	-	3.00	4.00	5.00

### 3.3.2 Encapsulation of AgNPs into polymeric nanospheres via emulsion polymerization

#### 3.3.2.1 Synthesis of polymeric nanospheres via emulsion polymerization

P(MMA-*co*-AA-*co*-TMVS) nanospheres were fabricated through the emulsion polymerization technique using 95 wt% of methyl methacrylate (MMA) with 5 wt% of acrylic acid (AA) (Lee, et al., 2021). Sodium dodecyl sulfate (SDS) was added as an emulsifier to stabilize the polymeric nanospheres in the emulsion by forming a stable emulsion system. Potassium persulfate (KPS) was added to act as a thermal initiator to promote the formation of free radicals to initiate the polymerization reaction. Different amount of trimethoxyvinylsilane (TMVS) was incorporated into the polymer molecules to act as a coupling agent to increase the adhesion strength between the organic

polymeric nanospheres and the inorganic Si substrates. Table 3.7 shows the amount of chemical ingredients used in the polymerization process.

**Table 3.7: Ingredients for emulsion polymerization**

<b>Ingredient</b>	<b>Quantity (g)</b>
Acrylic acid	5.00
Distilled water	390.00
Methyl methacrylate	95.00
Potassium persulfate	0.70
Sodium dodecyl sulfate	6.00
Trimethoxyvinylsilane	Varied from 5.0 to 9.0 wt%

To begin with, 200 mL of water was mixed together with 0.60 g of 30 % SDS solution in a five-neck reactor flask. The mixture was stirred at a constant speed of 600 rpm and heated up to 75 °C in a water bath. Subsequently, 12.5 mL of the initial monomers and 0.35 g of initiator KPS were added at the same time. After 15 minutes of continuous stirring, the remaining monomers with SDS and KPS were added dropwise into the mixture solution in the reactor flask for an hour. The polymerization reaction was allowed to carry on for another three hours, known as holding process. The copolymer latex was cooled down to room temperature and then transferred into a plastic bottle for further use.

### **3.3.2.2 Preparation of metallic-polymer nanocomposites**

The AgNPs with a size range between 3-7 nm (commercially available) and 10-30 nm (obtained from the synthesis process as described in section 3.3.1) were embedded inside the P(MMA-*co*-AA-*co*-TMVS) nanospheres during the emulsion polymerization process. The concentration of the metallic nanoparticles entrapped in the polymeric nanospheres varied from 6.25 ppm to 50.0 ppm.

### **3.3.3 Deposition of nanostructures on glass substrates**

Before coating process, glass substrates were cleaned with distilled water under ultra-sonication for about 15 minutes. This process was repeated by using fresh distilled water. The piranha solution was prepared by mixing distilled water, 30 % ammonia solution and hydrogen peroxide, with a composition ratio of 5:1:1. The mixture was heated to 67 °C. The glass substrates were immersed in the piranha solution for 30 minutes in order to hydrophilize their surface. The treated glass substrates were then rinsed with distilled water and dried in a vacuum oven at 65 °C.

Two types of chemical bath deposition methods based on the self-assembly coating technique, namely immersion coating and dip coating methods, were developed to coat the polymeric nanospheres on the surface of cleaned glass substrates. The polymer solutions were diluted with distilled water, with a dilution factor of 10. The coating process was performed using a high-precision

single dip coater (Tefini, DP1000C). For the immersion coating method, a cleaned glass substrate was immersed perpendicularly into the diluted polymer solutions using the dip coater, with a down speed of 50.0 mm/min. The substrate was then drawn out from the solution after 45 minutes of holding duration with an up speed of 50.0 mm/min. The coated substrates were subsequently cured in a vacuum oven at 65 °C. For the dipping method, the cleaned glass substrate was dipped perpendicularly into the diluted polymer solutions using the dip coater, with a down speed of 5.00 mm/min, and drawn out with an up speed of 0.12 mm/min. The dwell time was fixed at 60 seconds. The coated substrates were then cured in a vacuum oven at 65 °C. The coating process was repeated by varying the curing temperature from 45 to 105 °C, with a common difference of 20 °C.

#### **3.3.4 Chemically surface modification of precoated glass substrates**

The surface of precoated glass substrates was further chemically modified by immersing the substrates into a dipodal silane, i.e. 1,8-bis(triethoxysilyl)octane (BTO) solution with a holding time of 45 minutes. The concentration of the BTO solution was varied, specifically at 0.1, 0.5, 1.0, 2.0, 3.0, 4.0 and 5.0 v/v%, by using water and ethanol with a ratio of 1:9 as the solvent. Subsequently, the surface-modified glass substrates were drawn out from the silane solution, rinsed with ethanol and subsequently cured in a vacuum oven at 95 °C for 45 minutes. The surface modification process was repeated by immersing the substrates into a mixture of BTO and fluoroalkyl silane, i.e. nonafluorohexyltrimethoxysilane (FAS) solution, with a similar solvent ratio.

The concentration of BTO was fixed at 1.0 v/v% while the concentration of FAS was varied, specifically at 0.1, 0.25, 0.5, 1.0, 3.0 and 5.0 v/v%.

### **3.4 Characterization**

The fabricated AgNPs were characterized via Ultraviolet-Visible (UV-Vis) spectroscopy, field emission scanning electron microscopy (FESEM), energy dispersive X-ray (EDX) spectrometry, Fourier transform infrared (FTIR) spectroscopy and X-ray diffractometry (XRD) analyses. On the other hand, the synthesized P(MMA-*co*-AA) nanospheres with the incorporation of TMVS were characterized by determining the total solids content of the polymer emulsion, while the nanospheres were analyzed by UV-Vis spectroscopy, particle size analysis (PSA), FESEM, atomic force microscopy (AFM), EDX, FTIR, thermogravimetric analysis (TGA), differential scanning calorimetry (DSC) and XRD. Meanwhile, the prepared polymeric nanospheres with the encapsulation of AgNPs were characterized by utilizing UV-Vis spectroscopy, transmission electron microscopy (TEM) and TGA. Nonetheless, the precoated Si substrates which were surface modified chemically were characterized using UV-Vis spectroscopy, AFM, contact angle analysis and water droplet analysis.

### **3.4.1 Ultraviolet-visible spectroscopy**

UV-Vis spectrophotometer is one of the instruments employed for optical absorption and optical transmission analyses. At the same time, it can also confirm the formation of nanostructures by determining the absorption peak of polymeric nanospheres and the plasmonic peak of AgNPs. The solutions of AgNPs and P(MMA-*co*-AA-*co*-TMVS) nanospheres synthesized were diluted with the dilution factor of 10 and 25, respectively (Lee, et al., 2021). The diluted solutions were sonicated in order to make sure the nanostructures were dispersed well in the solutions. Subsequently, the solution was subjected to UV-Vis scanning with the wavelength range of 200 nm to 800 nm to obtain the UV-Vis spectrum.

### **3.4.2 Field emission scanning electron microscopy**

Field emission scanning electron microscope is an instrument utilized to study the surface morphology and composition of a substance. By coating on a clean glass substrate, the AgNPs and polymeric nanospheres synthesized were characterized and scanned using FESEM at an accelerating voltage of 4 kV. The sample was sputtered with a thin layer of platinum before analysis. The particle size and shape of the nanostructures were determined through the FESEM images captured at different magnification powers.



### **3.4.3 Energy dispersive X-ray spectroscopy**

EDX spectrometer is a useful instrument used in elemental composition analysis. The metallic nanoparticles solution, as well as the polymeric emulsion, were dried in an oven at 100 °C for two hours to make sure that all the solvent was totally evaporated. The solid sample of these nanostructures was subjected to EDX scanning at an accelerating voltage of 20 kV to determine the elements present in the sample.

### **3.4.4 Fourier transform infrared spectroscopy**

FTIR spectrometer is an instrument widely utilized for determining the functional groups present in a sample. Both the AgNPs solution and the P(MMA-*co*-AA) emulsion were dried in an oven at 100 °C for two hours to completely evaporate the solvent present in the samples. This is because the presence of solvent or moisture might interfere and affect the performance of the instrument due to its high sensitivity to the water molecules. The solid sample obtained was ground into powder form. Then, the powders were subjected to FTIR analysis at the wavenumbers range between 4000 cm<sup>-1</sup> and 400 cm<sup>-1</sup>. In this study, FTIR analysis was also used to determine the presence of the capping agent, in AgNPs.

### **3.4.5 X-ray diffractometry**

XRD analysis is widely conducted to determine the crystallinity and crystal phase of a sample. Both the AgNPs solution and the P(MMA-*co*-AA-*co*-TMVS) emulsion were dried in an oven at 100 °C for two hours to completely evaporate the solvent present in the samples. The samples in powder form were then subjected to XRD scanning in the range of 10° to 80°, with 0.60 second time constant at a scan rate of 2.0° min<sup>-1</sup>. XRD diffraction pattern was obtained with Cu  $K\alpha$  radiation at 40 kV and 30 mA.

### **3.4.6 Total solids content**

Total solids content is a quantitative measurement employed to determine the total amount of solids present in a fixed amount of emulsion polymer sample as well as the extent of monomer conversion. About 1.000 g of emulsion polymer was weighed in a pre-weighed aluminum dish. The polymer sample was then dried in an oven at 100 °C for two hours to evaporate and remove all unreacted monomers and water molecules completely. Subsequently, the sample was cooled down and the weight of the remaining solids residue was recorded. The processes were repeated until a constant weight was obtained. The test was replicated three times for each sample to obtain an average value (Goh, 2019).

### **3.4.7 Particle size analysis**

Particle size analyzer is a useful instrument that provides the information of the average particle size and the distribution details of particle size range. In this study, distilled water was used to dilute the polymer emulsion. In order to ensure that the polymeric nanospheres were well dispersed and homogeneous, the emulsion sample was sonicated for five minutes. The P(MMA-*co*-AA) nanospheres were then subjected to laser diffraction for particle size analysis. The refractive indexes of water and the polymer were fixed at 1.33 and 1.49 respectively (Goh, 2019).

### **3.4.8 Atomic force microscopy**

Atomic force microscope is another advanced instrument used in the study of surface morphology and topology of nanostructure samples. The P(MMA-*co*-AA) nanospheres with the incorporation of TMVS were coated on a glass substrate and characterized using AFM with a non-contact mode (Lee, et al., 2021). The 3-dimensional images captured by AFM provide clear magnified images of the surface of the sample scanned. Moreover, characteristics of the surface coverage, packing and distribution of the polymeric nanostructures on the glass surface can also be analyzed through the images obtained.

### **3.4.9 Thermogravimetric analysis**

Thermogravimetric analyzer is used to determine the thermal stability of the samples analyzed. Dried P(MMA-*co*-AA) nanospheres were used for the analysis. About 10 mg of polymer powder sample was weighed into an alumina crucible and subjected to TGA analysis for the determination of the thermal decomposition behaviour and the composition content of the sample (Lee, et al., 2021). In order to reduce the thermos-oxidative degradation of the sample, nitrogen gas was purged throughout the analysis. The nitrogen flow rate was fixed at 20 mL/min. The sample was heated from 25 °C to 700 °C with a heating rate of 20 °C/min (Lee, et al., 2021).

### **3.4.10 Differential scanning calorimetry**

Differential scanning calorimeter is used to determine the glass transition temperature of the sample analyzed. Dried P(MMA-*co*-AA) nanospheres were used for the analysis. About 10 mg of powder sample was weighed into an alumina crucible and sealed with an alumina lid using a sealing press. The sample was then subjected to DSC analysis under an inert atmosphere with the purging of nitrogen gas. The nitrogen gas flow rate was fixed at 20 mL/min. The sample was first heated from 25 °C to 150 °C with a heating rate of 10 °C/min (Lee, et al., 2021). Subsequently, the sample was cooled to 25 °C with a cooling rate of 50 °C/min. Finally, the sample was heated with another round of heating from 25 °C to 170 °C with a heating rate of 10 °C/min (Goh, 2019).

#### **3.4.11 Transmission electron microscopy**

Transmission electron microscope is a much more advanced and powerful instrument utilized in the study of surface morphology and topology of nanostructures. First of all, the metallic-polymer nanocomposite emulsion was sonicated for 10 minutes to ensure that the nanoparticles were well dispersed. Then, the polymer dispersion was spread onto a lacey copper grid and subjected to TEM scanning. TEM image was then captured and observed to identify the AgNPs embedded inside the polymeric nanospheres.

#### **3.4.12 Contact angle analysis**

A contact angle analyzer is an instrument used for inspecting the water contact angle (WCA) property of a substrate. In this study, the WCA of the chemically modified surface of glass substrates was investigated using a contact angle measurement system at ambient conditions. The WCA was measured by fitting and capturing the image of a deionized water droplet in a contact angle analyzer (Laplace-Young model) using a software program named Lauda Surface Analyzer (Lee, et al., 2021).

#### **3.4.13 Water droplet analysis**

Water droplet analysis is commonly adopted to examine the wettability of a coating on the surface of a substrate. A constant volume of 10  $\mu\text{L}$  distilled water was dropped on the chemically modified surface of the Si substrate. The

images of the water droplet formed on the surface were captured with a camera, observed and compared.

### **3.5 Peeling test**

A tape test based on ASTM D 3359-09 is commonly employed to access the adhesive strength of the coatings on a substrate (Lee, et al., 2021). In general, pressure-sensitive tape (3 M 600 Scotch transparent tape) was applied and covered evenly over the coating. The tape was then smoothened into place by rubbing it firmly using a ruler to ensure good contact between the adhesive tape and the coated surface. Within 2 minutes of application, the tape was removed by seizing the free end and pulling it off rapidly back upon itself at as close to an angle of  $180^\circ$  as possible (ASTM D3359-09, 2009). The output power of the coated solar modules prior to and after each cycle of peeling was measured using a solar simulator (Lee, et al., 2021).

### **3.6 Weathering resistance test**

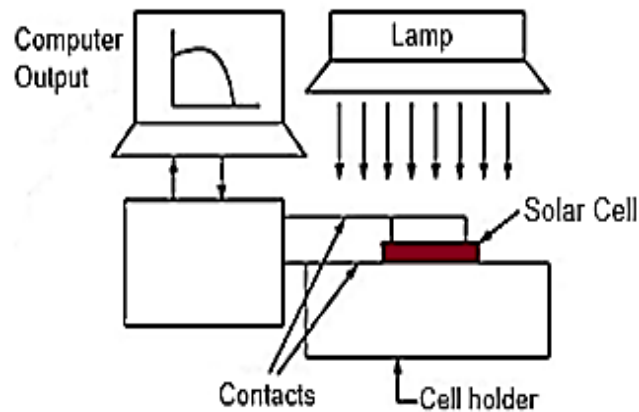
The weathering resistance of the coatings on glass substrate was evaluated via a natural weathering test which was conducted with the test specimens being mounted on a rack facing directly south ( $S\ 204^\circ$ ) at an angle of about  $30^\circ$ . The rack was located on the rooftop of the building of Faculty of Science at the Kampar campus of Universiti Tunku Abdul Rahman in Perak, Malaysia ( $4.3085\ N$ ,  $101.1537\ E$ ; relative humidity: 58-95% and temperature:  $22-34^\circ C$ ). A set of test specimens were collected every month for a duration of 4 months.

The specimens were rinsed with distilled water and dried. The condition of the polymer coatings was subsequently examined using AFM (Lee, et al., 2021).

### 3.7 Electrical measurement of solar modules

The electrical features of the photovoltaic modules (Sanyo, AM-8701CAR,  $P_{\text{max}} = 190 \text{ mW}$ ) before and after surface treatment and modification were measured using a Programmable DC electronic load LIV tester. The maximum normal surface irradiance applied in this work was set at  $100 \text{ mW cm}^{-2}$  while the solar module was illuminated under an AM1.5 solar simulator. The measurement was conducted consistently by fixing the solar module perpendicularly to the light source. Figure 3.1 illustrates the setup of the apparatus. Each sample was measured three times to obtain an average value. By using the current and voltage readings obtained, the electrical output power of the solar cell was calculated using Equation 3.1 (Tay, et al., 2020).

$$\text{Power (W)} = \text{current (A)} \times \text{voltage (V)} \quad (\text{Equation 3.1})$$



**Figure 3.1:** Schematic diagram of the experimental setup for solar cell output power measurement

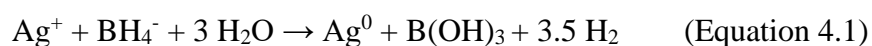
## CHAPTER 4

### FABRICATION AND CHARACTERIZATION OF SILVER NANOPARTICLES

#### 4.1 Synthesis of silver nanoparticles via the chemical reduction method

##### 4.1.1 Effect of reducing agent on the physical properties of AgNPs

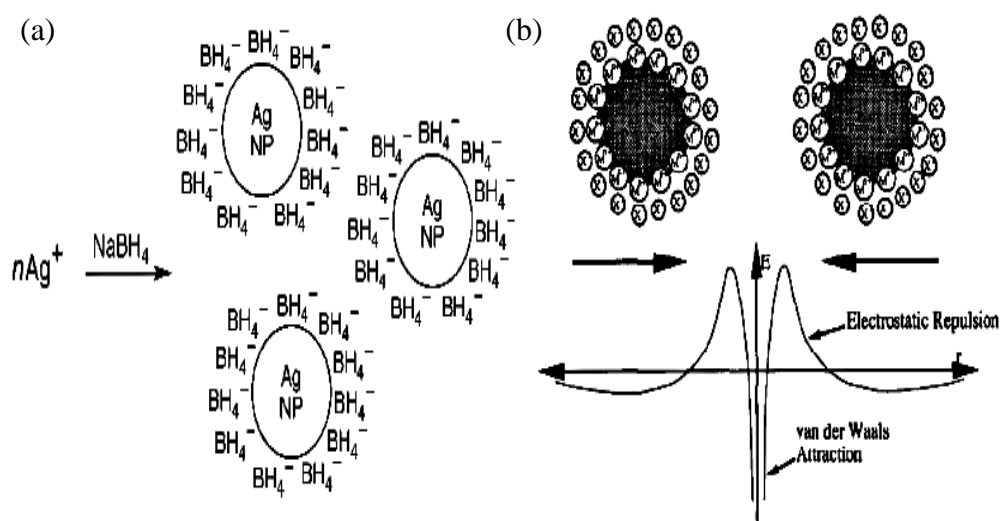
The chemical reduction method of the metal salt is a bottom-up approach for synthesizing metallic nanoparticles and it has been employed to synthesize the AgNPs in this study. In this work, NaBH<sub>4</sub> was used as the reducing agent to reduce Ag<sup>+</sup> ions (dissociated from the silver metal salt, AgNO<sub>3</sub>) to form Ag particles with either DDT or DDA as the capping agent. The ionic equation of the chemical reduction process is shown in Equation 4.1.



In a previous study, the effect of the concentration of reducing agent on the formation of AgNPs had been investigated (Tay, et al., 2020). The results obtained in the study confirm the theory reported by Song, et al. (2008), which states that AgNPs with smaller size can be synthesized by increasing the concentration of the reducing agent. When a small amount of NaBH<sub>4</sub> is added, the AgNPs would aggregate and agglomerate. This is because the boron hydroxide produced (Eq. 4.1) will attach to the surface of the nanoparticles. A low concentration of BH<sub>4</sub><sup>-</sup> would result in the reduction of surface electron



density. However, when an excess amount of  $\text{NaBH}_4$  is added, the AgNPs could be maintained in smaller size owing to the electrostatic stabilization attributed to the thick  $\text{BH}_4^-$  ion layer that surrounds the particles (Figure 4.1). The thick  $\text{BH}_4^-$  ion layer prevents the absorption of boron hydroxide to the surface of nanoparticles. Thus, the AgNPs are well-dispersed in the solvent. In this case,  $\text{NaBH}_4$  not only acts as a reducing agent but also serves as a stabilizer to protect the nanoparticles from agglomeration. The results obtained from this research showed that AgNPs with smaller size and better dispersion were obtained by increasing the concentration of  $\text{NaBH}_4$  from 0.24 to 0.36 M (Tay, et al., 2020). Therefore, the concentration of  $\text{NaBH}_4$  was fixed at 0.36 M in further study.

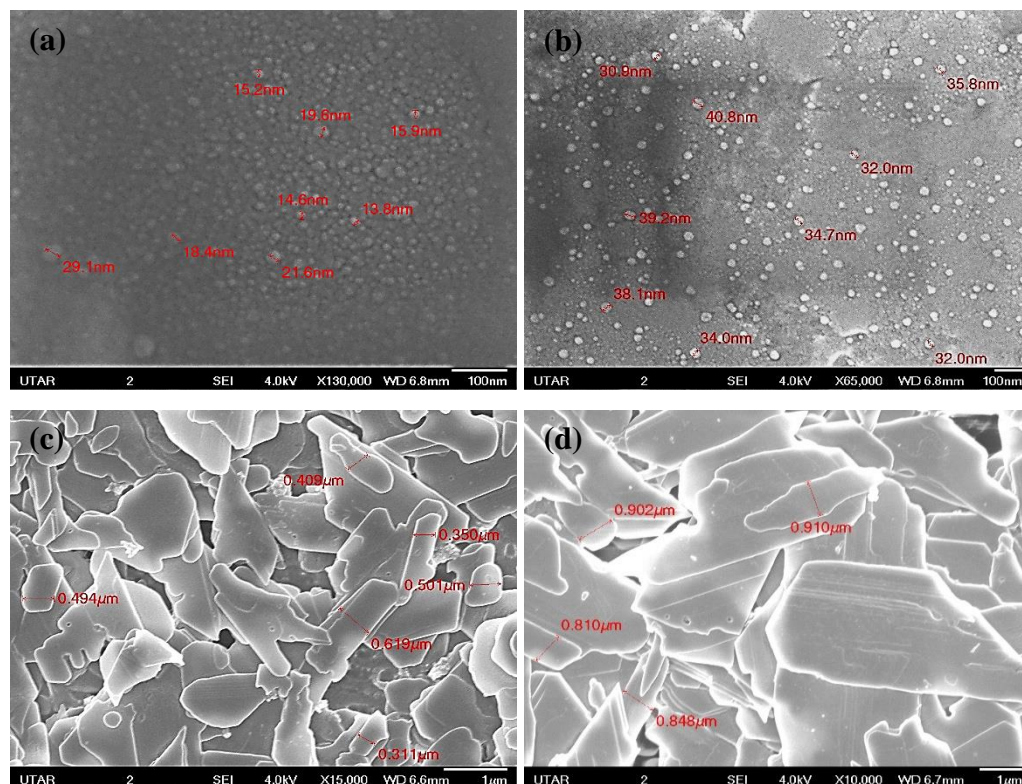


**Figure 4.1:** Schematic diagrams representing (a) absorption of  $\text{BH}_4^-$  ion layer to the surface of AgNPs and (b) electrostatic repulsion between nanoparticles (Singh, et al., 2018)

#### **4.1.2 Effects of capping agent and reaction temperature on the physical properties of AgNPs**

AgNPs with different structural and physical properties, which include the particle size and particle shape, were fabricated by manipulating the reaction parameters, namely the concentration of capping agent, the type of capping agent utilized and the reaction temperature during the chemical reduction reaction. The AgNPs synthesized were characterized using FESEM for morphological study; UV-Vis spectroscopy for optical analysis; EDX spectroscopy for elemental analysis; XRD for the study of crystallinity and crystal phase; and FTIR for the determination of functional groups.

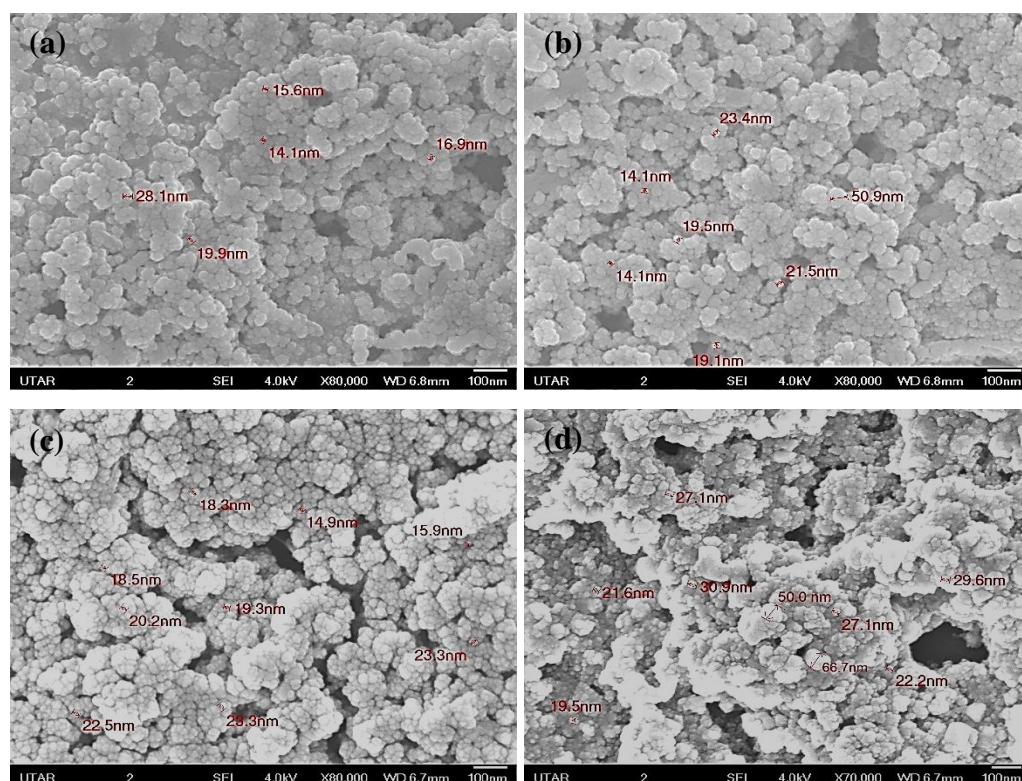
As aforementioned, the geometrical and structural properties of the synthesized metallic nanoparticles are strongly dependent on the concentration of the capping agent (Natsuki and Hashimoto, 2015). In this study, the AgNPs were fabricated in an ice bath (0 °C) using either DDT or DDA as the stabilizer by varying their concentration, while other reaction parameters were kept constant. The concentration of the capping agent is represented by the S value which denotes  $\frac{[\text{Capping agent}]}{[\text{AgNO}_3]}$  molar ratio. Figures 4.2 and 4.3 show the FESEM images of the synthesized AgNPs which were functionalized by DDT and DDA, respectively. The range of particle size obtained via FESEM are tabulated in Table 4.1.



**Figure 4.2:** FESEM images of AgNPs which were synthesized in an ice bath (0 °C) with different S value of DDT: (a) 2.78, (b) 5.56, (c) 11.1 and (d) 16.7, with a magnification of  $\times 130000$ ,  $\times 65000$ ,  $\times 15000$  and  $\times 10000$  respectively

**Table 4.1:** The particle size range of fabricated AgNPs corresponding to the S value and type of capping agent

S value	Particle size range (nm)	
	DDT	DDA
2.78	5-30	10-30
5.56	10-45	-
11.1	> 300	-
16.7	> 800	10-55
22.2	-	10-25
27.8	-	20-70



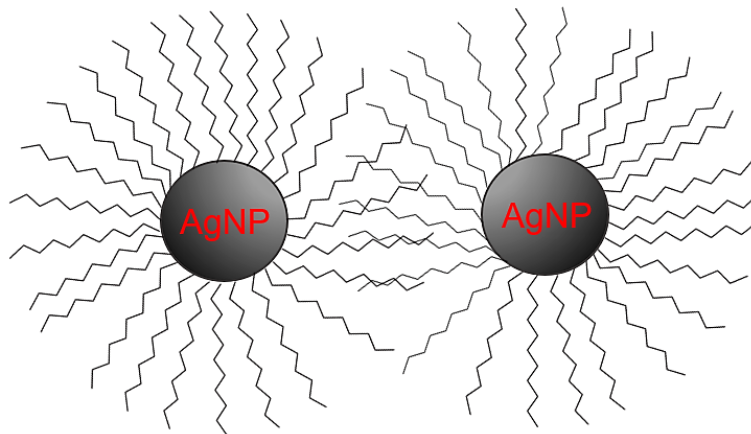
**Figure 4.3:** FESEM images of AgNPs which were synthesized in an ice bath (0 °C) with different S value of DDA: (a) 2.78, (b) 16.7, (c) 22.2 and (d) 27.8, with a magnification of  $\times 80000$

Based on the results obtained from the FESEM images, both sets of AgNPs functionalized by DDT and DDA exhibit a similar trend, where the particle size and particle size distribution increase and broaden with the concentration of the capping agent. The particle size of AgNPs synthesized utilizing DDT as a capping agent increased dramatically from 10-30 nm to more than 750 nm when the S value of DDT was increased from 0.278 to 16.7 (Figure 4.2). On the other hand, for the AgNPs functionalized by DDA, the particle diameter increased slightly from 10-30 nm to 20-70 nm when the S value of DDA was increased from 0.278 to 27.8 (Figure 4.3). It is obvious that DDA performed better than DDT as a capping agent to protect the metallic nanostructures from aggregation during the chemical reduction process. Over a wide range of

concentration, DDA has constantly yielded AgNPs with spherical shape as well as smaller particle diameter and narrower particle size range, which are mostly smaller than 100 nm (Figure 4.3). Nonetheless, the AgNPs which are stabilized by DDT grow to a larger scale with irregular structure when the S value of DDT exceeded the optimum concentration of 5.56 (Table 4.1, Figure 4.2). Therefore, DDA was used for further study.

Theoretically, metallic nanoparticles with smaller size are produced by increasing the amount of capping agent. This is because with higher concentration, more capping agent molecules are able to attach to the surface of metal colloids, thus preventing aggregation between the particles through steric stabilization (Tay, et al., 2020). As a result, the fabricated AgNPs are more well dispersed with smaller size. On the other hand, instead of reducing the particle size, an excessive amount of capping agent will lead to the growth of nanoparticles to larger size owing to the formation of bigger micelles. These larger micelles result in the destabilization of the nanostructures, thus giving rise to the occurrence of agglomeration, clusterization and enlargement of nano-colloid (Mirela, 2009). Consequently, the bulk particles with irregular shapes are formed. In view of this, an adequate amount of capping agent should be added during the synthesis process in order to produce AgNPs with desirable structural properties (Tay, 2019). In fact, the steric stabilization of a capping agent, which is attributed to long carbon chains, plays a predominant role in the capping of AgNPs. It prevents the nanoparticles from further growth in size and maintains them in a smaller size with a spherical shape (Farrell, et

al., 2013). Figure 4.4 demonstrates the schematic diagram of the steric stabilization effect contributed by a capping agent.

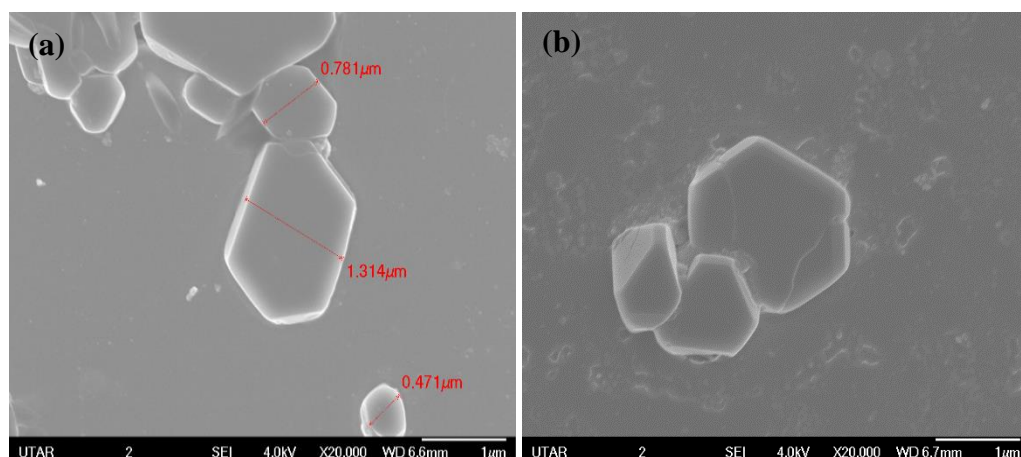


**Figure 4.4:** A schematic diagram of steric stabilization of AgNPs by capping agent molecules

The morphological features of the fabricated AgNPs would also be significantly affected by the reaction temperature of the chemical reduction process. The AgNPs capped with two different concentrations of DDA and synthesized at room temperature (25 °C) were characterized using FESEM (Figure 4.5). The particle size obtained by using different concentrations of DDA at the reaction temperature of 0 °C and 25 °C are tabulated in Table 4.2. By comparing the FESEM images obtained (Figure 4.3 (a), (b) and Figure 4.5), it is obvious that the particle diameter and shape were greatly affected by the reaction temperature. Contrary to the structural properties of the AgNPs synthesized in an ice bath, the nanostructures have significantly grown to a bigger scale with broader size distribution when the reaction temperature was raised from 0 °C to 25 °C. Meanwhile, the spherical nanoparticles (Figure 4.3) have turned into nanostructures with irregular shapes and sharp edges (Figure



4.5). Therefore, it can be concluded that AgNPs with smaller particle size, narrower size distribution and more regular shape were prepared at a lower temperature.



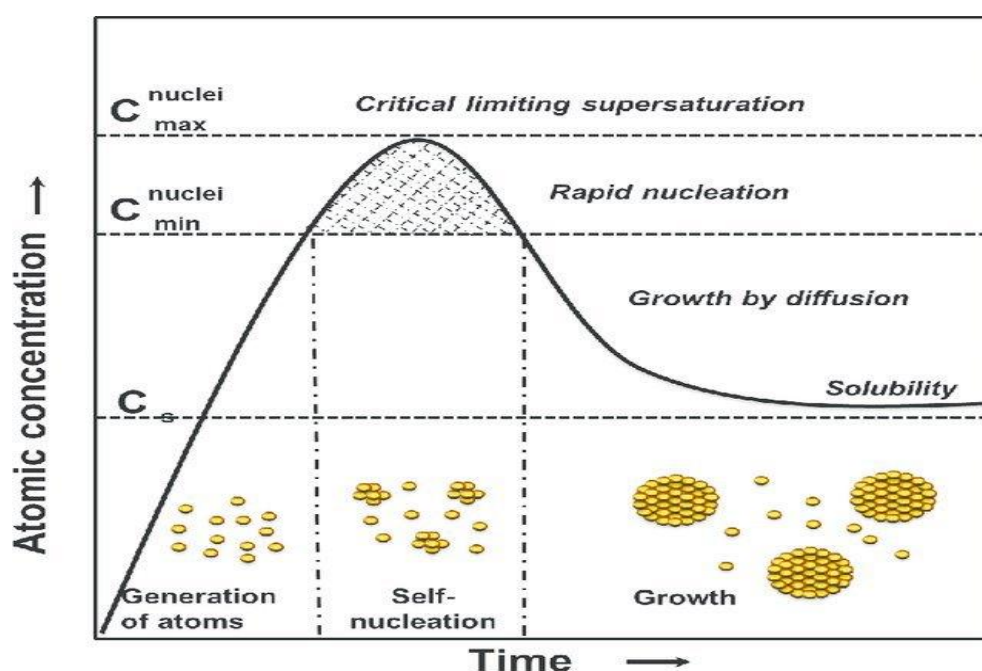
**Figure 4.5:** FESEM images of AgNPs which were synthesized at room temperature (25 °C) with two S values of DDA: (a) 2.78 and (b) 16.7, with a magnification of  $\times 20000$

**Table 4.2:** The particle size of AgNPs obtained by using different concentrations of DDA at the reaction temperature of 0 °C and 25 °C

S value	Particle size range (nm)	
	0 °C	25 °C
<b>2.78</b>	10-30	> 450
<b>16.7</b>	10-55	> 640

It had been found that the formation of metallic nanoparticles via the chemical reduction process occurs in the early stages of synthesis, specifically during the nucleation and growth process. Nucleation is the initial step of the formation of a thermodynamic new structure which grows irreversibly into a larger nucleus within the body of a metastable parent phase. Nucleation will only take place in a supersaturated solution which is thermodynamically unstable in order to

produce small size colloids. After forming stable nuclei from a solution, they grow through the absorption of soluble molecules onto the stable cluster surface, which is known as molecular addition. Secondary growth occurs when smaller unstable nuclei combine with stable particles, namely aggregation (Pacioni, et al., 2015). Figure 4.6 illustrates La Mer's mechanism of the nucleation and growth process of particles.



**Figure 4.6:** Representation of the La Mer's mechanism of the nucleation and growth process of particles

Variation in temperature might influence the reaction kinetic, aggregation and agglomeration mechanisms, including intra-particles ripening, oriented attachment and overgrowth (Pinero, et al., 2017). When the synthesis reaction is carried out at a high temperature, there is an increase in the reduction kinetic. According to the classical La Mer's mechanism, the atoms will aggregate to form colloidal particles. Meanwhile, the nucleation and growth process of nanoparticles accelerate. Subsequently, the nanoparticles will grow and



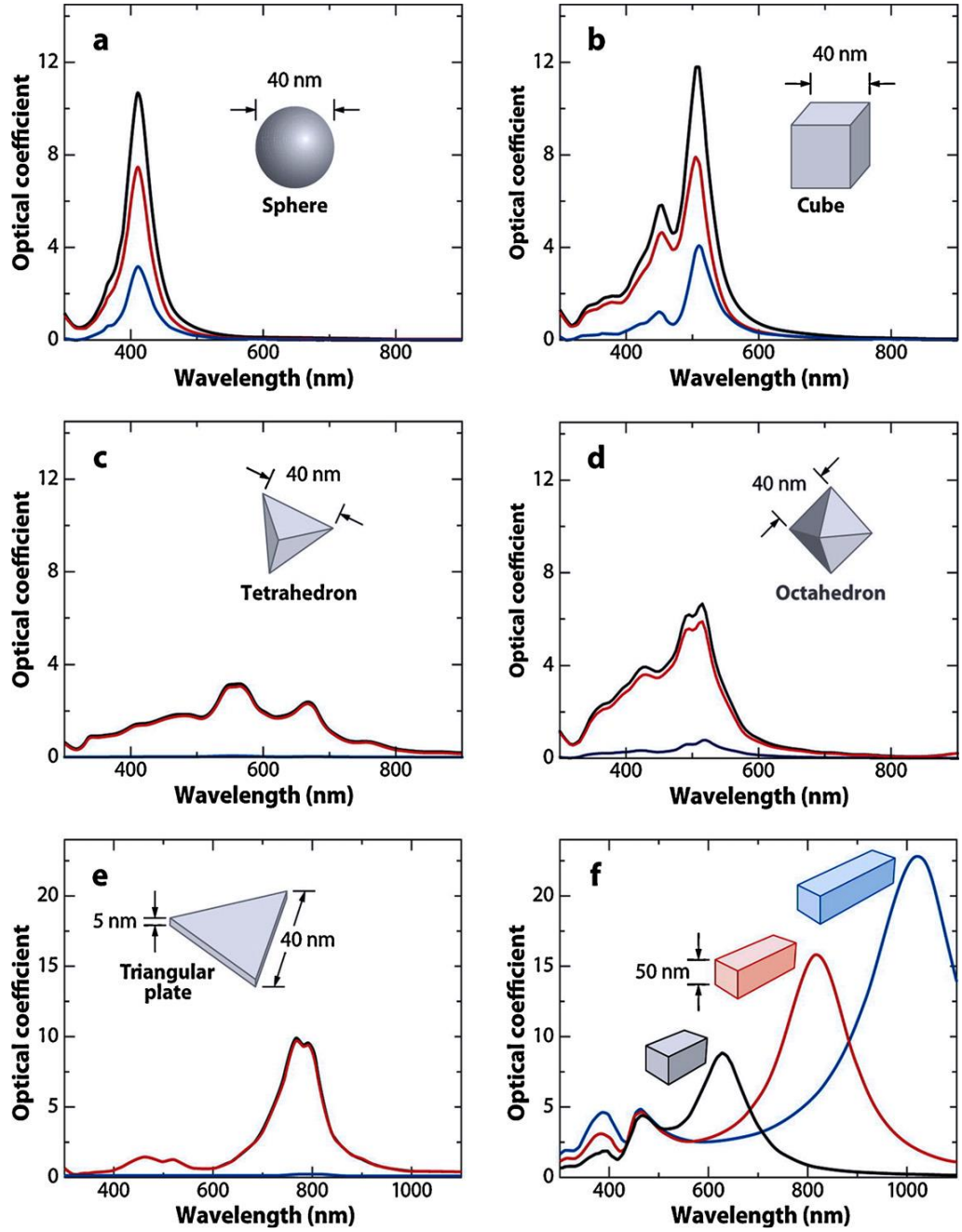
agglomerate during a secondary growth process. High temperature increases the rate of reduction of silver metal salt to form silver colloids due to the high frequency of effective collision between the particles. However, due to the high reduction kinetic, the stabilizer molecules are not able to attach to the surface of the particles immediately and spontaneously. Without the adsorption of the protective group, the nanoparticles will agglomerate and thus bulk particles will form. On the other hand, the rate of reduction decreases at a lower temperature with slower nucleation and growth of the nanoparticles. Hence, the capping agent molecules are able to attach to the surface of nanoparticles and maintain their size at the nanoscale by preventing them from aggregation (Tay, et al., 2020).

Among the nanostructures which have been fabricated with different reaction parameters, the spherical-shaped AgNPs with the size range of 10-30 nm were selected to be embedded inside the polymeric matrix in this study. The AgNPs were synthesized at 0 °C, using DDA with the S value of 2.78. Instead of using DDT as the capping agent, DDA is deemed more suitable for this work. This is because the thiol group present in DDT could possibly act as a chain transfer agent, which may affect the molecular weight of the polymer produced. Moreover, DDA has demonstrated its outstanding capping efficiency to produce AgNPs with smaller particle size, narrower size distribution and uniform spherical shape during the chemical reduction process (Figure 4.3). AgNPs with smaller size and spherical in shape are essential for them to be encapsulated into the polyacrylic nanospheres that are synthesized with an average particle size of 97 nm. In fact, small spherical nanoparticles are able to

scatter the incoming light more effectively, thus improving the light harvesting efficiency of the nanostructures.

#### **4.1.3 Localized surface plasmon resonance effect of fabricated AgNPs**

Different types of noble metallic nanoparticles exhibit the localized surface plasmon resonance (LSPR) effect at different wavelengths. As a matter of fact, the LSPR effect of metallic nanoparticles is highly dependent on their particles size and shape (Petryayeva and Krull, 2011). An increase in particle size and edges of the nanostructures will cause a red-shift effect in the absorption spectra, due to the high efficiency in charge separation (Tay, et al., 2020). On the other hand, a decrease in particle size will lead to a blue-shift phenomenon in the absorption spectra. Nanostructures which are more symmetrical in shape would enhance the LSPR intensity. According to Petryayeva and Krull (2011), the number of resonance absorption peak is determined by the number of modes of a structure that can be polarized by an incident light source. For instance, spherical nanoparticles have only one absorption peak while non-spherical nanostructures have more than one resonance absorption peak, depending on their structure (Figure 4.7). Moreover, the wavelength of the plasmon peak of these nanoparticles varies with their size and shape. For example, the spherical-shaped AgNPs with an average particle size of 40-90 nm exhibit a theoretical plasmon peak in the UV-Vis range of 380-480 nm due to the LSPR effect.



**Figure 4.7:** Number of the resonance absorption peak of silver nanoparticles with different shapes and structures (Petryayeva and Krull, 2011)

From the information obtained via UV-Vis spectroscopy, the bandgap energy of AgNPs could be determined. The bandgap energy,  $E_{bg}$  is the energy required to excite the electrons from the valance band to the conduction band. The  $E_{bg}$  of AgNPs has slightly deviated when their morphological and structural properties are different. Fredrick and Mangaka (2017) reported that AgNPs

exhibit a theoretical  $E_{bg}$  of 3.04 eV, but it is somehow dependent on the particle size and shape of the nanoparticles. Hence, the shifting of wavelength will affect the calculated value of  $E_{bg}$ .

The  $E_{bg}$  of AgNPs can be calculated directly from the UV-Vis absorption spectrum using Einstein's photon energy equation (Equation 4.2), where  $\lambda_{max}$  is the maximum absorbance wavelength,  $h$  is the Planck's constant and  $c$  is the speed of light. The  $E_{bg}$  of AgNPs synthesized with various  $S$  values was calculated as shown in Appendix A.

$$E_{bg} = \frac{hc}{\lambda_{max}} \quad (\text{Equation 4.2})$$

**Table 4.3:** The particle size, absorbance, wavelengths with the respective calculated  $E_{bg}$  of the AgNPs corresponding to the  $S$  value of DDA

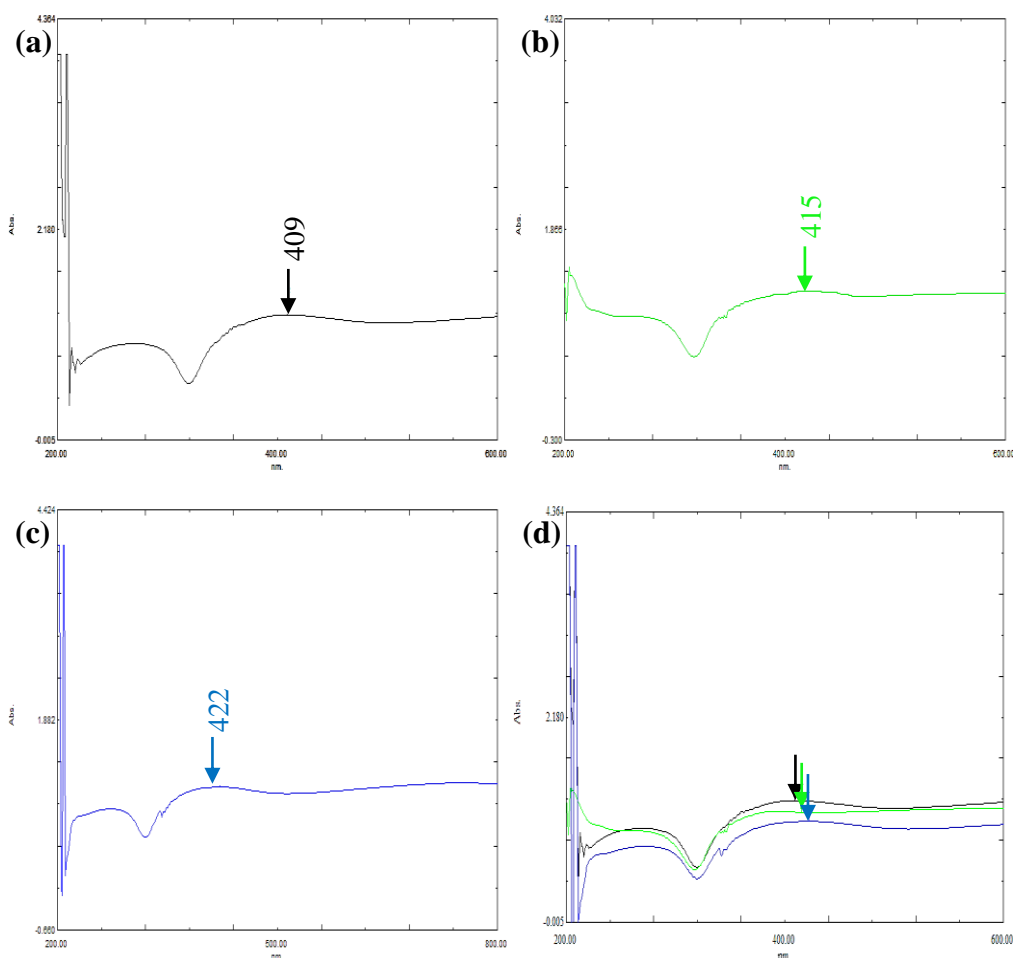
<b>S value</b>	<b>Particle size (nm)</b>	<b>Absorbance</b>	<b>Wavelength (nm)</b>	<b><math>E_{bg}</math> (eV)</b>
<b>2.78</b>	10-30	1.290	409	3.036
<b>16.7</b>	10-55	1.166	415	2.992
<b>27.8</b>	20-70	1.071	422	2.942

Based on the results obtained, the AgNPs fabricated using DDA with the  $S$  value of 2.78 gave an  $E_{bg}$  of 3.036, which is close to the theoretical value of 3.04 eV. Indeed, the AgNPs produced were smaller in particle size range (10-30 nm) (Table 4.1) and spherical in shape (Figure 4.3). Smaller particle size results in a larger value of the measured absorbance and a higher value of bandgap energy (Table 4.3). An increase in the bandgap energy and a decrease in the wavelength of the absorption peak is a phenomenon known as the blue-

shift effect. According to the quantum confinement theory, the blue-shift phenomenon is associated with a decrease in particle size. The holes and electrons are less confined by the potential barriers of the surface. Hence, the spacing of the electronic level and the bandgap energy increase with decreasing particle size (Singh, et al., 2018). The phenomenon that happens in a reversed condition is known as the red-shift effect. From the results shown in Table 4.3, the wavelength of the plasmon peak shifted from 409 to 422 nm (red-shift) with an increasing particle size range from 10-30 nm to 20-70 nm, while the calculated  $E_{bg}$  decreases from 3.036 to 2.942 eV.

Figure 4.8 shows the UV-Vis spectra of the solutions of AgNPs which were synthesized with different concentration of the capping agent DDA in an ice bath. From the spectra obtained, the AgNPs render a plasmon absorption peak in the range of 409-422 nm which well falls within the given theoretical range of AgNPs. The peak present is corresponding to the characteristic surface plasmon resonance signal of the AgNPs, which has proven that AgNPs were fabricated successfully (Venkatesham, et al., 2014). The broadening of the plasmon absorption peak could be a result of the formation of AgNPs with large particle size distribution. Besides that, the negative band occurs at around 320 nm in all of the AgNPs spectra obtained is possibly resulted by the dielectric constant of the medium and the dielectric factors of the surrounding environment. On the other hand, the noise bands observed at the wavelength range of 200-240 nm in the UV-Vis spectra are mainly due to the DDA capping agent molecules that are attached to the surface of Ag nano-colloids to serve as a protective layer by preventing the nanoparticles from aggregation

and clusterization. This could be consolidated by the absence of other peaks within the wavelength range of 335 to 560 nm. As reported by Venkatesham et al. (2014), no peaks located within this particular range evidence the absence of nanoparticles agglomeration.



**Figure 4.8:** UV-Vis spectra of AgNPs which were synthesized in an ice bath with different S values of DDA: (a) 2.78, (b) 16.7, (c) 27.8; and (d) overlay spectrum

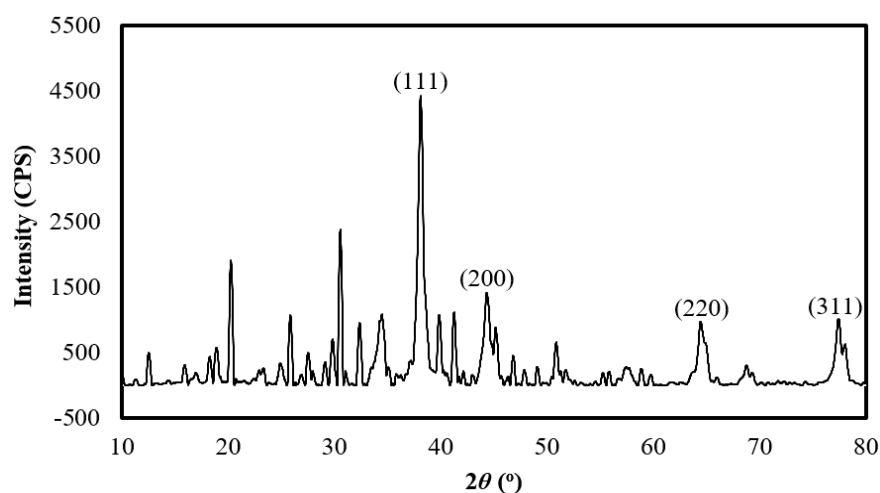
On the other hand, it was found that the absorbance of the plasmon peaks decreases from 1.290 to 1.071 when the S value of DDT increases from 2.78 to 27.8 (Table 4.3, Figure 4.8). According to the Mie scattering theory, the results depict the fact that AgNPs with bigger and broader particle size range have

been synthesized as evinced by the decrease in absorbance. The Rayleigh scattering theory describes the absorption and scattering of electromagnetic waves by a homogeneous isotropic colloid with a spherical shape. It suggests the situation where scattering particle size is much smaller than the wavelength of the incident light, specifically  $< 1/10$  wavelength (Lin, et al., 2014). As reported, the smaller the particle size, the greater the light radiation is scattered by the nanostructures and thus high fraction of incident light is being absorbed. Hence, a higher value of absorbance indicates that the AgNPs produced are smaller in size. Moreover, with the increasing amount of capping agent, the incident light scattered and absorbed by the AgNPs decreases due to the interference caused by the capping agent (Tay, 2019). As a result, the plasmonic effect of the AgNPs decreases.

#### **4.1.4 Crystallinity of AgNPs**

In this work, XRD was used to study the crystal phase and the degree of crystallinity of the fabricated AgNPs. Figure 4.9 shows the XRD pattern of AgNPs which were capped by DDA with the S value of 2.78 and synthesized in an ice bath via the chemical reduction process. The diffraction peaks at  $38.12^\circ$ ,  $44.36^\circ$ ,  $64.46^\circ$  and  $77.43^\circ$  are assigned to (111), (200), (220) and (311) planes of Ag, respectively. The data obtained have been phase analyzed using the instrument software to compare with the reference database from International Centre for Diffraction Data (ICDD). The outcomes of the matching analysis illustrate that the diffraction peaks of the fabricated AgNPs match well with the ICDD with the entry number of 01-077-6577:  $38.37^\circ$  (111),

44.60° (200), 64.91° (220) and 77.99° (311). Owing to a different type of capping agent that has been used in the fabrication process, the  $2\theta$  values of the diffraction peaks obtained are shifted slightly. The detected peaks shown in the diffraction pattern are corresponding to the face-centred cubic (FCC) structure of AgNPs and indicate the crystalline nature of AgNPs. Nonetheless, there are also other diffraction peaks shown in the XRD pattern which could be majorly due to the presence of impurities of a capping agent (DDA) and minorly attributed to the unreacted starting materials and by-products (Tay, et al., 2020). The capping agent serves as a stabilizer to functionalize AgNPs by preventing them from aggregation and agglomeration as well as maintaining their particle size in a smaller scale, which is not expected to affect final results significantly.



**Figure 4.9:** XRD pattern of the AgNPs functionalized by DDA

The results on the degree of crystallinity obtained from the programmable software of the XRD instrument (Match! From Crystal Impact) showed that the sample possesses 50.42% of crystallinity and 49.58% of amorphous content, by weight.



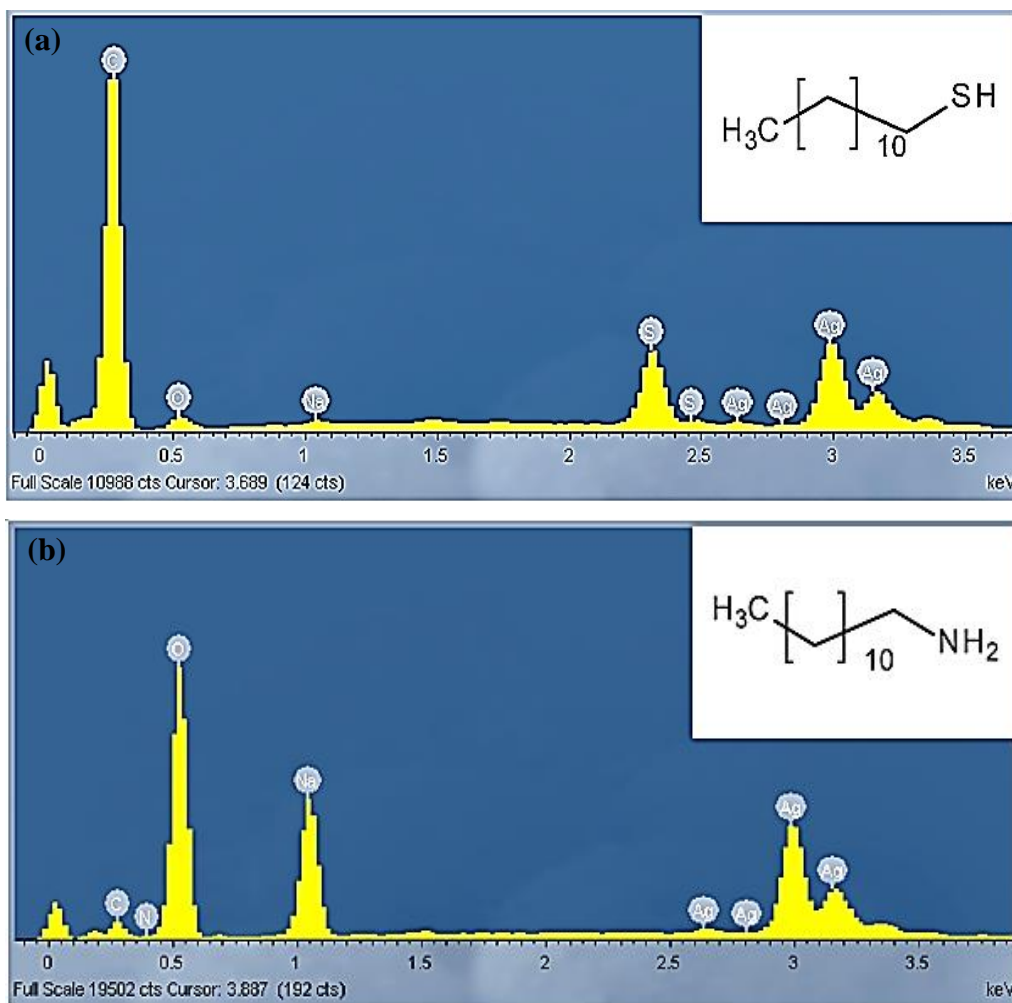
Besides that, the average crystallite size of the AgNPs synthesized was calculated using the Debye-Scherrer equation (Equation 4.3), where  $D$  is the crystallite diameter,  $k$  is the Scherrer's constant,  $\lambda$  is the wavelength of the X-ray source (Cu K $_{\alpha}$  radiation),  $\beta$  is the width of diffraction broadening at full-width half maximum (in radian  $2\theta$ ) and  $\theta$  is the Bragg's diffraction angle.

$$D = \frac{k\lambda}{\beta \cos \theta} \quad (\text{Equation 4.3})$$

The crystallite diameter of the nanoparticles at various diffraction angles was determined and the calculation steps are shown in Appendix B. The average crystallite size of the AgNPs was 16.44 nm. The calculated diameter of the AgNPs is consistent with the results obtained from FESEM analysis, which showed that the AgNPs produced were in the range of 10-30 nm.

#### **4.1.5 Elemental composition of AgNPs functionalized by a capping agent**

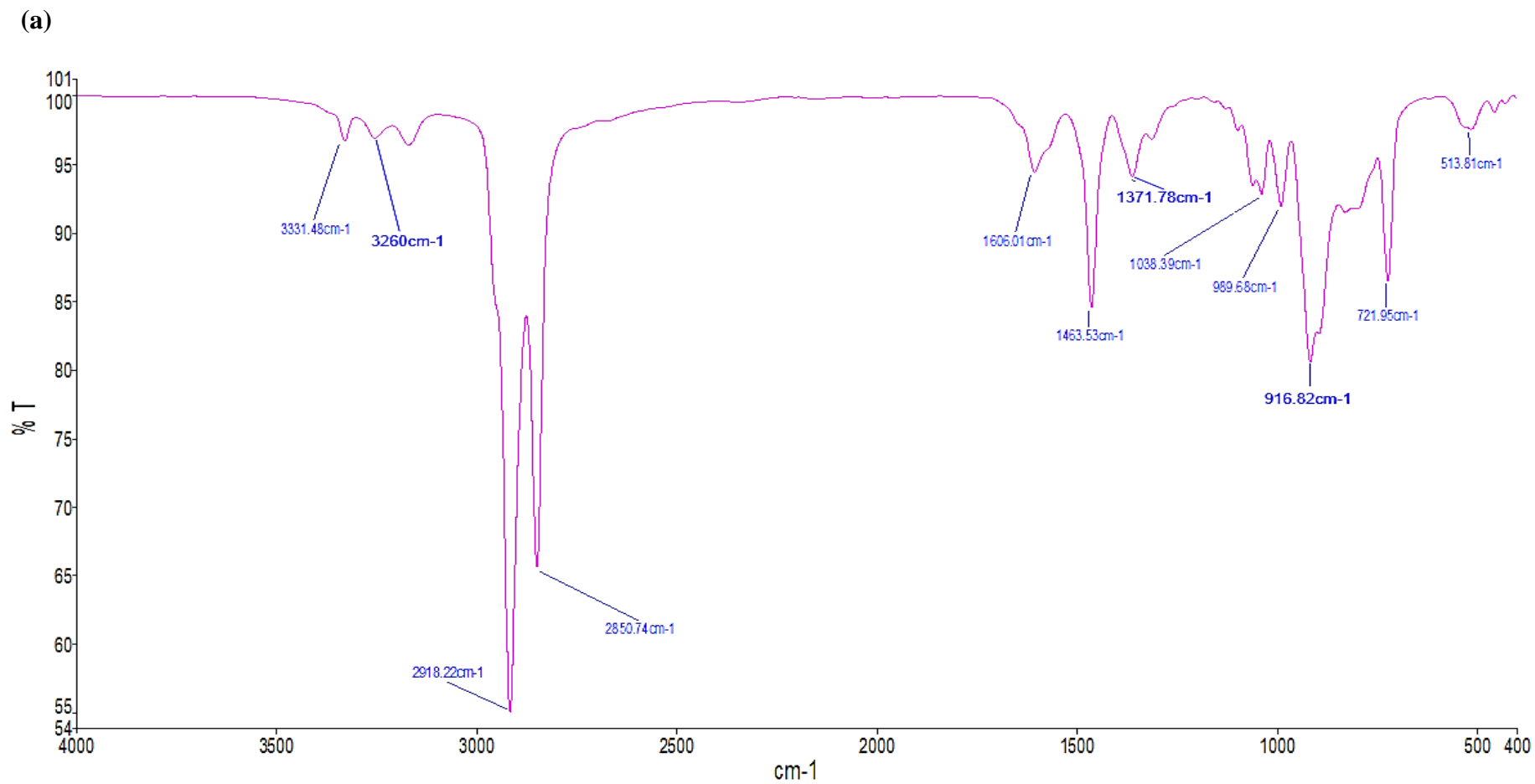
The AgNPs fabricated were characterized with elemental analysis using an EDX spectrometer. Figures 4.10 show the EDX spectra of the AgNPs which were functionalized with (a) DDT and (b) DDA, and the respective chemical structure of the capping agents. Both of the EDX spectra illustrate explicitly the presence of silver (Ag) element in the samples. The presence of the sulfur (S) and carbon (C) peaks in Figure 4.10 (a), and the presence of the nitrogen (N) and carbon (C) peaks in Figure 4.10 (b) have evinced the fact that the capping agent molecules were attached to the AgNPs after the chemical reduction process.



**Figure 4.10:** EDX spectra of AgNPs stabilized with (a) DDT and (b) DDA, and the respective chemical structure of the capping agents

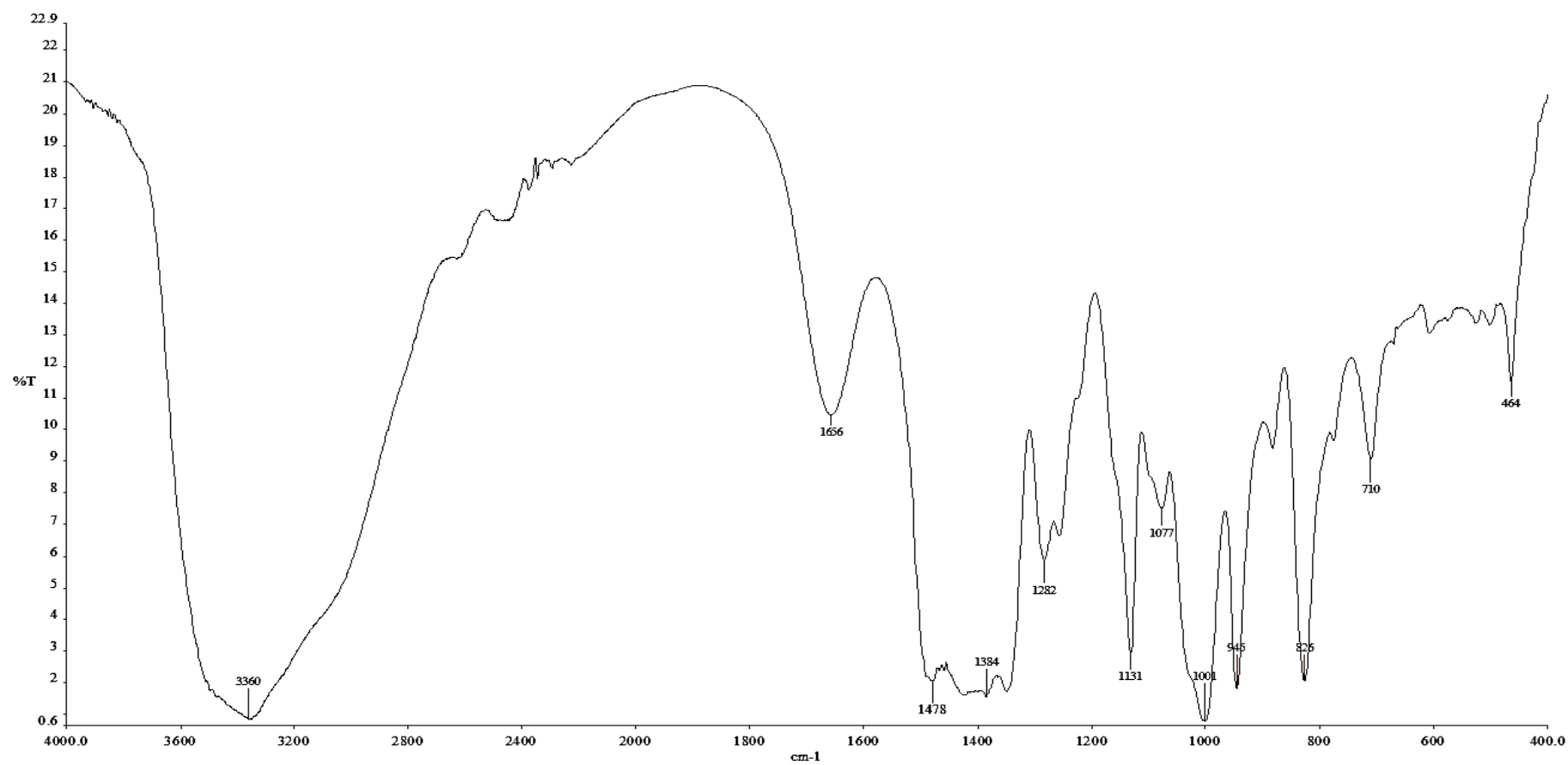
#### 4.1.6 Functional groups of DDA-capped AgNPs

FTIR was used to determine the functional groups present in the capping agent DDA and the DDA-functionalized AgNPs. Figure 4.11 shows the IR spectra of (a) pure DDA and (b) the AgNPs synthesized with DDA. The data extracted from the FTIR spectra are tabulated in Table 4.4. The existence of peaks of the amine functional group ( $-\text{NH}_2$ ) in the AgNPs proved that the fabricated AgNPs have been functionalized by DDA.



**Figure 4.11 (a):** FTIR spectrum of DDA

(b)



**Figure 4.11 (b):** FTIR spectrum of DDA-functionalized AgNP

**Table 4.4:** FTIR spectrum data of DDA and DDA-functionalized AgNPs

Sample	Wavenumber (cm <sup>-1</sup> )	Description	Vibration mode
<b>DDA</b>	3331, 3260	Very weak	N-H stretch
	2918, 2851	Very strong	C-H stretch
	1606	Weak	N-H bend
	1464	Medium	-CH <sub>2</sub> bend
	1371	Weak	-CH <sub>3</sub> bend
	1038	Weak	C-N stretch
	722	Medium	N-H wag
<b>DDA- functionalized AgNPs</b>	3360	Very strong	O-H stretch
	1656	Medium	N-H bend
	1478	Very strong	-CH <sub>2</sub> bend
	1384	Very strong	-CH <sub>3</sub> bend
	1077	Medium	C-N stretch
	710	Medium	N-H wag

For the FTIR spectrum of DDA, the peaks appear at 3331 and 3260 cm<sup>-1</sup> correspond to the asymmetrical and symmetrical N-H stretch. Moreover, the presence of N-H bend and N-H wag in the DDA molecule is evinced by the peaks at a wavenumber of 1606 and 722 cm<sup>-1</sup>. The peaks shown at 2918 and 2851 cm<sup>-1</sup> indicate the existence of the asymmetrical and symmetrical C-H stretch. Whereas the peaks that occur at 1464 and 1371 cm<sup>-1</sup> are attributed to the -CH<sub>2</sub> bend and -CH<sub>3</sub> bend. Another important peak exists at 1038 cm<sup>-1</sup> is attributed to the C-N stretch of the DDA structure.

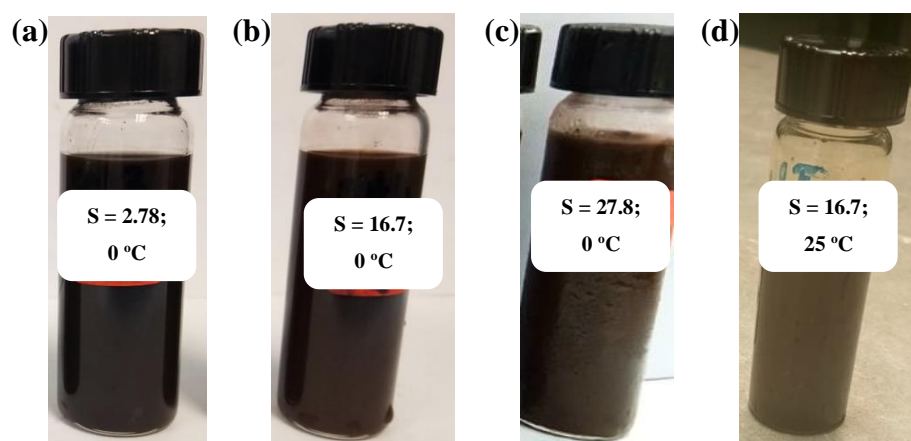
Comparatively, the important peaks found in the FTIR spectrum of DDA are also present in the spectrum of the DDA-functionalized AgNPs. The peak appears at 1656 cm<sup>-1</sup> arises from the N-H bend, while the peak shown at 710 cm<sup>-1</sup> corresponds to the N-H wag. The presence of the -CH<sub>2</sub> bend and -CH<sub>3</sub>

bend is indicated by the peaks occurring at 1478 and 1384  $\text{cm}^{-1}$ . Moreover, the peak for the C-N stretch, which occurs at 1077  $\text{cm}^{-1}$  agrees with the theoretical range. However, most of the peaks shown in the FTIR spectrum of DDA-functionalized AgNPs have shifted to higher wavenumbers. This evinces that there is a strong interaction between DDA and AgNPs. Nonetheless, a strong peak occurs unexpectedly at 3360  $\text{cm}^{-1}$ , which is attributed to the hydroxyl group (O-H stretch), indicating the presence of moisture in the AgNPs sample. The peaks of N-H stretch and C-H stretch are unable to be observed in the FTIR spectrum of DDA-capped AgNPs. This is because they have been overlapped or covered by the broad absorption peak of the hydroxyl functional group. In addition, the absence or the significant weakening of these absorption peaks indicates the coordination of DDA molecules to the surface of nanoparticles via their head group, as reported by Chen and Wang (2008) and Mo et al (2011). The AgNPs were proven to be protected by DDA.

#### **4.1.7 Optical properties of AgNPs**

Figure 4.12 illustrates the solutions of DDA-functionalized AgNPs which were synthesized with various concentration of DDA at 0 °C and 25 °C, through the chemical reduction approach. The solutions of dispersed AgNPs appeared in different colour tones when the concentration of the capping agent was varied. This is because the particle size of the nanostructures produced is strongly dependent on the concentration of the capping agent and the reaction temperature.

Based on the FESEM analysis, with the increase of the concentration of DDA (S value) and the reaction temperature, the particle size and size distribution of the nanocolloids increase and broaden, while the particle structure transforms to an irregular shape (Figure 4.3 and 4.5). By comparing the samples in Figure 4.12, the dark brown colour in solution (a) indicates that the AgNPs are smaller in particle diameter. With the increase in particle size, the AgNPs solution turns from dark brown to light brown and even to yellowish-brown [(b)-(d)]. The change in the solution colour observed in this study matches the results reported by Song et al. (2008).



**Figure 4.12:** The solutions of DDA-capped AgNPs which were fabricated with DDA with the S value of (a) 2.78, (b) 16.7 and (c) 27.8 at 0 °C; while (d) was fabricated with DDA with the S value of 16.7 at 25 °C

The colour of the solution of AgNPs varies from each other according to their structural and geometrical properties. This is mainly attributed to the localised surface plasmon resonance (LSPR) effect of metallic nanostructures. As stated by Mavani and Shah (2013), the LSPR effect of metallic nanoparticles exhibits a strong correlation with their particle size and shape. When the nanostructures aggregate, the optical properties of the solution will change. When the particle

size increases, the LSPR shifts to lower energy. Meanwhile, the scattering and absorption peaks of the AgNPs will shift to a longer wavelength. The conduction electrons which locate closer to the surface of the particles delocalize and are shared amongst neighbouring particles. Thus, the AgNPs with different size and shape will have different oscillation resonance. The statement explains the dependency of the colour outlook of synthesized AgNPs by their structural properties. Therefore, AgNPs with the colour of the solution that varied from dark brown to yellowish-brown were obtained in this work.

#### **4.1.8 Percentage yield of AgNPs**

The AgNPs were fabricated by the chemical reduction method, using  $\text{NaBH}_4$  as the reducing agent with DDA as the capping agent. The percentage yield of the AgNPs synthesized was 41.4%. The calculation of percentage yield is shown in Appendix C. The relatively low yield was mainly due to a significant weight loss during the transferring and purifying processes of the AgNPs solution. Subsequently, the AgNPs were re-dispersed in 15 mL of ethanol and utilized in further study. The final concentration of the AgNPs was  $3.585 \times 10^{-3}$  M.

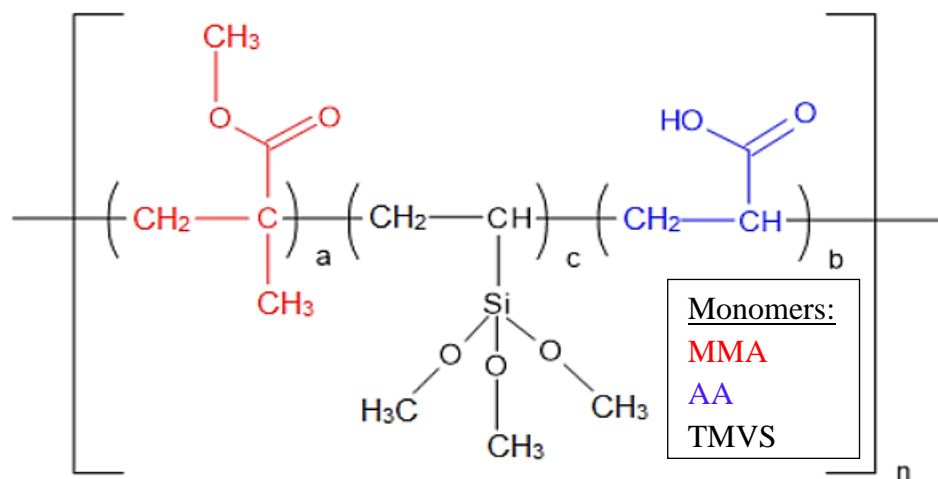


## CHAPTER 5

### SYNTHESIS AND CHARACTERIZATION OF P(MMA-*co*-AA-*co*-TMVS) NANOSPHERES

#### 5.1 Synthesis of P(MMA-*co*-AA-*co*-TMVS) nanospheres

Emulsion polymerization is a radical addition polymerization that proceeds in a heterogeneous system which is associated with the emulsification of hydrophobic building units using an oil-in-water emulsifier. This polymerization technique has been adopted to fabricate an emulsion which consists of P(MMA-*co*-AA) nanostructures. In this work, MMA and AA were used as the monomers in the dispersed phase with distilled water as the continuous phase. The polymerization process was initiated by KPS which is a water-soluble thermal initiator; while the hydrophobic monomers were stabilized by SDS in an aqueous medium. Meanwhile, TMVS was incorporated into the polymeric matrix during the polymerization process, with the purpose to investigate the effect of different amount of TMVS on the adhesion strength and bond durability of the modified polymer nanostructures on Si substrate (Lee, et al., 2021). Figure 5.1 illustrates the chemical structure of P(MMA-*co*-AA-*co*-TMVS).



**Figure 5.1:** The chemical structure of P(MMA-co-AA-co-TMVS) (Lee, et al., 2021)

In the P(MMA-co-AA) copolymer, the PMMA components form a matrix with high optical transparency in the visible range of the electromagnetic spectrum. The introduction of AA segments into the polymer chain is to improve the wetting properties and stability of P(MMA-co-AA) copolymer, which could enhance the adhesion strength of the polymeric nanostructures on the glass substrate (Goh, 2019; Lee, et al., 2021). The distinctive combination of both the mechanical and optical characteristics displayed by polyacrylate copolymer renders the advantages for the copolymer to be fabricated as light harvesting nanostructures. The polymeric nanoparticles are coated as an anti-reflective nanoarray on the glass surface of the solar module with the intention to increase the absorption of light into the photoactive site (Lee, et al., 2021). Thus, the PCE of solar modules can be enhanced.

In addition, in order to improve the adhesion strength and bond durability between the organic polyacrylate nanostructures and the inorganic surface of glass substrates, TMVS was incorporated into the polymer matrix (Lee, et al., 2021). By adding TMVS as an SCA that serves as an adhesion promoter, the covalent bonding between these two dissimilar materials will be strengthened. Therefore, it is anticipated that the adhesion of the polyacrylate nanostructures with TMVS on a glass substrate will be more durable against the weathering and ageing processes.

The methoxy silane groups ( $\text{Si-O-CH}_3$ ) in TMVS can be hydrolyzed by either water or a suitable solvent to form silanol groups ( $\text{Si-OH}$ ) which are further condensed to form siloxane groups ( $\text{Si-O-Si}$ ) (Liu, et al., 2001; Lee, et al., 2021). Besides forming covalent bonds via siloxane groups ( $\text{Si-O-Si}$ ) with the hydroxyl groups on a Si substrate, TMVS can also react with the silanol groups ( $\text{Si-OH}$ ) present in the copolymeric material. Thus, increases the molecular weight of the copolymer by forming crosslinked networks. The higher the network density of siloxane bonds, the stronger will be the cohesion strength as well as the adhesion durability of such material.

#### **5.1.1 Total solids content and percentage of monomer conversion of P(MMA-co-AA-co-TMVS) copolymer emulsion**

The total solids content and the percentage of monomer conversion of the polymer emulsion were determined. The results obtained are tabulated in Table 5.1. The experimental details of the total solids content in addition to the calculations of the theoretical total solids content of the polymer emulsion and

the percentage of monomer conversion are shown in Appendix D. The results showed that the total solids content of the polymer emulsion increases with an increasing amount of TMVS being incorporated into it (Lee, et al. 2021). For instance, the total solids content of the emulsion increased from 19.90% to 21.09% when the amount of TMVS incorporated increased from 0 wt% to 9 wt%. This is because more TMVS molecules have been incorporated into the polyacrylate copolymer. Based on the theoretical total solids content, the percentages of monomer conversion of all the polymer emulsion obtained were found satisfactory as more than 97% of the monomers has been converted to polymer. This indicates that the polymerization process has been carried out successfully to produce copolymer products with a reasonably high yield.

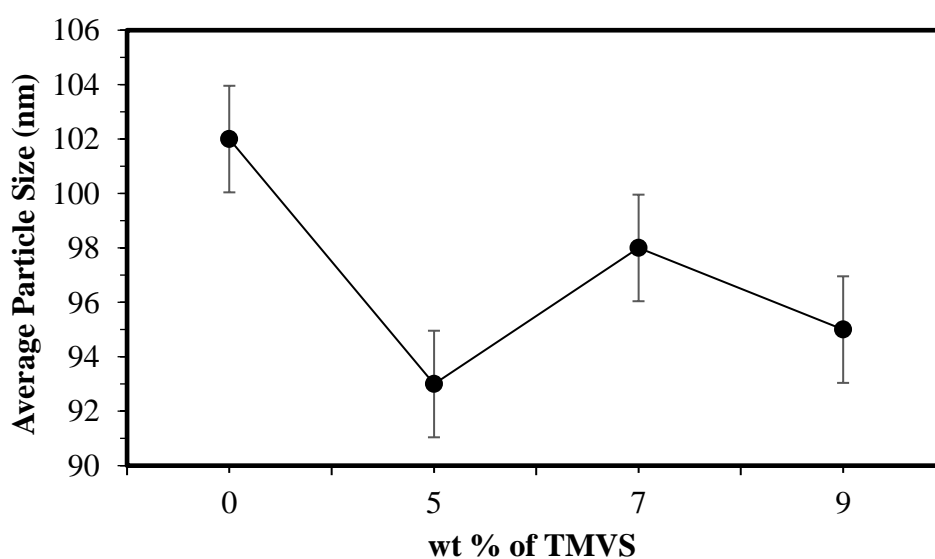
**Table 5.1:** The total solids content and the percentage of monomer conversion of P(MMA-*co*-AA) emulsion incorporated with different wt% TMVS

<b>wt% TMVS</b>	<b>Total solids content (%)</b>	<b>Monomer conversion (%)</b>
<b>0</b>	19.90	99.50
<b>5</b>	20.18	97.06
<b>7</b>	20.98	99.41
<b>9</b>	21.09	98.48

### **5.1.2 Structural properties of P(MMA-*co*-AA-*co*-TMVS)**

The particle size of P(MMA-*co*-AA-*co*-TMVS) nanostructures was characterised using a laser diffraction particle size analyzer. The analysis is based on a well-established method called “volume or mass moment mean” or normally known as De Broucker mean (Kulshreshtha, et al., 2010; Lee, et al., 2021). Figure 5.2 shows the average particle size of polyacrylate

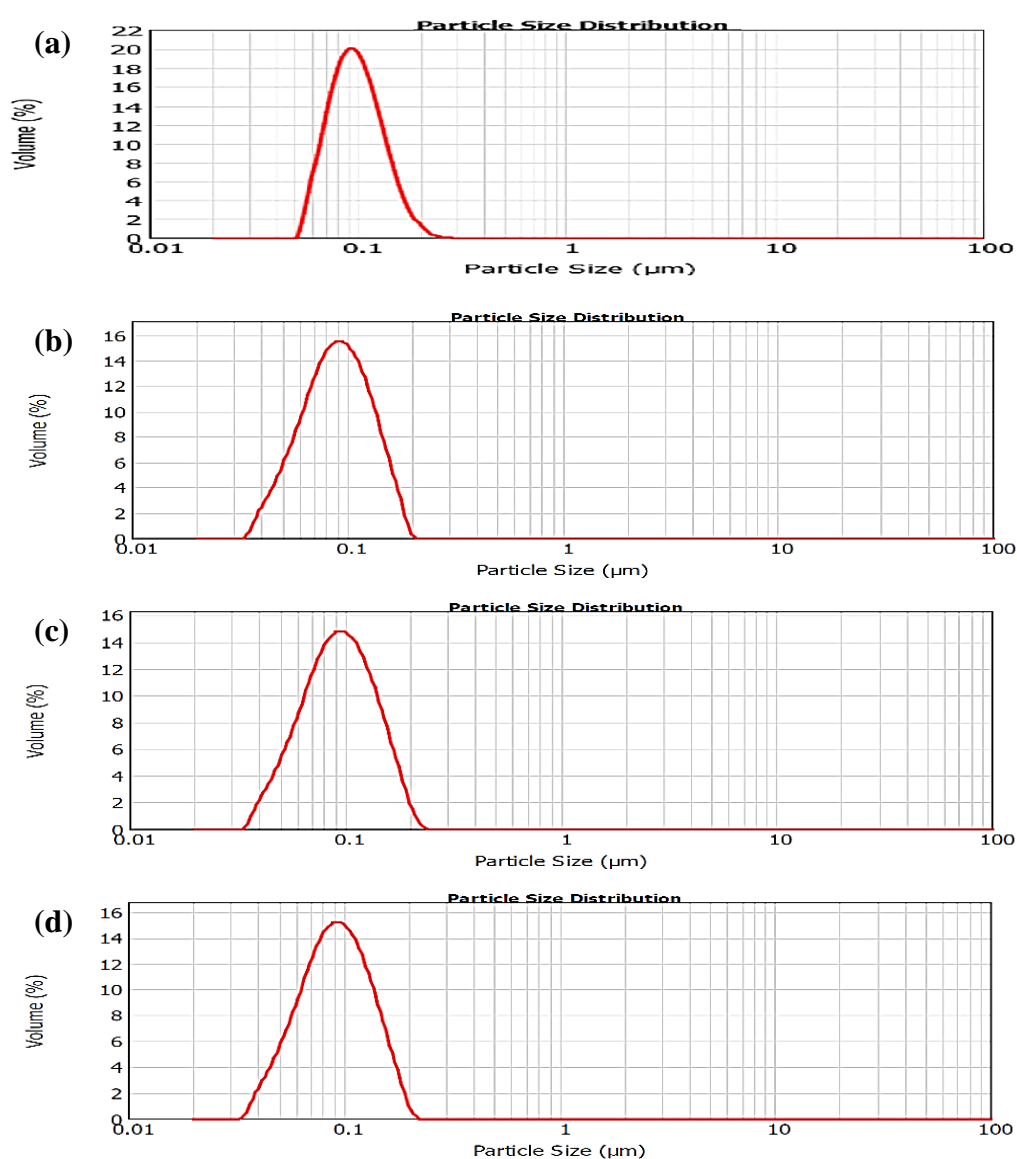
nanostructures synthesized with various wt% of TMVS. The detailed information obtained from the analysis is tabulated in Table 5.2. The PSA results show that the polymeric nanostructures possess an average particle size of  $97 \pm 5$  nm. It also reveals that the incorporation of TMVS into the P(MMA-*co*-AA) copolymer has resulted in a slight reduction of the average particle size. The mean particle size of the polyacrylate nanostructures decreased from 102 nm to less than 100 nm (93, 98, 95 nm) after the incorporation of various amount of TMVS. The slight shrinkage in size indicates that the presence of TMVS in the polymer chains could have induced some crosslinking to form networks within the polymer particle (Lee, et al., 2021). In order to control the particle size of the polymer nanostructures, certain processing parameters were kept constant during synthesis, which includes the amount of emulsifier used, the rate of addition of both emulsifier and monomer, and the speed of stirring during polymerization. The PSA results were further examined by using FESEM, which is discussed in the following section.



**Figure 5.2:** The average particle size of P(MMA-*co*-AA-*co*-TMVS) nanostructures as a function of the amount of TMVS incorporated

**Table 5.2:** The mean particle size and particle size distribution of the polyacrylate nanostructures corresponding to the wt% of TMVS incorporated

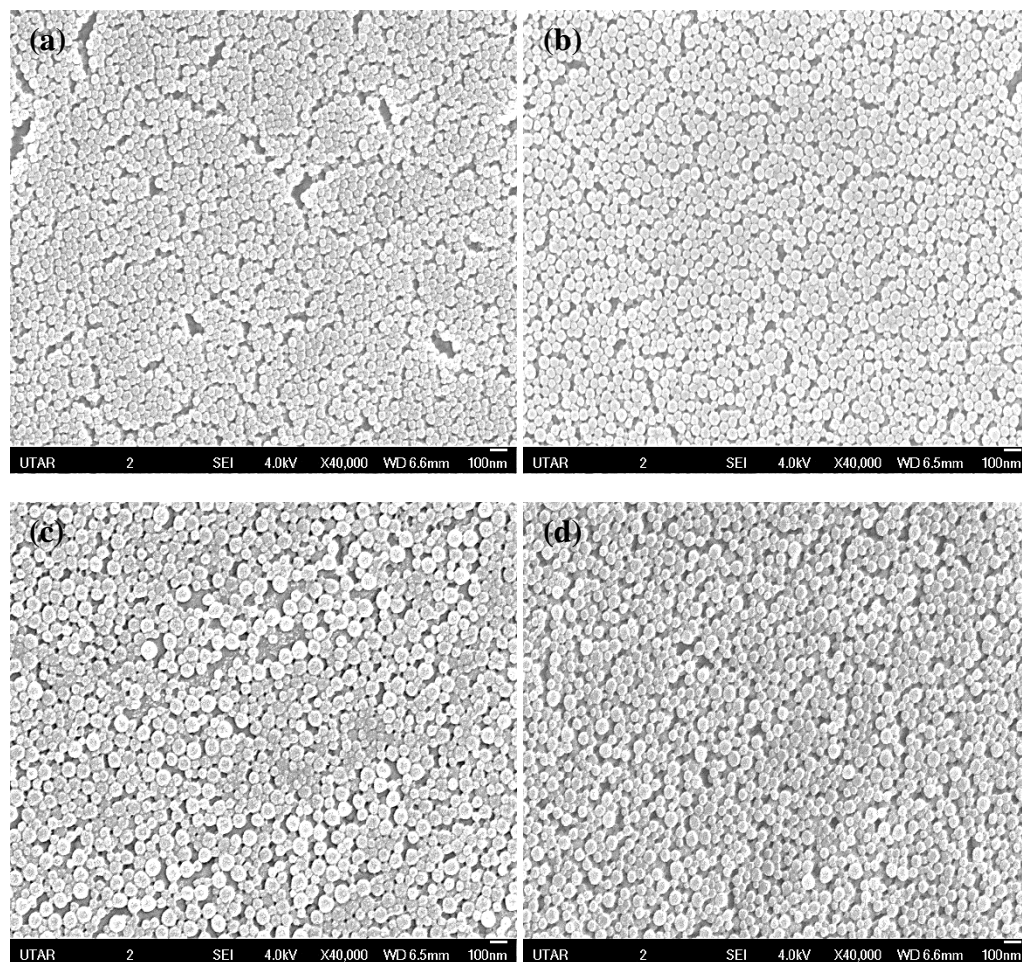
Polymer sample	Mean particle size (nm)	Particle size distribution (nm)			
		D <sub>10</sub>	D <sub>50</sub>	D <sub>90</sub>	Span
0 wt% TMVS	102	68	97	144	0.780
5 wt% TMVS	93	54	89	141	0.977
7 wt% TMVS	98	55	93	151	1.031
9 wt% TMVS	95	54	91	145	1.002



**Figure 5.3:** Particle size distribution of P(MMA-*co*-AA-*co*-TMVS) nanostructures with the incorporation of (a) 0 wt%, (b) 5 wt%, (c) 7 wt% and (d) 9 wt% of TMVS

The particle size distributions of P(MMA-*co*-AA-*co*-TMVS) nanostructures (Figure 5.3) depict that the incorporation of TMVS into the polymeric matrix has resulted in a slight increase in polydispersity. The pristine P(MMA-*co*-AA) nanostructures exhibit a particle size distribution from 68 to 144 nm with a span value of 0.780. With the incorporation of 7 wt% of TMVS, the particle size distribution has broadened from 55 to 151 nm with a span value of 1.031. This indicates that the presence of TMVS during the synthesis might have influenced the nucleation and growth processes of polymer chains, thus interrupting the growth in particle size of the polymer nanoparticles (Lee, et al., 2021).

In addition, the morphological study of the P(MMA-*co*-AA) nanostructures synthesized with and without TMVS was carried out using FESEM (Lee, et al., 2021). The FESEM images of the polyacrylate nanostructures are shown in Figure 5.4. Based on the measurements done on the FESEM images, the polyacrylate nanostructures have an average particle size of 97 nm, with the particle size distribution span between 50 to 130 nm. Similar results obtained from both PSA and FESEM confirmed that the average size of the nanoparticles is less than 100 nm. The FESEM images also revealed that all the polyacrylate nanostructures produced, whether with or without TMVS, appear as uniform spherical structures. The incorporation of TMVS would not affect the structural property of polyacrylate nanostructures in terms of particle shape. This result corresponds well with the outcomes of UV-Vis spectroscopy, which are discussed in Section 5.2.3.



**Figure 5.4:** FESEM images of the P(MMA-*co*-AA) polymeric nanospheres incorporated with (a) 0 wt % (b) 5 wt % (c) 7 wt % and (d) 9 wt % of TMVS, with a magnification of  $\times 40000$

### 5.1.3 Optical properties of P(MMA-*co*-AA-*co*-TMVS)

P(MMA-*co*-AA) nanospheres incorporated with different amount of TMVS were also characterized by UV-Vis spectroscopy. The UV-Vis spectra obtained are combined and shown in Figure 5.5. The UV-Vis spectra reveal that the absorption peak of both the P(MMA-*co*-AA) and P(MMA-*co*-AA-*co*-TMVS) nanospheres appears within the range of 270-274 nm (Lee, et al., 2021). This absorbance band corresponds to the characteristic band of the carbonyl chromophores which are present in the copolymer sample (Shanti, et al., 2017).



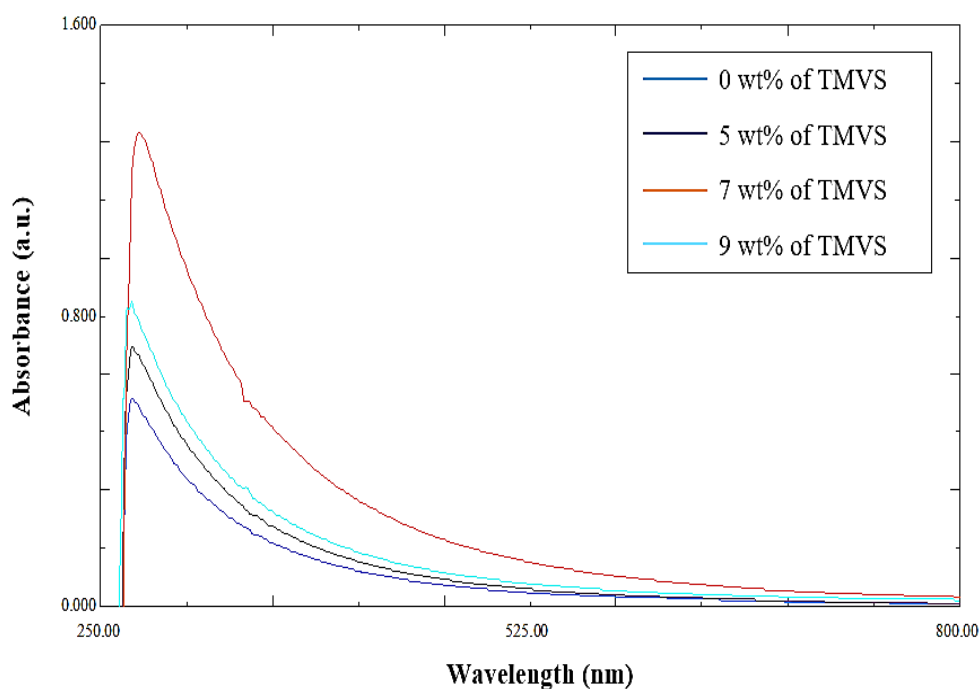
Moreover, it is obvious that only one absorption peak is present in each of the UV-Vis spectra of the polyacrylate samples. As discussed earlier, the number of resonance absorption peaks is dependent on the number of modes of the structure that can be polarized by light radiation (Petryayeva and Krull, 2011). For nanoparticles which is spherical in shape, there will be only one resonance absorption peak appearing in the spectrum (Lee, et al., 2021). The UV-Vis results evince the fact that polymeric nanostructures with spherical shape have been fabricated successfully in this work.

**Table 5.3:** The absorbance and wavelength of the absorption peak corresponding to the amount of TMVS incorporated into the polymeric matrix

<b>Polymer sample</b>	<b>Wavelength (nm)</b>	<b>Absorbance</b>
<b>0 wt% TMVS</b>	271	0.573
<b>5 wt% TMVS</b>	270	0.838
<b>7 wt% TMVS</b>	274	1.305
<b>9 wt% TMVS</b>	270	0.715

Interestingly, the UV-Vis results depict clearly that the amount of TMVS incorporated into the copolymer does not influence the wavelength while affecting the absorbance of the absorption peak significantly (Lee, et al., 2021). The wavelength and absorbance intensity of the resonance peak corresponding to the amount of TMVS incorporated in the polymeric matrix are tabulated in Table 5.3. The polymeric nanospheres with 7 wt% of TMVS yielded the highest absorbance. The absorbance results correlated well with the percentage of PCE improvement of the Si solar cell coated with the nanostructures. The solar module coated with the P(MMA-*co*-AA-*co*-TMVS) nanospheres containing 7 wt% of TMVS rendered the highest PCE enhancement, this

indicates that a significant amount of UV radiation was absorbed and coupled into the photoactive site of the solar module (Lee, et al., 2021). Further details on the effect of the polymeric nanospheres on the PCE of Si solar module coated with it are discussed in Section 5.2.3.

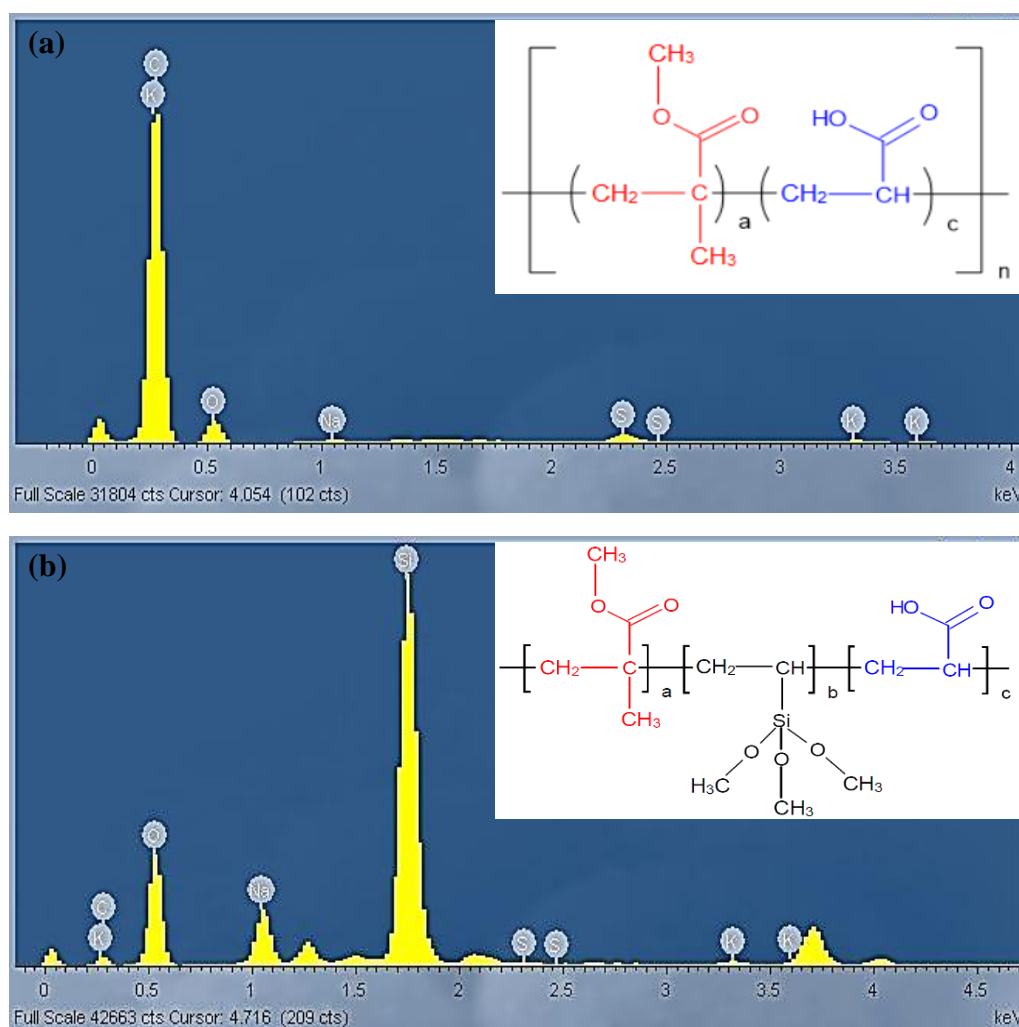


**Figure 5.5:** Overlaid UV-Vis spectra of P(MMA-*co*-AA) nanospheres incorporated with different amounts of TMVS

#### 5.1.4 Elemental composition of P(MMA-*co*-AA-*co*-TMVS)

The elemental composition of both P(MMA-*co*-AA) and P(MMA-*co*-AA-*co*-TMVS) was characterized using EDX spectroscopy (Lee, et al. 2021). Figure 5.6 shows the EDX spectra and the respective chemical structure of (a) P(MMA-*co*-AA) and (b) P(MMA-*co*-AA-*co*-TMVS). As shown clearly in Figure 5.6 (b), a distinct Si peak is present in the EDX spectrum of P(MMA-*co*-AA-*co*-TMVS). This indicates that the SCA (TMVS) has been successfully

incorporated into the polymeric matrix. On the other hand, the Si peak is absent in the EDX spectrum of P(MMA-*co*-AA) (Lee, et al., 2021). The carbon (C) and oxygen (O) peaks are mainly contributed by the polymer itself; while the presence of other peaks such as sodium (Na), potassium (K) and sulfur (S) was due to residual contamination of SDS and KPS from the emulsion system.

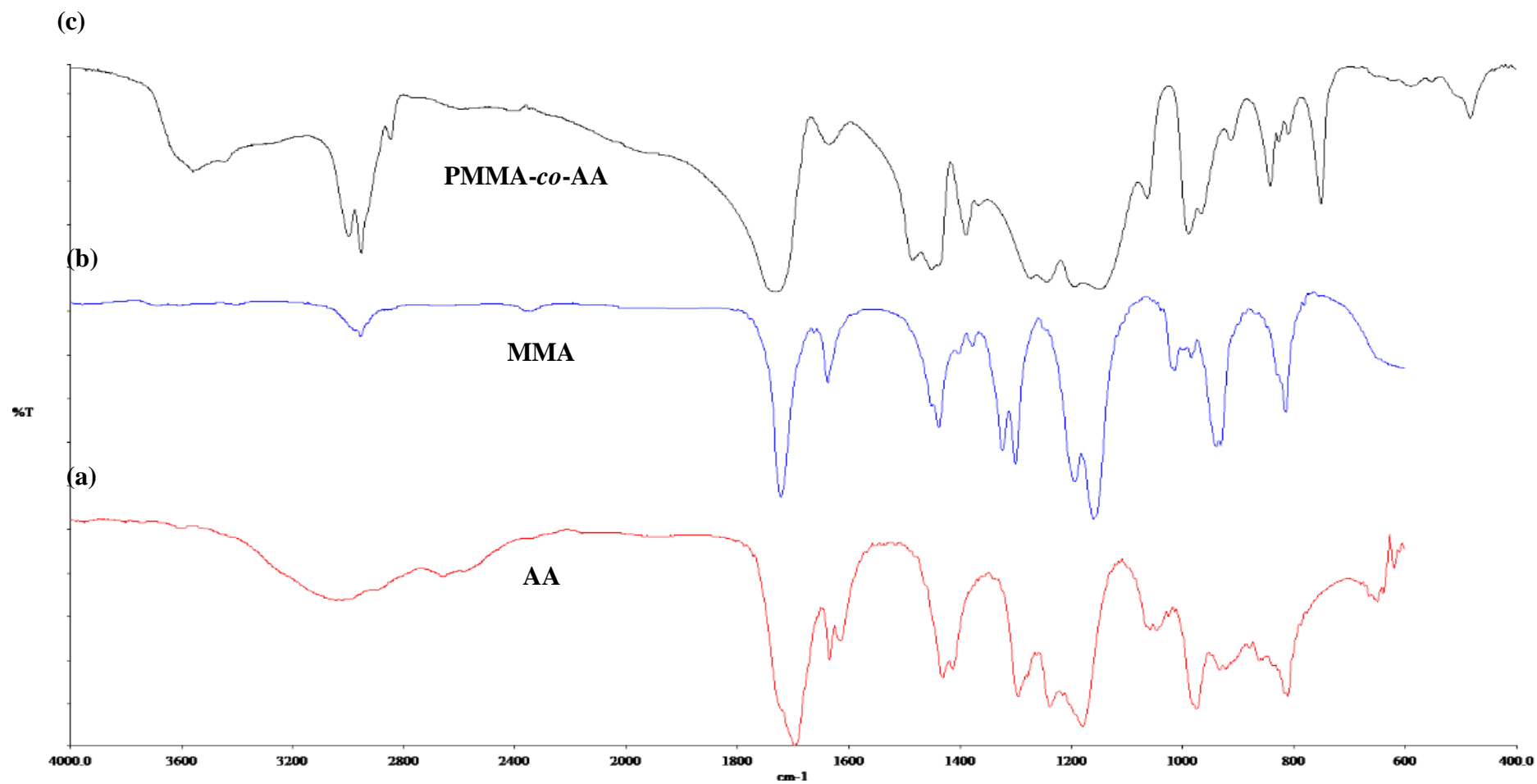


**Figure 5.6:** EDX spectra and the respective chemical structure of (a) P(MMA-*co*-AA) and (b) P(MMA-*co*-AA-*co*-TMVS)

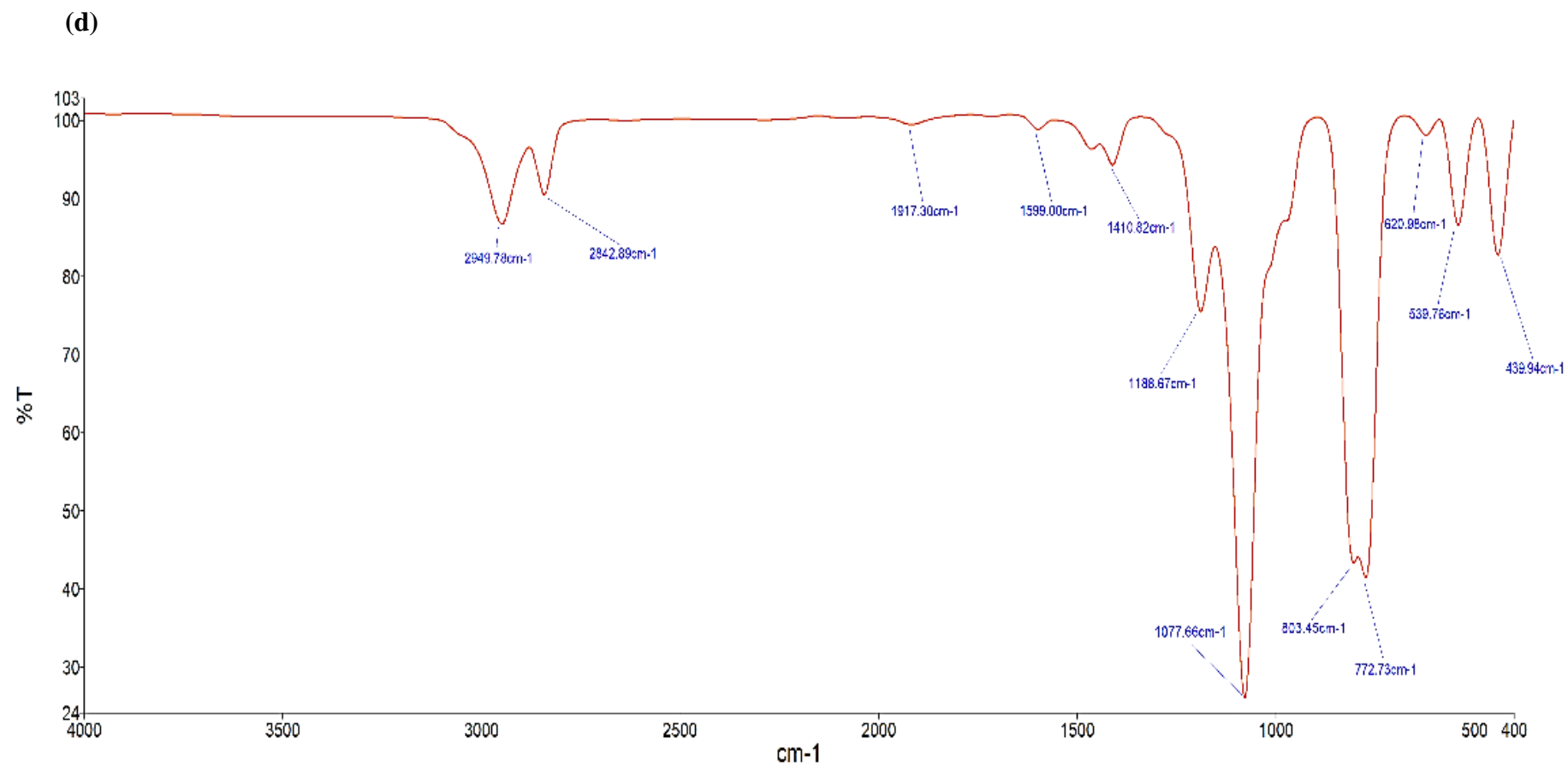
### 5.1.5 Functional groups of P(MMA-*co*-AA-*co*-TMVS)

FTIR analysis was performed to determine the functional groups present in the monomers, the SCA and the polymer samples. The spectra of the samples were obtained in the range of 4000-400  $\text{cm}^{-1}$ . The FTIR spectra of MMA, AA, TMVS, P(MMA-*co*-AA) and P(MMA-*co*-AA-*co*-TMVS) are illustrated in Figure 5.7. Table 5.4 shows the wavenumber and the corresponding vibration mode of the functional groups in the samples.

AA is a carboxylic acid with the molecular formula of  $\text{CH}_2=\text{CHCOOH}$ . The vinyl group present in the molecule is connected to the carbonyl carbon ( $\text{C}=\text{O}$ ), forming an unsaturated carboxylic acid. The hydroxyl group ( $-\text{OH}$ ) attached to the carbonyl is characterized by a strong and broad peak which occurs at 3045  $\text{cm}^{-1}$  in the spectrum. This peak is extended and covers the peaks appearing between 2500-3300  $\text{cm}^{-1}$ , thus overlapping with the C-H stretching peak. The carbonyl group causes the vibration with strong intensity at 1698  $\text{cm}^{-1}$  which falls within the fingerprint region of 1670-1820  $\text{cm}^{-1}$  of  $\text{C}=\text{O}$ . Because the  $\text{C}=\text{O}$  group is part of the acid, it has a relatively lower wavenumber. This is because the carboxylic acid group does not exist in a free state but rather it forms hydrogen bonding with other carboxylic acids. The peaks that appear at 1634 and 1295  $\text{cm}^{-1}$  with medium intensity are attributed to  $\text{C}=\text{C}$  and C-O stretches, respectively.



**Figure 5.7:** FTIR spectra of (a) AA, (b) MMA and (c) P(MMA-co-AA)



**Figure 5.7 (d):** FTIR spectrum of TMVS

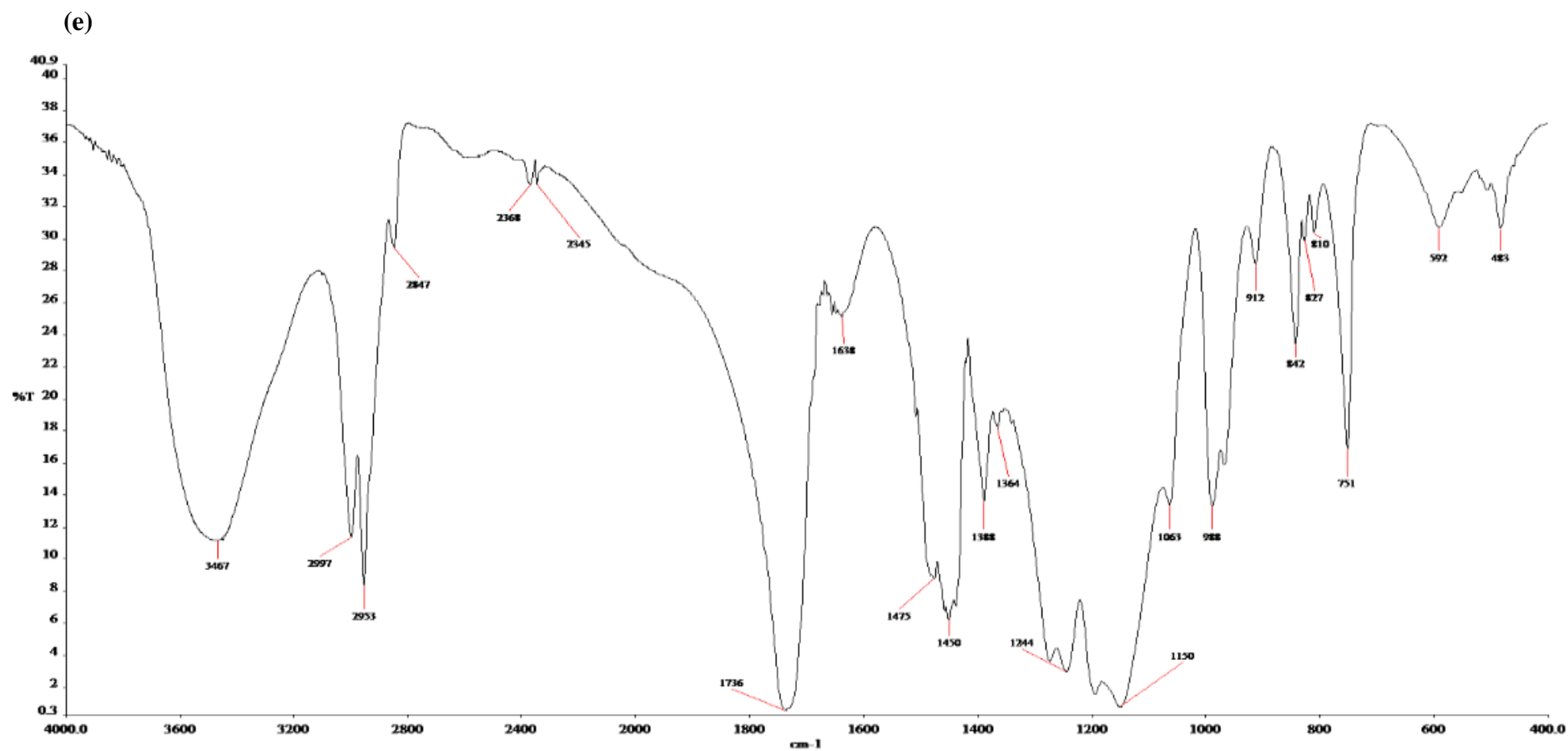


Figure 5.7 (e): FTIR spectrum of P(MMA-co-AA-co-TMVS)

**Table 5.4:** Data extracted from FTIR of AA, MMA, TMVS, P(MMA-*co*-AA) and P(MMA-*co*-AA-*co*-TMVS)

Sample	Wavenumber (cm <sup>-1</sup> )	Description	Vibration mode
AA	3045	Weak	O-H stretch
	1698	Very strong	C=O stretch
	1634	Medium	C=C stretch
	1295	Strong	C-O stretch
MMA	2956	Very weak	C-H stretch
	1721	Very strong	C=O stretch
	1637	Weak	C=C stretch
	1377	Very weak	-CH <sub>3</sub> bend
	1300	Strong	C-O stretch
P(MMA- <i>co</i> -AA)	3448	Medium	O-H stretch (water)
	2997	Strong	O-H stretch (carboxylic acid)
	2953	Strong	C-H stretch
	1734	Very strong	C=O stretch
	1474	Strong	-CH <sub>2</sub> bend
	1388	Medium	-CH <sub>3</sub> bend
	1273	Strong	C-O stretch
TMVS	2950, 2843	Weak	C-H stretch
	1599	Very weak	C=C stretch
	1189	Medium	C-O stretch
	1078	Very strong	Si-O stretch
	803	Strong	Si-C stretch
	772	Strong	Si-O bend



**Table 5.4:** Data extracted from FTIR of AA, MMA, TMVS, P(MMA-*co*-AA) and P(MMA-*co*-AA-*co*-TMVS) (continued)

Sample	Wavenumber (cm <sup>-1</sup> )	Description	Vibration mode
<b>P(MMA-<i>co</i>-AA-<i>co</i>-TMVS)</b>	3467	Strong	O-H stretch (water)
	2997	Strong	O-H stretch (carboxylic acid)
	2953	Strong	C-H stretch
	1736	Very strong	C=O stretch
	1475	Strong	-CH <sub>2</sub> bend
	1388	Medium	-CH <sub>3</sub> bend
	1273	Strong	C-O stretch
	1150	Very strong	Si-OH stretch
	1063	Medium	Si-O stretch
	988	Medium	Si-O-Si stretch
	842	Weak	Si-O-Si bend
	810	Very weak	Si-C stretch

As for MMA, the peak that occurs at 2956 cm<sup>-1</sup> is attributed to the C-H stretch. The unsaturation of C=C stretch of the monomer contributes to the appearance of a peak at 1637 cm<sup>-1</sup>. The presence of methyl group (-CH<sub>3</sub>) in the MMA molecule is evinced by the peak that emerges at the wavenumber of 1377 cm<sup>-1</sup> as a result of -CH<sub>3</sub> bending. The C=O group of an ester functional group causes the existence of a peak at 1721 cm<sup>-1</sup> which is within the theoretical range of 1725-1700 cm<sup>-1</sup>. The peak appears at a higher wavenumber than the C=O group of AA due to the withdrawing effect of the electronegative oxygen. Another important peak that exists at 1300 cm<sup>-1</sup> arises from the C-O single bond group which proves the presence of an ester group in the molecule.

The FTIR spectrum of P(MMA-*co*-AA) copolymer is similar to a combination of the MMA and AA spectra, except with the absence of the peak of unsaturated C=C double bond in the wavenumber range of 1690-1610  $\text{cm}^{-1}$ . This indicates that MMA and AA monomers have been reacted to form polymer chains in the copolymerization process. The peaks that appear at 3448 and 2997  $\text{cm}^{-1}$  are assigned to the O-H stretch, where the former is attributed to the hydroxyl group in the water molecule while the latter is contributed by the carboxylic acid moiety of AA segments in the polyacrylate chain. Likewise, the absorption peaks which occur at 2953, 1734, 1474, 1388 and 1273  $\text{cm}^{-1}$  in the FTIR spectrum are attributed to the vibration modes of C-H stretch, C=O stretch,  $-\text{CH}_2$  bend,  $-\text{CH}_3$  bend and C-O stretch, respectively, of both the MMA and AA repeating units in the polymer chains. Contrary to the individual monomers, the wavenumbers of these functional groups are slightly shifted, which could be due to the different chemical environment of the monomers and the polymer chains (Mohy, et al., 2017; Goh, 2019).

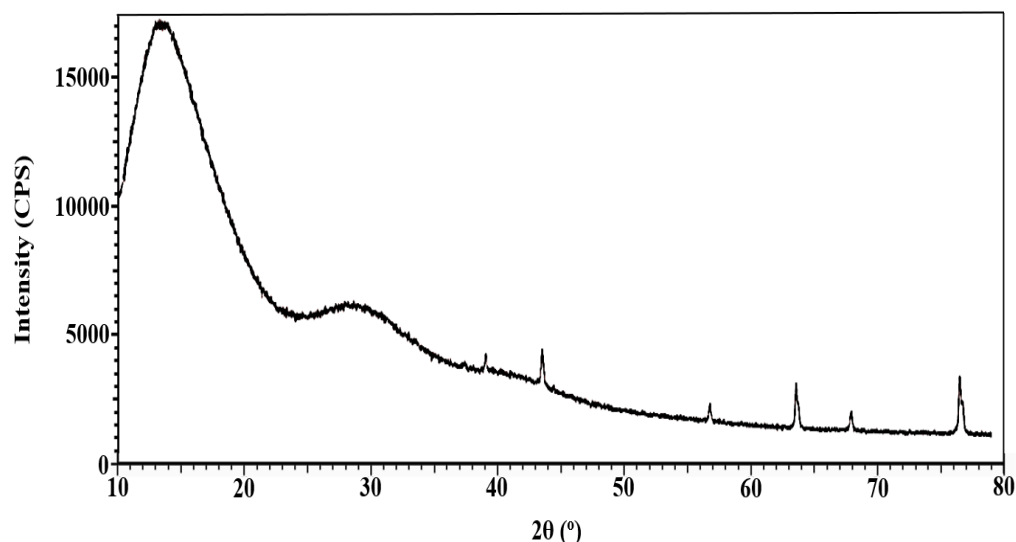
For the FTIR spectrum of TMVS, the peaks that exist at 2950 and 2843  $\text{cm}^{-1}$  correspond to the asymmetrical and symmetrical C-H stretches. Whereas the stretching of the unsaturated C=C double bond in the TMVS molecule contributes to the appearance of an absorption peak at 1599  $\text{cm}^{-1}$ . The presence of the C-O stretch is indicated by the peak at 1189  $\text{cm}^{-1}$ . In addition, the important peaks of Si-O that occur at 1078 and 772  $\text{cm}^{-1}$  are contributed by the stretching and bending vibration modes of Si-O of the molecule. The absorption peak that exists at 803  $\text{cm}^{-1}$  is assigned to the Si-C stretch. All the

peaks found in the spectrum correlate well with the functional groups of TMVS (Figure 1.8).

Obviously, the FTIR spectrum of P(MMA-*co*-AA-*co*-TMVS) shows additional peaks as compared to the spectrum of P(MMA-*co*-AA). For instance, the Si-OH stretch from TMVS causes the appearance of an absorption peak at 1150  $\text{cm}^{-1}$ . The existence of the functional group of Si-OH in the former is a result of the hydrolysis of Si-OCH<sub>3</sub> in TMVS. The peak that occurs at 1063  $\text{cm}^{-1}$  is resulted by the Si-O stretch; whereas the peaks at 988 and 842  $\text{cm}^{-1}$  are assigned to the stretching and bending vibration modes of Si-O-Si. Siloxane bonds (Si-O-Si) are formed via a condensation reaction between neighbouring silanol groups (Si-OH), with water as a by-product. This result indicates that the polymer chains have indeed cross-linked with each other via siloxane bonds. Another important absorption peak that proves the presence of TMVS in the copolymer is shown at 810  $\text{cm}^{-1}$  which arises from the stretching of Si-C. In addition, the absorption peak of the vinyl group of TMVS is not found in the FTIR spectrum, which should appear in the range of 1680-1620  $\text{cm}^{-1}$ . Again, it proves that the vinyl groups have reacted in the polymerization process. The absence of an unsaturated C=C double bond and the presence of silane functional groups (i.e. Si-O, Si-O-Si and Si-C) evinced that TMVS has been successfully incorporated into the polymer chain. Moreover, the presence of the Si-OH group indicates that there is still an active site available for subsequent condensation reaction between the silane moiety in the polymer chain and the hydroxyl group on a glass substrate.

### 5.1.6 Crystallinity of P(MMA-*co*-AA-*co*-TMVS)

P(MMA-*co*-AA-*co*-TMVS) nanospheres with various amount of TMVS were also characterised by XRD to determine the degree of crystallinity and structural order of the polymeric matrix. Figure 5.8 shows the XRD pattern of the P(MMA-*co*-AA) copolymer. The diffractograms obtained for the copolymers with and without TMVS exhibit almost the same peaks at similar  $2\theta$  values. The diffraction peaks occur at  $13.82^\circ$ ,  $30.00^\circ$ ,  $39.51^\circ$  and  $43.98^\circ$  are probably contributed by the MMA segments in the polymer chains. According to Mohy et al. (2017) and Hashem et al. (2017), similar diffraction peaks at  $13.80^\circ$ ,  $30.0^\circ$ ,  $38.0^\circ$  and  $44.0^\circ$  were observed in the diffractogram of PMMA homopolymer. On the other hand, the diffraction pattern of PAA was characterized by a relatively strong and broad peak at  $17.2^\circ$  and a shoulder at  $35.0^\circ$  (Todica, et al., 2014). Therefore, the diffraction peak that appears at  $33.68^\circ$  in the diffractogram could be attributed to the AA components in the polymer chains. The slight shift in the  $2\theta$  values of the diffraction peaks could be due to the interaction of certain functional groups between the repeating units in the polymer chains, such as the siloxane and silanol groups from TMVS, and the carboxylic acid group from AA repeating units (Goh, 2019; Lee, et al., 2021).



**Figure 5.8:** XRD pattern of P(MMA-*co*-AA) polymer nanospheres

Based on Bragg's law, crystalline materials show a sharp diffraction peak with a distinct value of the diffraction angle (Todica, et al., 2014). Nonetheless, the diffraction peaks of an amorphous system, such as a polymeric material, are broad and consist of a number of individual lines. Copolymerization of two different monomers introduces higher amorphous content as compared to homopolymerization. The pattern in Figure 5.8 exhibits a typical amorphous characteristic of a polymeric material with the presence of a broad peak at  $13.82^\circ$ . The degree of crystallinity can be further confirmed by employing programmable software in the XRD analysis. A summary of the results obtained from the crystallinity analysis is tabulated in Table 5.5. It was found that the P(MMA-*co*-AA) copolymer consists of high amorphous content (89.22 wt%) with a low degree of crystallinity (10.78 wt%). The amorphous content increased slightly when a higher amount of TMVS was incorporated into the polymer matrix. This could be due to the presence of siloxane and silanol groups in the copolymers, which restrict the chain movement and hinder the packing of polymer chains in the polymer matrix (Lee, et al., 2021).

**Table 5.5:** The amorphous content and degree of crystallinity correlated with the P(MMA-*co*-AA) nanospheres with the incorporation of various wt% of TMVS

Polymer sample	Amorphous content	Degree of crystallinity
	(wt%)	(wt%)
<b>0 wt% TMVS</b>	89.22	10.78
<b>5 wt% TMVS</b>	90.54	9.46
<b>7 wt% TMVS</b>	91.61	8.39
<b>9 wt% TMVS</b>	91.96	8.04

### 5.1.7 Thermal stability of P(MMA-*co*-AA-*co*-TMVS)

Exposing a polymer to a high temperature will inevitably cause the polymer to degrade and change its chemical and physical properties (Lee, et al., 2021). TGA was conducted to investigate the thermal stability of the P(MMA-*co*-AA) and P(MMA-*co*-AA-*co*-TMVS) copolymers. The TGA thermograms of the polyacrylate copolymers are illustrated in Figure 5.9. All the TGA thermograms of the P(MMA-*co*-AA) variants, whether with or without TMVS, show a similar degradation pattern. Table 5.6 shows the degradation temperature ( $T_d$ ) and percentage of residue at 550 °C of the copolymer samples.

(a)

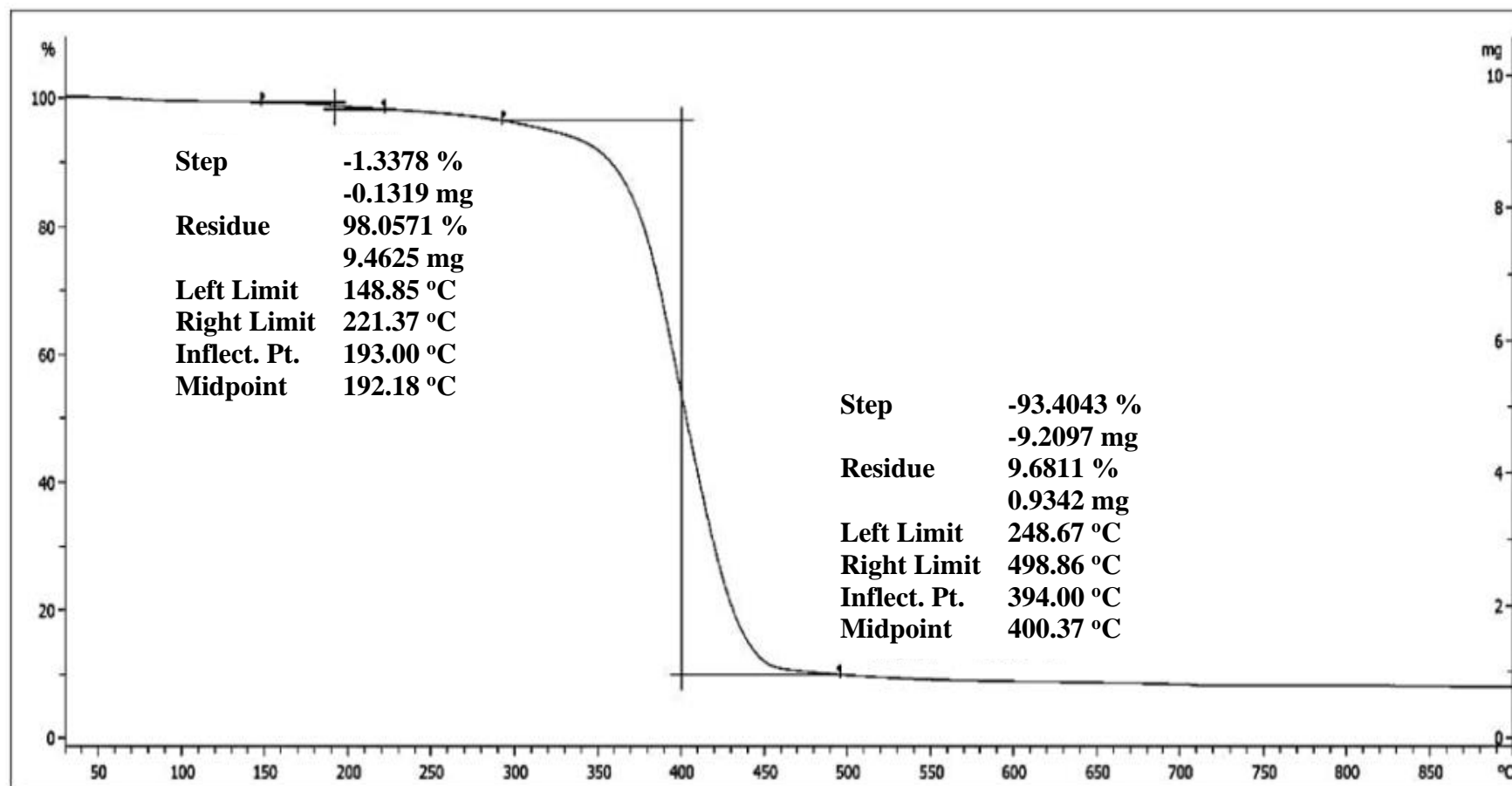
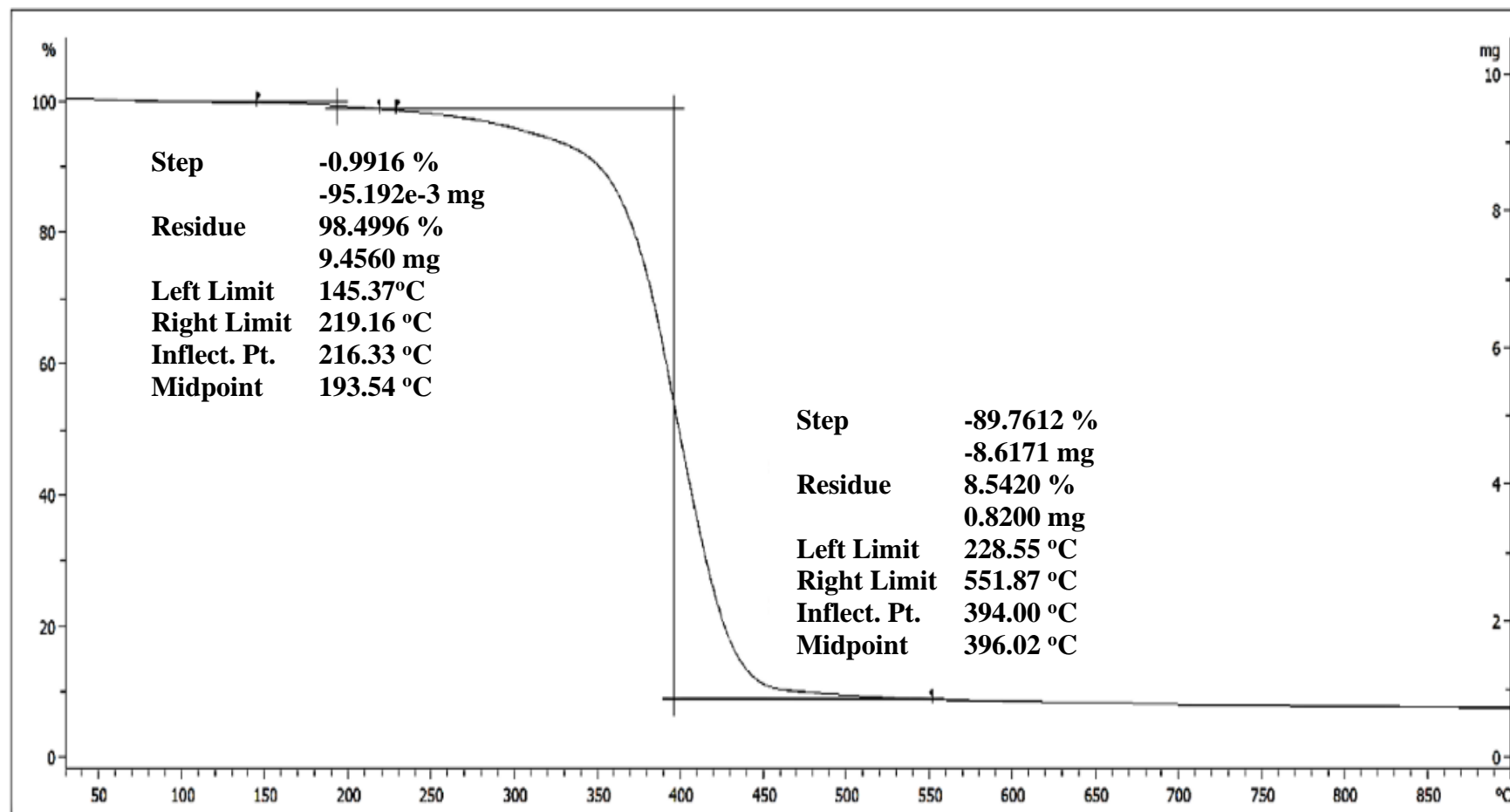


Figure 5.9 (a): TGA thermogram of P(MMA-co-AA)

(b)



**Figure 5.9 (b):** TGA thermogram of P(MMA-co-AA-co-TMVS) with 7 wt% of TMVS (Lee, et al., 2021)



**Table 5.6:**  $T_d$  and percentage of residue at 550 °C of P(MMA-*co*-AA-*co*-TMVS) with different wt% of TMVS

Polymer sample	Degradation temperature, $T_d$ (°C)		Percentage of residue after degradation (%)	
	First	Second	First	Second
	degradation	degradation	degradation	degradation
<b>0 wt% TMVS</b>	193.00	394.00	98.06	9.68
<b>5 wt% TMVS</b>	212.67	395.00	98.19	6.70
<b>7 wt% TMVS</b>	216.33	394.00	98.50	8.54
<b>9 wt% TMVS</b>	200.33	394.33	98.82	9.45

Based on the TGA, it was found that the thermal decomposition of both the P(MMA-*co*-AA) and P(MMA-*co*-AA-*co*-TMVS) copolymers consists of two stages (Lee, et al., 2021). The first stage of degradation occurred in the temperature range of 142-215 °C with an average inflection temperature of  $205.58 \pm 9.38$  °C. According to Moharram and Khafagi (2006), the first degradation stage of PAA homopolymer started at about 157 °C and ended at 225 °C, with the maximum decomposition rate occurring at 197 °C. The first decomposition stage of PAA is due to the removal of the -COOH side group by dehydration followed by a decarboxylation reaction (Lee, et al., 2021). On the other hand, PMMA homopolymer showed its first  $T_d$  at 180 °C, which resulted from the depolymerization of the head-to-head linkages, as reported by Galka and his teammates (2014). Therefore, the first degradation stage of the copolymer is mainly caused by the breakdown of -COOH side groups of the AA repeating units as well as the depolymerization of the head-to-head linkages of the MMA repeating units (Lee, et al., 2021). After the first degradation stage, an average of 98.39% of residue was left.

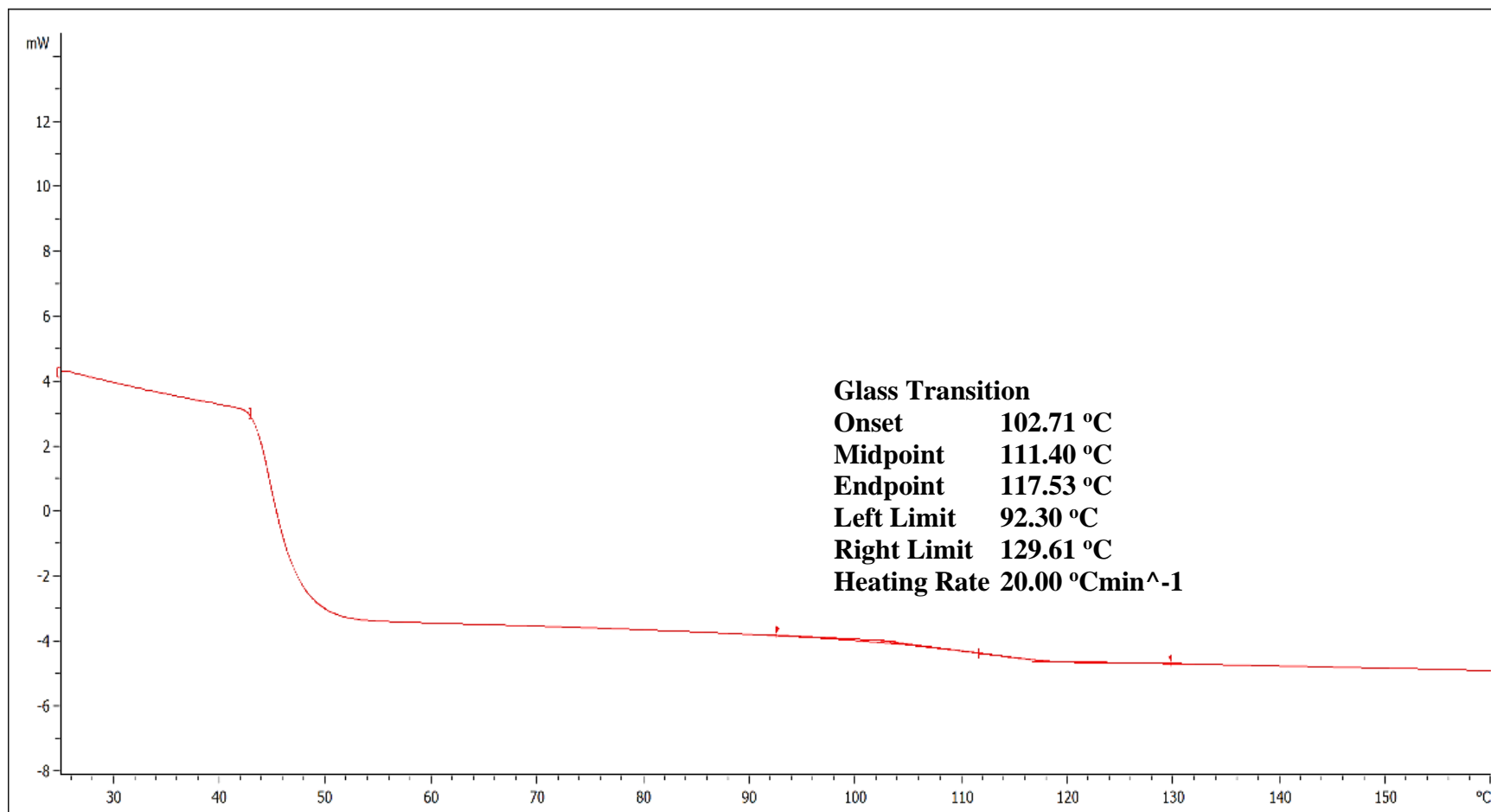
As the temperature increased, a second degradation was observed between 262 and 524 °C with an average inflection temperature of  $394.33 \pm 0.41$  °C. For the PAA homopolymer, the second degradation stage started to occur at 301 °C and ended at 476 °C, with a maximum degradation rate emerging at 372 °C (Moharram and Khafagi, 2006). This decomposition was the major cause of the degradation of polyacrylic anhydride (Lee, et al., 2021). On the other hand, the second degradation stage of PMMA homopolymer began between 350 and 400 °C, which was attributed to the chain scission of the backbone bonding of the polymer chains (Galka, et al., 2013). Therefore, the substantial weight loss of the second degradation stage is due to the breakdown of the polymer backbone of carbon-carbon bonds (Lee, et al., 2021). The average percentage of residue left after the second stage of decomposition was 8.59% at 550 °C.

It was found that the copolymers produced in this study exhibit higher thermal degradation temperature than the pure homopolymers. This might be owing to the presence of AA segments in the copolymer chains which have enhanced the interaction between the polymeric chains. Thus, the thermal stability of the copolymer chains is improved (Shanti, et al., 2016). Besides that, it can be perceived from Table 5.6 that the incorporation of TMVS into the polyacrylate copolymer increased the first  $T_d$  slightly but left the second  $T_d$  unaffected. This evinces the fact that the presence of TMVS reinforces the interaction between the polymer chains via silanol groups and siloxane linkages. Nonetheless, the presence of TMVS in the polymer chain does not influence the thermal stability of carbon-carbon bonding in the polymer backbone (Lee, et al., 2021).

On the other hand, the glass transition temperature ( $T_g$ ) of the P(MMA-*co*-AA) and P(MMA-*co*-AA-*co*-TMVS) copolymers was studied by employing the differential scanning calorimetry (DSC).  $T_g$  is defined as the mid-point on the thermal curve corresponding to half of the heat flow difference between the extrapolated onset and extrapolated end-set temperatures when a polymer transforms from a glassy state to a rubbery state. The polymer chains gain larger mobility when a polymer is heated to a specific temperature. Thus, the polymer becomes soft and flexible. In this work, the polymer samples were subjected to DSC analysis with two heating cycles, of which the first heating cycle was aimed to remove the thermal history of the polymer. Figure 5.10 shows the DSC thermograms of both P(MMA-*co*-AA) and P(MMA-*co*-AA-*co*-TMVS). The  $T_g$  obtained are presented in Table 5.7.

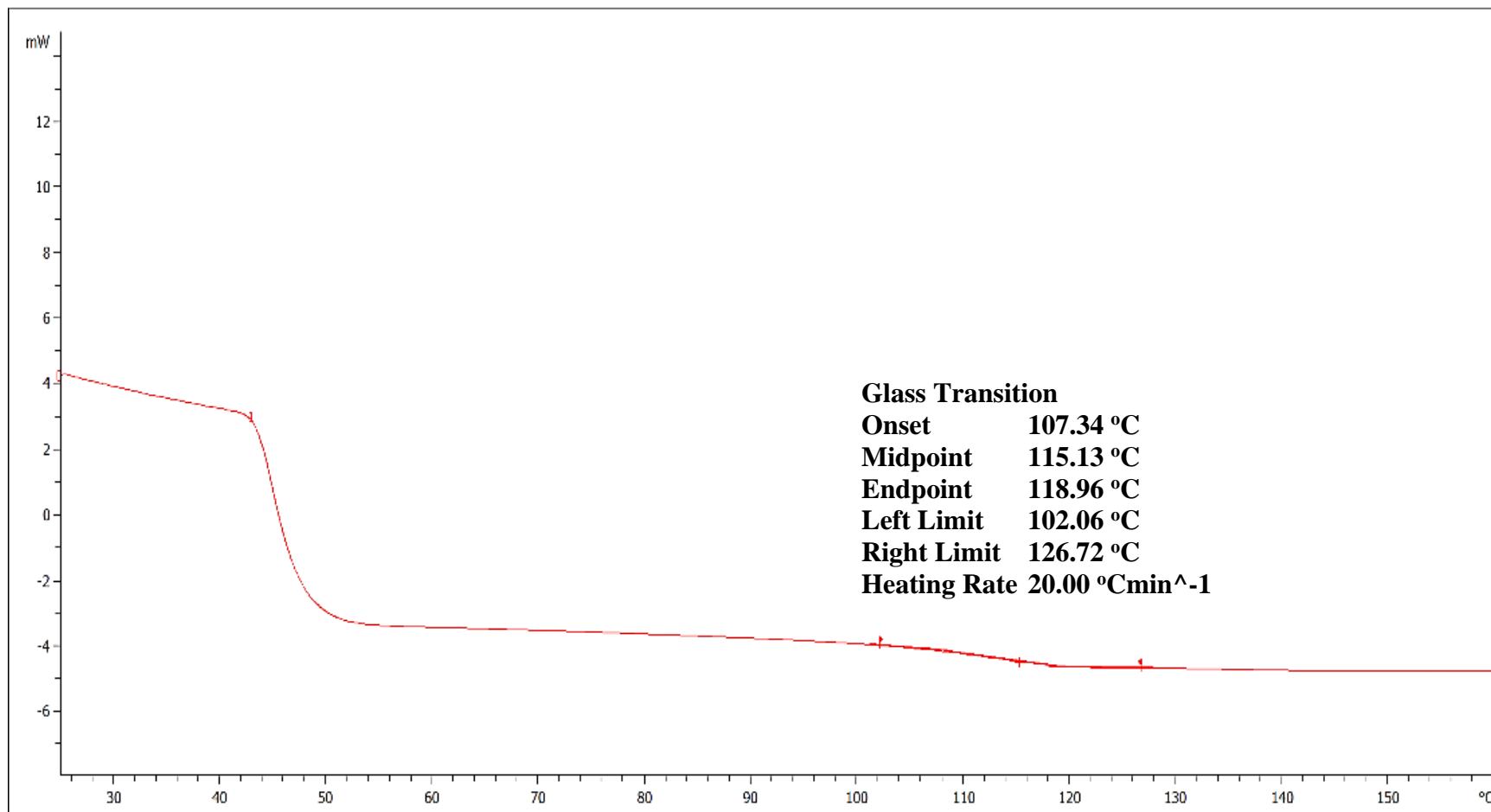
The thermograms of all the polymer samples exhibit a similar thermal curve pattern as the ones shown in Figure 5.10. It was found that the P(MMA-*co*-AA) copolymer has a  $T_g$  value of 111.40 °C (Table 5.7), which is slightly higher than the  $T_g$  of PMMA homopolymer which is at 108 °C (Porter and Blum, 2000). This is mainly attributed to the introduction of AA segments into the polymer chains. The carboxylic acid group of the AA contributes to a higher secondary attractive force between the polymer chains, which restricts the free rotation of the polymer chains. Therefore, the polymer system with lower chain mobility has resulted in a higher  $T_g$  value.

**(a)**



**Figure 5.10 (a):** DSC thermogram of P(MMA-*co*-AA)

(b)



**Figure 5.10 (b):** DSC thermogram of P(MMA-*co*-AA-*co*-TMVS) with 7 wt% of TMVS

**Table 5.7:**  $T_g$  of P(MMA-*co*-AA-*co*-TMVS) variants

Polymer sample	Glass transition temperature, $T_g$ (°C)
<b>0 wt% TMVS</b>	111.40
<b>5 wt% TMVS</b>	113.95
<b>7 wt% TMVS</b>	115.13
<b>9 wt% TMVS</b>	118.08

Furthermore, the DSC results depict an increasing trend in the  $T_g$  of the copolymers as the amount of TMVS in the copolymer increases. The  $T_g$  of the P(MMA-*co*-AA) copolymer has increased from 111.40 °C to 118.08 °C, with a difference of 6.68 °C, when the amount of TMVS incorporated was increased from 0 wt% to 9 wt%. The results demonstrate that with the presence of TMVS, the rotation and mobility of the polymer chains have been further restricted owing to the presence of silanol groups as well as the formation of siloxane linkages in the polymer network (Lee, et al., 2021). As aforementioned, the silanol groups of TMVS present on the polymer chains will interact with each other through condensation reaction to form stable siloxane bonds (Arkles, et al., 2014). An increasing number of silanol groups on the polymer chain leads to higher crosslink density between the polymer chains. According to Shefer and Gottlieb (1992), a higher degree of crosslinking in the polymer network decreases the mobility of the polymer system while increasing the  $T_g$  value. Hence, a higher amount of TMVS increases the number of silanol groups present in the polymer system and induces a higher crosslink density between the polymer chains, thus raising the  $T_g$  of the copolymers (Lee, et al., 2021).

## **5.2 Effect of coating method and amount of TMVS incorporated on the deposition of P(MMA-*co*-AA-*co*-TMVS) nanospheres on a glass substrate**

In this part of the research work, two types of chemical bath deposition techniques based on the self-assembly coating principle, namely the immersion method and the dip coating method, were designed and implemented. P(MMA-*co*-AA-*co*-TMVS) nanospheres synthesized with various amount of TMVS were deposited on Si glass substrate via these two techniques. In order to obtain a self-assembled structure with excellent quality, the glass substrate must be cleaned by treating it with a base piranha solution prior to the coating process. According to Ooij, et al. (2005), the alkaline cleaning exhibited extraordinary performance as a pre-treatment for the application of an SCA as an adhesion promoter for an organic polymeric matrix to adhere to a Si substrate. This treatment is effective in removing contaminants and pollutants on a glass surface. Besides, it is also able to improve the wettability of glass substrate with water owing to the adsorption of hydrophilic radical (hydroxyl group) on the glass surface during the cleaning process (Haugan, 2011; Goh, 2019). As reported by Liu et al. (2001), the adsorption of SCA onto the Si substrate is strongly dependent on the amount of -OH groups available on the surface. The higher the number of -OH groups, the more effective will be the adsorption of SCA onto the Si surface; hence a coating with an array of homogeneous particle distribution can be assembled on it.

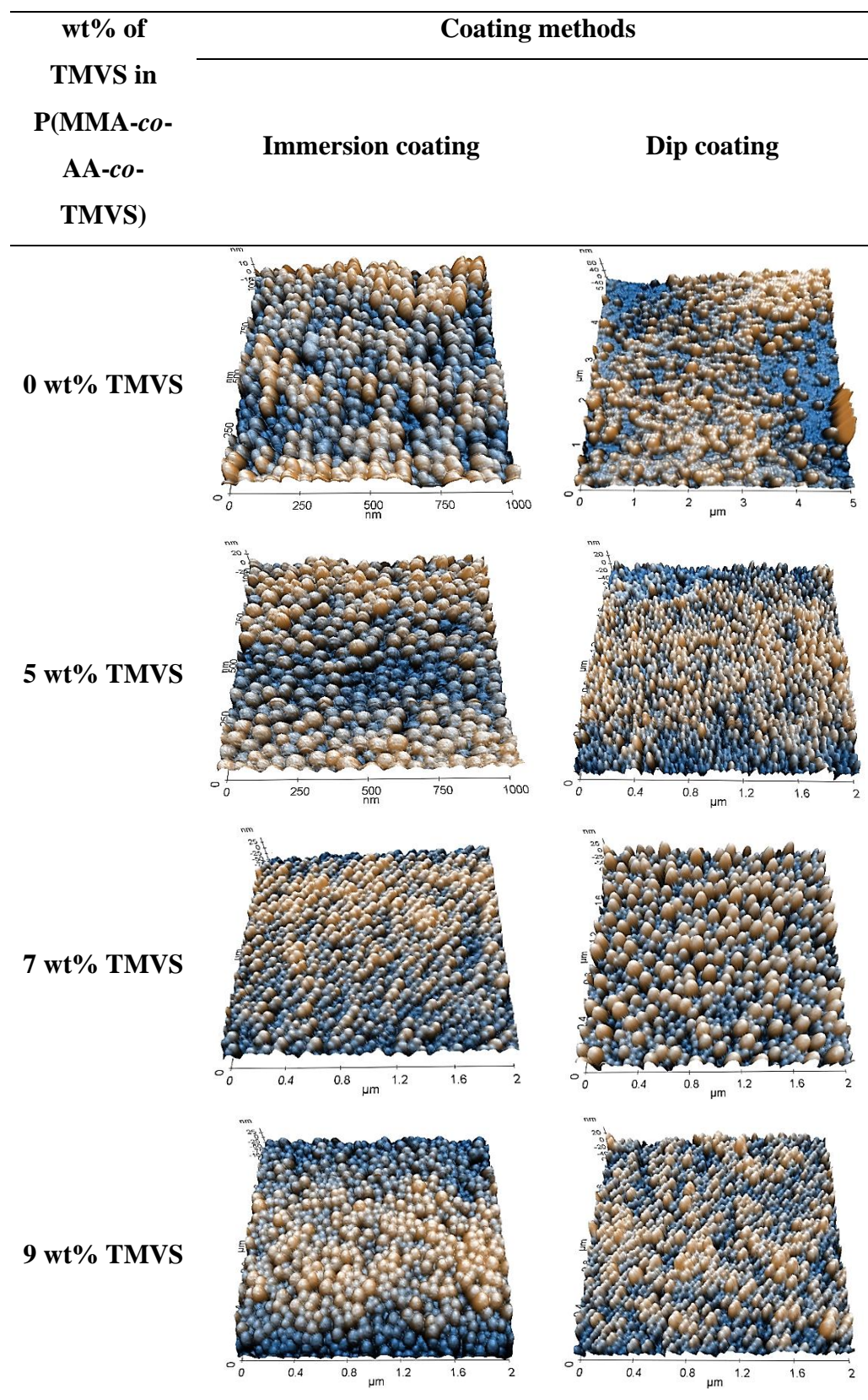
During the coating process, a pre-treated substrate was either dipped or immersed perpendicularly into the polyacrylic emulsion. The substrate was subsequently drawn from the emulsion at a fixed speed. When a substrate is drawn from an emulsion or a latex, a meniscus region is formed on the glass surface due to capillary force (Liu, et al., 2006). The self-assembly process involves the transfer and accumulation of nanostructures in the meniscus to the interface formed among air, emulsion and substrate (Askar, et al., 2013). The impact of both of the coating techniques on particle surface distribution, homogeneity and density was investigated by AFM for morphological and topological examinations. Concurrently, the effect of the concentration of TMVS in the polyacrylate copolymer on the distribution of the self-assembled polymeric nanospheres was also studied using AFM. The influence of these two deposition approaches on the light trapping efficiency of the polymer nanostructures coated on  $\alpha$ -Si solar modules was examined by using a solar simulator to acquire the details of different photovoltaic parameters. The results obtained are evaluated and discussed in the following sections.

### **5.2.1 Surface morphological characteristics of deposited P(MMA-*co*-AA-*co*-TMVS) nanoarray**

The AFM images of P(MMA-*co*-AA-*co*-TMVS) nanospheres containing various amount of TMVS, which had been deposited on a glass surface via both the immersion and dip coating methods, are shown in Figure 5.11. The AFM images depict that the immersion coating technique enables the formation of a polymeric nanoarray with homogeneous particle distribution and superior surface coverage on the substrate surface. However, the same was



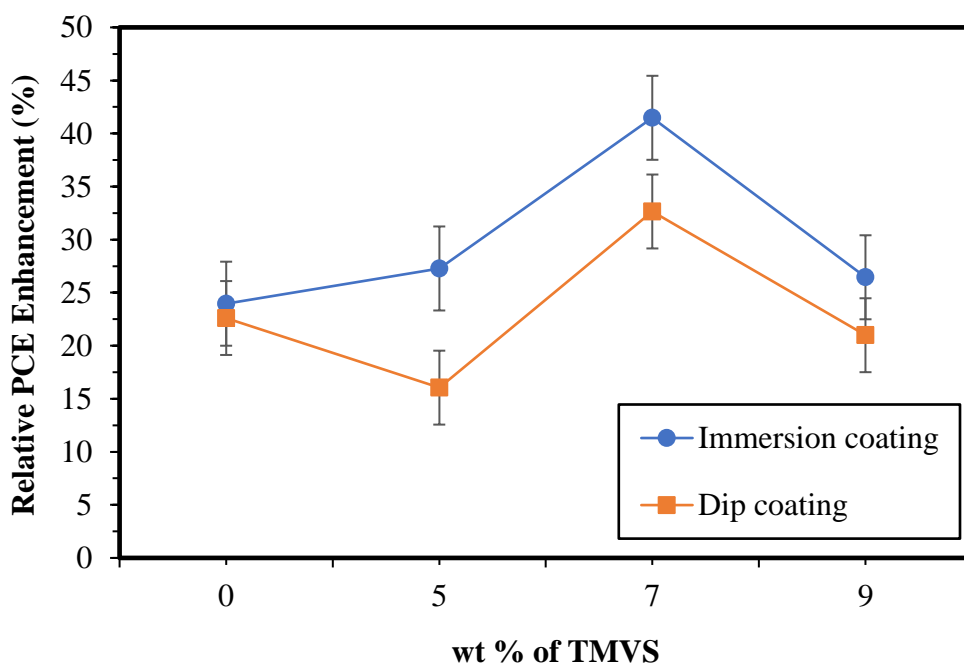
not obtained by using the dip coating technique. Besides, it was found that the amount of TMVS incorporated into the polyacrylate would affect the particle density, surface coverage, particle distribution as well as the thickness of the nanoarray coated onto a glass surface (Lee, et al., 2021). With increasing amount of TMVS, a polymeric nanoarray with higher particle density and better surface coverage was formed. In addition, by coating the glass surface of a solar module with polymeric nanoarray having good surface distribution, the solar module attained a remarkable PCE improvement. The output power measurement of solar modules is further discussed in Section 5.2.2.



**Figure 5.11:** AFM images of P(MMA-*co*-AA-*co*-TMVS) nanostructures deposited on a glass surface via the immersion and dip coating methods corresponding to the amount of TMVS in the copolymers

### 5.2.2 Electrical measurement of solar modules

The influence of both the coating method and the amount of TMVS in P(MMA-*co*-AA-*co*-TMVS) nanospheres on the light trapping efficiency of the solar module was investigated via electrical measurement using a solar simulator. The output power measurements of the solar modules prior to coating and after coating were examined using the solar simulator (Lee, et al., 2021). Figure 5.12 shows the relative PCE improvement attained by the solar modules coated with P(MMA-*co*-AA-*co*-TMVS) nanospheres containing various wt% of TMVS by using the immersion and the dip coating methods. The photovoltaic parameters of the surface-modified solar modules are presented in Table 5.8.



**Figure 5.12:** Relative enhancement in PCE of solar module coated with P(MMA-*co*-AA-*co*-TMVS) nanospheres containing various wt% of TMVS via the immersion and the dip coating techniques

**Table 5.8:** Photovoltaic parameters of the uncoated and coated solar modules, with the latter being deposited with P(MMA-*co*-AA-*co*-TMVS) nanospheres containing various wt% of TMVS using (a) the immersion and (b) the dip coating methods

Amount of TMVS	Solar module sample	$J_{sc}$ (mA cm <sup>-2</sup> )	$V_{oc}$ (V)	FF (%)	PCE (%)	Relative enhancement (%) <sup>a</sup>
(a) Immersion coating method						
0 wt%	Uncoated	2.050	6.050	0.5845	7.249	24.04
TMVS	Coated	2.519	6.225	0.5734	8.992	
5 wt%	Uncoated	2.172	6.024	0.5485	7.177	27.67
TMVS	Coated	2.693	6.132	0.5549	9.163	
7 wt%	Uncoated	1.494	6.077	0.7274	6.604	41.90
TMVS	Coated	2.259	6.011	0.6901	9.371	
9 wt%	Uncoated	1.981	6.084	0.5732	6.908	26.77
TMVS	Coated	2.676	6.010	0.5445	8.757	
(b) Dip coating method						
0 wt%	Uncoated	2.068	5.932	0.5865	7.195	22.46
TMVS	Coated	2.415	6.097	0.5984	8.811	
5 wt%	Uncoated	2.207	5.993	0.5376	7.110	16.05
TMVS	Coated	2.519	6.175	0.5327	8.251	
7 wt%	Uncoated	2.102	6.068	0.5061	6.455	32.25
TMVS	Coated	2.554	6.102	0.5477	8.536	
9 wt%	Uncoated	2.224	6.008	0.5469	7.308	20.64
TMVS	Coated	2.519	6.229	0.5619	8.816	

$$^a \text{Relative enhancement (\%)} = \frac{100(\text{PCE}_{\text{coated}} - \text{PCE}_{\text{uncoated}})}{\text{PCE}_{\text{uncoated}}}$$

Figure 5.12 depicts the relative enhancement in PCE of solar modules coated with P(MMA-*co*-AA-*co*-TMVS) nanospheres. The results show that coating the glass surface of an  $\alpha$ -Si solar module with the polyacrylate nanospheres containing 7 wt% of TMVS via the immersion coating method resulted in the

highest relative enhancement of about 42%. The prominent enhancement in the PCE of the solar modules is attributed by the outstanding anti-reflective property of the polyacrylate copolymer nanostructures. The ARC with graded refractive index facilitates an efficient light transmission across the interface with slow transition from air to Si through destructive interference between incident rays (Esmaeilzad, et al., 2020). The low surface reflection coupled with the high light transmission is achieved by the destructive interference between the light reflected from the interfaces of ARC/substrate and air/ARC (Deng, et al., 2011). In other words, the effects of interference in the coating have resulted in the occurrence of an out-of-phase phenomenon between the waves reflected from the ARC top surface and the wave reflected from the Si substrate surface. These out-of-phase reflected waves destructively interfere with one another, leading to zero net reflected energy. As a result, the light transmittance of the polymer-coated glass surface of the solar module is enhanced and thus more photon is absorbed into the active layer of the solar module (Lee, et al., 2021). Consequently, the generation of electron-hole pairs is significantly increased, which subsequently enhances the overall electrical output power (Tay, et al., 2020).

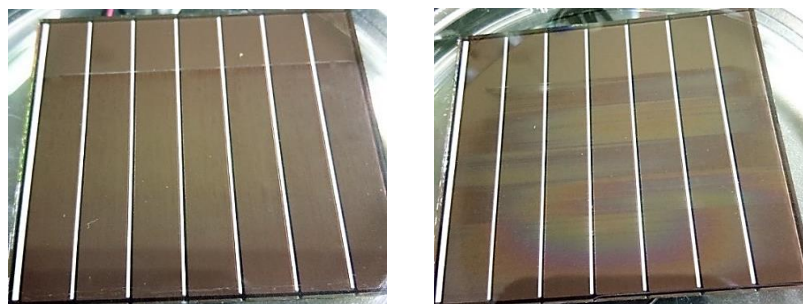
From the results acquired from electrical measurement, it is obvious that the solar modules coated with P(MMA-*co*-AA-*co*-TMVS) nanospheres containing 7 wt% of TMVS, via both the coating approaches, exhibited the highest current density as compared to their respective uncoated solar modules (Lee, et al., 2021). It clearly demonstrates that there is a significant improvement in light trapping efficiency via the deposited polymeric nanoarray. This could also be

contributed by a combination of the scattering mechanisms, namely Rayleigh and Mie scattering, that may reduce the surface reflection and enable a large fraction of light to be coupled into the active region of the solar module (Lee, et al., 2018). It has been reported that Rayleigh scattering occurs when the diameter of nanostructures is about one-tenth of the incident light wavelength, whereas nanostructures with a diameter comparative to the wavelength of the incoming light will undergo Mie scattering (Lin, et al., 2014). As such, Rayleigh scattering and Mie scattering are the dominant mechanisms for light scattering by nanoparticles with smaller size (<100 nm) and larger size, respectively. In this work, a multilayer of the nanoarray of polyacrylate copolymeric nanospheres with an average particle size of 97 nm has exhibited superior light harvesting efficiency. This could be due to the scattering of incident light predominantly through Mie scattering with minor Rayleigh scattering mechanisms. Hence, it led to the highest PCE improvement of 42% in this series of study.

The PCE of the solar modules coated with P(MMA-*co*-AA-*co*-TMVS) nanospheres increased with an increasing amount of TMVS being incorporated into the copolymer until an optimum amount of 7 wt% of TMVS was added (Lee, et al., 2021). This is due to the ordered close-packed arrangement of the nanoarray of nanospheres, which could have acted as an effective intermediate layer that creates an imperative intermediate refractive index to suppress the Fresnel reflection and avoid the abrupt transmission of light from the air to the Si solar module (Shanmugam, et al., 2020). With more than 7 wt% of TMVS, the relative PCE enhancement has shown a downward trend, possibly due to

the formation of a thicker multilayer of nanospheres. A thicker multilayer of such nanoarrays will certainly block the incident light and thus, reduce the light trapping efficiency of the solar module. Therefore, the solar cell coated with P(MMA-*co*-AA-*co*-TMVS) nanostructures containing 9 wt% of TMVS has shown a reduction in the PCE improvement. The results obtained from the electrical measurement of the solar modules are found to be consistent with the UV-Vis absorbance results discussed in Section 5.1.3.

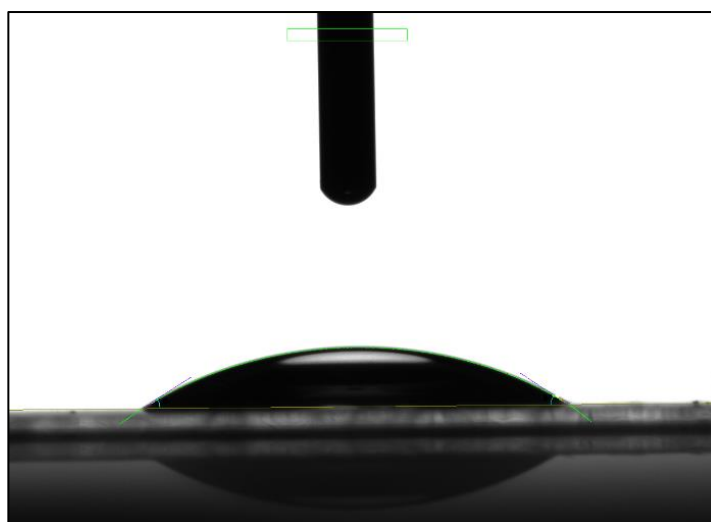
Figure 5.12 also portrays that P(MMA-*co*-AA-*co*-TMVS) nanospheres deposited onto the glass surface of the solar module via the immersion coating method resulted in higher PCE improvement compared to the dip coating method. Figure 5.13 shows the photographs of  $\alpha$ -Si solar modules coated with the polymeric nanospheres via the immersion and the dip deposition techniques respectively. The images portray that the coating obtained with the immersion technique is more uniform, homogeneous with even surface distribution; while the coating obtained with the dip coating technique gave a ‘rainbow effect’ which indicates an uneven surface coverage on the surface of the solar module (Lee, et al.,2021). The above findings shed light on the superiority of the immersion method to the dip coating technique. Hence, the immersion coating method was identified as the preferred technique to attain higher PCE enhancement for the solar module.



**Figure 5.13:** The images of  $\alpha$ -Si solar modules coated with P(MMA-*co*-AA-*co*-TMVS) nanospheres that were deposited via (left) the immersion technique, and (right) the dip coating technique

### 5.3 Effect of amount of TMVS on the surface wettability of P(MMA-*co*-AA-*co*-TMVS) nanoarray

The surface wettability of P(MMA-*co*-AA-*co*-TMVS) nanospheres was studied by WCA analysis. In order to measure the WCA, the image of a water droplet formed on the surface of a glass substrate that was coated with polyacrylic nanoarray was captured by a contact angle analyzer as illustrated in Figure 5.14.



**Figure 5.14:** The image of a water droplet formed on the surface of a glass substrate which was captured by the contact angle analyzer fitted in the Laplace-Young model



Table 5.9 shows the average WCA of a water droplet formed on the surface of the treated glass substrate, corresponding to the amount of TMVS incorporated into the P(MMA-*co*-AA-*co*-TMVS) copolymer. The results in Table 5.9 show that with a coating of P(MMA-*co*-AA-*co*-TMVS) nanoarray on the glass surface, the average WCA has increased from 35.4° to more than 42.6°. Interestingly, the water resistance of the system is further improved with an increasing amount of TMVS in the copolymer, which is evinced by the increase of the average WCA value. An increasing amount of TMVS in the copolymer increases the film thickness of the coated nanoarray (Lee, et al., 2021). According to Vidal, et al. (2019), surface roughness and hydrophobicity increase with the coating thickness. Based on the Cassie-Baxter model, a rough structured coating film with low surface energy reduces the accessibility of water to the surface by means of air entrapment in the grooves and gaps between the nanostructures, thus giving rise to promising water repellence and high WCA. Therefore, the coating of P(MMA-*co*-AA-*co*-TMVS) nanoarray with 9 wt% of TMVS renders the highest WCA of 60.2° with superior hydrophobicity (Lee, et al., 2021).

**Table 5.9:** The average WCA of a water droplet formed on the surface of the modified glass substrate, corresponding to the amount of TMVS incorporated into the P(MMA-*co*-AA-*co*-TMVS) nanostructures

Substrate sample	Average WCA (°)
<b>Without coating</b>	35.4
<b>0 wt% TMVS</b>	42.6
<b>5 wt% TMVS</b>	49.2
<b>7 wt% TMVS</b>	52.0
<b>9 wt% TMVS</b>	60.2

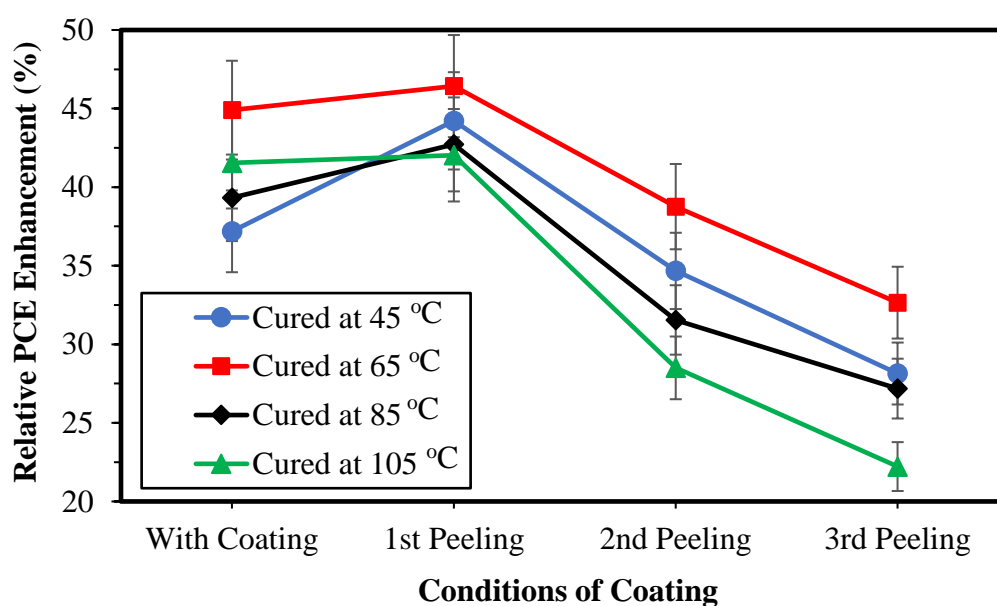
#### **5.4 Effect of curing temperature on the adhesive durability of P(MMA-*co*-AA-*co*-TMVS) nanospheres**

Curing temperature plays an important role in the efficiency of the coupling mechanism of SCA. As a result, it influences the formation of the siloxane (Si-O-Si) bonds at the interphase region between an inorganic Si glass substrate and an organic polymer coating.

In order to study the effect of curing temperature on the adhesion strength of P(MMA-*co*-AA-*co*-TMVS) nanospheres on a glass substrate, the copolymer synthesized with 7 wt% of TMVS was coated on the glass surface of solar modules via the immersion coating method, followed by curing it at different temperatures (Lee, et al., 2021). Subsequently, the output power of the surface-modified solar modules was measured using a solar simulator, before and after multiple cycles of peeling. The results are tabulated in Table 5.10. Meanwhile, the relative PCE improvement of the coated solar modules before and after each cycle of peeling is presented in Figures 5.15.

**Table 5.10:** The output power of solar modules with and without a coating of P(MMA-*co*-AA-*co*-TMVS) nanospheres containing 7 wt% of TMVS, corresponding to the curing temperature and the peeling cycle

Conditions of coating	Output power of solar module (W)			
	Curing temperature (°C)			
	45 °C	65 °C	85 °C	105 °C
<b>Without coating</b>	0.199	0.196	0.206	0.207
<b>With coating</b>	0.273	0.284	0.287	0.293
<b>1<sup>st</sup> peeling</b>	0.287	0.287	0.294	0.294
<b>2<sup>nd</sup> peeling</b>	0.268	0.272	0.271	0.266
<b>3<sup>rd</sup> peeling</b>	0.255	0.260	0.262	0.253



**Figure 5.15:** Relative PCE enhancement of solar modules deposited with P(MMA-*co*-AA-*co*-TMVS) nanospheres with 7 wt% of TMVS, which were subjected to three cycles of peeling process correlating to different curing temperatures

The acquired results shown in Table 5.10 and Figure 5.15 support that 65 °C was a suitable curing temperature for coating the P(MMA-*co*-AA-*co*-TMVS) nanospheres on the glass surface of a solar module. It induces better adhesive durability and mechanical stability of polyacrylic nanoarray on the glass substrate as the best results in relative PCE enhancement of coated solar modules were retained throughout the peeling test. Indeed, the highest relative PCE improvement of 44.9% with an output power of 0.284 W was attained by the coated solar module cured at 65 °C, as relative to the one without coating with an original output power of 0.196 W. On the other hand, the relative enhancement in PCE of all coated solar modules with different curing temperatures shows a similar trend, where the relative PCE improvement increases after the first peeling cycle. This may be due to the elimination of the detrimental loosely bound physisorbed copolymeric layer from the surface of the substrate and thus reduces the polymeric film thickness. The thinner polyacrylic nanoarray performs better as an ARC because it introduces a higher light transmission by reducing the surface light reflection. As a result, a large fraction of light radiation is absorbed and coupled into the active region of the solar modules.

Nonetheless, a gradual decline in PCE enhancement has been observed for all coated solar modules with different curing temperatures after subjecting to several cycles of the peeling process. This may be owing to the disruption as well as the alteration of the order of the nanosphere array caused by the applied mechanical forces of a pressure-sensitive tape (Lee, et al., 2021). Among them, the coated solar modules which were cured at 65 °C illustrated a delighted

result with the highest relative PCE enhancement of 32.65% with the least decline in PCE improvement after three peeling cycles. According to Monticelli et al. (2006), a higher curing temperature facilitates the complete solvent evaporation and promotes more condensation of silanol bonds to form siloxane bonds at the interphase region. A higher cross-link density of the silane layer will create a tighter siloxane network with stronger adhesive bond strength. Therefore, curing at 65 °C could attain a polyacrylic nanoarray with high adhesive durability which is able to endure the mechanical stress to a higher extent. As a result, it required more effort to peel off the polyacrylic nanoarray from the substrate. On the contrary, a curing temperature which is over an optimum value may result in an adverse effect of bond weakening. This is evidenced by the coated solar module that was cured at 105 °C, which attained the lowest relative PCE improvement of 22.22% with the largest decline in PCE enhancement after three cycles of peeling.

The ARC of polyacrylate nanospheres containing 7 wt% of TMVS that was deposited on the glass surface of  $\alpha$ -Si solar modules with various curing temperatures exhibited an average relative PCE improvement of  $40.74 \pm 2.85\%$ . The results obtained are well correlated with the outcomes discussed previously in Section 5.2.2. This illustrates that this approach of depositing polyacrylate nanospheres on the glass surface of a solar module is feasible and effective, as it has constantly elevated the PCE of solar modules with reproducible improvement in the susceptible range.

## **5.5 Effect of natural weathering exposure on the adhesion strength of P(MMA-*co*-AA-*co*-TMVS) nanospheres**

The adhesion strength of the coating of P(MMA-*co*-AA *co*-TMVS) nanoarray on the glass surface of an  $\alpha$ -Si solar cell, which was coated via either the immersion or the dip coating method, was also investigated by natural weathering exposure (Lee, et al., 2021). The weathering test demonstrates the actual working environment of the solar panels which are usually installed outdoor. In view of this, the solar panels must be able to endure and withstand extreme outdoor weathering processes.

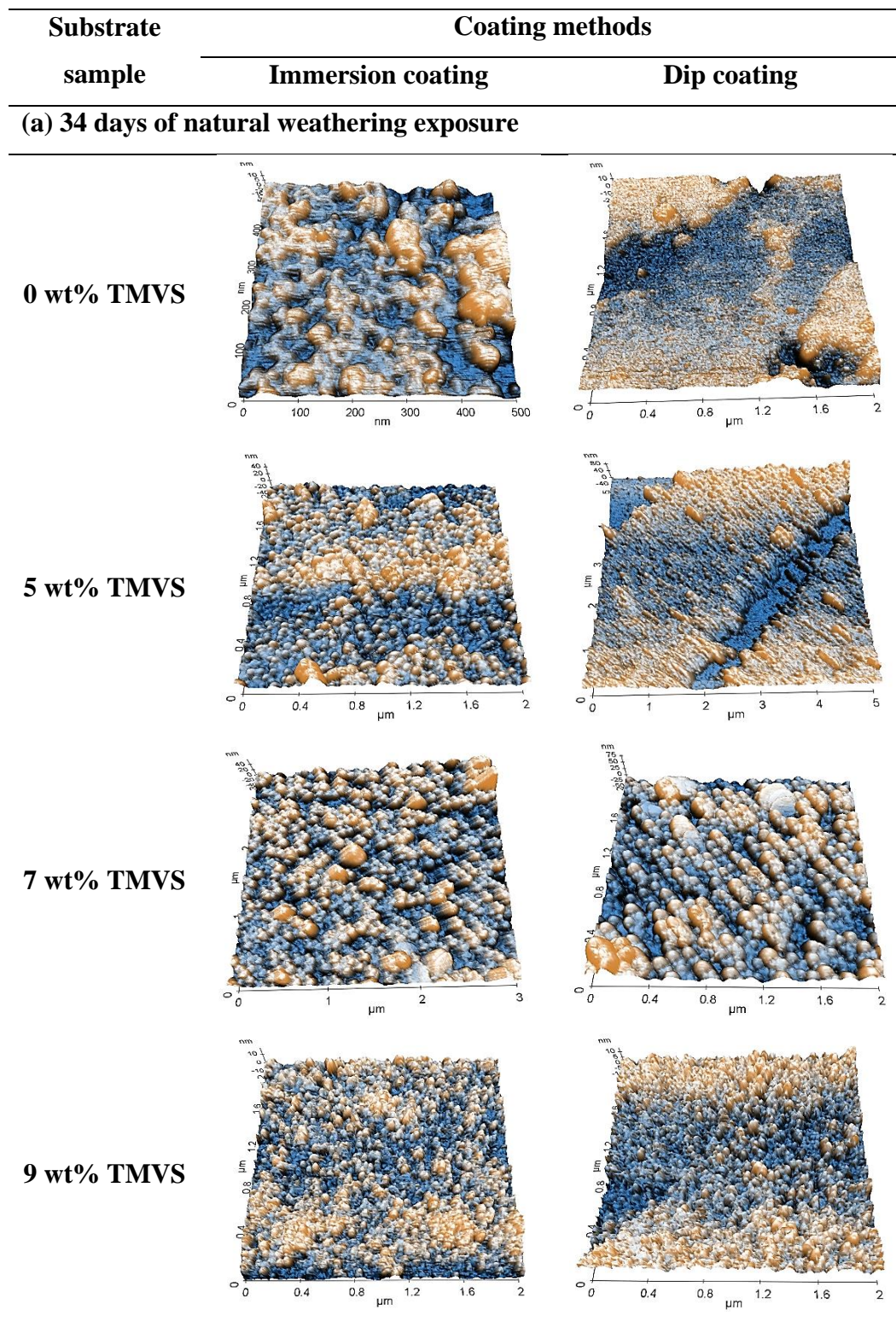
In this study, the effect of outdoor natural weathering on P(MMA-*co*-AA-*co*-TMVS) nanoarray deposited on the glass surface was examined with the aid of AFM for morphological and topological study; while the output power of the surface-modified solar modules was measured utilizing an AM 1.5 solar simulator (Lee, et al., 2021). The results acquired from AFM and electrical measurement are presented and discussed in the following sections.

### **5.5.1 Surface morphological characteristics of deposited P(MMA-*co*-AA-*co*-TMVS) nanoarray**

The AFM images shown in Figure 5.16 demonstrate the effect of outdoor natural weathering on the P(MMA-*co*-AA-*co*-TMVS) nanoarray coated on the glass surface. In contrast to the AFM images of the polymer coatings before exposure (Figure 5.11), it was found that after natural weathering exposure, the smooth array of the polyacrylic nanospheres with homogeneous distribution

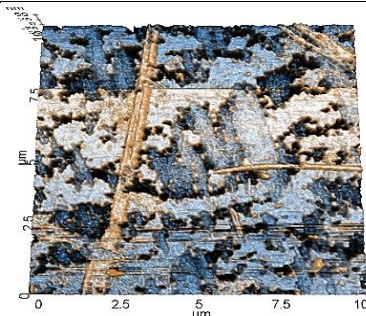
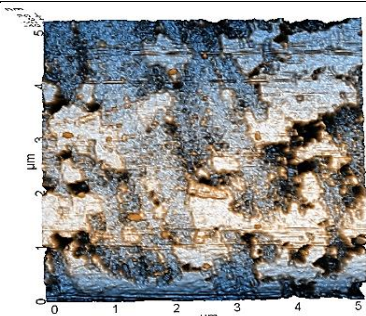
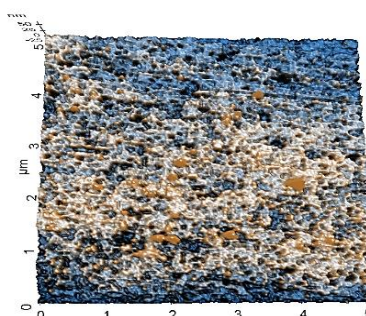
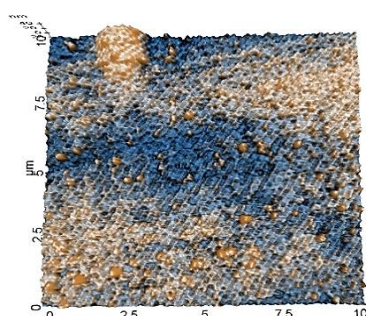
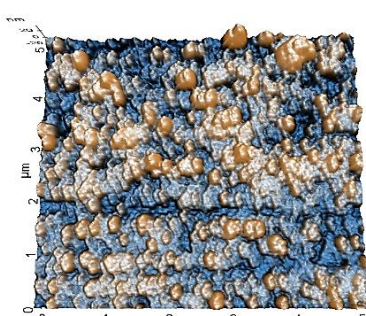
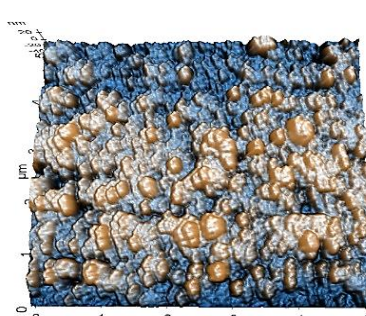
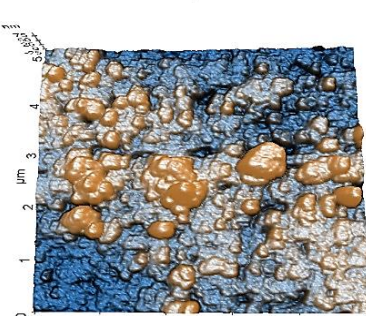
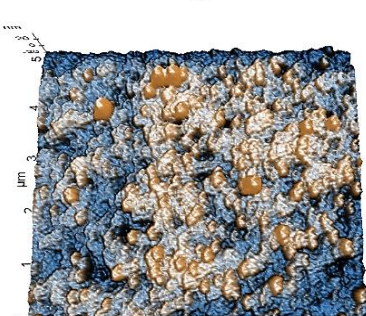
has been disrupted to a different degree. The degree of disruption was dependent on the amount of TMVS incorporated into the copolymer, the coating method and the duration of weathering exposure (Lee, et al., 2021).

The results obtained show that the polymeric nanoarray with less than 7 wt% of TMVS suffered a higher degree of disruption. After 34 days of natural weathering exposure, the nanoarray of the polyacrylate nanospheres with no TMVS incorporation have shown the worst damage in term of surface coverage and surface distribution. On the other hand, P(MMA-*co*-AA-*co*-TMVS) nanospheres with 7 and 9 wt% of TMVS exhibited higher weathering resistance with a lower degree of disruption on the surface coverage and distribution of the nanoarray (Lee, et al., 2021). The better outcomes of the latter could be partly due to the lower surface energy and higher water resistance of the system, as illustrated by the larger WCA obtained (Table 5.9).



**Figure 5.16:** (a) AFM images of the nanoarray of P(MMA-*co*-AA-*co*-TMVS) nanospheres containing various wt% of TMVS, which was deposited on a glass substrate via the immersion and the dip coating methods after 34 days of natural weathering exposure



Substrate sample	Coating methods	
	Immersion coating	Dip coating
<b>(b) 130 days of natural weathering exposure</b>		
<b>0 wt% TMVS</b>		
<b>5 wt% TMVS</b>		
<b>7 wt% TMVS</b>		
<b>9 wt% TMVS</b>		

**Figure 5.16:** (b) AFM images of the nanoarray of P(MMA-*co*-AA-*co*-TMVS) nanospheres containing various wt% of TMVS, which was deposited on a glass substrate via the immersion and the dip coating methods after 130 days of natural weathering exposure

Besides that, the AFM images also demonstrate that the immersion coating method has resulted in the homogeneous surface distribution of the P(MMA-*co*-AA-*co*-TMVS) nanoarray on glass surface with better weathering resistance as compared to the dip coating technique. This is clearly illustrated by the images of the copolymeric nanostructures with 7 wt% of TMVS, which was coated via the immersion coating method, that displays better surface coverage with a lower degree of disruption after 34 and 130 days of natural weathering exposure, respectively. These results again proved that the immersion coating method is a better choice than the dip coating technique.

In addition, it is obvious that the longer the duration of outdoor exposure a polymer coating undergoes in the natural weathering process, the higher will be the degree of disruption and damage of such coating. After 130 days of natural weathering exposure, the condition of the polymeric nanoarray has worsened with more damages incurred (Lee, et al., 2021).

From the outcomes of the AFM study, it is anticipated that the light trapping efficiency of the surface-modified solar modules and thus their PCE will be jeopardized after the natural weathering process. This is because an even and well-distributed array of nanospheres on the substrate surface is mandatory in enhancing the light harvesting efficiency of solar modules and thus improving their PCE. The AFM results are consolidated by the electrical output power results of the solar modules which were coated similarly with P(MMA-*co*-AA-*co*-TMVS) nanospheres as in the AFM study (Lee, et al., 2021).

### 5.5.2 Electrical measurement of solar modules

The influence of outdoor natural weathering on P(MMA-*co*-AA-*co*-TMVS) nanoarray deposited on the glass surface of  $\alpha$ -Si solar modules was investigated by measuring the electrical features of the solar modules (Lee, et al., 2021). Concurrently, the durability of P(MMA-*co*-AA-*co*-TMVS) nanostructures was also assessed. Table 5.11 demonstrates the average output power of the solar modules coated with P(MMA-*co*-AA-*co*-TMVS) nanostructures containing various amount of TMVS, over a duration of 130 days of natural weathering exposure. The average relative PCE enhancement of the surface-modified solar modules is illustrated in Figure 5.17. The average output power of the solar modules was analysed as a function of the amount of TMVS incorporated, the coating method and the duration of natural weathering exposure.

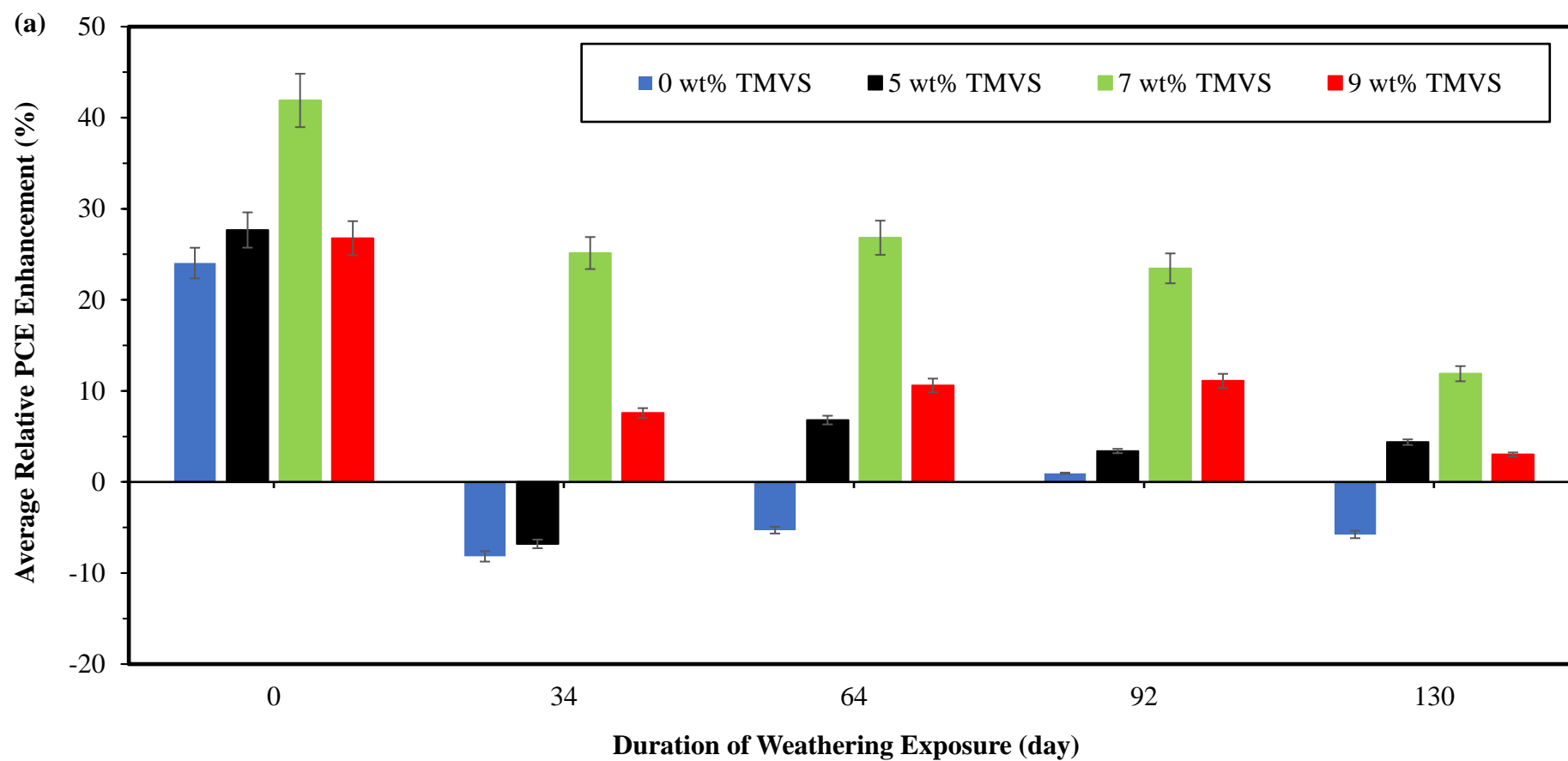
Before the natural weathering exposure (0 days), the solar modules coated with P(MMA-*co*-AA-*co*-TMVS) nanospheres containing 7 wt% of TMVS demonstrate a higher relative PCE enhancement of 42.0% and 32.4% for the immersion and dip coating methods, respectively. The improvement in the relative PCE enhancement of the surface-modified solar modules is mainly attributed to the promising anti-reflective properties of polyacrylate nanospheres which are with homogeneous surface distribution and uniform surface coverage (Lee, et al., 2021). The polymeric nanoarray has efficiently harvested the light radiation and subsequently scattered it into the active region of photovoltaic cells. Therefore, more electron-hole pairs are generated.

However, after the outdoor weathering exposure, all the surface-modified solar modules have suffered a decline in relative PCE enhancement. The degree of degradation increases with the increase of the duration of weathering exposure. The acquired results clearly show that the P(MMA-*co*-AA-*co*-TMVS) nanospheres containing 7 wt% of TMVS have again demonstrated a better performance in light trapping as a higher relative PCE enhancement with a lower decline in PCE improvement was retained after the natural weathering test (Lee, et al., 2021). After 130 days of outdoor weathering exposure, the higher relative enhancement in PCE of 11.9% and 14.0% were obtained by the solar modules thus coated via the immersion and dip coating methods, respectively, as compared with the initial PCE improvement of 42.0% and 32.4% before weathering exposure.

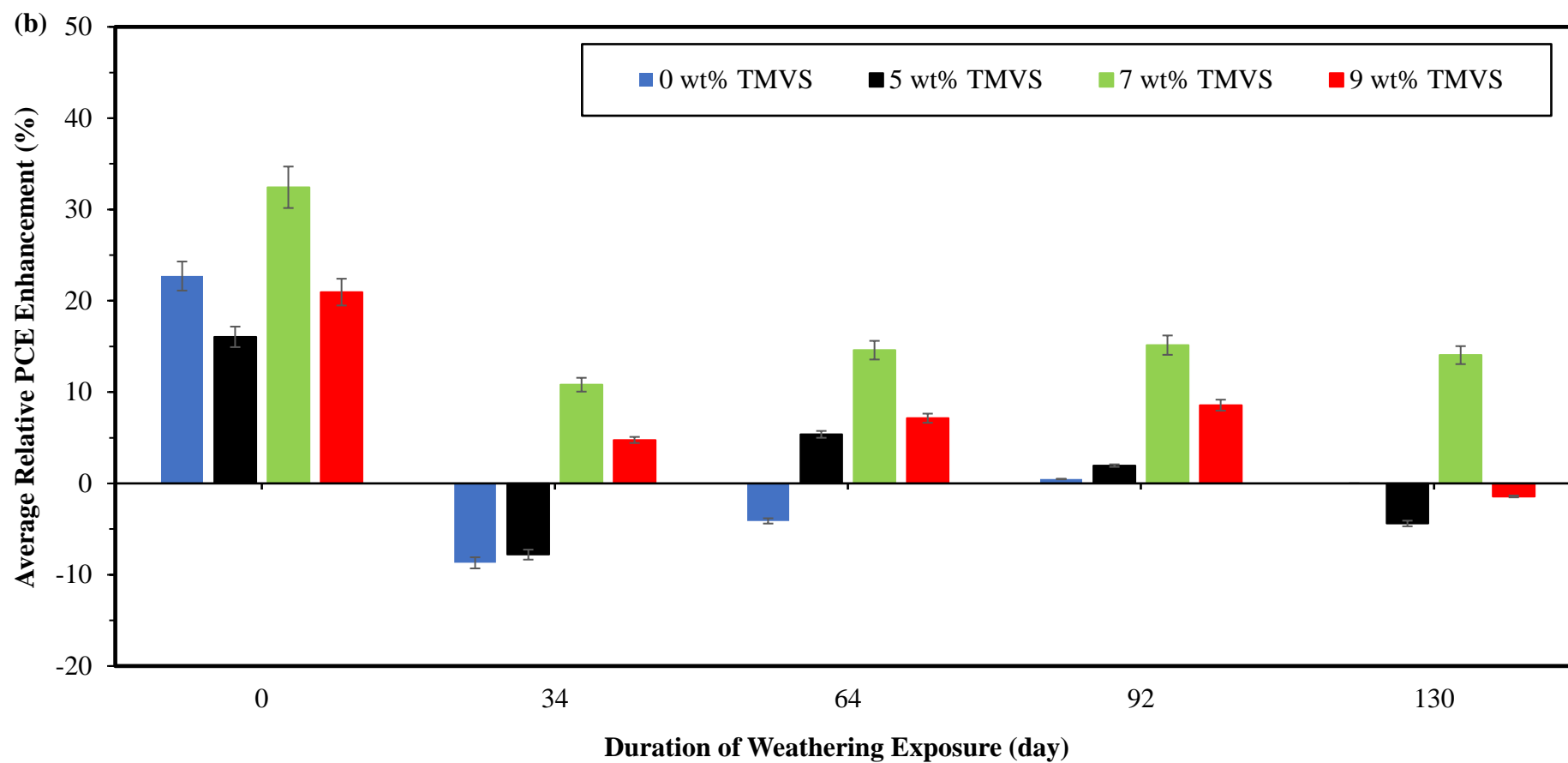
Nevertheless, the solar module which was coated with the pristine P(MMA-*co*-AA) nanospheres has suffered a huge declination in relative PCE enhancement, specifically -5.8% as compared to its initial PCE enhancement of 24%. This was due to the disruption and damage of the polymeric coating as a result of prolonged natural weathering processes. Meanwhile, it was found that with the incorporation of a suitable amount of TMVS in P(MMA-*co*-AA-*co*-TMVS) nanospheres, which was 7 wt% as found in this study (Lee, et al., 2021). The average relative PCE of solar modules was significantly improved while the decline in PCE enhancement was effectively reduced as seen over 130 days of outdoor natural weathering exposure (Table 5.11 and Figure 5.17). The results of the electrical measurement of solar modules correlate well with the AFM results of the exposed polyacrylate nanoarrays as discussed in Section 5.5.1.

**Table 5.11:** Average output power of uncoated and coated solar modules, with the latter deposited with P(MMA-*co*-AA-*co*-TMVS) nanospheres containing various wt% of TMVS via (a) the immersion and (b) the dip coating techniques as a function of the duration of natural weathering exposure

Amount of TMVS	Solar module sample	Average output power of solar module (W)				
		Duration of natural weathering exposure (day)				
		0	34	64	92	130
<b>Control</b>		0.211	0.191	0.213	0.215	0.216
<b>(a) Immersion coating method</b>						
<b>0 wt%</b>	Uncoated	0.208	-	-	-	-
<b>TMVS</b>	Coated	0.258	0.191	0.197	0.210	0.196
<b>5 wt%</b>	Uncoated	0.206	0.206	0.206	0.206	0.206
<b>TMVS</b>	Coated	0.263	0.192	0.220	0.213	0.215
<b>7 wt%</b>	Uncoated	0.179	0.179	0.179	0.179	0.179
<b>TMVS</b>	Coated	0.254	0.224	0.227	0.221	0.200
<b>9 wt%</b>	Uncoated	0.198	0.198	0.198	0.198	0.198
<b>TMVS</b>	Coated	0.251	0.213	0.219	0.220	0.204
<b>(b) Dip coating method</b>						
<b>0 wt%</b>	Uncoated	0.207	-	-	-	-
<b>TMVS</b>	Coated	0.254	0.189	0.199	0.208	0.207
<b>5 wt%</b>	Uncoated	0.205	0.205	0.205	0.205	0.205
<b>TMVS</b>	Coated	0.238	0.189	0.216	0.209	0.196
<b>7 wt%</b>	Uncoated	0.185	0.185	0.185	0.185	0.185
<b>TMVS</b>	Coated	0.245	0.205	0.212	0.213	0.211
<b>9 wt%</b>	Uncoated	0.210	0.210	0.210	0.210	0.210
<b>TMVS</b>	Coated	0.254	0.220	0.225	0.228	0.207



**Figure 5.17 (a):** Average relative enhancement in PCE of  $\alpha$ -Si solar modules coated with P(MMA-*co*-AA-*co*-TMVS) nanospheres with different wt% of TMVS through the immersion coating methods as a function of the duration of outdoor natural weathering exposure



**Figure 5.17 (b):** Average relative enhancement in PCE of  $\alpha$ -Si solar modules coated with P(MMA-*co*-AA-*co*-TMVS) nanospheres with different wt% of TMVS through the dip coating methods as a function of the duration of outdoor natural weathering exposure





In addition, an evenly distributed polymeric nanoarray with uniform surface coverage produced via the immersion coating method was found to be better in elevating the light harvesting efficiency of ARC of polyacrylic nanoarray. Overall, the immersion coating method induced better weathering resistance, compared to the dip coating method. This is evinced by attaining a higher average relative PCE enhancement for most copolymeric variants, over 130 days of outdoor weathering exposure.

Undoubtedly, natural weathering leads to the disruption of the polymeric nanoarray coated on the surface of solar modules and jeopardizes the function of such polymeric coating as an anti-reflective layer (Lee, et al., 2021). This is because the formation of siloxane bonds via the condensation of silanol groups of TMVS is a reversible reaction in the presence of water. As a result, the siloxane bonds that bind the P(MMA-*co*-AA-*co*-TMVS) nanospheres to the glass surface are broken when they are hydrolyzed by water molecules from the surrounding (Lee, et al., 2021). Consequently, the polymeric nanospheres coated on the surface of solar modules were washed off during rainy days, which is clearly portrayed by the disrupted polymeric nanoarray in the AFM images in Figure 5.16.

In fact, the loss in relative PCE enhancement of a solar module is partly caused by the accumulation of dust or pollutants on its surface (Lee, et al., 2021). This is obviously seen after 34 days of natural weathering exposure, during which the atmosphere in the area where the solar cells were located was filled with haze particles emitted from a forest fire which has lasted for about a month.

The presence of dust and pollutants block the incident light and reduce the transmittance of the light photons into the active layer of a solar module (Lee, et al., 2021). According to Casanova, et al. (2011), the accumulation of dust on the surface of photovoltaic devices decreases the incoming irradiance to the cell and results in power losses of at least 15%. Therefore, it may be necessary to introduce a hydrophobic protective film with distinctive self-cleaning properties on the coated surface of solar modules to promote higher water resistance while reducing dust accumulation.

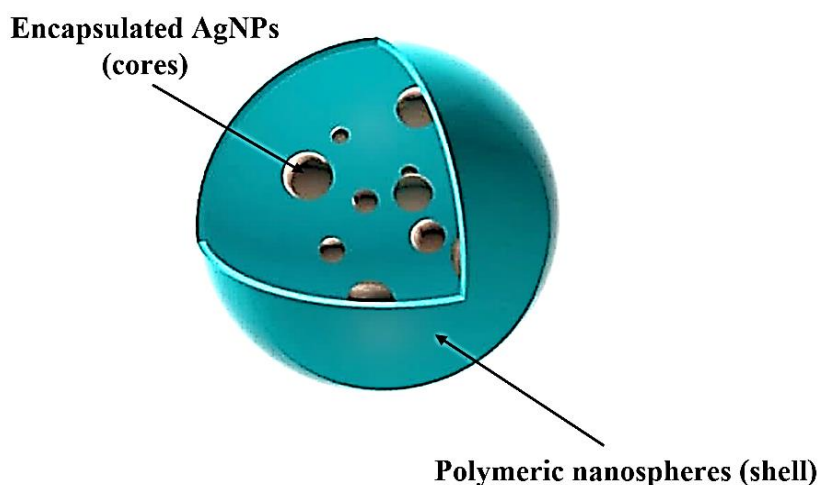
## CHAPTER 6

### FABRICATION AND CHARACTERIZATION OF METALLIC-POLYMER NANOCOMPOSITES

#### 6.1 Encapsulation of AgNPs into P(MMA-*co*-AA-*co*-TMVS) nanospheres via emulsion polymerization

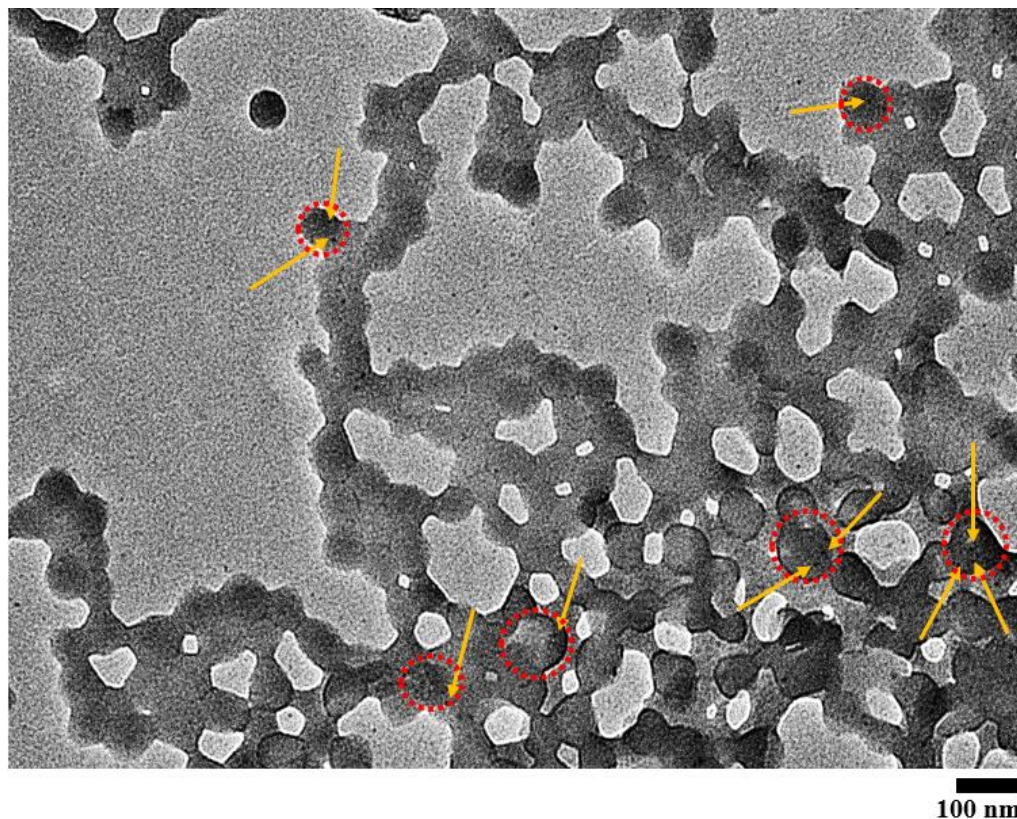
Nanoencapsulation is a process which involves particle(s) (core) entrapment in a capsule (shell or matrix) at the nanoscale with a variety of structural properties, depending on the synthetic route, recipe and ingredients. The nanoencapsulation technique is categorized into two major classes: (a) a core being surrounded by a polymer matrix shell and (b) a core being embedded within a polymeric continuous network (Cano-Sarabia and Maspocho, 2015). Being a class (b) technique, metallic nanostructures with smaller particle size are generally encapsulated in bigger polymeric nanoparticles through the heterogeneous emulsion polymerization process. The advantages of such process include the impartment of nanocapsules with high purity and uniformity, dispersibility, small particle size with narrow distribution, readily scalable and accentuated chemical homogeneity. By encapsulating metallic nanoparticles inside polymeric nanospheres, the metallic nanocolloids can be prevented from aggregation, agglomeration and oxidation under high ionic strength and extreme oxidation conditions via an effective barrier of the polymeric shell (Scarabelli, et al., 2019).

In this study, AgNPs with two particle size ranges of 3-7 nm and 10-30 nm were embedded respectively inside P(MMA-*co*-AA-*co*-TMVS) nanospheres, which were specifically designed to give an average particle size of about 100 nm, via an emulsion polymerization process. Figure 6.1 illustrates the schematic diagram of a polymeric nanosphere shell encapsulated with numerous smaller sized AgNP cores. In view of the anti-reflective property of the polymeric nanoarrays in addition to the localized surface plasmon resonance (LPSR) and surface plasmon polariton effects of the metallic nanoparticles, it is anticipated that an array of such nanostructures on the glass surface of solar module could enhance its light trapping efficiency (Lee, et al., 2021). Such functional nanoarrays have combined the advantageous elements of light trapping efficiency via effective light scattering mechanisms and LPSR effect.



**Figure 6.1:** Schematic representation of a polymeric nanosphere shell encapsulated with AgNP cores

### 6.1.1 Topological characteristics of metallic-polymer nanocomposites



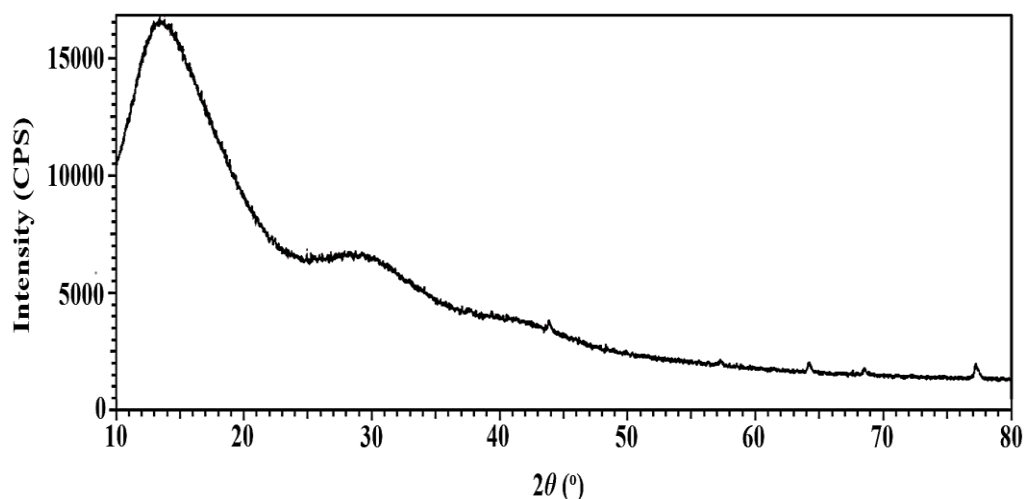
**Figure 6.2:** TEM image of metallic-polymer nanocomposites

The TEM image of the metallic-polymer nanocomposites is shown in Figure 6.2. As portrayed in the image, a great amount of AgNPs (orange arrow) are entrapped in the copolymeric nanospheres (red dotted line circle), with some of them scatter outside the nanospheres. The TEM image depicts that the metallic nanoparticles had been encapsulated successfully inside the polymeric nanospheres through the emulsion copolymerization process. Besides, no agglomeration and clustering of AgNPs are observed in the image. As the AgNPs are entrapped in the polymeric matrix, it is expected that the metallic nanoparticles will be protected from extreme conditions of the surrounding environment. Furthermore, the well-dispersed AgNPs should be able to render

a high light trapping efficiency through accentuated LSPR effect, surface plasmon polaritons and light scattering mechanisms.

### **6.1.2 Crystallinity of metallic-polymer nanocomposites**

The metallic-polymer nanocomposites were characterised using XRD to determine the degree of crystallinity of the polymer composite. The diffractogram of P(MMA-*co*-AA-*co*-TMVS) nanospheres embedded with AgNPs (Figure 6.3) shows that it is similar to the diffraction pattern of the copolymer without AgNPs (cf. Figure 5.8). The diffraction peaks that occur at  $13.54^\circ$ ,  $30.20^\circ$ , and  $43.85^\circ$  are mainly attributed to the MMA segments, while  $33.78^\circ$  is contributed by the AA components in the polymer chains. The  $2\theta$  values of the diffraction peaks obtained were slightly shifted, which may be due to the presence of AgNPs in the polymer matrix that may affect the interaction between the polymer chains and thus result in some extent of changes in the nanocomposite. Nevertheless, the presence of AgNPs, which was  $\leq 50$  ppm, in the polyacrylate nanospheres could not be detected by XRD.



**Figure 6.3:** XRD pattern of metallic-polymer nanocomposites with 7 wt% of TMVS

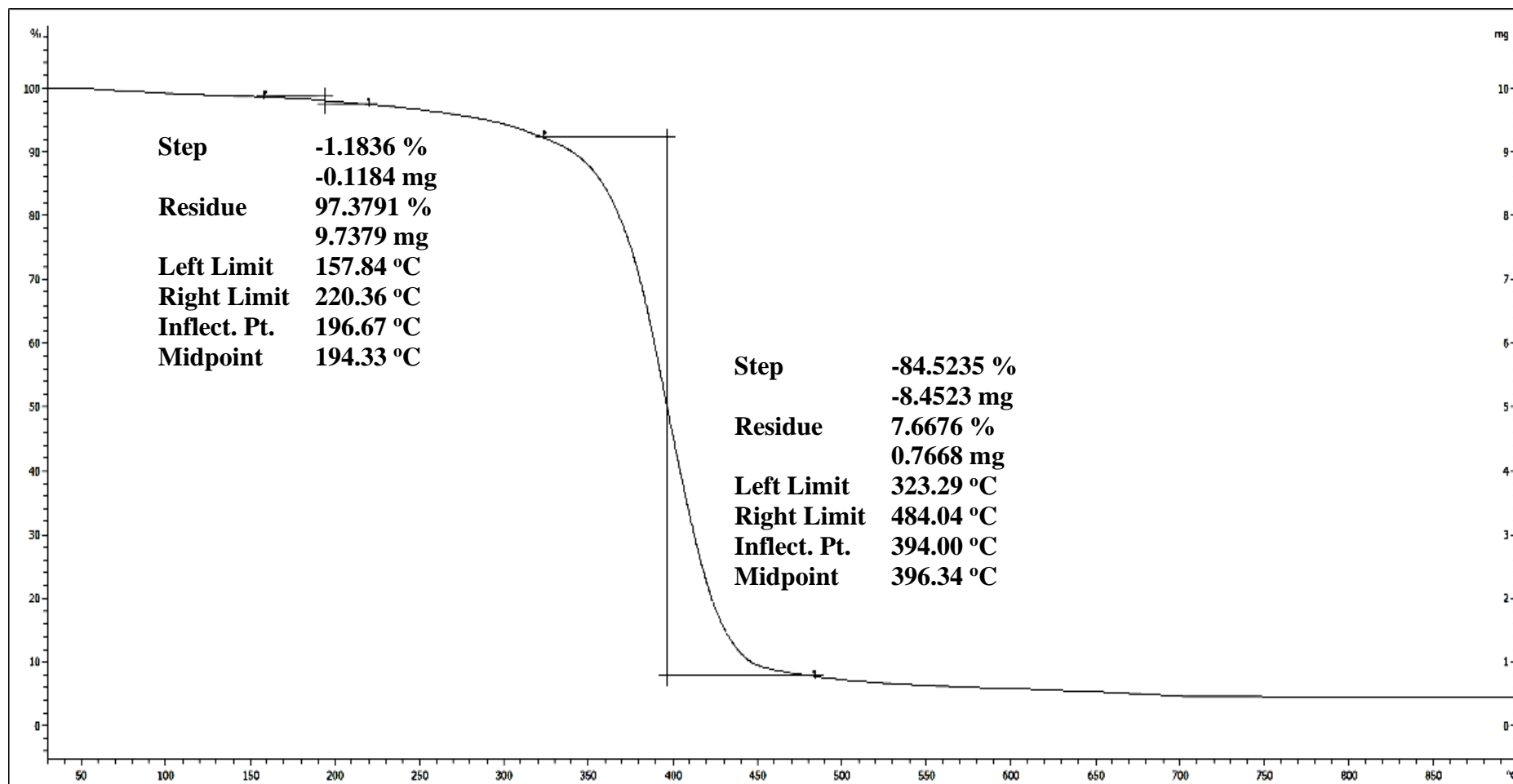
Moreover, the diffraction sharp peaks with low intensity in the diffractogram shown in Figure 6.3 also implies that the degree of crystallinity of the functional polymeric nanocomposite is lower than the polymeric matrix without AgNPs. This is further consolidated by the analysis of the degree of crystallinity which was conducted using a programmable software of XRD. The results obtained show that the metallic-polymer nanocomposite possesses a low degree of crystallinity of 7.65% which is 0.74% lower than the polymeric matrix without AgNPs (cf. Section 5.1.6). The slight drop in the degree of crystallinity of the metallic-polymer nanocomposite is due to the presence of AgNPs in the polymer matrix that prevents the polymer chains from packing uniformly. Therefore, the nanocomposite with a loosely packed polymer structure is highly amorphous.

### 6.1.3 Thermal stability of metallic-polymer nanocomposites

In this study, TGA was carried out to investigate the thermal stability of the metallic-polymer nanocomposite by determining the thermal degradation temperature ( $T_d$ ) and the percentage of residue after degradation (Lee, et al., 2021). Figure 6.4 is the TGA thermogram of the metallic-polymer nanocomposite. It shows a similar degradation pattern with the polyacrylic nanospheres without AgNPs, where the thermal decomposition process also occurred in two stages.

The first stage of degradation started at 157.8 °C and ended at 220.4 °C with an inflection point at 196.7 °C. The first thermal degradation is mainly due to the removal of carboxyl side groups of AA building blocks, via the depolymerization of the head-to-head linkages of the MMA segments in the polymer chains (Lee, et al., 2021). The average percentage of residue left after this stage of degradation was 97.38%. On the other hand, the second degradation started at about 323.3 °C and ended at 484.0 °C with the maximum degradation rate emerging at 394.0 °C. The second thermal decomposition is mainly caused by the chain scission of the polymer backbone. After the second degradation stage, an average of 7.67% residue was left at 550 °C. Compared to the TGA thermogram of polyacrylate with 7 wt% of TMVS that was without AgNPs, as shown in Figure 5.9 (b), only a marginally change in the  $T_d$  of the first stage of thermal degradation is observed, while the  $T_d$  of the second degradation stage remains constant. This reveals that the presence of AgNPs in the copolymeric nanospheres does not significantly affect the characteristics of the polymer matrix in terms of its physical and chemical properties.





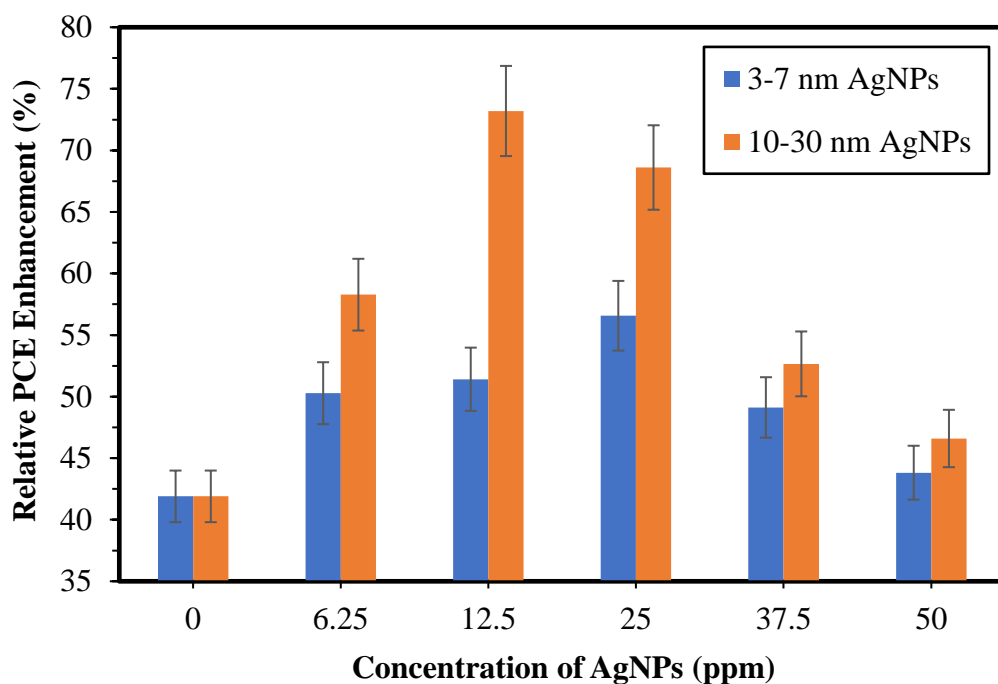
**Figure 6.4:** TGA thermogram of metallic-polymer nanocomposite with 7 wt% of TMVS

## **6.2 Effect of concentration and particle size of AgNPs entrapped into P(MMA-*co*-AA-*co*-TMVS) nanospheres on the light harvesting efficiency of nanocomposites**

In this study, the impact of the concentration and particle size of AgNPs encapsulated as well as the amount of TMVS incorporated in the copolymeric nanospheres on the light trapping efficiency of nanocomposites was investigated. The concentration of AgNPs with the particle size ranges of 3-7 nm and 10-30 nm varied between 6.25 ppm and 50.0 ppm. The metallic-polymer nanocomposites were deposited on the glass surface of  $\alpha$ -Si solar modules via the immersion self-assembly coating method. The output power of solar modules prior to and after surface treatment was determined using an AM 1.5 solar simulator; while the light transmission of glass substrates with and without polymeric ARC was accessed using UV-Vis spectroscopy.

### **6.2.1 Electrical measurement of solar modules**

Figure 6.5 depicts the percentage of relative PCE improvement obtained from solar modules coated with the nanoarray of metallic-polymer nanocomposites, corresponding to the particle size and concentration of AgNPs. Meanwhile, the photovoltaic parameters of solar modules before and after surface modification are summarized in Table 6.1.

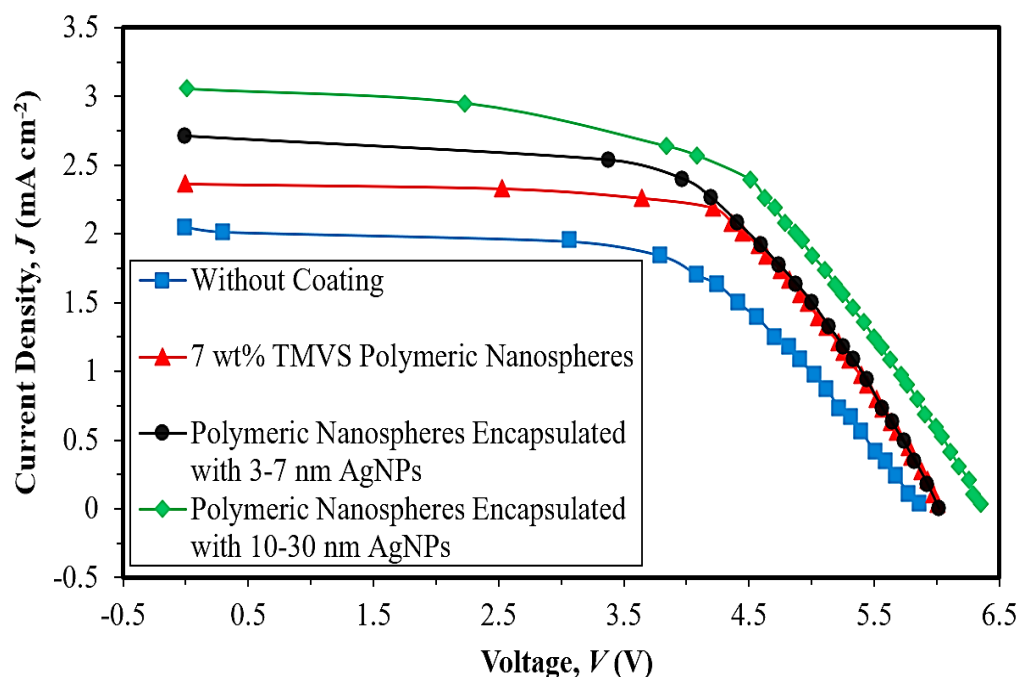


**Figure 6.5:** Relative PCE enhancement of solar modules coated with metallic-polymer nanocomposites containing different sizes of AgNPs, as a function of the concentration of AgNPs

It is depicted clearly in Figure 6.5 that the solar modules coated with P(MMA-*co*-AA-*co*-TMVS) nanospheres containing AgNPs with the size range of 10-30 nm attained consistently higher relative PCE improvement than those having AgNPs with 3-7 nm in size. This is in line with the *J-V* curves of the solar modules as shown in Figure 6.6. The *J-V* curve of the solar module deposited with P(MMA-*co*-AA-*co*-TMVS) nanospheres containing AgNPs with the size range of 10-30 nm is definitely higher than the one having AgNPs with 3-7 nm in size. This is basically due to the higher-order modes exhibited by AgNPs with larger size which increases the scattered light being forwarded into the solar module (Dai, et al., 2012). Therefore, increase the probability of exciton generation and dissociation and thus a larger current density.

**Table 6.1:** Photovoltaic parameters of the uncoated and coated solar modules, with the latter being coated with P(MMA-*co*-AA-*co*-TMVS) nanospheres encapsulated with (a) AgNPs (3-7 nm) and (b) AgNPs (10-30 nm) corresponding to AgNP concentration

AgNP concentration	Solar module sample	$J_{sc}$ (mA cm <sup>-2</sup> )	$V_{oc}$ (V)	FF (%)	PCE (%)	Relative enhancement (%)
Without coating	-	2.043	6.000	0.533	6.780	-
0 ppm	Uncoated	1.494	6.077	0.7274	6.604	41.90
	Coated	2.259	6.011	0.6901	9.371	
(a) AgNPs with a particle size range of 3-7 nm						
6.25 ppm	Uncoated	1.842	5.920	0.5641	6.151	50.28
	Coated	2.085	6.329	0.7005	9.244	
12.5 ppm	Uncoated	1.494	6.066	0.6786	6.150	51.43
	Coated	2.502	6.117	0.6085	9.313	
25.0 ppm	Uncoated	1.251	5.710	0.8513	6.081	56.55
	Coated	2.745	6.017	0.5764	9.520	
37.5 ppm	Uncoated	1.181	6.196	0.8117	5.939	49.17
	Coated	3.266	6.078	0.4463	8.859	
50.0 ppm	Uncoated	1.633	5.972	0.6342	6.185	43.83
	Coated	2.363	6.089	0.6183	8.896	
(b) AgNPs with a particle size range of 10-30 nm						
6.25 ppm	Uncoated	1.668	5.901	0.6425	6.324	58.29
	Coated	2.988	6.048	0.5537	10.01	
12.5 ppm	Uncoated	1.564	5.923	0.6866	6.360	69.97
	Coated	2.398	6.356	0.7091	10.81	
25.0 ppm	Uncoated	1.598	6.005	0.6335	6.079	68.61
	Coated	2.536	6.226	0.6491	10.25	
37.5 ppm	Uncoated	1.911	6.021	0.5677	6.532	52.66
	Coated	2.988	6.152	0.5425	9.972	
50.0 ppm	Uncoated	1.946	5.838	0.5842	6.637	46.59
	Coated	2.884	6.064	0.5563	9.729	



**Figure 6.6:**  $J$ - $V$  curves of solar modules with and without a coating of P(MMA-*co*-AA-*co*-TMVS) nanospheres with 7 wt% of TMVS, and with the polyacrylic nanospheres encapsulated with 12.5 ppm of AgNPs (10-30 nm) and 25.0 ppm of AgNPs (3-7 nm)

The optimum concentration for the AgNPs with the size range of 3-7 nm was 25.0 ppm, and it was 12.5 ppm for the AgNPs with 10-30 nm in size. The higher percentage of PCE improvement achieved was 56.6% and 73.2%, respectively. Indeed, PCE enhancement has a direct correlation with the amount of AgNPs encapsulated in a polymeric medium (Yamak, 2013). The scattering cross-section of AgNPs is associated with the concentration of the metallic nanoparticles entrapped in a polymeric medium. Consequently, this parameter is crucial in achieving the maximum quantum efficiency. However, an excessive amount of AgNPs has shown to give an adverse effect and it is detrimental to the light trapping efficiency of the photovoltaic cell. This is attributed to the fact that with an excessive amount of AgNPs, most of the incident light is reflected by the AgNPs coated on the surface of solar modules.

In addition, Derkacs et al. (2006) also reported that an excessive number of metallic nanoparticles would lead to undesirable optical loss due to electromagnetic reflection.

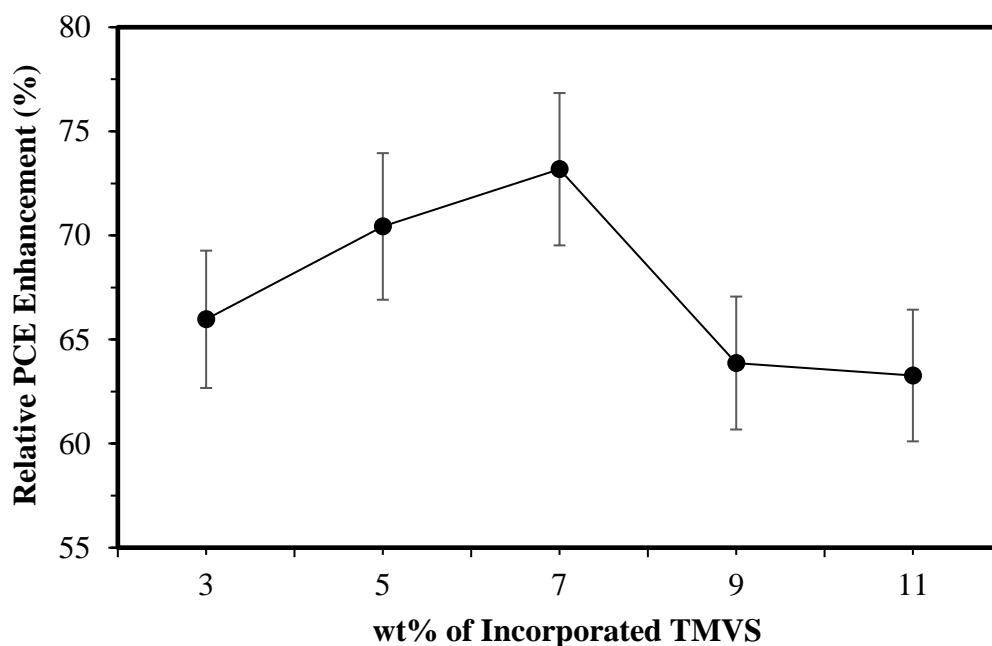
Moreover, Figure 6.6 shows that  $\alpha$ -Si solar modules deposited with the functional nanoarray of metallic-polymer nanocomposites exhibited higher short circuit current density than the solar modules that were without or with a coating of P(MMA-*co*-AA-*co*-TMVS) nanospheres alone. A higher value in current density indicates that the light trapping efficiency of the solar module has been elevated by the introduction of metallic-polymer nanocomposites on the glass surface of the solar module. Such improvement is attributed to both Rayleigh and Mie scattering mechanisms. As discussed previously, Mie scattering is predominant for the pristine polyacrylic nanospheres. Whereas, for polyacrylic nanospheres encapsulated with AgNPs which are much smaller in size than the former, it is expected that both the Rayleigh and Mie scattering mechanisms are triggered and thus lead to a significant increase in light trapping efficiency. Hence, a large fraction of incident light is scattered into the active region of the solar module thus treated, and higher PCE is obtained.

In addition, the LSPR effect of metallic nanoparticles also plays a crucial role in improving the light harvesting efficiency of the solar modules coated with the functional nanoarrays of metallic-polymer nanocomposites. The obvious PCE improvement of these solar modules (Figure 6.6) indicates that the LSPR effect couples with the forward scattering mechanisms to elevate the light trapping efficiency (Yamak, 2013). It has been reported that LSPR resonance

gives rise to a dramatic improvement in the generation of photocurrent via light scattering mechanisms of metallic nanoparticles and through the intensity increment of the strong near-field electromagnetic field as well as far-field propagating waves due to plasmon excitation (Guilatt, et al., 2009). When the natural frequency of incident light matches the oscillation frequency of the conduction electrons of AgNPs, the light radiation will then be redirected by the formation of waveguide mode and preferentially scattered by the metallic nanoparticles into the active layer of a solar module (Jeng, et al., 2015). Furthermore, the embedded AgNPs demonstrate a higher radiative efficiency across the solar spectrum (Temple, et al. 2009). They provide an efficient radial charge-carrier collection in addition to forwarding scattering effects that result in the scattering of light radiation into a distribution angle and thus increase the path length of the light within the absorbing layer (Lee, et al., 2017). Therefore, the deposition of the functional nanoarrays of metallic-polymer nanocomposite on solar modules has contributed to excellent light trapping efficiency, which subsequently leads to an increase in the generation of free carriers, thus improving the PCE of solar modules.

In order to establish a comprehensive study, various amount of TMVS was incorporated into the metallic-polymer nanocomposites, in which a fixed amount of 12.5 ppm of AgNPs with the particle size range of 10-30 nm was encapsulated. Subsequently, the functional polymeric nanocomposites were coated on the glass surface of  $\alpha$ -Si solar modules. Figure 6.7 illustrates the relative PCE enhancement of the surface-modified solar modules corresponding to the amount of TMVS incorporated. The photovoltaic

parameters of both the uncoated and coated solar modules are summarized in Table 6.2. The results obtained show a similar trend to P(MMA-*co*-AA-*co*-TMVS) nanospheres that were without AgNPs (Figure 5.12) which are discussed in Chapter 5.



**Figure 6.7:** Relative PCE enhancement of solar modules deposited with P(MMA-*co*-AA-*co*-TMVS) nanospheres encapsulated with 12.5 ppm of AgNPs with the particle size range of 10-30 nm by varying the wt% of TMVS in the copolymer

Similarly, the relative PCE enhancement of the surface-modified solar module increases with the concentration of TMVS incorporated until it reaches the peak at 73.2% with 7 wt% of TMVS. As aforementioned, a higher concentration of SCA enables the generation of an orderly array which is closely packed. The array serves as an intermediate layer with a graded refractive index which is capable in elevating the light trapping efficiency by increasing the light transmission and decreasing the light surface reflection of



the glass panel on the solar cell. Nonetheless, an excessive amount of TMVS was found detrimental to light transmission. The formation of a thicker layer of nanoarray blocks a fraction of the incident light, and thus reduce the absorption of photons and generation of free carriers. The relative PCE enhancement of the solar modules has dropped below 64.0% when they were treated with the metallic-polymer nanocomposites with 9 and 11 wt% of TMVS.

**Table 6.2:** Photovoltaic parameters of the uncoated and coated solar modules, with the latter being deposited with P(MMA-*co*-AA-*co*-TMVS) nanospheres containing different wt% of TMVS and encapsulated with 12.5 ppm of AgNPs with the particle size range of 10-30 nm

<b>Amount of TMVS</b>	<b>Solar module sample</b>	<b><math>J_{sc}</math> (mA cm<sup>-2</sup>)</b>	<b><math>V_{oc}</math> (V)</b>	<b>FF (%)</b>	<b>PCE (%)</b>	<b>Relative enhancement (%)</b>
<b>3 wt%</b>	Uncoated	2.085	5.877	0.5416	6.636	65.91
<b>TMVS</b>	Coated	3.023	6.004	0.6069	11.01	
<b>5 wt%</b>	Uncoated	2.050	5.770	0.5464	6.463	70.35
<b>TMVS</b>	Coated	3.023	6.097	0.5976	11.01	
<b>7 wt%</b>	Uncoated	1.598	6.005	0.6480	6.218	73.21
<b>TMVS</b>	Coated	2.954	6.004	0.6074	10.77	
<b>9 wt%</b>	Uncoated	1.911	5.784	0.6004	6.636	63.95
<b>TMVS</b>	Coated	3.197	5.980	0.5689	10.88	
<b>11 wt%</b>	Uncoated	1.911	5.655	0.6302	6.810	63.29
<b>TMVS</b>	Coated	3.023	6.039	0.6091	11.12	

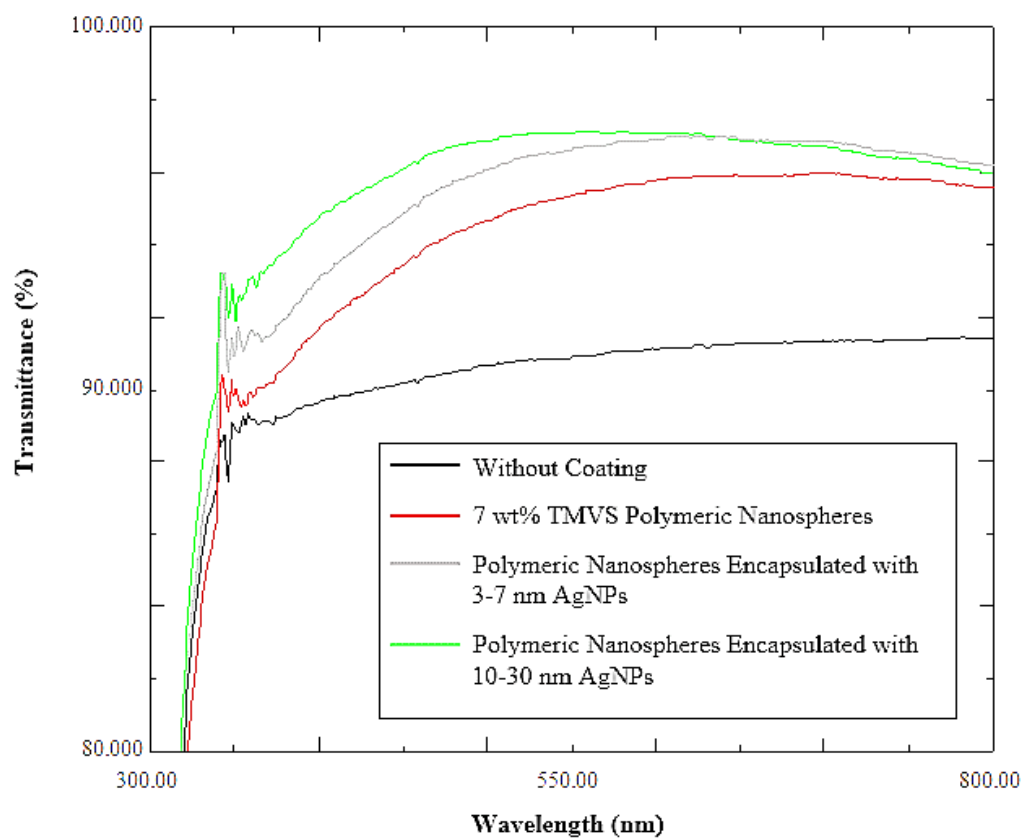
The results prove that such technique of depositing an anti-reflective functional nanoarray of metallic-polymer nanocomposites on the glass surface of  $\alpha$ -Si solar modules to enhance their PCE is a feasible approach (Lee, et al., 2021).

### 6.2.2 Optical transmission of the polyacrylic coating

The enhancement of the light harvesting efficiency is further evidenced and consolidated by the high UV-Vis light transmittance of the metallic-polymer nanocomposites (Figure 6.8 and Table 6.3). The metallic-polymer nanocomposites containing 12.5 ppm of AgNPs with the particle size range of 10-30 nm has attained a remarkable transmittance of 97.13%; while the polymeric nanospheres encapsulated with 25 ppm of AgNPs with the particle size range of 3-7nm has a slightly lower transmittance of 96.97%. The polyacrylic nanospheres without AgNPs demonstrated a lower transmittance of 96.00%, while the uncoated sample has the lowest light transmittance of 91.44%. It can be clearly seen that the trend observed in UV-Vis spectroscopy correlates well with the PCE results as illustrated in Figure 6.6.

**Table 6.3:** UV-Vis transmittance of the uncoated and coated glass substrates, with the latter being coated with P(MMA-*co*-AA-*co*-TMVS) nanospheres with 7 wt% of TMVS, and with the polyacrylic nanospheres encapsulated with 12.5 ppm of 10-30 nm AgNPs and 25.0 ppm of 3-7 nm AgNPs respectively

Sample	Transmittance (%)
Without coating	91.44
Polyacrylic nanospheres with 7 wt% TMVS	96.00
Polyacrylic nanospheres encapsulated with 3-7 nm AgNPs	96.97
Polyacrylic nanospheres encapsulated with 10-30 nm AgNPs	97.13



**Figure 6.8:** UV-Vis spectra of glass substrates with and without a coating of P(MMA-*co*-AA-*co*-TMVS) nanospheres with 7 wt% of TMVS, and with the polyacrylic nanospheres encapsulated with 12.5 ppm of AgNPs (10-30 nm) and 25.0 ppm of AgNPs (3-7 nm) respectively

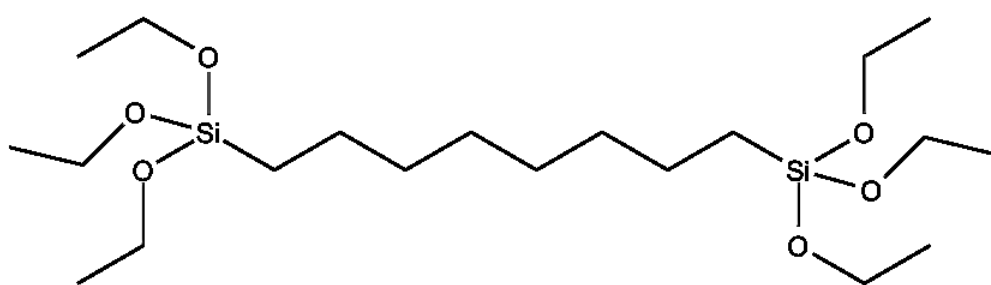
## CHAPTER 7

### GENERATION OF A HYDROPHOBIC SURFACE USING A MIXTURE OF A DIPODAL AND A FLUOROALKYL SILANES

#### 7.1 Elevation of adhesion strength of ARC system utilizing a dipodal silane

A dipodal silane is a bis-organofunctional silane compound that possesses two organosilane moieties in the molecule. Based on the equilibrium constant of dissociation of siloxane (Si-O-Si) bond to silanol (Si-OH) bond, dipodal functional silane acts as a promising adhesion promoter with up to 10000 times higher hydrolytic stability compared to conventional silane. This is owing to their capability in forming six covalent bonds to couple with the surface of a substrate. Therefore, dipodal silane exhibits higher efficiency to form oxane bonds on a less reactive surface due to its distinctive advantage of offering extra points for surface attachment. The hydrolytic stability, shelf life, substrate bonding durability, as well as mechanical and adhesive strengths of the coupling system, can significantly improve wettability and crosslink density at interphase. Dipodal silane demonstrates superior protection to resist deterioration by the intrusion of water between an organic compound and an inorganic substrate. This is because the dipodal material is able to extend from the surface and thus providing superior resistance to the hydrolysis process (Singh, et al., 2014).

In this study, a dipodal silane, namely 1,8-bis(triethoxysilyl)octane (BTO) was coated on the glass surface of an  $\alpha$ -Si solar module, which had been pre-coated with P(MMA-*co*-AA-*co*-TMVS) nanospheres containing 7 wt% of TMVS and 12.5 ppm of AgNPs with 10-30 nm in size. The chemical structure of BTO silane is shown in Figure 7.1. The dipodal silane is chemically attached to the surface of the pre-coated solar module by forming siloxane bonds with free hydroxyl groups present on the glass surface and with free silanol groups of TMVS on the polyacrylic nanospheres, by means of silanation reaction. The silane coating can serve as a protective layer to shield the nanoarray of AgNPs-polyacrylate nanocomposites from the destruction caused by the weathering processes. The layer of BTO enhances the overall adhesion strength of the coupling system via improved crosslink density and bond durability, thereby resulting in higher resistance toward extreme environmental conditions. Hence, the lifetime of an array of metallic-polymer nanocomposites on a glass substrate could be extended significantly.



**Figure 7.1:** The chemical structure of 1,8-bis(triethoxysilyl)octane dipodal silane

The dipodal silane was pre-hydrolyzed in an acidic medium before it was applied on a glass substrate. As reported by Paquet et al (2012), the relative ratio of solvent composition will influence the reactivity and reaction yield of the system by altering the rate of hydrolysis and self-condensation of silane. The relative water ratio should be lower than the number of hydrolyzable groups, with a maximum of 20 w/w%. Therefore, BTO was prepared in a solvent mixture of ethanol and water with a solvent ratio of 9:1 in this research work. Ethanol was employed to improve the miscibility between silane and water, while water was used to accelerate the hydrolysis reaction. Moreover, the pH of the solvent mixture was adjusted to about 4 with acetic acid. This is because the acidic condition favours the acceleration of the hydrolysis reaction and prevents precipitation and formation of the larger structures. In addition, the hydrolyzed silane is protected against condensation as well as against the formation of silanol-bearing derivatives in acidic pH.

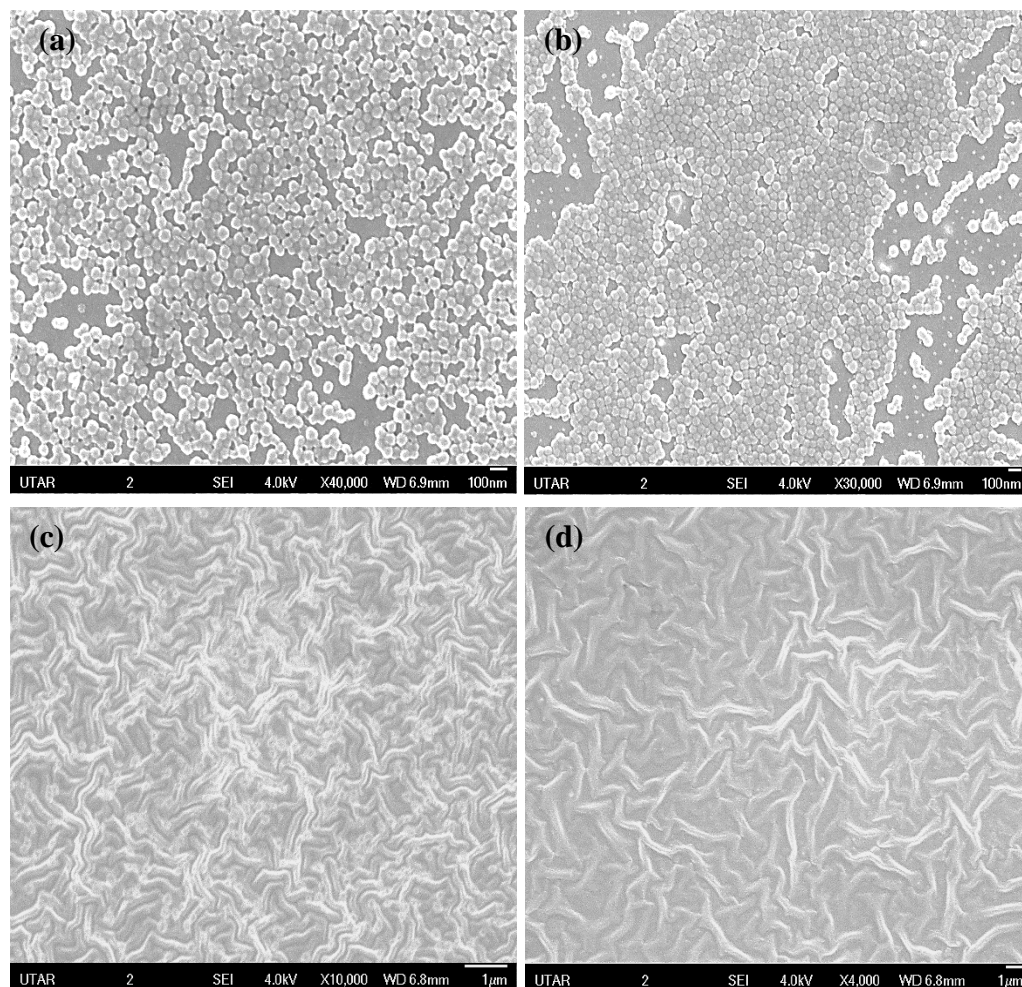
#### **7.1.1 Effect of concentration of BTO silane**

The pre-hydrolyzed BTO silane with various concentrations (0.1 to 5.0 v/v%) was deposited on the surface of the pre-coated nanoarray of metallic-polymer nanocomposites through an immersion coating method. The surface that had been modified chemically was then characterized by the following analyses: FESEM for surface morphological study; UV-Vis spectroscopy for light transmission examination, water contact angle analysis and water droplet test for surface wettability analysis. A programmable direct circuit electronic load LIV tester (AM 1.5 solar simulator) was used to determine the electrical

parameters and the output power of solar modules. Furthermore, a peeling test was carried out in conjunction with an electrical measurement to assess the adhesion strength and bond durability of the silane protected coating as a function of the concentration of dipodal functional silane.

#### **7.1.1.1 Surface morphological characteristics of the BTO silane coating**

After being chemically modified with different concentrations of BTO silane, the substrate was subsequently subjected to FESEM scanning. Figure 7.2 illustrates the FESEM images of the treated substrates. It can be observed that the spherical shaped metallic-polymer nanocomposite were covered by a thin layer of BTO when the silane concentrations were relatively low, i.e. between 0.1 v/v% and 1.0 v/v%. This amount of BTO was just sufficient to cover all the polyacrylic nanospheres. This indicates that the hydrolyzed BTO silane has reacted with the free silanol bonds of TMVS present in the metallic-polymer nanocomposite and adheres to the surface of the nanospheres. It is believed that self-condensation between the BTO silane molecules has also occurred as the silane has seemingly formed a layer of thin film on the polymeric nanospheres and joined the nanoparticles together.

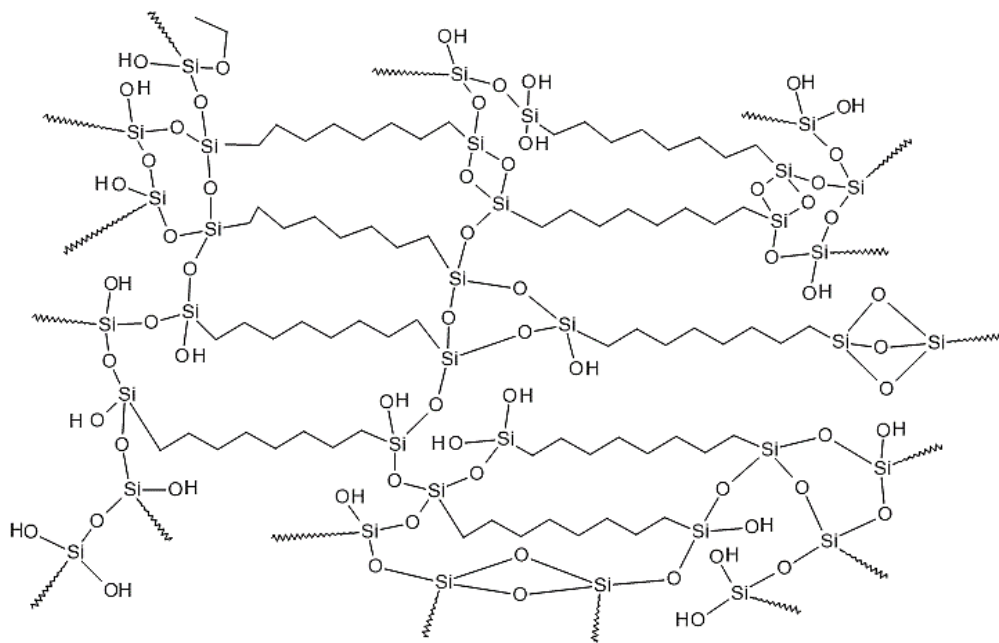


**Figure 7.2:** FESEM images of glass substrates pre-coated with metallic-polymer nanocomposites and further chemically surface modified with various concentration of BTO silane: (a) 0.1 v/v%, (b) 1.0 v/v%, (c) 3.0 v/v% and (d) 5.0 v/v%, with a magnification of  $\times 40000$ ,  $\times 30000$ ,  $\times 10000$  and  $\times 4000$  respectively

On the other hand, Figures 7.2 (c) and (d) distinctly reveal that the nanoarray of metallic-polymer nanocomposites was covered underneath a thick silane layer when the concentration of BTO was increased to 3 v/v% and above. As a result, the dipodal silane layer acts as a protective shield for the composite nanoarray to protect them from harsh environmental conditions. The durability of the ARC will be improved at a higher dipodal silane concentration owing to the formation of more oxane bonds between the ethoxysilyl functional groups



present in the BTO molecules. Besides, with the hydrophobic octane backbone in the molecules, they could resist water attack by forming a crosslinked network, as illustrated in Figure 7.3.

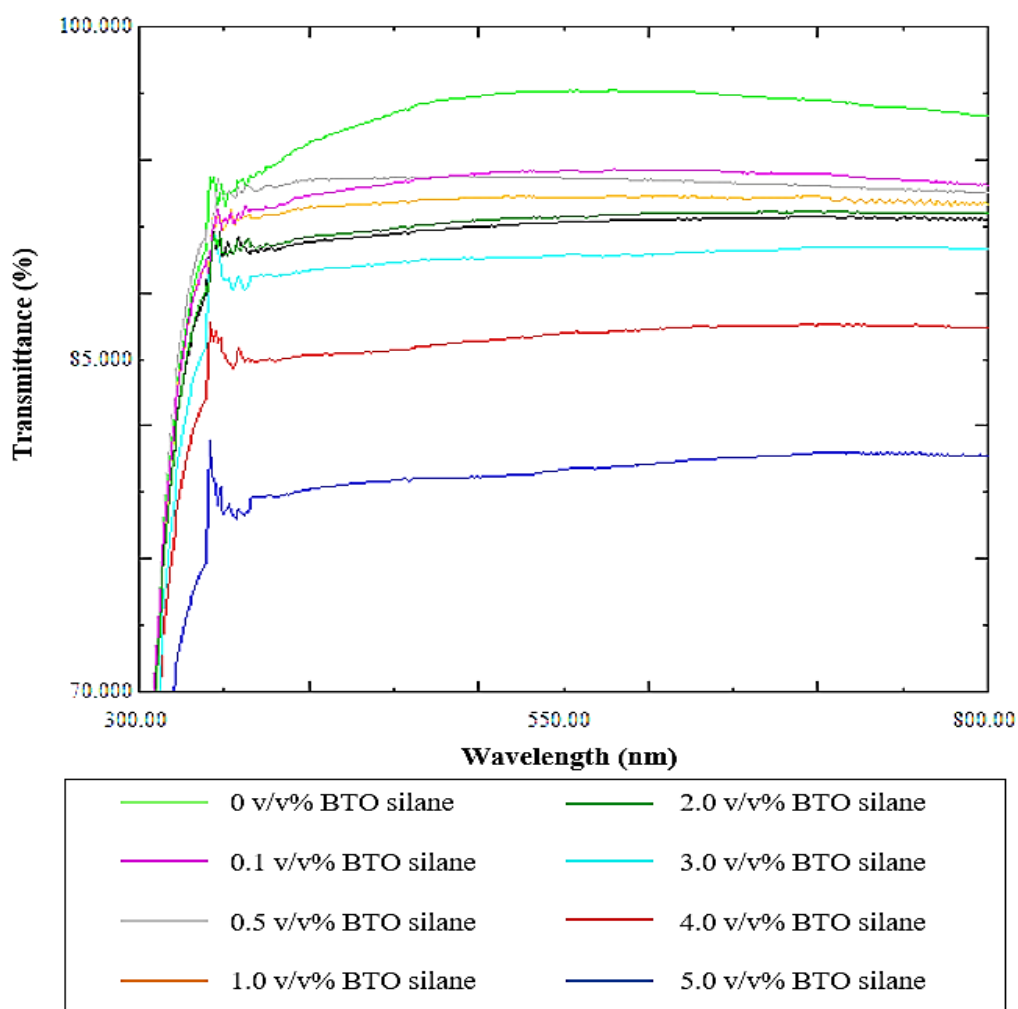


**Figure 7.3:** Schematic representation of a BTO silane crosslinked network

#### 7.1.1.2 Optical transmission of the BTO silane coating

Subsequently, BTO silane with various concentrations was used to chemically modify a surface of a glass substrate that had been pre-coated with an array of P(MMA-*co*-AA-*co*-TMVS) nanospheres incorporated with 7 wt% of TMVS and encapsulated with 12.5 ppm of AgNPs which were 10-30 nm in size. It is necessary to conduct an optical analysis on the glass substrate because a piece of protective Si glass is always laminated on a solar module. The light transmission of this glass is crucial to the light trapping efficiency of solar modules (Lee, et al., 2021). The UV-Vis spectra of the treated glass substrate

are shown in Figure 7.4. The detailed transmittance readings of the samples obtained from UV-Vis spectroscopy are summarized in Table 7.1. The acquired results portray that the light transmittance of the treated glass substrate declined from 97.13% to 93.57% after it had been chemically modified with 0.1 v/v% of BTO. This might be due to the enfoldment of the BTO silane layer which has certainly impacted the light trapping efficiency of the coating system. Thereby, a fraction of light radiation is possibly blocked by the silane layer and thus reduces the light transmission.



**Figure 7.4:** UV-Vis spectra of glass substrates pre-coated with metallic-polymer nanocomposites and further chemically modified with various concentrations of the BTO silane

**Table 7.1:** Light transmittance of glass substrates pre-coated with metallic-polymer nanocomposites and further chemically modified with various concentrations of the BTO silane

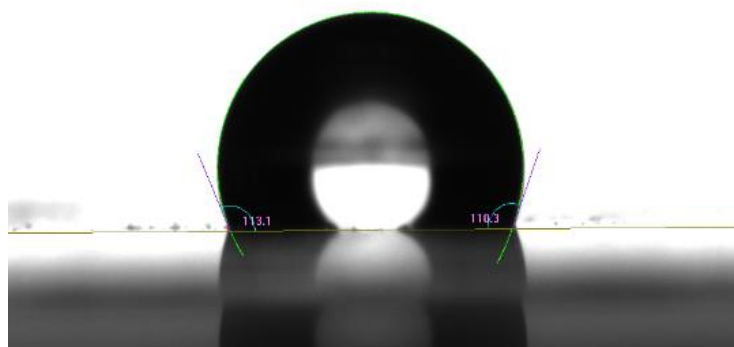
<b>Concentration of BTO silane</b>	<b>Transmittance (%)</b>
<b>0 v/v% BTO silane</b>	97.13
<b>0.1 v/v% BTO silane</b>	93.57
<b>0.5 v/v% BTO silane</b>	93.25
<b>1.0 v/v% BTO silane</b>	92.37
<b>2.0 v/v% BTO silane</b>	91.65
<b>3.0 v/v% BTO silane</b>	90.63
<b>4.0 v/v% BTO silane</b>	86.62
<b>5.0 v/v% BTO silane</b>	81.34

The light transmittance was further reduced to 81.34% when the concentration of BTO was increased to 5.0 v/v%. A higher concentration of BTO has increased the silane film thickness until it fully enclosed the polyacrylic nanospheres. As a result, the light transmission of the treated glass substrate decreased significantly. The outcomes of UV-Vis spectroscopy are evidenced and consolidated by the FESEM images of the treated glass substrates (Figure 7.2). The light radiation is unable to transmit across the thicker silane layer, so lesser incident light is detected by the detector of the UV-Vis spectrophotometer, and thus lower transmittance is obtained. Xu and He (2012) also reported a similar trend that the light transmittance of coated glass substrates decreased with the increasing concentration of SCA. This is mainly due to an increase in light scattering, thereby giving rise to lower transparency. The reduction of light transmission will lead to a negative consequence of depletion in the light harvesting efficiency of a solar module because fewer photons are absorbed into the active region of the photovoltaic device. The

results obtained from UV-Vis spectroscopy were further confirmed by the electrical measurement of solar modules which will be discussed in section 7.1.1.4.







#### **7.1.1.3 Surface wettability of the BTO silane coating**

The glass substrate pre-coated with P(MMA-*co*-AA-*co*-TMVS) nanospheres containing 12.5 ppm of AgNPs with 10-30 nm in size was further chemically surface-modified with various concentrations of BTO silane. The surface wettability of BTO silane coating was characterized using a contact angle analyzer and via the water droplet test. To obtain the WCA value, the image of a deionized water droplet formed on the surface of a treated glass substrate was fitted in the Laplace-Young model and captured by a contact angle analyzer as illustrated in Figure 7.5 (Lee, et al., 2021). In this case, only the WCA of pre-coated glass substrate which had been further modified with 1.0 v/v% of BTO silane was determined. This is because 1.0 v/v% of BTO has been found to induce stronger adhesion durability with higher mechanical resistance while maintaining a remarkable light trapping efficiency. These results will be discussed in detail in the next section. Figure 7.6 shows the photographs of a water droplet formed on the surface of a glass substrate pre-coated with metallic-polymer nanocomposites and subsequently modified with various concentrations of BTO.



**Figure 7.5:** The image of a water droplet formed on the surface of a treated glass substrate which was captured by the contact angle analyzer fitted in the Laplace-Young model (Lee, et al., 2021)

It was found that BTO with a concentration of 1.0 v/v% induced an average WCA of  $103.2^\circ$  compared to a WCA of  $52.0^\circ$  when the surface was coated with P(MMA-*co*-AA) nanospheres containing 7 wt% of TMVS, which reveals that the former has better hydrophobicity and lower surface energy. This is mainly attributed to the hydrophobic effect of the octane chains present in BTO. According to Bulliard et al. (2010), an alkylsilane molecule with a longer hydrocarbon chain would provide higher hydrophobicity. After the formation of a tighter siloxane crosslinked network at the interphase region by means of silanation of free silanol functional groups, the octane chains of BTO molecules will be oriented outward. As a result, the degree of surface wettability decreases with an increase in WCA value. The results obtained from contact angle analysis are well correlated with the water droplet test. The water droplet formed on the surface of the pre-coated glass substrate with further surface modification with 1.0 v/v% of BTO was found more spherical in shape compared to those treated with lower concentrations of BTO (Figure 7.6).

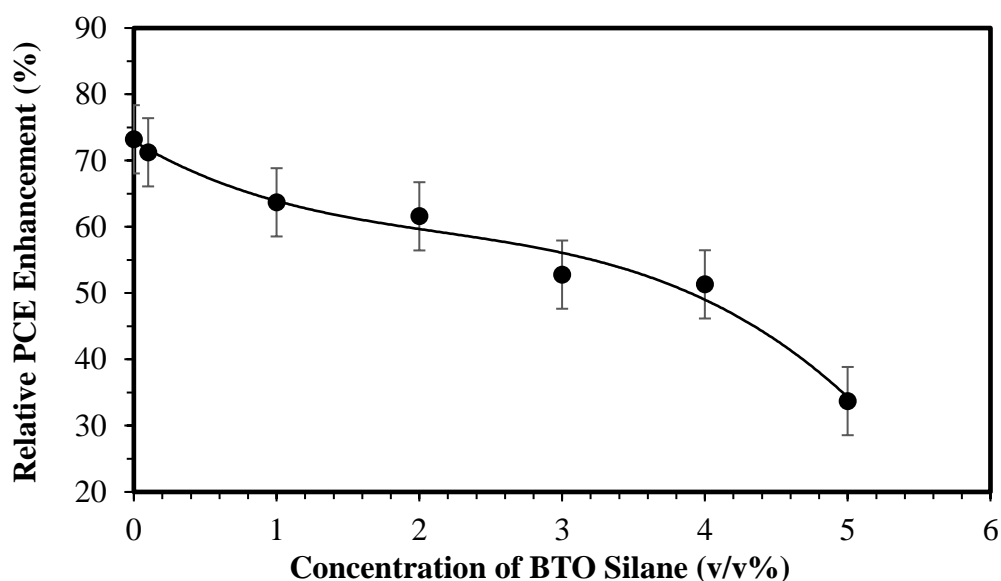
Substrate sample	Water droplet image
0.1 v/v% BTO silane	
0.5 v/v% BTO silane	
1.0 v/v% BTO silane	
3.0 v/v% BTO silane	
4.0 v/v% BTO silane	
5.0 v/v% BTO silane	

**Figure 7.6:** The images of a water droplet formed on the surface of a glass substrate pre-coated with metallic-polymer nanocomposites and subsequently modified with various concentrations of BTO

Furthermore, the bouncing effect of water droplets increased with the concentration of BTO silane. At 5 v/v% of BTO, the water droplet formed has rebounded into a perfect spherical shape. This evinces that an excellent hydrophobic surface with a higher value of WCA can be created with higher concentrations of BTO. The film thickness also increases with the concentration of BTO. As a result, it increases surface roughness and reduces surface wettability. According to Cassie-Baxter's model, the rough structured silane layer with low surface energy restricts the accessibility of water molecules to the bonded siloxane coupling network at the interphase region, leading to remarkable water resistance and hydrophobicity (Vidal, et al., 2019). Hence, the overall adhesion durability of the coupling system is expected to increase.

#### **7.1.1.4 Electrical measurement of solar modules**

The effect of the concentration of BTO silane on the light trapping efficiency of  $\alpha$ -Si solar modules was investigated, by self-assembling the dipodal silane on the glass surface of a solar module which had been pre-coated with P(MMA-*co*-AA-*co*-TMVS) nanospheres that containing 7 wt% of TMVS and 12.5 ppm of AgNPs with 10-30 nm in size. The electrical measurement of the solar modules before and after the surface modification was conducted using an AM 1.5 solar simulator. Figure 7.7 illustrates the relative improvement in PCE of the surface-treated solar modules as a function of the concentration of BTO silane. Moreover, the acquired photovoltaic parameters for both the untreated and treated solar modules are summarized in Table 7.2.



**Figure 7.7:** Relative PCE enhancement of solar modules pre-coated with metallic-polymer nanocomposites followed by surface modified with various concentrations of BTO silane

The presented results depict that the relative PCE enhancement of the solar modules treated with 0.1 v/v% of BTO silane had decreased slightly from 73.21% to 71.25% after surface modification. This is mainly attributed to the enfoldment of the dipodal silane layer which has certainly influenced the anti-reflective feature of metallic-polymer nanocomposites by decreasing their light transmission. Furthermore, the relative PCE improvement of the treated solar modules was further reduced from 71.25% to 51.32% with an increasing concentration of BTO from 0.1 v/v% to 4.0 v/v%. There was a declining slope that occurred in the plotted graph (Figure 7.7). The relative enhancement in PCE of the chemically surface-modified solar module was more adversely reduced to 33.71% when 5 v/v% of BTO was applied. The silane film thickness exhibits a strong correlation with the concentration of BTO silane. A higher concentration of BTO has increased the film thickness via the generation of a silane multilayer. This has then led to an adverse effect of

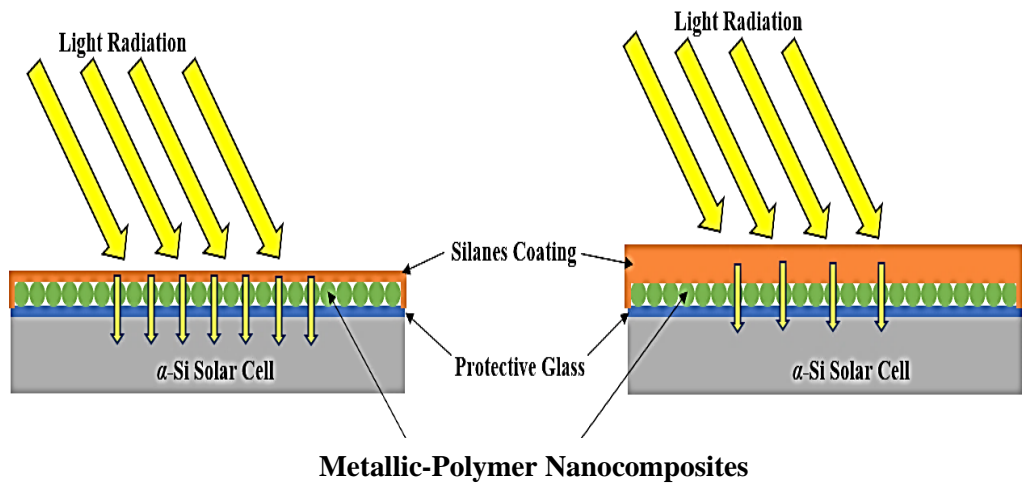


blocking the light radiation to be transmitted across the silane layer and thus detrimental to both the radiative efficiency of the metallic-polymer nanocomposites and the quantum efficiency of the solar module. The elaborated inference is consolidated by the morphological images obtained from FESEM (Figure 7.2). Lower light transmittance has eventually caused a decline in light scattering and photon absorption within the active region of the photovoltaic device. Hence, lesser free mobile electrons are produced and lower PCE is yielded.

**Table 7.2:** Photovoltaic parameters of both the untreated and treated solar modules, with the latter pre-coated with metallic-polymer nanocomposites and subsequently chemically surface modified with various concentrations of BTO silane

<b>BTO concentration</b>	<b>Solar module sample</b>	<b><math>J_{sc}</math> (mA cm<sup>-2</sup>)</b>	<b><math>V_{oc}</math> (V)</b>	<b>FF (%)</b>	<b>PCE (%)</b>	<b>Relative enhancement (%)</b>
<b>0 v/v%</b>	Untreated	1.598	6.005	0.6480	6.218	73.21
	Treated	2.954	6.004	0.6074	10.77	
<b>0.1 v/v%</b>	Untreated	1.807	5.835	0.5965	6.289	71.25
	Treated	3.232	6.106	0.5459	10.77	
<b>1.0 v/v%</b>	Untreated	1.807	5.880	0.6066	6.445	63.07
	Treated	2.745	6.157	0.6217	10.51	
<b>2.0 v/v%</b>	Untreated	2.015	5.750	0.5667	6.566	61.59
	Treated	2.954	6.072	0.5929	10.63	
<b>3.0 v/v%</b>	Untreated	2.015	5.750	0.5457	6.323	52.79
	Treated	2.537	5.992	0.6355	9.661	
<b>4.0 v/v%</b>	Untreated	1.842	5.631	0.6132	6.360	51.32
	Treated	2.571	6.024	0.6214	9.624	
<b>5.0 v/v%</b>	Untreated	2.154	5.871	0.5055	6.393	33.71
	Treated	2.328	6.045	0.6074	8.548	

However, the incident light is yet concurrently being scattered and coupled into the absorbing layer of the solar module by the superior functional nanoarray of metallic-polymer nanocomposites via its extraordinary anti-reflective property and scattering mechanisms in conjunction with the accentuated LSPR effect, as illustrated in Figure 7.8. This increases the probability of exciton generation and dissociation and thus a larger current density. Therefore, a high relative PCE enhancement of 51.32% was still attained by the pre-coated solar module treated with 4 v/v% of BTO. The results obtained from electrical measurement are well correlated with the transmission outcomes acquired from UV-Vis spectroscopy (Figure 7.4).



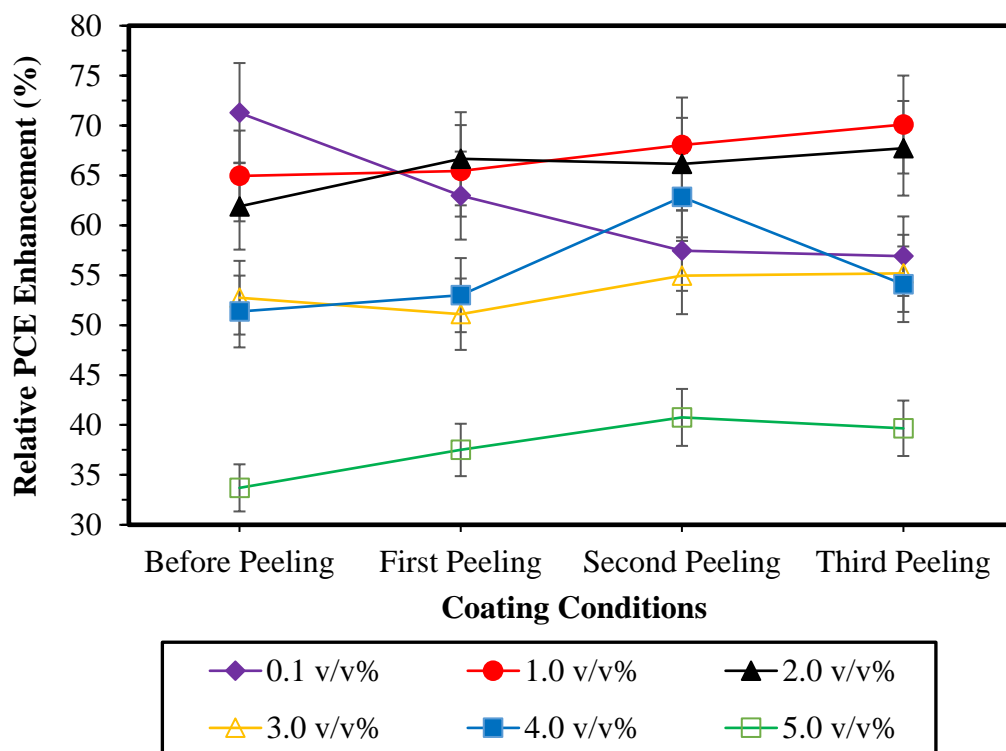
**Figure 7.8:** Schematic diagram of light trapping of an  $\alpha$ -Si solar module pre-coated with metallic-polymer nanocomposites and further chemically surface modified using different concentrations of BTO silane

### 7.1.1.5 Adhesive durability of the BTO silane coating

A peeling test was carried out using pressure-sensitive tape to evaluate the effect of the concentration of BTO silane on the adhesion strength of the coupling system. In this case, the glass surface of the solar module that had been pre-coated with metallic-polymer nanocomposites was further chemically modified with different concentrations of BTO silane through the immersion coating method. Subsequently, three peeling cycles were conducted and the output power of the solar modules after each cycle of the peeling process was measured using an AM 1.5 solar simulator (Lee, et al., 2021). The acquired results are summarized and tabulated in Table 7.3. Meanwhile, Figure 7.9 shows the relative enhancement in PCE of the chemically surface-modified solar module before and after several peeling cycles.

**Table 7.3:** Output power measurement of both the uncoated and coated solar modules, with the latter pre-coated with metallic-polymer nanocomposites and further chemically surface modified with various concentrations of BTO silane as a function of the coating conditions

Coating conditions	Output Power Measurement (W)					
	Concentration of BTO Silane (v/v%)					
	0.1	1.0	2.0	3.0	4.0	5.0
<b>Uncoated</b>	0.181	0.194	0.189	0.182	0.183	0.184
<b>Coated</b>	0.310	0.320	0.306	0.278	0.277	0.246
<b>1<sup>st</sup> Peeling</b>	0.295	0.321	0.315	0.275	0.280	0.253
<b>2<sup>nd</sup> Peeling</b>	0.285	0.326	0.314	0.282	0.298	0.259
<b>3<sup>rd</sup> Peeling</b>	0.284	0.330	0.317	0.284	0.282	0.257



**Figure 7.9:** Relative enhancement in PCE of solar modules pre-coated with metallic-polymer nanocomposite and further chemically surface modified with various concentrations of dipodal silane corresponding to the coating conditions

The reported results portray that a higher concentration of BTO silane has induced stronger mechanical strength with prominent bond adhesion durability. From the plotted graph shown in Figure 7.9, it illustrates that the relative PCE enhancement of the treated solar module was increased gradually after each cycle of peeling when 1.0 v/v% and above of BTO was utilized. Among them, 1.0 v/v% of BTO silane showed delighted results of higher relative PCE enhancement of 70.1% after three peeling cycles. The results also indicate that with this amount of BTO, the adhesive and mechanical strengths of the coating system had been reinforced. This is owing to the elimination of deficient physisorbed dipodal silane layer which has then reduced the silane film

thickness. The thinner chemisorbed silane layer with remarkable adhesive durability could withstand high mechanical abrasion stress and peeling forces, meanwhile, allowing a large fraction of light radiation to be directed into the active region of a solar module. Therefore, the light harvesting efficiency, as well as the quantum efficiency of the solar module, were increased (Lee, et al., 2021). In view of that, 1.0 v/v% of BTO was adopted in further study as it had demonstrated an optimized trade-off between the light trapping efficiency of the treated solar module and the adhesion strength of the coupling system, which exhibited a strong correlation with the silane film thickness.

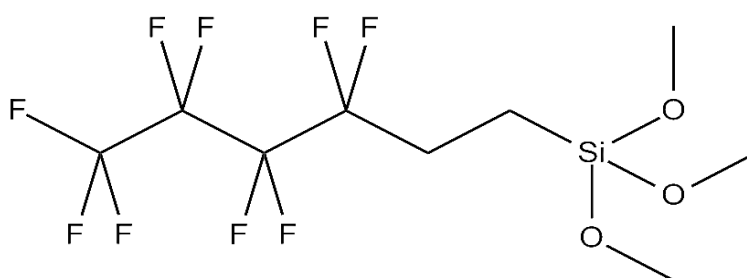
After the third peeling cycle, the film with 5 v/v% of BTO exhibited the least decline in relative PCE enhancement. This is attributed to the formation of a thicker silane network layer via the silanation of the silanol functional groups that are present in the bis-silane molecules which offer extra points for bonding. A thicker dipodal silane film could serve as an impressive protective layer with extraordinary adhesive strength to protect the array of metallic-polymer nanocomposites from being peeled off from the surface of a substrate. Nevertheless, a thicker dipodal silane layer has the adverse effect of blocking the light radiation from being transmitted into the active layer of the solar modules, thereby diminishing the light harvesting efficiency. In addition, an excessive amount of dipodal silane would also form a weak physisorbed silane layer that might act as a defect and cause a lubricant effect, which possibly reduces surface hydrophobicity and water resistance.

It was found that the silane film with 0.1 v/v% of BTO rendered the lowest mechanical stability. This was demonstrated by the highest decline in PCE enhancement of the treated solar module from 71.3% to 55.3% after three peeling cycles. This could be due to the disruption and removal of the array of metallic-polymer nanocomposites from the glass surface of the solar module by the pulling forces of a pressure adhesive tape (Lee, et al., 2021). The peeling process has caused the diminishment of the light trapping features of the metallic-polymer nanocomposites arrays. Consequently, a low PCE is yielded. This evinces the elaborated inference that BTO at 0.1 v/v% is unable to endure strong mechanical peeling stress.

## **7.2 Generation of a highly hydrophobic surface via surface modification using a mixture of dipodal and fluoroalkyl silanes**

BTO silane with an optimum concentration of 1.0 v/v% was proven to be efficient in elevating the adhesion and mechanical strengths of the coating system. This is due to the formation of a densely crosslinking network and durable covalent bonds at the interphases between the silane film, the polymeric nanoarray and the glass substrate. Although the dipodal silane promotes higher crosslink density with better hydrolytic stability as compared to monosilane, the siloxane bonds (Si-O-Si) might still be re-hydrolyzed to silanol bonds (Si-OH) in the presence of moisture, since silanation reaction is a reversible reaction. In addition, the solar panels are generally installed outdoors and exposed to high humidity environment, especially during rainy days. Therefore, it is necessary to create a silane film with excellent hydrophobic nature to protect the pre-coated array of metallic-polymer nanocomposites on

the glass surface of a solar module. In this study, a fluoroalkyl silane (FAS) with low surface energy, namely nonafluorohexyltrimethoxysilane was mixed with BTO and subsequently coated onto the surface of a pre-coated solar module. The chemical structure of nonafluorohexyltrimethoxysilane is shown in Figure 7.10.



**Figure 7.10:** The chemical structure of nonafluorohexyltrimethoxysilane

FAS is a non-functional organosilane coupling agent that is used to reduce the surface energy and surface wettability of a substrate without imparting any chemical reactivity (Liu, et al., 2015). The non-polar organic substituents, specifically the fluorine elements, present in the FAS molecule induce a more subtle distinction of the hydrophobic entity that can elevate the surface water repellence and shield the surface from water interaction. In this case, the FAS was mixed with BTO silane in an acidic medium (a mixture of ethanol and water with a solvent ratio of 9:1 at which the pH value was adjusted to 4-5 using acetic acid) for a duration of 45 minutes. The concentration of BTO was fixed at 1.0 v/v%.

The silane mixture was then coated onto the surface of a pre-coated glass substrate via the immersion coating method with a dwell time of 45 minutes. It was expected that the silane coating would create a highly hydrophobic surface with remarkable water repelling features and self-cleaning properties. In conjunction with that, the pollutants and dust particles that stick on the film surface would be collected by the water droplets formed on it and rolled off from the surface, thereby resulting in self-cleaning. Moreover, the introduction of FAS would increase the surface hydrophobicity and improve the water resistance of the silane film. According to Bulliard et al. (2010), the hydrophobic effect of a non-polar substitution exhibits a strong correlation with the free energy of hydrocarbon molecules transferring from the aqueous phase to the hydrocarbon phase.

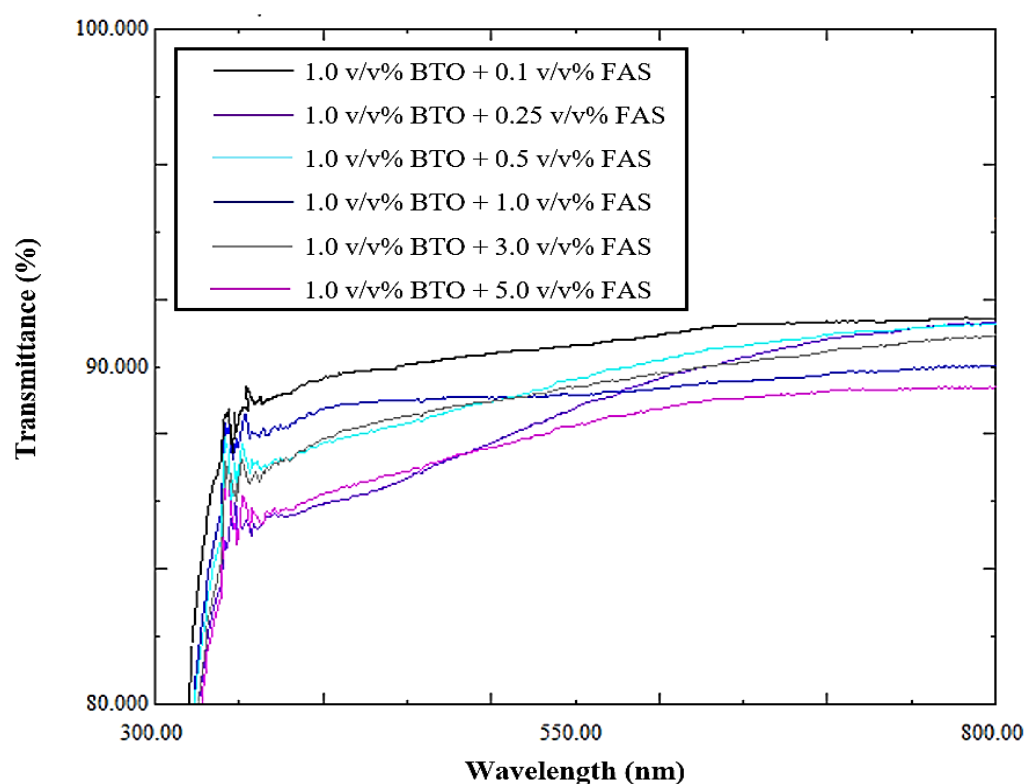
#### **7.2.1 Effect of concentration of fluoroalkyl silane**

The mixture of BTO and FAS was pre-hydrolyzed and subsequently deposited on a glass substrate that had been pre-coated with an array of P(MMA-*co*-AA-*co*-TMVS) nanospheres with 12.5 ppm of AgNPs which were 10-30 nm in size. The concentration of BTO silane was fixed at 1.0 v/v% while the concentration of FAS varied from 0.1 to 5.0 v/v%. The effects of the concentration of FAS on the light transmittance, surface wetting behaviour and light harvesting efficiency of the silane coatings were accessed using UV-Vis spectroscopy, water droplet analysis and electrical measurement of solar modules.



### 7.2.1.1 Optical transmission of the silane mixture coating

The glass substrate pre-coated with metallic-polymer nanocomposites was further coated with either the FAS or a mixture of BTO and FAS. Subsequently, it was subjected to light transmittance examination by employing a UV-Vis spectrophotometer. Figure 7.11 illustrates the UV-Vis spectra of the treated glass substrate as a function of the concentration of FAS. The light transmittance results obtained from UV-Vis spectroscopy are summarized in Table 7.4.

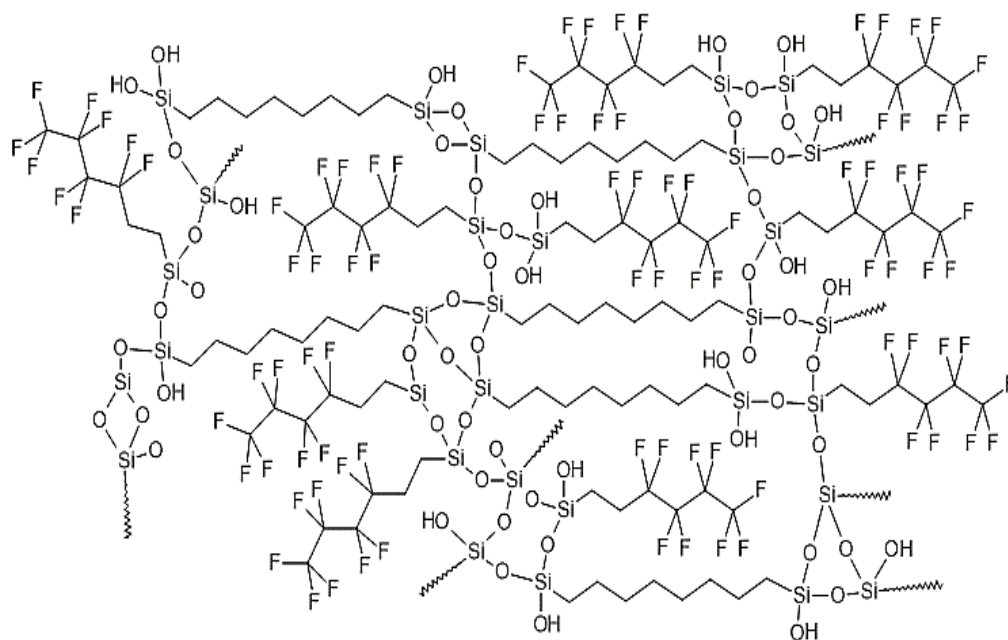


**Figure 7.11:** UV-Vis spectra of glass substrates which had been pre-coated with metallic-polymer nanocomposites and followed by further surface modification with a mixture of 1.0 v/v% of BTO with various concentrations of FAS

Unlike the BTO silane (as discussed in section 7.1.1.2), a higher concentration of FAS has demonstrated a very little adverse effect on light transmission. The light transmittance of the treated glass substrate decreased slightly from 91.39% to 89.38% when the concentration of FAS increased from 0.1 to 5.0 v/v%. Besides, the introduction of FAS has slightly reduced the light transmission of that with 1.0 v/v% of BTO (92.37%). This might be due to the formation of a slightly thicker silane layer. The hydrolyzed dipodal and fluoroalkyl silanes might self-condense with each other to form a complex siloxane crosslinked network which would then further increase the deposited silane film thickness, as illustrated in Figure 7.12. As a result, the light radiation could be blocked and reflected by the hydrophobic silane layer and consequently lesser incident light was transmitted through it. Therefore, the anti-reflective feature of the metallic-polymer nanocomposites was suppressed and lower light transmittance was obtained.

**Table 7.4:** Light transmittance of glass substrates which had been pre-coated with metallic-polymer nanocomposites and followed by further surface modification with a mixture of 1.0 v/v% of BTO with various concentrations of FAS

Substrate sample	Transmittance (%)
<b>1.0 v/v% BTO</b>	92.37
<b>1.0 v/v% BTO + 0.1 v/v% FAS</b>	91.39
<b>1.0 v/v% BTO + 0.25 v/v% FAS</b>	91.32
<b>1.0 v/v% BTO + 0.5 v/v% FAS</b>	91.26
<b>1.0 v/v% BTO + 1.0 v/v% FAS</b>	90.03
<b>1.0 v/v% BTO + 3.0 v/v% FAS</b>	90.92
<b>1.0 v/v% BTO + 5.0 v/v% FAS</b>	89.38









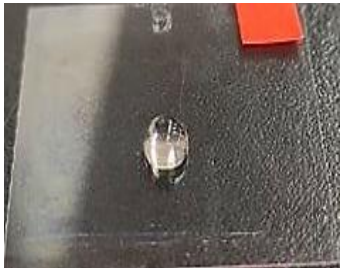

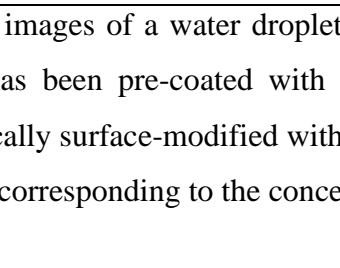
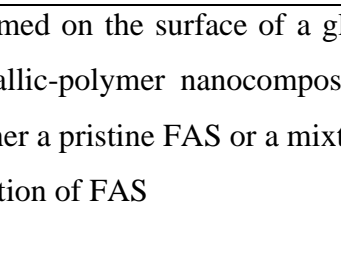
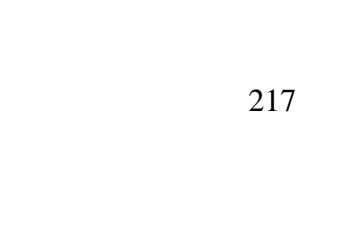



**Figure 7.12:** Schematic representation of a silane mixture of BTO and FAS crosslinked network

#### 7.2.1.2 Surface wettability of the silane mixture coating

The water droplet test was conducted to inspect the surface wetting behaviour of a glass substrate pre-coated with metallic-polymer nanocomposites and further chemically surface-modified with either a pristine FAS or a silane mixture of BTO and FAS. The photographs of a water droplet formed on the surface of a treated glass substrate as a function of the concentration of FAS are shown in Figure 7.13. The images of water droplets portray that the silane mixture has introduced higher hydrophobicity than the pristine FAS as the water droplet is comparatively less accessible to the treated surface and apparently bounced up into a more spherical shape. This is due to a combination of the hydrophobic effect contributed by the long hydrocarbon chains of BTO and the low surface free energy attributed to the fluoroalkyl functional group of FAS. Moreover, the surface wettability and surface free

energy of a treated substrate is further reduced with an increase in silane film thickness and surface roughness. The Cassie-Baxter and Wenzel models have well explained that a coating film with a rough structure and low surface energy could efficiently decrease the affinity of water to the surface, thus giving rise to promising water repellence and high WCA. As a result, the water droplet has less contact with the treated surface.

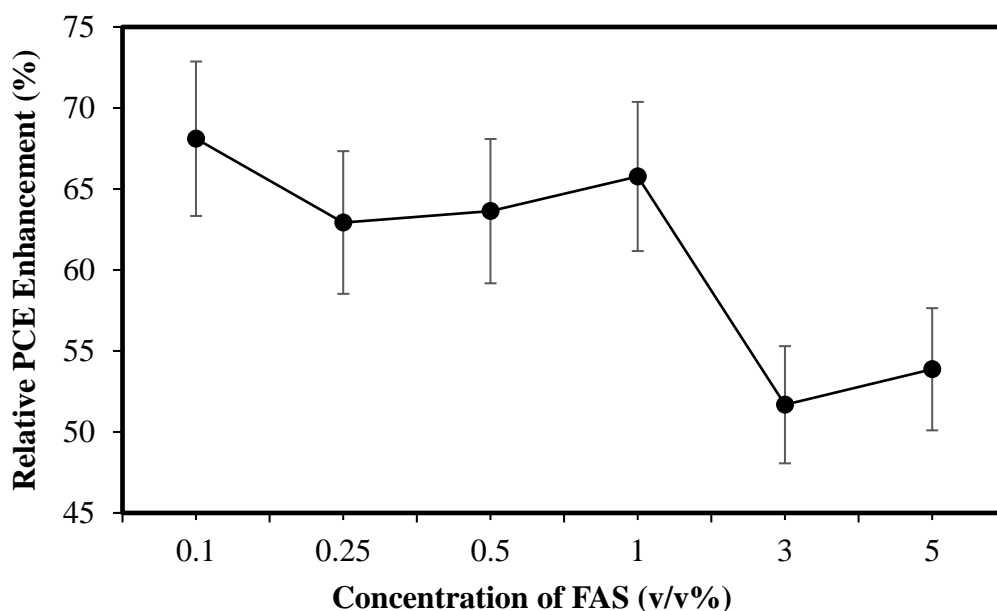
Concentration of FAS (v/v%)	Substrate sample	
	Pristine FAS	Mixture of silanes
0.1		
		
0.5		
		
1.0		
		
3.0		
5.0		

**Figure 7.13:** The images of a water droplet formed on the surface of a glass substrate which has been pre-coated with metallic-polymer nanocomposites and further chemically surface-modified with either a pristine FAS or a mixture of BTO and FAS, corresponding to the concentration of FAS

Interestingly, it was also observed that the bouncing effect of a water droplet is associated with the concentration of FAS. At a higher concentration of FAS, the water droplet appeared in a more spherical shape indicating that a higher value of WCA was obtained. Indeed, FAS is capable of reducing the surface wettability due to the presence of a hydrophobic fluoroalkyl functional group at the tail-end of the silane's molecule (Kaynak, et al., 2017). According to Liu et al. (2009), the fluorine atom is the most effective element for lowering the surface free energy owing to its small atomic radius and higher electronegativity. FAS with higher concentration enables the formation of a uniform and homogeneously distributed silane layer with a higher film thickness and better surface coverage on the surface of a glass substrate. The fluorine atoms present in the molecule of FAS are densely packed and oriented outward on the surface, thereby rendering higher hydrophobicity as well as reducing the surface free energy and surface wettability. Hence, a water droplet with a stronger bouncing effect and higher WCA value is formed on the surface of a substrate that is chemically modified with a higher concentration of FAS. In a nutshell, the mixture of fluoroalkyl and dipodal silanes is capable of creating an impressive hydrophobic surface that induces an excellent surface water repellence and higher WCA. Nonetheless, Sutha et al. (2017) have reported that a trade-off relationship existed between hydrophobicity and light transmission. The acquired results are well correlated with that, whereby the mixture of silanes has rendered higher hydrophobicity but reduced the light transmittance. The latter has been consolidated and proven by the UV-Vis spectra as presented in Figure 7.11.

### 7.2.1.3 Electrical measurement of solar modules

The  $\alpha$ -Si solar module was pre-coated with P(MMA-*co*-AA-*co*-TMVS) nanospheres containing 7 wt% of TMVS and 12.5 ppm of AgNPs with 10-30 nm in size, which was subsequently chemically modified with a silane mixture BTO and FAS. The amount of BTO was fixed at 1.0 v/v% while the concentration of FAS varied from 0.1 to 5.0 v/v%. The solar modules before and after surface treatment were subjected to the output power measurement using a programmable direct circuit electronic load LIV tester to obtain the details of their electrical features. Figure 7.14 illustrates the relative PCE enhancement of the treated solar modules as a function of the concentration of FAS. The acquired photovoltaic parameters are summarized in Table 7.5.



**Figure 7.14:** Relative enhancement in PCE of solar modules which had been pre-coated with metallic-polymer nanocomposites and subsequently chemically modified with a silane mixture of BTO and FAS corresponding to the concentration of FAS

**Table 7.5:** Photovoltaic parameters of both the untreated and treated solar modules, with the latter pre-coated with metallic-polymer nanocomposites and subsequently chemically modified with a silane mixture of BTO and FAS, as a function of the concentration of FAS

Concentration of FAS	Solar module sample	$J_{sc}$ (mA cm <sup>-2</sup> )	$V_{oc}$ (V)	FF (%)	PCE (%)	Relative enhancement (%)
<b>0.1 v/v%</b>	Untreated	1.633	5.919	0.6666	6.443	68.09
	Treated	3.058	6.241	0.5673	10.83	
<b>0.25 v/v%</b>	Untreated	1.969	5.756	0.5470	6.199	62.93
	Treated	2.652	6.134	0.6209	10.10	
<b>0.5 v/v%</b>	Untreated	1.957	5.744	0.5464	6.142	63.63
	Treated	2.838	6.198	0.5711	10.05	
<b>1.0 v/v%</b>	Untreated	1.714	5.823	0.6546	6.533	65.77
	Treated	2.618	6.141	0.6735	10.83	
<b>3.0 v/v%</b>	Untreated	1.703	5.762	0.6234	6.117	51.68
	Treated	3.023	6.173	0.4972	9.278	
<b>5.0 v/v%</b>	Untreated	2.120	5.667	0.5265	6.325	53.87
	Treated	3.093	6.144	0.5121	9.732	

From the results presented in Figure 7.14, it was found that a higher relative PCE enhancement of 65.77% to 68.09% was attained by further treating the surface of the solar modules with a silane mixture containing 1.0 v/v% of BTO and 0.1 to 1.0 v/v% of FAS. Nonetheless, the relative PCE enhancement of the treated solar modules was drastically decreased to < 54% when > 3.0 v/v% of FAS was used. This is mainly attributed to the generation of a thicker hydrophobic silane layer at higher concentrations of FAS. The formation of a complex siloxane (Si-O-Si) network via self-condensation reaction between BTO and FAS would increase the deposited silane film thickness. The silane layer has jeopardized the anti-reflective property of the array of metallic-



polymer nanocomposites covered by it and blocked a fraction of the light radiation from being coupled and scattered into the active region of a solar module. Consequently, lesser charge carriers and electron-hole pairs were generated, thereby yielding a low relative PCE enhancement. As compared to the UV-Vis spectra shown in Figure 7.11, this finding reveals that a slight decrease in light transmittance could lead to a large diminishment in PCE of a solar module. Beyond the simple attribute, the mixtures of 1.0 v/v% of BTO with 0.25 to 1.0 v/v% of FAS were adopted in the following study.

### **7.3 Effect of natural weathering exposure on the adhesive durability of the coating system**

In the evaluation of the efficacy of various silane coatings, 1.0 v/v% of BTO silane, 1.0 v/v% of FAS, and a mixture of 1.0 v/v% of BTO with different concentrations of FAS (i.e. 0.1, 0.25, 0.5 and 1.0 v/v%) were coated respectively to serve as a protective layer for P(MMA-*co*-AA) nanospheres containing 7 wt% of TMVS and 12.5 ppm of AgNPs with a size range of 10-30 nm. The coating system was assessed via an outdoor weathering exposure test. The weathering resistance analysis is a real-time test that demonstrates the actual working environment of the solar modules in outdoor areas. The deposited silane coatings were expected to shield the functional anti-reflective array of metallic-polymer nanocomposite from damages caused by the natural weathering processes. The silane coatings which had exhibited self-cleaning properties and induced remarkable adhesive durability, mechanical stability as well as good water repellence might be able to induce higher weathering resistance and prolong the lifespan of the ARC under outdoor exposure. The

natural weathering exposure test was conducted in conjunction with the following assessments: morphological and topological examinations via AFM; surface wettability analysis by determining the WCA value; and electrical measurement to determine the PCE of the surface-modified solar modules.

### **7.3.1 Surface morphological characteristics of the polymeric array with a silane coating**

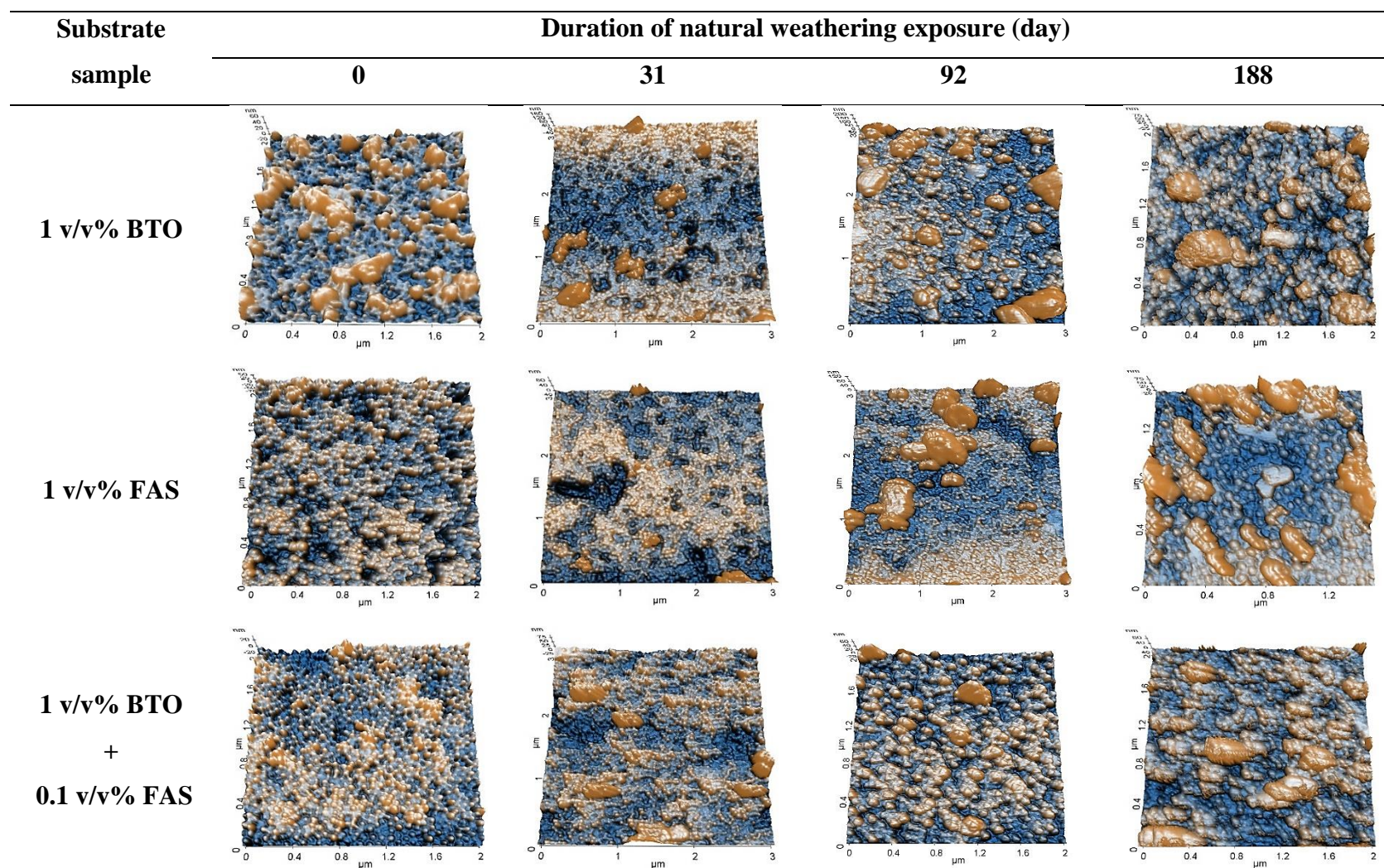
The effect of natural weathering processes on the surface coverage and particle distribution of the self-assembled ARC of metallic-polymer nanocomposites which had been protected by a silane layer, over 182 days, was analyzed via AFM (Figure 7.15). As displayed by the AFM images, smooth arrays of metallic-polymer nanocomposites with homogeneous surface distribution were observed prior to natural weathering exposure (0 days). It was found that these arrays of metallic-polymer nanocomposites had been disrupted to different degrees after a period of outdoor weathering exposure.

The extent of damage on the polymeric nanoarray is dependent on the type of silane coatings applied on it and the duration of natural weathering exposure. The AFM images in Figure 7.15 illustrate that the mixtures of BTO and FAS had provided excellent protection to the metallic-polymer nanocomposites up to 92 days of outdoor weathering exposure. This is evinced by the spherical-shaped nanocomposites which remained to adhere well on the surface of the glass substrates. A quality coating of polymeric nanoarray with good surface coverage had been retained by the silane mixtures. Anyhow, as compared to the coating condition before outdoor weathering exposure, the functional

polymeric nanoarray has been disrupted by the natural weathering processes to a different extent.

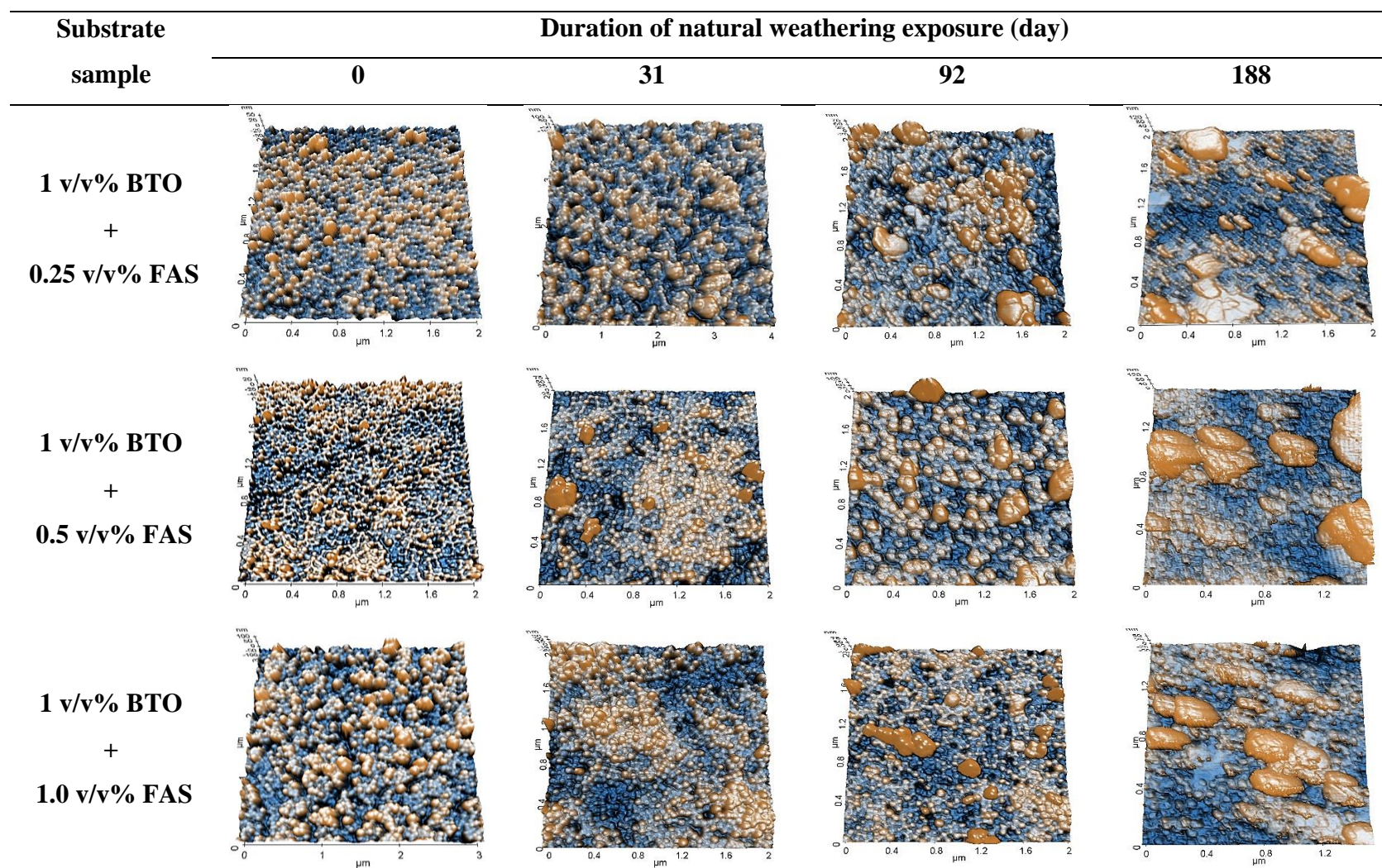
The results indicate that the silane coatings have certainly protected the metallic-polymer nanocomposites from being damaged by the weathering processes. The silane coating indeed induces a remarkable resistance toward harsh outdoor environments. This was accomplished because the silane film with its hydrophobic nature can elevate water repellence and reduce the surface wettability. Besides, the corrugated silane layer with low surface free energy can prevent the occurrence of reversible reactions to form silanol bonds through the hydrolysis of siloxane bonds. As a result, it prevents the breakdown of the adhesive bonds at the interphase region and thus the detachment of the P(MMA-*co*-AA-*co*-TMVS) nanospheres from the glass surface (Lee, et al., 2021).

Indeed, a defective coverage of an ARC is detrimental to the light harvesting efficiency of the solar module (Lee, et al., 2021). Instead of suppressing the surface light reflection, the incident light is partially blocked and reflected by the polymeric nanospheres with an uneven surface distribution. These findings are supported by the results obtained from electrical measurements.



**Figure 7.15:** AFM images of the glass substrates pre-coated with metallic-polymer nanocomposites and subsequently chemically modified with various silane coatings, as a function of the duration of natural weathering exposure





**Figure 7.15:** AFM images of the glass substrates pre-coated with metallic-polymer nanocomposites and subsequently chemically modified with various silane coatings, as a function of the duration of natural weathering exposure (continued)

### **7.3.2 Surface wettability of the polymeric array with a silane coating**

The surface wetting behaviour of glass substrate pre-coated with metallic-polymer nanocomposites and further chemically modified with either a BTO or a FAS or a mixture of both silanes was investigated. The characterization was carried out by means of a water droplet analysis prior to and after natural weathering exposure. The test was conducted to evaluate the surface wettability of a chemically modified glass substrate by taking a photo of the water droplet formed on the substrate surface, as illustrated in Figure 7.16. Other than that, WCA measurement was also conducted on selected samples utilizing a contact angle analyzer. The acquired results are summarized in Table 7.6.













Before the outdoor natural weathering exposure, the surface coated with a silane mixture of BTO and FAS had shown better water repellence compared to those coated with either individual BTO or FAS. The water droplet formed on the surface of a glass substrate treated with a mixture of silanes has apparently tossed up into a more spherical shape with a lesser contact area. This observation was confirmed by the higher value of WCA obtained from the contact angle analysis. The surfaces coated with a silane mixture obviously exhibited a higher average WCA of at least  $113.7^\circ$  while the surfaces coated with a single silane obtained an average WCA of  $103.2^\circ$  and below. This could be attributed to the hydrophobic effect of the fluorine elements and the hydrocarbon chains that are present in the FAS and BTO molecules, respectively. In addition, the self-condensation reactions that occur between

these two silanes further increased the silane film thickness and surface roughness. As a result, the surface wettability of the coating was reduced and a water droplet was shown to have a lesser contact area with the treated surface.

**Table 7.6:** The average WCA of glass substrates pre-coated with metallic-polymer nanocomposites and further chemically surface-modified with various silanes coatings before and after 188 days of natural weathering exposure

Substrate sample	Average WCA (°)		Degraded percentage (%)
	Before weathering exposure	After weathering exposure	
<b>1 v/v% BTO</b>	103.2	75.9	26.45
<b>1 v/v% FAS</b>	93.4	66.4	28.91
<b>1 v/v% BTO + 0.25 v/v% FAS</b>	113.7	60.3	46.97
<b>1 v/v% BTO + 0.5 v/v% FAS</b>	128.4	67.9	47.12
<b>1 v/v% BTO + 1.0 v/v% FAS</b>	117.5	68.1	42.04













The efficiency of the silane coating to serve as a protective layer with hydrophobic nature decreases gradually with prolonged natural weathering exposure. But yet, the surfaces treated with the silane coatings still demonstrated higher water resistance after 92 days of natural weathering exposure. This can be clearly observed from the images in Figure 7.16.

Substrate sample	Duration of natural weathering exposure (day)			
	0	31	92	182
1 v/v% Dipodal silane				
1 v/v% FAS				
1 v/v% Dipodal silane + 0.1 v/v% FAS				

\* The straw colour background is due to the yellowing of a piece of double-sided tape which was stuck at the back of the glass substrates

**Figure 7.16:** The images of a water droplet formed on the glass substrates which had been pre-coated with metallic-polymer nanocomposites and subsequently chemically modified with various silane coatings, as a function of the duration of natural weathering exposure



Substrate sample	Duration of natural weathering exposure (day)			
	0	31	92	182
1 v/v% Dipodal silane + 0.25 v/v% FAS				
1 v/v% Dipodal silane + 0.5 v/v% FAS				
1 v/v% Dipodal silane + 1.0 v/v% FAS				

\* The straw colour background is due to the yellowing of a piece of double-sided tape which was stuck at the back of the glass substrates

**Figure 7.16:** The images of a water droplet formed on the glass substrates which had been pre-coated with metallic-polymer nanocomposites and subsequently chemically modified with various silane coatings, as a function of the duration of natural weathering exposure (continued)

After 188 days of natural weathering exposure, the glass substrate treated with a single silane (either 1.0 v/v% of BTO or 1.0 v/v% of FAS) showed to have higher water repellence and lower surface wettability than the mixture of silanes, as the water droplet formed on the surface of a treated glass substrate was bounced up to form a more spherical shape. These findings had agreed well with the results obtained from the contact angle analysis. The substrates treated with 1.0 v/v% of pristine BTO and FAS had attained an average WCA value of 75.9° and 66.4°, respectively, after 188 days of outdoor weathering exposure. These correspond to 26.45% and 28.91% of degradation compared to the average WCA value of 103.2° and 93.4° before exposure. However, with the mixture of silanes, a higher degradation percentage of more than 42.0% was observed after 188 days of outdoor exposure. This could be due to the hydrolyzed silanes which have self-condensed with each other to form a continuous coating instead of attaching to the surface of the P(MMA-*co*-AA-*co*-TMVS) nanospheres, by forming the siloxane (Si-O-Si) covalent bonds with TMVS. Therefore, the coatings of the silane mixture are less capable to withstand and endure the weathering processes and thus can be easily washed off by rainwater. As a consequence, lower WCA values were obtained after prolonged natural weathering exposure.

### 7.3.3 Electrical measurement of solar modules

The efficacy of various silane coatings to protect the array of metallic-polymer nanocomposites which had been deposited on the glass surface of solar modules against harsh environmental conditions was investigated. The electrical features of solar modules thus treated before and after outdoor weathering exposure were measured. The photovoltaic parameters obtained are summarized in Table 7.7. Figure 7.17 shows the relative PCE enhancement of the treated solar modules prior to and after 188 days of natural weathering exposure, compared to the uncoated solar module as a control.

From Figure 7.17, it is clearly shown that the solar modules which had been coated with both Metallic-polymer nanocomposites and silane coating had retained higher PCE compared to the untreated solar modules. Indeed, the highest relative PCE enhancement of 24.0% has been retained for the pre-coated solar module treated with 1.0 v/v% of FAS after 188 days of outdoor weathering exposure, as compared with its original relative PCE enhancement of 67.7%. In other words, a high PCE of 7.715% has been obtained by the treated solar module after the weathering test (Table 7.7) compared to the original PCE of 6.221% of the untreated solar module.

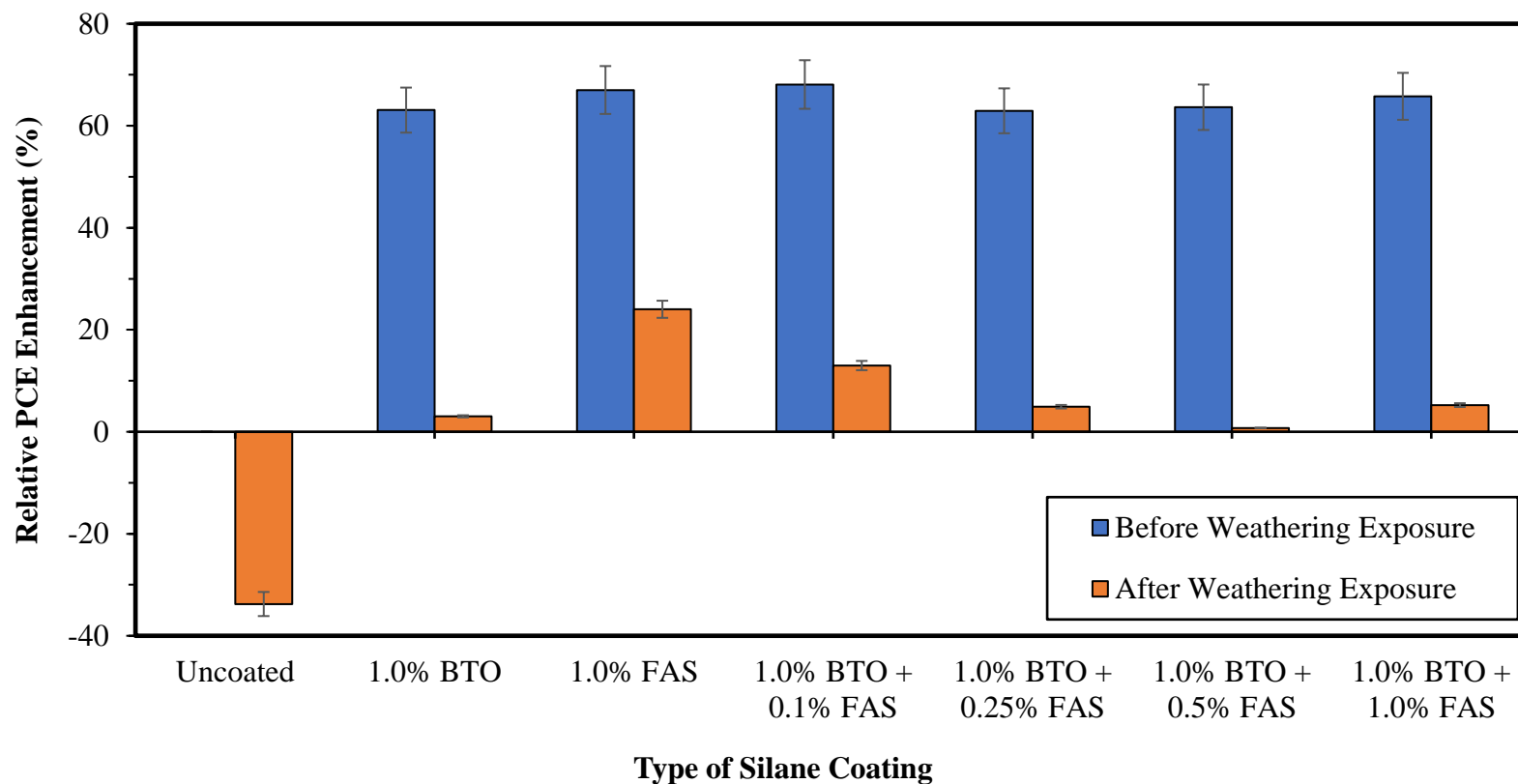
On the other hand, the electronic performance of solar modules without the protection of such coatings had degraded significantly, with their PCE being drastically reduced from 6.382% to 4.227% after the same period of outdoor weathering exposure. The uncoated solar modules (control) had suffered a

large decline in PCE of -33.77% after 188 days of natural weathering exposure (Table 7.7, Figure 7.17). Based on the results obtained, it could be concluded that by introducing an additional layer of silane coating, the solar modules overlaid with an array of polyacrylate nanocomposites became more resistant to weathering processes, such as UV radiation and high temperature.

**Table 7.7:** Photovoltaic parameters of both the untreated and treated solar modules, with the latter pre-coated with metallic-polymer nanocomposites and further chemically surface modified with various silane coatings, before and after 188 days of natural weathering exposure

<b>Silane coating</b>	<b>Solar module sample</b>	<b><math>J_{sc}</math> (mA cm<sup>-2</sup>)</b>	<b><math>V_{oc}</math> (V)</b>	<b>FF (%)</b>	<b>PCE (%)</b>	<b>Relative enhancement (%)</b>
<b>Uncoated</b>	Before	2.131	5.961	0.5024	6.382	-33.77
	After	2.376	5.202	0.3420	4.227	
<b>1.0% BTO</b>	Untreated	1.807	5.880	0.6066	6.445	3.026
	Treated	2.780	5.467	0.4369	6.640	
<b>1.0% FAS</b>	Untreated	1.703	5.837	0.6258	6.221	24.02
	Treated	3.197	5.564	0.4337	7.715	
<b>1.0% BTO + 0.1% FAS</b>	Untreated	1.633	5.896	0.6387	6.150	13.02
	Treated	2.398	6.263	0.4628	6.951	
<b>1.0% BTO + 0.25% FAS</b>	Untreated	2.085	5.815	0.5146	6.239	4.921
	Treated	2.571	5.409	0.4707	6.546	
<b>1.0% BTO + 0.5% FAS</b>	Untreated	1.957	5.744	0.5532	6.218	0.756
	Treated	2.467	5.630	0.4511	6.265	
<b>1.0% BTO + 1.0% FAS</b>	Untreated	1.714	5.823	0.6577	6.564	5.241
	Treated	2.745	5.516	0.4562	6.908	

\* All silanes used are in v/v%



\* All silanes used are in v/v%

**Figure 7.17:** Relative PCE enhancement of solar modules pre-coated with metallic-polymer nanocomposites and further chemically surface modified with various silanes coatings before and after 188 days of natural weathering exposure, compared to the uncoated solar module

In spite of the surface treatment, a decline in the relative PCE enhancement of the treated solar modules was inevitable after prolonged weathering exposure. This is mainly due to the degradation of the array of polyacrylate nanocomposites as well as of the solar modules caused by the weathering processes and harsh environmental conditions.

**Table 7.8:** The shunt resistance and series resistance of solar modules pre-coated with metallic-polymer nanocomposites and further chemically surface modified with various silanes coatings before and after 188 days of natural weathering exposure

Solar module sample	Shunt resistance ( $\Omega$ )		Series resistance ( $\Omega$ )	
	Before	After	Before	After
<b>Uncoated</b>	562.9	90.12	38.44	45.14
<b>1.0% BTO</b>	447.4	88.88	26.90	38.29
<b>1.0% FAS</b>	284.3	140.1	29.41	34.38
<b>1.0% BTO + 0.1% FAS</b>	608.6	88.38	33.61	48.62
<b>1.0% BTO + 0.25% FAS</b>	511.8	90.13	28.22	37.39
<b>1.0% BTO + 0.5% FAS</b>	309.5	80.99	31.62	43.19
<b>1.0% BTO + 1.0% FAS</b>	519.7	79.45	26.03	37.26

\* All silanes used are in v/v%

The damage to the array of polyacrylate nanocomposites is revealed by the AFM images shown in Figure 7.15. After prolonged natural weathering exposure, the uniformly distributed array of metallic-polymer nanocomposites was disrupted and degraded to a different extent. An array of polymeric nanospheres with defective coverage and uneven surface distribution definitely lose its anti-reflective characteristics. It gives rise to an adverse effect on the scattering and Fresnel reflection of incident light. As a consequence, fewer

photons are absorbed into the active layer of the solar module, thereby reducing exciton generation and dissociation and thus lowering the PCE.

The degradation of the solar modules was evidenced by the low shunt resistance and high series resistance of the solar modules after prolonged outdoor exposure as summarized in Table 7.8. The information of electrical resistance features presented here is obtained from the electrical measurement using AM 1.5 solar simulator. Shunt resistance refers to any parallel high-conductivity routes (shunts) across the p-n junction of the photovoltaic cell or on the cell edges (Meyer and Dyk, 2005). These shunt routes are critical defects that divert the electrical currents from the intended load and give rise to the shunt current which is detrimental to the performance of the photovoltaic device, particularly at low-intensity levels. As reported, a lowering in shunt resistance had led to an increase in power dissipation which could then cause a malfunction in localized regions of the p-n junction. A high electric field produced by the reverse bias has eventuated in an avalanche multiplication in the depletion region. It is the most significant mechanism that resulted in junction failure. As a consequence, the shunt paths across the p-n junctions are developed and thus decrease shunt resistance. These could be mainly attributed to the impurities in and near the junction in addition to the crystal damage. The latter might be a negative effect resulting from UV light-induced degradation and age-related degradation as the solar modules were exposed to extreme weathering processes and harsh environmental conditions (Jordan and Kurtz, 2011; Rodríguez, 2021). For instance, heavy rainfall and high temperature lead to the hardening of the crystalline silicon. Meanwhile, the electronic

performance of a solar module decreases after prolonged outdoor weathering exposure due to the reactions in the semiconductor materials utilized in the solar cell. A decrease in shunt resistance and an increase in series resistance evidence that a solar module has degraded.



## CHAPTER 8

### CONCLUSIONS AND FUTURE PERSPECTIVE

The conclusions are organized into four major sections, including the fabrication and characterization of silver nanoparticles, the synthesis and characterization of P(MMA-*co*-AA-*co*-TMVS) nanospheres, the fabrication and characterization of functional P(MMA-*co*-AA-*co*-TMVS) nanospheres encapsulated with AgNPs, and the generation of a hydrophobic surface through chemically surface-modification using a mixture of dipodal and fluoroalkyl silanes. Moreover, the recommendations for the current study and suggestions for further research are included for future improvement.

#### 8.1 Conclusions

##### 8.1.1 Fabrication and characterization of silver nanoparticles

AgNPs with different structural properties had been successfully fabricated through the chemical reduction process. The type and concentration of capping agent as well as the reaction temperature were found to affect significantly the particle size and shape of the AgNPs formed. AgNPs with smaller diameters (which were mostly smaller than 100 nm) and spherical in shape had been successfully synthesized at 0 °C by employing DDA with *S* values between 2.78 and 22.2. DDA performed better than DDT as a capping agent to protect the metallic nanoparticles from agglomeration during the reaction. Both the

EDX and FTIR analyses showed that the capping agent, whether DDA or DDT, were attached to the synthesized AgNPs.

### **8.1.2 Synthesis and characterization of P(MMA-*co*-AA-*co*-TMVS) nanospheres**

P(MMA-*co*-AA-*co*-TMVS) nanospheres with an average particle size of  $97 \pm 5$  nm, a uniform spherical shape and a reasonably high yield ( $> 97\%$  of monomer conversion) were synthesized through the emulsion polymerization process. The presence of a distinct Si peak in the EDX spectrum of P(MMA-*co*-AA-*co*-TMVS) nanostructures evidenced that TMVS has been successfully incorporated into the polymer chain. The synthesized copolymer has a glass transition temperature,  $T_d$ , of  $111.4\text{--}118.1^\circ\text{C}$  and a high decomposition temperature,  $T_g$ , of  $394.3^\circ\text{C}$ .

Two coating techniques, namely an immersion method and a dip coating method, were employed to deposit the polyacrylic nanospheres on a glass substrate. Overall, the immersion coating method resulted in a coating with better weathering resistance than the dip coating method. The polymeric coating cured at  $65^\circ\text{C}$  was found to exhibit the highest adhesive durability on glass substrates. In addition, the average WCA of a glass surface had increased from  $35.4^\circ$  to more than  $42.6^\circ$  after an array of the polyacrylic nanospheres was deposited on it. Coating the glass surface of an  $\alpha$ -Si solar module with the polyacrylic nanospheres containing 7 wt% of TMVS via the immersion coating method resulted in the highest relative PCE enhancement of about 42%. The

prominent enhancement in the PCE of the solar module is attributed to the outstanding anti-reflective property of the polyacrylic nanostructures.

After 130 days of natural weathering exposure, the polyacrylic nanospheres with 7 wt% of TMVS remained to adhere well to the glass surface of a solar module. The polymeric coating obtained via the immersion coating method exhibited better surface coverage and a lower degree of disruption. The solar module thus coated was able to maintain a higher relative PCE enhancement over 130 days of outdoor weathering exposure.

#### **8.1.3 Fabrication and characterization of functional P(MMA-*co*-AA-*co*-TMVS) nanospheres encapsulated with silver nanoparticles**

AgNPs with different particle size ranges (i.e. 3-7 nm and 10-30 nm) and amounts (i.e. 6.25 – 50.0 ppm) had been successfully embedded into P(MMA-*co*-AA-*co*-TMVS) nanospheres containing 7 wt% of TMVS via the emulsion polymerization process. No agglomeration or clustering of the encapsulated AgNPs in the polyacrylic nanospheres was observed in TEM images. Furthermore, the solar modules coated with P(MMA-*co*-AA-*co*-TMVS) nanospheres containing AgNPs with the size range of 10-30 nm attained consistently higher relative PCE improvement than those having AgNPs with 3-7 nm in size. This is due to the higher-order modes exhibited by AgNPs with larger size which increases the scattered light being forwarded into the solar modules. The highest PCE improvement achieved was 73.2% when solar modules were coated with the polyacrylic nanospheres containing 7 wt% of TMVS and 12.5 ppm of AgNPs with 10-30 nm in size. The PCE result is in

line with the excellent light transmission of 97.13% of the same nanocomposite coated on a glass substrate, which was obtained from UV-Vis spectroscopy.

#### **8.1.4 Generation of a hydrophobic surface using a silane mixture of a dipodal and a fluoroalkyl silanes**

The dipodal silane, i.e. BTO, with various concentrations was coated on a glass surface which had been pre-coated with P(MMA-*co*-AA-*co*-TMVS) nanospheres containing 7 wt% of TMVS and 12.5 ppm of AgNPs with the particle size range of 10-30 nm. The peeling test results demonstrate that 1.0 v/v% of BTO had induced impressive adhesive strength with prominent adhesive durability. The highest relative PCE enhancement attained was 70.1% after three cycles of peeling. Similarly, when the pre-coated glass surface was treated with a silane mixture of BTO (1.0 v/v%) and FAS (0.1 to 1.0 v/v%), the relative PCE enhancement of 65.77-68.09% was achieved.

The solar modules coated with metallic-polymer nanocomposites and with various combinations of silane coatings had retained higher PCE compared to the untreated solar modules after undergoing a period of outdoor weathering exposure. The highest relative PCE enhancement of 24.0% had been obtained by the pre-coated solar module treated with 1.0 v/v% of FAS after 188 days of natural weathering exposure, as compared to 67.7% of the initial relative PCE enhancement before the outdoor exposure. It was obvious that the array of metallic-polymer nanocomposite together with a layer of silane coating had effectively slowed down the degradation of solar modules caused by UV radiation and harsh environmental conditions.

The AFM images illustrate that with an additional layer of silane coating, the smooth array of metallic-polymer nanocomposites with even surface distribution was less disrupted after 188 days of outdoor weathering exposure. This indicates that the silane coatings had certainly protected the polyacrylic nanocomposites from harsh environmental conditions. This was largely due to the excellent water resistance of the silane coatings.

The coatings of the silane mixtures had an average WCA of  $113.7^\circ$  and above; while the coatings of either BTO or FAS gave an average WCA of  $103.2^\circ$  and below. However, after 188 days of natural weathering exposure, the coatings of a single silane exhibited higher water resistance and lower surface wettability than the coatings of the silane mixtures. The former had attained higher average WCA values of  $75.9^\circ$  and  $66.4^\circ$  with lower degrees of degradation of 26.45% and 28.91% when only BTO or FAS was used respectively.

## **8.2 Recommendations and future perspective**

More analyses can be conducted to consolidate the findings of this research work. For instance, quantum efficiency measurement can be adopted to explore the performance of the solar module exposed to a wider wavelength range of light in the solar spectrum. This may be beneficial for the improvement of the light harvesting and power conversion efficiencies of a photovoltaic device. Besides that, the spectral reflectance curve of the solar module can be studied to evaluate the antireflective efficiency of the nanospheres array that is coated on the glass surface of a solar module.

Some future studies are suggested below:

1. To investigate the effect of AgNPs with larger particle size ( $>30$  nm) on the light harvesting efficiency of solar modules.
2. To study the relationship between surface roughness and light transmission of a glass substrate coated with metallic-polymer nanocomposites.
3. To create an optically transparent superhydrophobic surface with better water repellence and weathering resistance by employing different types of dipodal and fluoroalkyl silanes.
4. To study the effect of such ARC of metallic-polymer nanocomposites and silane coatings on the light harvesting efficiency of other types of solar cells.

## REFERENCES

- Ajitha, B., Reddy, Y.A.K., Reddy, P.S., Jeon, H.J. and Ahh, C.W., 2016. Role of capping agents in controlling silver nanoparticles size, antibacterial activity and potential application as optical hydrogen peroxide sensor. *RSC Advances*, 6, pp. 36171-36179.
- Alaqad, K. and Saleh, T.W., 2016. Gold and Silver Nanoparticles: Synthesis Methods, Characterization Routes and Applications towards Drugs. *Journal of Environmental & Analytical Toxicology*, 6(4), pp. 1-10.
- Alkan, C., Aksoy, S.A. and Anayurt, R.A., 2014. Synthesis of poly(methyl methacrylate-co-acrylic acid)/n-eicosane microcapsules for thermal comfort in textiles. *Textile Research Journal*, 85(19), pp. 2051-2058.
- Anigol, L.B., Charantimath, J.S. and Gurubasavaraj, P.M., 2017. Effect of Concentration and pH on the Size of Silver Nanoparticles Synthesized by Green Chemistry. *Organic & Medicinal Chemistry International Journal*, 3, pp. 1-5.
- Arkles, B., Pan, Y., Larson, G.L. and Singh, M., 2014. Enhanced Hydrolytic Stability of Siliceous Surfaces Modified with Pendant Dipodal Silanes. *Chemistry European Journal*, 20, pp. 9442-9450.
- Asapu, R., Claes, N., Bals, S., Denys, S., Detavernier, C., Lenaerts, S. and Verbruggen, S.W., 2016. Silver-polymer core-shell nanoparticles for ultrastable plasmon-enhanced photocatalysis. *Applied Catalysis B: Environmental*, 200, pp. 31-38.

Asim, N., Mohammad, M. and Badiei, M., 2018. Novel Nanomaterials for Solar Cell Devices. In: B.A. Bhanvase, V.B. Pawade, S.J. Dhoble, S.H. Sonawane and M. Ashokkumar (eds.). *Nanomaterials for Green Energy*. Oxford: Elsevier. pp. 227-277.

Askar, K. Phillips, B.M., Dou, X., Lopez, J., Smith, C., Jiang, B. and Jiang, P., 2012. Self-assembled nanoparticle antiglare coatings. *Optics Letters*, 37(21), pp. 4380-4382.

Askar, K., Phillips, B.M., Fang, Y., Choi, B. and Gozubenli, N., 2013. Self-assembled self-cleaning broadband anti-reflection coatings. *Colloids & Surfaces A: Physicochemical & Engineering Aspects*, 439, pp. 84-100.

ASTM D3359-09, 2009. *Standard test methods for measuring adhesion by tape test*. ASTM International: West Conshohocken

Awad, M.A., Hendi, A.A., Ortashi, K.M.O., Alanazi, A.B., Alzahrani, B.A. and Soliman, D.A., 2019. Greener Synthesis, Characterization, and Antimicrobiological Effects of Helba Silver Nanoparticle-PMMA Nanocomposite. *International Journal of Polymer Science*, pp. 1-7.

Bacal, D.M., Lal, N., Jumabekov, A.N., Hou, Q., Hu, Y., Lu, J., Chesman, A.S.R. and Bach, U., 2020. Solution-processed antireflective coating for back-contact perovskite solar cells. *Optics Express*, 28(9), pp. 12650-12660.

Bagher, A.M., Vahid, M.M.A. and Mohsen, M., 2015. Types of Solar Cells and Application. *American Journal of Optics and Photonics*, 3(5), pp. 94-113.

Barman, B., Dhasmana, H., Verma, A., Kumar, A., Singh, D., and Jain, V., 2018. Fabrication of silver nanoparticles on glass substrate using low-temperature rapid thermal annealing. *Energy & Environment*, 29(3), pp. 358–371.



Barry, A., 2018. Silane Coupling Agents. *Gelest Inc.* [online] Available at: <[https://www.gelest.com/wp-content/uploads/Silane\\_Coupling\\_Agents.pdf](https://www.gelest.com/wp-content/uploads/Silane_Coupling_Agents.pdf)> [Accessed 23 April 2021].

Bulliard, X., Ihn, S.G., Yun, S., Kim, Y., Choi, D., Choi, J.Y., Sim, M., Park, J.H., Choi, W. and Cho, K., 2010. Enhanced Performance in Polymer Solar Cells by Surface Energy Control. *Advanced Functional Materials*, 20, pp. 4381-4387.

Cano-Sarabia, M. and MasPOCH, D., 2015. Nanoencapsulation. In: B. Bharat (ed.). *Encyclopedia of Nanotechnology*. Springer: Dordrecht, pp. 1-16.

Caruso, F., 2004. *Colloids and colloidal assemblies: synthesis, modification, organization and utilization of colloid particles*. Weinheim: Wiley-VCH.

Casanova, J.Z., Piliougin<sup>1</sup>, M., Carretero<sup>1</sup>, J., Bernaola<sup>1</sup>, P., Carpena<sup>1</sup>, P., Mora-López, L., and Sidrach-de-Cardona<sup>1</sup>, M., 2011. Analysis of dust losses in photovoltaic modules. *World Renewable Energy Congress 2011*, Linköping, Sweden, pp. 2985-2992.

Chen, Y., Chang, W.L., Huang, C.K. and Sun, K.W., 2011. Biomimetic nanostructured antireflection coating and its application on crystalline silicon solar cells. *Optics Express*, 19(15), pp. 14411-14419.

Chen, Y. and Sun, K.W., 2010. Enhancement of the light conversion efficiency of silicon solar cells by using nanoimprint anti-reflection layer. *Solar Energy Materials & Solar Cells*, 94(3), pp. 629-633.

Chen, Y. and Wang, X., 2008. Novel phase-transfer preparation of monodisperse silver and gold nanoparticles at room temperature. *Materials Letters*, 62, pp. 2215-2218.

Chen, Y., Zhang, Y., Shi, L., Li, J., Xin, Y., Yang, T. and Guo, Z., 2012. Transparent superhydrophobic/superhydrophilic coatings for self-cleaning and anti-fogging. *Applied Physics Letters*, 101, pp. 1-4.

Chern, C.S., 2008. *Application of emulsion polymerization*. New Jersey: Wiley.

Chmielewska, B., Czarnecki, L., Sustersic, J. and Zajc, A., 2006. The influence of silane coupling agents on the polymer mortar. *Cement & Concrete Composites*, 28, pp. 803-810.

Cho, E.C., Chang-Jian, C.W., Chen, H.C., Chuang, K.S., Zheng, J.H., Hsiao, Y.S., Lee, K.C. and Huang, J.H., 2017. Robust multifunctional superhydrophobic coatings with enhanced water/oil separation, self-cleaning, anti-corrosion, and anti-biological adhesion. *Chemical Engineering Journal*, 314, pp. 347-357.

Chou, C.H. and Chen, F.C., 2014. Plasmonic nanostructures for light trapping in organic photovoltaic devices. *Nanoscale*, 6(15), pp. 8444-8458.

Chungsiriporn, J., Pongyeela, P. and Chairerk, N., 2020. Sol-gel self-cleaning superhydrophobic nanocoating for glass surface of solar cell. *Songklanakarin Journal of Science & Technology*, 42 (4), 923-927.

Dai, H., Li., M., Li, Y., Yu, H., Bai, F. and Ren, X., 2012. Effective light trapping enhancement by plasmonic Ag nanoparticles on silicon pyramid surface. *Optics Express*, 20(4), pp. 502-509.

Deng, X., Mammen, L., Zhao, Y., Lellig, P., Müllen, K., Li, C., Butt, H-J. and Vollmer, D., 2011. Transparent, Thermally Stable and Mechanically Robust Superhydrophobic Surfaces Made from Porous Silica Capsules. *Advanced Materials*, 23, pp. 2962-2965.

Derkacs, D., Lim, S.H., Matheu, P., Mar, W. and Yu, E.T., 2006. Improved performance of amorphous silicon solar cells via scattering from surface plasmon polaritons in nearby metallic nanoparticles. *Applied Physics Letters*, 89, pp. 093103(1)–093103(3).

El-hoshoudy, A.N.M.B., 2018. Emulsion Polymerization Mechanism. *Intech Open Science*, (1), pp. 3-14.

Elnoby, R. M., Mourad, M. H., Elnaby, S. L. H., and Abou Kana, M. T. H., 2018. Monocrystalline solar cells performance coated by silver nanoparticles: Effect of NPs sizes from point of view Mie theory. *Optics & Laser Technology*, 10(1), pp. 208–215.

El-Nour, K.M.M.A., Eftaiha, A., Al-Warthan, A. and Ammar, R.A.A., 2010. Synthesis and application of silver nanoparticles. *Arabian Journal of Chemistry*, 3, pp. 135-140.

Esmailzad, N.S., Demir, A.K., Hajivandi, J., Ciftpinar, H., Turan, R., Kurt, H. and Bek, A., 2020. Nanosphere Concentrated Photovoltaics with Shape Control. *Advanced Optical Materials*, 9(3), pp. 2000943.

Fang, C.Y., Liu, Y.L., Lee, Y.C., Chen, H.L., Wan, D.H. and Yu. C.C., 2013. Nanoparticle Stacks with Graded Refractive Indices Enhance the Omnidirectional Light Harvesting of Solar Cells and the Light Extraction of Light-Emitting Diodes. *Advanced Functional Materials*, 23, pp. 1412-1421.

Farrell, Z., Shelton, C., Dunn, C., and Green, D., 2013. Straightforward, One-Step Synthesis of Alkanethiol-capped Silver Nanoparticles from an Aggregative Model of Growth. *Langmuir*, 29(30), pp. 9291–9300.

Fredrick, O.O. and Mangaka, C.M., 2017. Electrochemical and optical band gaps of bimetallic silver-platinum varying metal ratios nanoparticles. *African Journal of Pure and Applied Chemistry*, 11(1), pp. 1-8.

Galka, P., Kowalonek, J. and Kaczmarek, H., 2014. Thermogravimetric analysis of thermal stability of poly(methyl methacrylate) films modified with photoinitiators. *Journal of Thermal Analysis and Calorimetry*, 115, pp. 1387–1394.

Goh, W.S., 2019. *Augmentation of Power Conversion Efficiency of Photovoltaic Cell Utilizing Poly(Methyl Methacrylate-co-Acrylic Acid) Nanospheres Encapsulated With Silver or Gold Nanoparticles*. Master. Universiti Tunku Abdul Rahman.

Grzelczak, M., Vermant, J., Furst, E.M. and Liz-Marzan, L.M., 2010. Directed Self-Assembly of Nanoparticles. *ACS Nano*, 4(7), pp. 3591-3605.

Gulati, S., Sachdeva, M. and Bhasin, K.K., 2018. Capping agents in nanoparticle synthesis: Surfactant and solvent system. *American Institute of Physics Conference Proceedings*, 1953, pp. 1-4.

Guilatt, O., Apter, B. and Efron, U., 2009. Study of LSPR-Enhanced Absorption for Solar Cell Applications: Preliminary results. *Nanoscale Photonic & Cell Technologies for Photovoltaics II*, 7411, pp. 1-9.

Guire, M.R.D., Bauermann, L.P., Parikh, H. and Bill, J., 2013. Chemical Bath Deposition. In: T. Schneller, R. Waser, M. Kosec and D. Payne (eds.). *Chemical Solution Deposition of Functional Oxide Thin Films*. New York: Springer Vienna. pp. 319-339.

Guzel, R. and Erdal, G., 2018. Synthesis of Silver Nanoparticles. In: Khan, M. (ed.). *Silver Nanoparticles Fabrication, Characterization and Applications*. London: IntechOpen. pp. 3-18.

Harish, K.K., Venkatesh, N., Bhowmik, H. and Kuila, A., 2018. Metallic Nanoparticle: A Review. *Biomedical Journal of Scientific & Technical Research*, 4(2), pp. 3765-3775.

Hashem, M., Rez, M.F.A., Fouad, H., Elsarnagawy, M.A. Elsharawy, A.U., Assery, M. and Ansari, S.G., 2017. Influence of Titanium Oxide Nanoparticles on the Physical and Thermomechanical Behavior of Poly Methyl Methacrylate (PMMA): A Denture Base Resin. *Science of Advanced Materials*, 9(6), pp. 938-944.

Haugan, E., Granlund, H., Gjessing, J. and Marstein, E.S., 2011. Colloidal Crystals as Templates for Light Harvesting Structures in Solar Cells. *Energy Procedia*, 10, pp. 292-296.

He, G., Pan, Q. and Remple, G.L., 2003. Synthesis of Poly(methyl methacrylate) Nanosize Particles by Differential Microemulsion Polymerization. *Macromolecular Rapid Communications*, 24(9), pp. 585-588.

Hussain, C.M. and Mishra A.K., 2018. *New Polymer Nanocomposite for Environmental Remediation*, 1st ed. Oxford: Elsevier.

ICIS, 2009. Methyl Methacrylate (MMA) Uses and Market Data. *ICB Chemical*. [online] Available at: <<https://www.icis.com/explore/resources/news/2007/11/05/9076049/methyl-methacrylate-mma-uses-and-market-data/>> [Accessed 28 March 2020]

Jeng, M., Chen, Z., Xiao, Y., Chang, L., Ao, J., Sun, Y., Popko, E., Jacak, W. and Chow, L., 2015. Improving Efficiency of Multicrystalline Silicon and CIGS Solar Cells by Incorporating Metal Nanoparticles. *Materials*, 8(10), pp. 6761-6771.

Jiang, X.C., Chen, W.M., Chen, C.Y., Xiong, S.X. and Yu, A.B., 2011. Role of Temperature in the Growth of Silver Nanoparticles Through a Synergetic Reduction Approach. *Nanoscale Research Letters*, 6(1), pp. 32.

Jiao, T., Wei, D., Song, X., Sun, T., Yang, J., Yu, L., Feng, Y., Sun, W., Wei, W., Shi, H., Hu, C. and Du, C., 2016. High-efficiency, stable and non-chemical-doped graphene-Si solar cells through interface engineering and PMMA antireflection. *RSC Advances*, 6(12), pp. 10175-10179.

Jin, C., Li, J., Han, S., Wang, J. and Sun, Q., 2014. A Durable, Superhydrophobic, Superoleophobic and Corrosion-Resistant Coating with Rose-Like ZnO Nanoflowers on a Bamboo Surface. *Applied Surface Science*, 320, pp. 322-327.

Jordan, D.C. and Kurtz, S.R., 2011. Photovoltaic Degradation Rates — an Analytical Review. *Progress in Photovoltaics*, 21(1), pp. 12-29.

Kalita, D. and Netravali, A., 2015. Interfaces in Green Composites: A Critical Review. *Reviews of Adhesion & Adhesive*, 3(4), pp. 386-443.

Kaynak, B., Alpan, C., Kratzer, M., Ganser, C., Teichert, C. and Kern, W., 2017. Anti-adhesive layers on stainless steel using thermally stable dipodal perfluoroalkyl silanes. *Applied Surface Science*, 416, pp. 824-833.

Kaynak, C., Celikbilek, C. and Alkocali, G., 2013. Use of silane coupling agents to improve epoxy–rubber interface. *European Polymer Journal*, 39, pp. 1125-1132.

Kelly, K.L., Coronado, E., Zhao, L.L., Schatz, G.C., 2002. The Optical Properties of Metal Nanoparticles: The Influence of Size, Shape, and Dielectric Environment. *Journal of Physical Chemistry B*, 107, pp. 668-677.

Khan, I., Saeed, K. and K, I., 2019. Nanoparticles: Properties, applications and toxicities. *Arabian Journal of Chemistry*, 12(7), pp. 1-24.

Kong, I., 2016. Polymers with Nano-Encapsulated Functional Polymers. In: S. Thomas, R. Shanks, S. Chandrasekharakurup (eds.). *Design and Applications of Nanostructured Polymer Blends and Nanocomposite Systems*. Oxford: Elsevier. pp. 125–154.

Krayden, 2009. Silane Coupling Agent. [online] Available at: <[https://krayden.com/pdf/xia\\_silane\\_chemistry.pdf](https://krayden.com/pdf/xia_silane_chemistry.pdf)> [Accessed 6 April 2020]

Kulshreshtha, A.K., Singh, O.N. and Wall, G.M., 2010. *Pharmaceutical suspensions: From formulation development to manufacturing*. Berlin: Springer.

Landi, G., Lisi, L. and Russo, G., 2005. Oxidation of propane and propylene to acrylic acid over vanadyl pyrophosphate. *Journal of Molecular Catalysis A: Chemical*, 239(2), pp. 172-179.

Lee, C.L., Goh, W.S., Chee, S.Y. and Lai, K.Y., 2017. Enhancement of light harvesting efficiency of silicon solar cell utilizing arrays of poly(methyl methacrylate-co-acrylic acid) nano-spheres and nano-spheres with embedded silver nano-partilces. *Photonic & Nanostructures–Fundamentals & Applications*, 23, pp. 36-44.

Lee, C.L., Goh, W.S., Chee, S.Y. and Lai, K.Y., 2018. Augmentation of power conversion efficiency of amorphous silicon solar cell employing poly(methyl methacrylate-co-acrylic acid) nanospheres encapsulated with gold nanoparticles. *Journal of Materials Science*, 53, pp. 5183-5193.

Lee, M.J.R., Chee, S.Y., Tay, B.Y., Lee, C.L., Lim, F.C. and Sepeai, S., 2021. Affixing poly(methyl methacrylate-co-acrylic acid) nanospheres with trimethoxyvinylsilane on silicon solar module to enhance its power conversion efficiency. *Journal of Materials Science*, 56(21), pp. 1-19.

Leonics, 2017. Basic of Solar Cell, Solar Photovoltaic Modules. [online] Available at: [http://www.leonics.com/support/article2\\_13j/articles2\\_13j\\_en.php](http://www.leonics.com/support/article2_13j/articles2_13j_en.php) [Accessed 13 April 2020]

Lin, G.J., Wang, H.P., Lien, D.H., Fu, P.H., Chang, H.C. Ho, C.H., Lin, C.A., Lai, K.Y. and He, J.H., 2014. A broadband and omnidirectional light-harvesting scheme employing nanospheres on Si solar cells. *Nano Energy*, 6, pp. 36-43.

Liu, H., Szunerits, S., Xu, W. and Boukherroub, R., 2009. Preparation of Superhydrophobic Coatings on Zinc as Effective Corrosion Barriers. *ACS Applied Materials & Interfaces*, 1(6), pp. 1150-1153.

Liu, Q., Ding, J., Chambers, D.E., Debnath, S., Wunder, S.L. and Baran, G.R., 2001. Filler-coupling agent-matrix interactions in silica/polymethyl methacrylate composites. *Journal of Biomedical Materials Research*, 57(3), pp. 384-393.

Liu, S., Liu, X., Lathe, S.S., Gao, L., An, S., Yoon, S.S., Liu, B. and Xing, R., 2015. Self-cleaning Transparent Superhydrophobic Coatings through Simple Sol-gel Processing of Fluoroalkylsilane. *Applied Surface Science*, 351, pp. 897-903.

Liu, Z., Ya, J., Xin, Y., Ma, J. and Zhou, C., 2006. Assembly of polystyrene colloidal crystal templates by a dip-drawing method. *Journal of Crystal Growth*, 2917(1), pp. 223-227.

Lu, X.Y., Wu, D.C., Li, Z.J. and Chen, G.Q., 2011. Polymer Nanoparticles. *Nanoparticles in Translational Science & Medicine*, 104, pp. 299-323.

Maradudin, A.A., 2014. Introduction: Plasmonics and its Building Blocks. *Handbook of Surface Science*, 1, pp. 1-36.

Mavani, K. and Shah, M., 2013. Synthesis of Silver Nanoparticles by using Sodium Borohydride as a Reducing Agent. *International Journal of Engineering Research & Technology*, 2(3), pp. 1-5.

Meyer, E.L. and Dyk, E.E., 2005. The effect of reduced shunt resistance and shading on photovoltaic module performance. *Conference Record of the Thirty-first IEEE Photovoltaic Specialists Conference, 2005*, pp. 1131-1334.

Ming, W., Jones, F.N. and Fu, S., 1998. High solids-content nanosize polymer latexes made by microemulsion polymerization. *Macromolecular Chemistry & Physics*, 199, pp. 1075-1079.



Mirela, D., 2009. Metallic Nanoparticles. [online] Available at: <[https://sabot.in.ung.si/~sstanic/teaching/Seminar/2009/20091214\\_Dragomir\\_MetNP.pdf](https://sabot.in.ung.si/~sstanic/teaching/Seminar/2009/20091214_Dragomir_MetNP.pdf)> [Accessed on 20 March 2020]

Mizuno, H., Sai, H., Matsubara, K. and Kondo, M., 2012. Light Trapping by Ag Nanoparticles Chemically Assembled inside Thin-Film Hydrogenated Microcrystalline Si Solar Cells. *Japanese Journal of Applied Physics*, 51(4), pp. 2302-2307.

Mo, L., Liu, D., Li, W., Li, L., Wang, L. and Zhou, X., 2011. Effects of dodecylamine and dodecanethiol on the conductive properties of nano-Ag films. *Applied Surface Science*, 257, pp. 5746-5753.

Mody, V.V., Siwale, R., Singh, A. and Mody, H.R., 2010. Introduction to metallic nanoparticles. *Journal of Pharmacy & Bioallied Science*, 2(4), pp. 282-289.

Moharram, M.A. and Khafagi, M.G., 2006. Thermal behavior of poly(acrylic acid)–poly(vinyl pyrrolidone) and poly(acrylic acid)–metal–poly(vinyl pyrrolidone) complexes. *Journal of Applied Polymer Science*, 102, pp. 4049-4057.

Mohy, E.M.S., Elaassar, M.R., Elzatahry, A.A. and Al-Sabah, M.M.B., 2017. Poly (acrylonitrile-co-methyl methacrylate) nanoparticles: I. Preparation and characterization. *Arabian Journal of Chemistry*, 10(8), pp. 1153-1166.

Monticelli, F., Toledano, M., Osorio, R. and Ferrari, M., 2006. Effect of temperature on the silane coupling agents when bonding core resin to quartz fiber posts. *Dental Materials*, 22, pp. 1024-1028.

Nair, P.K., Nair, M.T.S., Garcia, V.M., Arenas, O.L., Pena, Y., Castillo, A., Ayala, I.T., Gomezdaza, O., Shanchez, A., Champos, J., Hu, H., Suarez, R. and Rincon, M.E., 1997. Semiconductor thin films by chemical bath deposition for solar energy related applications. *Solar Energy Materials & Solar Cells*, 52, pp. 313-344.

Nasrollahzadeh, M., Issaabadi, Z., Sajjadi, M., Sajadi, S.M. and Atarod, M., 2019. Types of Nanostructures. *Interface Science & Technology*, 28(2), pp. 29-80.

Natsuki, J., Natsuki, T. and Hashimoto, Y., 2015. A Review of Silver Nanoparticles: Synthesis Methods, Properties and Applications. *International Journal of Materials Science & Applications*, 4(5), pp. 353-332.

Nersisyan, H.H., Lee, J.H., Son, J.H., Won, C.W., Maeng, D.Y., 2003. A new and effective chemical reduction method for preparation of nanosized silver powder and colloid dispersion. *Materials Research Bulletin*, 3(8), pp. 949–956.  
Ooij, W.J.V., Stacy, D.Z.M., Seth, A., Mugada, T., Gandhi, J. and Puomi, P., 2005. Corrosion Protection Properties of Organofunctional Silanes—An Overview. *Tsinghua Science & Technology*, 10(6), pp. 639-664.

Pacioni, N.L., Borsarelli, C.D., Rey, V. and Veglia, A.V., 2015. Synthetic Routes for the Preparation of Silver nanoparticles. In: E. Alarcon, M. Griffith, K. Udekwu (eds.). *Silver Nanoparticle Applications. Engineering Materials*. Springer, Switzerland

Pal, G., Rai, P. and Pandey, A., 2019. Green synthesis of nanoparticles: a greener approach for a cleaner future. In: K.A. Shukla and S. Irvani (eds.). *Green synthesis, characterization and applications of nanoparticles*. Elsevier, Amsterdam

Pape, P.G. and Plueddemann, E.P., 1991. Methods for improving the performance of silane coupling agents. *Journal of Adhesion Science & Technology*, 5(10), pp. 831-842.

Pape, P.G., 2011. Adhesion Promoters: Silane Coupling Agents. *Applied Plastics Engineering Handbook*, 29, pp. 503-571.

Paquet, O., Salon, M.C.B., Zeno, E. and Belgacem, M.N., 2012. Hydrolysis-condensation kinetics of 3-(2-amino-ethylamino)propyl-trimethoxysilane. *Materials Science & Engineering C*, 32, pp. 487-493.

Patra, J.K. and Baek, K.H., 2014. Green Nanobiotechnology: Factors Affecting Synthesis and Characterization Techniques. *Journal of Nanomaterials*, 2014, pp. 1-12.

Pavlovic, E. and Kramer, E.J., 2011. Curing Temperature Effects on Network Structure and Chemistry of Silane Coupling Agent Layers and Their Influence on Water-Assisted Crack Growth. *The Journal of Adhesion*, 87, pp. 272-289.

Petryayeva, E. and Krull, U.J., 2011. Localized surface plasmon resonance: nanostructures, bioassays and biosensing—a review. *Analytica Chimica Acta*, 706(1), pp. 8–24.

Phan, C.M. and Nguyen, H.M., 2017. Role of Capping Agent in Wet Synthesis of Nanoparticles. *Journal of Physical Chemistry A*, 121, pp. 3213-3219.

Pillai, S., Catchpole, K.R., Trupke, T. and Green, M.A., 2007. Surface plasmon enhanced silicon solar cells. *Journal of Applied Physics*, 101, 093105.

Pinero, S., Camero, S. and Blanco, S., 2017. Silver nanoparticles: Influence of the temperature synthesis on the particle's morphology. *Journal of Physics: Conference Series*, 786, 012020.

Porter, C.E. and Blum, F.D., 2000. Thermal characterization of PMMA thin films using modulated differential scanning calorimetry. *Macromolecules*, 33(19), pp. 7016-7020.

Ramrakhiani, M., 2012. Nanostructures and their applications. *Recent Research in Science & Technology*, 4(8), pp. 14-19.

Ranabhat, K., Patrikeev, L., Revina, A.A., Andrianov, K., Lapshinsky, V. and Sofronova, E., 2016. An Introduction To Solar Cell Technology. *Journal of Applied Engineering Science*, 14(4), pp. 481-491.

Rehacek, V. and Hotovy, I., 2017. Deposition of gold nanoparticles from colloid on TiO<sub>2</sub> surface. *Journal of Electrical Engineering*, 68(6), pp. 487-491.

RGS, 2015. What are Solar Cells? [online] Available at: <<https://rgsenergy.com/how-solar-panels-work/what-are-solar-cells/>> [Accessed 11 April 2020]

Rodríguez, L., 2021. Why and how do solar panels degrade? 5 key factors. [online] Available at: <<https://ratedpower.com/blog/solar-panels-degradation/>> [Accessed 27 March 2022]

Sahoo, S.K., Manoharan, B. and Sivakumar, N., 2018. Introduction: Why Perovskite and Perovskite Solar Cells?. In: S. Thomas and A. Thankappan (eds.). *Perovskite Photovoltaics Basic to Advanced Concepts and Implementation*. Cambridge: Academic Press. pp. 1-24.

Saleema, N., Sarkar, D.K., Paynter, R.W. and Chen, X.G., 2011. Chemical Nature of Superhydrophobic Aluminium Alloy Surfaces Produced via a One-Step Process Using Fluoroalkyl-Silane in a Base Medium. *ACS Applied Materials & Interfaces*, 3, pp. 4775-4781.

Samsudina, M. S. N., Rahman, M. M. and Wahid, M. A., 2016. Power Generation Sources in Malaysia: Status and Prospects for Sustainable Development. *Journal of Advanced Review on Scientific Research*, 25(1), pp. 11-28.

Saengkaew, J., Le, D., Samart, D., Sawada, D., Nashida, M., Chanlek, N., Kongparakul, S. and Kiatkamjornwong, S., 2018. Superhydrophobic Coating from Fluoroalkylsilane Modified Natural Rubber Encapsulated SiO<sub>2</sub> Composites for Self-Driven Oil/Water Separation. *Applied Surface Science*, 462(31), pp. 164-174.

Scarabelli, L., Schumacher, M., Aberasturi, D.J., Merkl, J.P., Lacey, M.H., Oliveira, T.M., Janschel, M., Schmidtke, C., Bals, S., Weller, H. and Marzán, L.M.L., 2019. Encapsulation of Noble Metal Nanoparticles through Seeded Emulsion Polymerization as Highly Stable Plasmonic Systems. *Advanced Functional Materials*, 29(14), pp. 1809071.

Scott, A.J. and Penlidis, A., 2017. Copolymerization. In: J. Reedijk (ed.). *Reference Module in Chemistry, Molecular Sciences & Chemical Engineering*. Elsevier: Waltham, pp. 1-11.

Shanmugam, N., Pugazhendhi, R., Elavarasan, R.M., Kasiviswanathan, P. and Das, N., 2020. Anti-Reflective Coating Materials: A Holistic Review from PV Perspective. *Energies*, 13(10), pp. 2631

Shanti, R., Hadi, A.N., Salim, Y.S., Chee, S.Y., Ramesh, S. and Ramesha, K., 2017. Degradation of ultra-high molecular weight poly(methyl methacrylate-co-butyl acrylate-coacrylic acid) under ultra violet irradiation. *RSC Advances*, 7, pp. 112-120.

Shefer, A. and Gottlieb, M. (1992). Effect of crosslinks on the glass transition temperature of end-linked elastomers. *Macromolecules*, 25(15), pp. 4036-4042.

Simya, O.K., Radhakrishnan, P. and Ashok, A., 2018. Nanomaterials for Solar-Energy Generation. In: C.M. Hussain (ed.). *Handbook of Nanomaterials for Industrial Applications*. Cambridge: Elsevier. pp. 751-767.

Singh, M., Goyal, M. and Devlal, K., 2018. Size and shape effects on the band gap of semiconductor compound nanomaterials. *Journal of Taibah University for Science*, 12(4), pp. 470-475.

Singh, M.P., Keister, H.K., Matisons, J.G., Pan, Y., Zazyczny, J. and Arkles, B., 2014. Dipodal Silanes: Important Tool for Surface Modification to Improve Durability. *Material Research Society Proceedings*, 1648, pp. 1-6.

Solanki, C.S., 2015. *Solar photovoltaics: fundamentals, technologies and applications*. 3rd ed. Delhi: PHI Learning.

Solomon, S. D., Bahadory, M., Jeyarajasingam, A. V. and Rutkowsky, S. A., 2007. Synthesis and Study of Silver Nanoparticles. *Journal of Chemical Education*, 84(2), pp.322-325.

Song, K.C., Lee, S.M., Park, T.S. and Lee, B.S., 2008. Preparation of colloidal silver nanoparticles by chemical reduction method. *Korean Journal of Chemical Engineering*, 26(1), pp. 153-155.

Sterman, S. and Marsden, J.G., 1966. Silane Coupling Agents. *Industrial & Engineering Chemistry*, 58(3), pp. 33-37.

Sun, Y., Yin, Y., Mayers, B.T., Herricks, T. and Xia, Y., 2002. Uniform silver nanowires synthesis by reducing AgNO<sub>3</sub> with ethylene glycol in the presence of seeds and poly(vinyl pyrrolidone). *Chemistry of Materials*, 14(11), pp. 4736-4745.

Suriati, G., Mariatti, M. and Azizan, A., 2014. Synthesis of Silver Nanoparticles by Chemical Reduction Method: Effect of Reducing Agent and Surfactant Concentration. *International Journal of Automotive & Mechanical Engineering*, 10, pp. 1920-1927.

Sutha, S., Suresh, S., Raj, B. and Ravi, K.R., 2017. Transparent alumina based superhydrophobic self-cleaning coatings for solar cell cover glass applications. *Solar Energy Materials & Solar Cells*. 165, pp. 128-137.

Swami, A., Selvakannan, P.R., Pasricha, R. and Sastry, M., 2004. One-Step Synthesis of Ordered Two-Dimensional Assemblies of Silver Nanoparticles by the 108 Spontaneous Reduction of Silver Ions by Pentadecylphenol Langmuir Monolayers. *Journal of Physical Chemistry B*, 108(50), pp. 19269-19275.

Tang, L., Yang, J., Zhang, S., Yang, J. and Wu, Y., 2003. Emulsifier-Minor Emulsion Copolymerization of BAMMA-St-MAA (or AA)-N-MA. *Journal of Applied Polymer Science*, 92, pp. 2923-2929.

Tay, B.Y., 2019. *Nanofabrication and Characterization of Silver Nanoparticles*. Degree. Universiti Tunku Abdul Rahman.

Tay, B.Y., Chee, S.Y., Lee, C.L., Sepeai, S. and Aminuzzaman, M., 2020. Improvement of light-harvesting efficiency of amorphous silicon solar cell coated with silver nanoparticles anchored via (3- mercaptopropyl) trimethoxysilane. *Applied Nanoscience*, 10(9), pp. 3553-3567.

Temple, T.L., Mahanama, G.D.K., Reehal, H.S. and Bagnall, D.M. 2009. Influence of localized surface plasmon excitation in silver nanoparticles on the performance of silicon solar cells. *Solar Energy Materials & Solar Cells*, 93(11), pp. 1978-1985.

Todica, M., Stefan, T., Simon, S., Balasz, I. and Daraban, L., 2014. UV-Vis and XRD investigation of graphite-doped poly(acrylic acid) membranes. *Turkish Journal of Physics*, 38(2), pp. 261–267.

Troupis, A., Hiskia, A., and Papaconstantinou, E., 2002. Synthesis of Metal Nanoparticles by Using Polyoxometalates as Photocatalysts and Stabilizers. *Angewandte Chemie International Edition*, 41(11), pp. 1911.

Venkatesham, M., Ayodhya, D., Madhusudhan, A., Kumari, A.S., Veerabhadram, G. and Mangatayaru, K.G., 2014. A Novel Green Synthesis of Silver Nanoparticles Using Gum Karaya: Characterization, Antimicrobial and Catalytic Activity Studies. *Journal of Cluster Science*, 25(2), pp. 409-422.

Vidal, K., Gomez, E., Goitandia, A.M., Ibanez, A.A. and Aranzabe, E., 2019. The Synthesis of a Superhydrophobic and Thermal Stable Silica Coating via Sol-Gel Process. *Coating*, 9(10), pp. 627.

Vozel, K. and Arcon, D., 2011. *Solar Cells*. Ljubljana: Faculty of Mathematics and Physics, University of Ljubljana.

Willets, K.A. and Duyne, R.P.V., 2007. Localized Surface Plasmon Resonance Spectroscopy and Sensing. *Annual Review of Physical Chemistry*, 58, pp. 267-297.

Xu, L. and He, J., 2012. Fabrication of Highly Transparent Superhydrophobic Coatings from Hollow Silica Nanoparticles. *Langmuir*, 28(19), pp. 7512-7518.

Gan, X., Lv., R., Zhu, H., Ma. L.P., Wang, X., Zhang, Z., Huang, Z.H., Zhu, H., Ren, W., Terrones, M. and Kang, F., 2016. Polymer-Coated Graphene Films as Anti-Reflective Transparent Electrodes for Schottky Junction Solar Cells. *Journal of Materials Chemistry A*, 4(36), pp.13795-13802.

Yamak, H.B., 2013. Emulsion Polymerization: Effects of Polymerization Variables on the Properties of Vinyl Acetate Based Emulsion Polymers. *Intech Open Science*, (2), pp. 35-72.

Zaman, M., Ahmad, E., Qadeer, A., Rabbani, G., Khan, Rizwan H., 2014. Nanoparticles in relation to peptide and protein aggregation. *International Journal of Nanomedicine*, 9(1), pp. 899-912.

Zarick, H.F., Erwin, W.R., Boulesba, A., Hurd, O.K., Webb, J.A., Puretzky, A.A., Geohegan, D.B. and Bardhan, R., 2016. Improving light harvesting in dye-sensitized solar cells using hybrid bimetallic nanostructures. *ACS Photonics*, 3(3), pp. 385-394.



Zhang, Q.F., Myers, D., Lan, J., Jenekhe, S.A. and Cao, G.Z., 2012. Applications of light scattering in dye-sensitized solar cells. *Physical Chemistry Chemical Physics*, 14(43), pp. 14982-14998.

Zi, W., Ren, X., Xiao, F., W, H., Gao, F. and Liu, S., 2016. Ag nanoparticle enhanced light trapping in hydrogenated amorphous silicon germanium solar cells on flexible stainless-steel substrate. *Solar Energy Materials & Solar Cells*, 144, pp. 63-67.

## APPENDICES

### Appendix A

Calculation for band gap energy,  $E_{bg}$  for synthesized AgNPs:

$$E_{bg} = \frac{hc}{\lambda_{max}}$$

Where,

$$h \text{ (Planck's constant)} = 6.63 \times 10^{-34} \text{ m}^2 \text{ kg s}^{-1}$$

$$c \text{ (speed of light)} = 3.00 \times 10^8 \text{ m s}^{-1}$$

$\lambda_{max}$  (absorption wavelength in UV-Vis region)

When S value of DDA = 2.78,  $\lambda_{max} = 409 \text{ nm}$

$$\begin{aligned} E_{bg} &= \frac{(6.63 \times 10^{-34} \text{ m}^2 \text{ kg s}^{-1}) \times (3.00 \times 10^8 \text{ m s}^{-1})}{409 \times 10^{-9} \text{ m}} \\ &= (4.863 \times 10^{-19}) \times (6.242 \times 10^{18} \text{ eV}) = 3.036 \text{ eV} \end{aligned}$$

When S value of DDA = 16.7,  $\lambda_{max} = 415 \text{ nm}$

$$\begin{aligned} E_{bg} &= \frac{(6.63 \times 10^{-34} \text{ m}^2 \text{ kg s}^{-1}) \times (3.00 \times 10^8 \text{ m s}^{-1})}{415 \times 10^{-9} \text{ m}} \\ &= (4.793 \times 10^{-19}) \times (6.242 \times 10^{18} \text{ eV}) = 2.992 \text{ eV} \end{aligned}$$

When S value of DDA = 27.8,  $\lambda_{max} = 422 \text{ nm}$

$$\begin{aligned} E_{bg} &= \frac{(6.63 \times 10^{-34} \text{ m}^2 \text{ kg s}^{-1}) \times (3.00 \times 10^8 \text{ m s}^{-1})}{422 \times 10^{-9} \text{ m}} \\ &= (4.713 \times 10^{-19}) \times (6.242 \times 10^{18} \text{ eV}) = 2.942 \text{ eV} \end{aligned}$$

## Appendix B

Calculation for crystallite size by Debye-Scherrer equation:

$$D = \frac{k\lambda}{\beta \cos \theta}$$

Where,

k (Scherrer's constant) = 0.94

$\lambda$  (Wavelength of X-ray source) =  $1.5406 \times 10^{-10}$  m

$$\beta = \frac{FWHM \text{ in } 2\theta \times \pi}{180^\circ}$$

At Bragg's diffraction angle ( $2\theta$ ) of  $38.12^\circ$ ,

FWHM = 0.5482,  $\theta = 19.06^\circ$

$$\beta = \frac{0.5482 \times \pi}{180^\circ} = 9.568 \times 10^{-3}$$

$$D = \frac{0.94 \times (1.5406 \times 10^{-10} \text{ m})}{(9.568 \times 10^{-3}) \times \cos 19.06} = 16.01 \text{ nm}$$

At Bragg's diffraction angle ( $2\theta$ ) of  $44.36^\circ$ ,

FWHM = 0.6524,  $\theta = 22.18^\circ$

$$\beta = \frac{0.6524 \times \pi}{180^\circ} = 0.0114$$

$$D = \frac{0.94 \times (1.5406 \times 10^{-10} \text{ m})}{0.0114 \times \cos 22.18} = 13.73 \text{ nm}$$

At Bragg's diffraction angle ( $2\theta$ ) of  $64.46^\circ$ ,

$$\text{FWHM} = 0.5318, \theta = 32.23^\circ$$

$$\beta = \frac{0.5318 \times \pi}{180^\circ} = 9.282 \times 10^{-3}$$

$$D = \frac{0.94 \times (1.5406 \times 10^{-10} \text{ m})}{(9.282 \times 10^{-3}) \times \cos 32.23} = 18.44 \text{ nm}$$

At Bragg's diffraction angle ( $2\theta$ ) of  $77.43^\circ$ ,

$$\text{FWHM} = 0.6051, \theta = 38.72^\circ$$

$$\beta = \frac{0.6051 \times \pi}{180^\circ} = 0.0106$$

$$D = \frac{0.94 \times (1.5406 \times 10^{-10} \text{ m})}{0.0106 \times \cos 38.72} = 17.58 \text{ nm}$$

Calculation for average crystallite diameter of AgNPs:

$$D_{avg} = \frac{(16.01 + 13.73 + 18.44 + 17.58) \text{ nm}}{4} = 16.44 \text{ nm}$$

## Appendix C

Mass of centrifuge tube = 9.8404 g

Mass of centrifuge tube + AgNPs = 9.8860 g

Mass of AgNPs = 0.0456 g

The chemical equation of reduction of AgNO<sub>3</sub> by NaBH<sub>4</sub>:



Due to excess amount of reducing agent was added, the AgNO<sub>3</sub> would be limiting agent in this case. From the chemical equation shown above, it can be observed that one mole of AgNO<sub>3</sub> will produce one mole of Ag particles.

Calculation for theoretical value:

Mass of AgNO<sub>3</sub> = 0.1735 g

Molar mass of AgNO<sub>3</sub> = 169.87 g mol<sup>-1</sup>

Molar mass of Ag = 107.87 g mol<sup>-1</sup>

$$\text{mole} = \frac{\text{mass, g}}{\text{molar mass, g mol}^{-1}}$$

$$\text{Mole of AgNO}_3 \text{ used} = \frac{0.1735 \text{ g}}{169.87 \text{ g mol}^{-1}} = 1.021 \times 10^{-3} \text{ mol}$$

Based on the chemical equation shown above, one mole of  $\text{AgNO}_3$  will produce one mole of Ag, therefore:

$$\text{Mole of AgNO}_3 = \text{Mole of Ag} = 1.021 \times 10^{-3} \text{ mol}$$

$$\begin{aligned} \text{Theoretical mass of Ag} &= 1.021 \times 10^{-3} \text{ mol} \times 107.87 \text{ (g mol}^{-1}\text{)} \\ &= 0.1101 \text{ g} \end{aligned}$$

$$\begin{aligned} \text{Percentage yield} &= \frac{\text{actual mass, g}}{\text{theoretical mass, g}} \times 100\% \\ &= \frac{0.0456 \text{ g}}{0.1101 \text{ g}} \times 100\% = 41.4\% \end{aligned}$$

For calculate the concentration of AgNPs which re-dispersed in 15 mL of solvent:

1 mL of AgNPs solution obtains 0.0058 g of Ag

$$\text{Mole of Ag} = \frac{0.0058 \text{ g}}{107.87 \text{ g mol}^{-1}} = 5.377 \times 10^{-5} \text{ mol}$$

$$\text{mole} = \frac{\text{molar (M)} \times \text{volume (mL)}}{1000}$$

$$\text{Molar} = \frac{\text{mole} \times 1000}{\text{volume}}$$

$$\text{Molar} = \frac{5.377 \times 10^{-5} \text{ mol} \times 1000}{1 \text{ mL}} = 0.0538 \text{ M}$$

$$M_1V_1 = M_2V_2$$

$$(0.0538 \text{ M}) \times (1 \text{ mL}) = M_2 \times 15 \text{ mL}$$

$$M_2 = 3.585 \times 10^{-3} \text{ M}$$

## Appendix D

Details of experimental total solids content:

Polymer sample	Average polymer liquid (g)	Average polymer solids (g)	Total solids content (%)
0 wt% TMVS	1.0478	0.2085	19.90
5 wt% TMVS	1.0357	0.2090	20.18
7 wt% TMVS	1.0415	0.2185	20.98
9 wt% TMVS	1.0213	0.2154	21.09

$$* \text{Total solids content} = \frac{\text{Polymer solids}}{\text{Polymer liquid}} \times 100 \%$$

Calculation for theoretical total solids content for P(MMA-*co*-AA) copolymer with and without incorporation of TMVS:

Total weight of ingredients = 500 + weight of incorporated TMVS g

Total weight of comonomers = 100 + weight of incorporated TMVS g

$$\text{Total solids content} = \frac{\text{Total weight of comonomers (g)}}{\text{Total weight of ingredients (g)}} \times 100 \%$$

Calculation for percentage of conversion of the P(MMA-*co*-AA) copolymer with and without incorporation of TMVS:

$$\text{Monomer conversion} = \frac{\text{Actual total solids content (\%)}}{\text{Theoretical total solids content (\%)}} \times 100\%$$

For 0 wt% of TMVS:

Actual total solids content = 19.90%

$$\textit{Theoretical total solids content} = \frac{100 \text{ g}}{500 \text{ g}} \times 100 \% = 20.00\%$$

$$\textit{Monomer conversion} = \frac{19.90\%}{20.00\%} \times 100\% = 99.50\%$$

For 5 wt% of TMVS:

Actual total solids content = 20.98%

$$\textit{Theoretical total solids content} = \frac{107 \text{ g}}{507 \text{ g}} \times 100 \% = 21.10\%$$

$$\textit{Monomer conversion} = \frac{20.98\%}{21.10\%} \times 100\% = 99.41\%$$

For 7 wt% of TMVS:

Actual total solids content = 20.18%

$$\textit{Theoretical total solids content} = \frac{105 \text{ g}}{505 \text{ g}} \times 100 \% = 20.79\%$$

$$\textit{Monomer conversion} = \frac{20.18\%}{20.79\%} \times 100\% = 97.06\%$$

For 9 wt% of TMVS:

Actual total solids content = 21.09%

$$\textit{Theoretical total solids content} = \frac{109 \text{ g}}{509 \text{ g}} \times 100 \% = 21.41\%$$

$$\textit{Monomer conversion} = \frac{21.09\%}{21.41\%} \times 100\% = 98.48\%$$



## LIST OF PUBLICATIONS

Tay, B.Y., Chee, S.Y., Lee, C.L., Sepeai, S. and Aminuzzaman, M., 2020. Improvement of light-harvesting efficiency of amorphous silicon solar cell coated with silver nanoparticles anchored via (3- mercaptopropyl) trimethoxysilane. *Applied Nanoscience*, 10(9), pp. 3553-3567.

Lee, M.J.R., Chee, S.Y., Tay, B.Y., Lee, C.L., Lim, F.C. and Sepeai, S., 2021. Affixing poly(methyl methacrylate-co-acrylic acid) nanospheres with trimethoxyvinylsilane on silicon solar module to enhance its power conversion efficiency. *Journal of Materials Science*, 56(21), pp. 1-19.

